

UC Santa Barbara

UC Santa Barbara Electronic Theses and Dissertations

Title

Reduced-ordered in vitro models to study mechanical signaling through cell-cell contacts

Permalink

<https://escholarship.org/uc/item/6j31f1wk>

Author

Dow, Liam

Publication Date

2023

Peer reviewed|Thesis/dissertation

UNIVERSITY OF CALIFORNIA

Santa Barbara

**Reduced-ordered *in vitro* models to study mechanical signaling through cell-cell
contacts**

A dissertation submitted in partial satisfaction
of the requirements for the degree

Doctor of Philosophy

in

Biochemistry and Molecular Biology

by

Liam Paul Dow

Committee in charge:

Professor Beth L. Pruitt, Chair

Professor Dorit Hanein

Professor M. Cristina Marchetti

Professor Denise J. Montell

December 2023

The dissertation of Liam Paul Dow is approved.

Professor Denise J. Montell

Professor Dorit Hanein

Professor M. Cristina Marchetti

Professor Beth L. Pruitt, Committee Chair

December 2023

Reduced-ordered in vitro models to study mechanical signaling through cell-cell
contacts

Copyright © 2023

by

Liam Paul Dow

Acknowledgements

Everything that I am and everything that I've done is a product of everyone in my life. As hard as I've worked over the last five years, I'm certain it is impossible to be where I am without the help of many others. And so, I want to celebrate my PhD with them.

I was fortunate to grow up in a family that pushed me to explore my curiosity. My parents allowed me to pursue my interests and fully supported every aspect of my life. The older I get, the more impressed I am at their level of support. They've always had full confidence in me, or at least (and maybe more importantly), that's how I've felt. They taught me that what I got out of something was dependent on how much I put in. I learned to take pride in my work and responsibility for my actions. Because of you both, I take immense pride in the small details of every figure I make or every paper that I publish.

I'm thankful for my two older brothers, Nathan and Derek. Undoubtedly, they instilled in me a competitive nature that made me want to push myself. We shared many of the same teachers up through high school and my goal was clear: score a better grade than they did. The challenge was difficult. Nate and Derek are two of the smartest, most determined men I know. I'm thankful I had both of you growing up.

To my partner, Amanda, your unconditional support is unmatched. I've treasured our bike rides home after work, the coffee shops we've explored in Santa Barbara, and every moment in which we've helped each other become better researchers.

I can't talk about my family support without talking about my grandparents. Throughout my life, all four of them believed in me, often when I didn't believe in myself. Even now, my Nana and Grampa regularly send me copies of the Scientific American magazine. I can't imagine where I'd be without their support.

And of course, I've developed close friends who are like family. I'm thankful for my friend Henry, whom I lived with throughout my time at Lehigh. You've supported me in every aspect of my life and are the cornerstone of so many of my great experiences at Lehigh. To my other Lehigh friends, Cole, Gill, Katie, and Fei, I'm thankful for so many of our late-night talks about life and biology. There are so many other special people from my time at Lehigh that made me a better person and laid the foundation for my PhD: my academic advisor Dr. Susan Perry, my research advisor Dr. Frank Zhang, my philosophy professor Dr. Dillon, among many other friends and colleagues.

My success in graduate school has undoubtedly been helped by numerous other mentors. Dr. Jenna Balestrini taught me how to present science more effectively, including the "funnel" approach for an elevator pitch or ensuring context for every slide of a presentation. Dr. Pradeep Sathyanarayana and Dr. Aldona Karaczyn introduced me to the world of microRNAs and how we can use bioinformatics to study them in cancer. Dr. Leeya Engel introduced me to the world of using microsystems to control epithelial cells. Leeya, I'm thankful for all your advice over the years and am excited to continue our friendship!

I could not be more thankful for everyone (past and present) in the Pruitt Lab who has supported me, including Sam Feinstein, Marissa Gionet-Gonzales, Orlando Chirikian, Kerry Lane, Miguel Sanchez-Lozano, Gabby Villalpando Torres, Yair Kaufman, Erica Castillo, Anna Kim, Matthew Hopcroft, and Cheavar Blair. I joined the lab alongside Kerry, Orlando, and Sam and their friendships throughout my PhD have meant everything to me. I'm thankful that every day I came into the office or the lab, I had them to put life in perspective when research was the most stressful. In addition, I've had several fantastic undergraduate researchers including Reagan Kennedy, Katya Morozov, and Stacey Surace. I've been

thankful to have been a fellow within the BioPACIFIC Materials Innovation Platform, which provided a community for my interests in biomaterials. I made new friends and enjoyed conversations about my research with Dr. Juan Manuel Urueña and Dr. Angela Pitenis.

I've been supported by so many other faculty and staff at UCSB since the nature of my research is heavily interdisciplinary. My committee members Dr. Denise Montell, Dr. Dorit Hanein, and Dr. Cristina Marchetti have given me helpful advice and support in understanding electron microscopy, epithelia modeling, experimental procedures, paper writing, among others!

A unique part of my experience at UCSB was the work I did outside of research. I had opportunities to participate in professional development programs and even co-chaired the 22nd Annual Bioengineering Institute of California Symposium. In all these programs, I worked with several fantastic individuals including Elizabeth Jensen, Angelina Toporov, Leslie Edwards, Erin Kozaki, and Steve Ramirez (among others). During my PhD, it has been easy to feel research is my entire life. Working with you all in programs outside of research helped put my PhD into a bigger context.

I owe much of my success to my advisor and mentor, Dr. Beth Pruitt. Beth has given me the freedom to explore my ideas, test new experiments, and pursue my creative voice while communicating science. She has instilled in me a confidence as a researcher that will be invaluable in my career. Beth has also supported me in ways that go beyond research by helping me develop my career interests. For example, she has heavily supported (even encouraged) every professional activity I've been involved in. I'm incredibly thankful for the opportunities she's given me in my PhD. I recognize many other PhD students don't have the same opportunities that I've had. Beth, thank you for everything.

Finally, I'd like to acknowledge the numerous funding agencies over the last five years that have paid for my living stipends and research. These funds include: The UCSB Regents Fellowship, the NSF (award No. 1834760), the U.S. Army Research Office for the Institute for Collaborative Biotechnologies (award No. W911NF-19-2-0026), the NIH (R01 GM119948), the BioPACIFIC Materials Innovation Platform of the NSF (Award No. DMR-1933487), and travels grants from the UCSB Academic Senate.

Curriculum Vitae

Liam P. Dow

November 2023

RESEARCH INTERESTS

Biomaterials, mechanobiology, biophysics, cellular mechanics and biomechanics, and synthetic biology

EDUCATION

University of California, Santa Barbara

- *Doctor of Philosophy* in Biochemistry and Molecular Biology, with emphasis in Biophysics and Bioengineering
- Advisor: Dr. Beth L. Pruitt, Professor of Bioengineering, of Mechanical Engineering, and of Biomolecular Science and Engineering

Lehigh University, Bethlehem, PA

- *Bachelor of Science* in Bioengineering (*Cum Laude*), Psychology (minor) (2018)
- Emphasis in Biomechanics and Biomaterials

RELEVANT RESEARCH EXPERIENCE

Pruitt Lab, University of California Santa Barbara- *Graduate Researcher* (2018-Present)

- Utilized a custom fabricated MEMS device to apply shear forces to epithelia under high resolution microscopy
- Designed and fabricated a novel reduced order microsystem to study mechanisms of epithelial migration from mechanical force perturbations
- Implemented novel protein micropatterning techniques for structural analysis (via cryo-ET and X-Ray diffraction) of spatially regulated epithelial cells and cardiomyocytes
- Integrated a microfluidic system within a pneumatic cell stretching platform for long-term mechanical stretch studies
- Employed computational methods and machine learning based cell segmentation for high-throughput image analysis as a means to understand epithelial cell-cell communication from mechanical force perturbations
- Developed novel methods including dual protein extracellular matrix patterning to advance studies targeting the importance of cell-cell interactions in regulating cardiomyocyte contraction
- Developed a protocol to morphologically control cardiomyocytes on multi-electrode arrays for high-throughput studies of cardiomyocyte electrophysiology

BioPACIFIC Materials Innovation Platform, NSF- *Research Fellow* (2022-Present)

- Collaborated with chemists, biologists, and engineers to develop functional biomimetic and bioinspired materials for applications in synthetic biology
- Performed lab automation via ThermoFisher Scientific's Spinnaker microplate robot in parallel with Tecan Fluent and Momentum software interfaces

Valentine Lab, University of California Santa Barbara- *Graduate Rotation Student* (2018)

- Re-designed, modeled, and 3-D printed a custom cell stretching device to induce epithelial crowding
- Utilized computational techniques including digital image correlation (DIC) to characterize strain fields
- Generated a first-author research article

Xiaohui (Frank) Zhang Lab, Lehigh University - Research Assistant (2016-2018)

- Led measurements in mechanical binding interactions behind T-cell activation in CAR-T therapy using atomic force microscopy
- Analyzed relationships between mechanical stimulation and biochemical signaling in cells

Draper Laboratory, Cambridge, MA- Biomaterials Engineering Intern (2017)

- Team member in design, test, and fabrication of novel microfluidic platforms to optimize single cell electrotransfection

STARx™ Asthma and Allergy Center, Springfield, NJ- Project Engineer/Team Leader (2017-2018)

- Worked in a team of undergraduate engineers to design, prototype, and market an automated pollen detection device
- Led research on biological properties of pollen to enhance methods of sample classification
- Surveyed potential market and designed product with customer concept testing

Maine Medical Center Research Institute, Scarborough, ME - Research Intern (2016)

- Analyzed microRNA gene regulation in acute myeloid leukemia using bioinformatics
- Performed and designed solo experiments *in vitro* to test phenotypic effect of various protein inhibitors
- Discovered transcriptional regulation of miR-199b for the first time in leukemic cell lines

LEADERSHIP POSITIONS

- *Co-Chair*- UCSB Bioengineering Institute of California Symposium (2022)
 - Designed the program for the Biotech Industry Showcase
 - Organized and led a student committee to facilitate conference tasks and speaker management
 - Helped recruit over \$100k in sponsorship from local biotech companies
- *Graduate Mentor*- UCSB/U.S. Navy PIPELINES Program (2021)
 - Designed an 8-week summer project with the Navy for an undergraduate research team
 - Delegated tasks and projected goals for team members
 - Identified areas of need and support for the academic growth of the undergraduates
- *Chairperson*- 4th Annual UCSB Biotechnology Industry Showcase (2020)
 - Annual event that recruited 20+ biotech companies and 150+ attendees
- *Steering Committee Member* for 3rd Annual UCSB Biotechnology Industry Showcase (2019)
- *Co-founder and President*, BMES UCSB Student Chapter (2018-2023)
 - Campus organization that hosts professional, social, and outreach events
- *Speaker* -138th meeting of the Board of Trustees, UCSB (2019)

- Presented overview of research in advocacy for bioengineering funding at UCSB
*Audience members included UCSB chancellor and Dean of Engineering (2019)
- *Co-founder and executive board member, BMES Lehigh Student Chapter (2017)*

TEACHING AND MENTORSHIP

- *Teaching Assistant, ME258 (Mechanobiology)-Graduate level course (2020)*
 - Included independent lectures on i) Microscopy and soft lithography and ii) FRET Tension Sensors
- *Teaching Assistant, ENGR220B (Cellular Bioengineering) (2020)*
 - Designed and graded HW problems, led weekly office hours
 - Included guest lecture on protein micropatterning in mechanobiology
- *Research Mentees (2019-Present)*
 - Stacey Surace, Undergraduate Student, *UCSB (2022-Present)*
 - Daniella Walter, Graduate Rotation Student, *UCSB (2022)*
 - Katrene Morozov, Undergraduate Student, *UCSB (2021-2022)*
 - Reagan Kennedy, Undergraduate Student, *UCSB (2020-2021)*
 - Chrisangela Patrice Martin, *Georgia State University REU student (2020)*
 - Olivia Konttinen, Graduate Rotation Student, *UCSB (2019)*
 - Brendan Curran, Undergraduate Student, *Lehigh University (2017)*
 - Megan Gavey, Undergraduate Student, *Lehigh University (2017)*
- *Youth Innovation Club- Santa Barbara, CA (2018-Present)*
 - Science fair Project Adviser and math tutor
- *Senior Peer Mentor- Technical Entrepreneurship Capstone, Lehigh University (2018)*
 - Advised multiple teams of undergraduate engineers to design, develop, and market a product
- *Guest Lecturer- BioE 001, BioE020, Lehigh University (2017)*

MEMBERSHIPS AND SOCIETIES

- Peer Reviewer, *PNAS* and *ACS Biomaterials*
- American Physical Society, Biophysical Society, Biomedical Engineering Society, Sigma Xi (nomination only)
- NCAA Division 1 Lehigh University Cross Country, Track and Field- Athlete

AWARDS AND HONORS

- 3rd Place, Mechanical Engineering Grad Slam Competition, *UCSB (2021)*
 - Award given to best 3-minute research talk that is clear, direct, and engages diverse audiences
- Academic Senate Doctoral Student Travel Grant, *UCSB (2021)*
 - For giving an oral presentation at the MicroTas Conference in Palm Springs, CA
- NSF GRFP Honorable Mention (2020)
 - From NSF.gov: "The NSF accords Honorable Mention to meritorious applicants who do not receive Fellowship awards. This is considered a significant national academic achievement and provides access to cyberinfrastructure resources through the XSEDE."

- Graduate Students Association Conference Travel Grant Award, *UCSB* (2020)
 - For giving a presentation at the Biophysical Society Annual Meeting in San Diego, CA (2020)
- Regents Fellowship, *UCSB* (2018)
 - A year-long fellowship supporting research and lab-rotations in recognition of an outstanding scholastic record and promise of productive scholarship
- Student Forum Research Grant, *Lehigh University* (2017)
 - Additional research funds supporting development and implementation of atomic force microscopy experiments
- Susan D. Konkel Scholarship Recipient, *Maine Medical Center* (2016)
 - Financial support to study the effects of miRNA in acute myeloid leukemia

TECHNICAL AND RESEARCH SKILLS

- **Technical Experience:** Mammalian cell culture, microfluidics/microfluidic platforms, electrotransfection, fluorescence microscopy, confocal microscopy, atomic force microscopy and dynamic force spectroscopy, protein patterning and protein adsorption, protein conjugation, particle image velocimetry, CAD/3-D printing, cleanroom/microfabrication (chemical etching, vapor deposition, photolithography and development), polymer casting, western blotting, qPCR, flow cytometry
- **Computer/Programming Experience:** MATLAB, Python, ImageJ, Origin, ZEN, Micromanager, LASX, Adobe Illustrator, Inkscape, SolidWorks, L-Edit, VIC-2D
- **Engineering Management/Leadership:** Technical team leadership, project management (technical, schedule), engineering design

SELECT ABSTRACTS AND INVITED TALKS

1. Lane, K.V., **Dow, L.P.**, et. al., Dual-Protein Patterning to Investigate Effects of Cell-Cell Adhesions on hiPSC-CM Maturity, *Biophysical Society Annual Meeting- Oral presentation* (2023)
2. Parmar, T., **Dow, L.P.**, Pruitt, B.L., Marchetti M.C. Strain response of epithelial cell trains, *American Physical Society Annual Meeting- Oral presentation* (2023)
3. **Dow, L.P.** *, Morozov, K. *, Kim, A., Feinstein, S., Pruitt, B.L. Using cell segmentation to understand how changes in cell morphology contribute to epithelial force propagation, *22nd Annual Bioengineering Institute of California Symposium poster presentation* (2022).
4. **Dow, L.P.**, Kim, A., Morozov, K., et al., Collective mechanical signaling through cell-contacts, *Invited oral presentation for the American Physical Society Annual Meeting* (2022)
5. Parmar, T., **Dow, L.P.**, Pruitt, B.L., et al., Epithelial monolayer response to boundary mechanical perturbations, *American Physical Society Annual Meeting* (2022)
6. **Dow, L.P.**, Kennedy, R., and Pruitt, B.L. Linear micropatterned epithelial model to study migratory effects of intercellular force transfer (*MicroTas Annual Meeting Oral Presentation, peer reviewed paper with <9% acceptance for presentation, audience of 300-400 people, Palm Springs, CA, 2021*)
7. **Dow, L.P.**, A maskless and contactless tool for cell protein patterning and hydrogel fabrication, *Invited talk for UCSB Biological Nanostructures Lab Webinar Series* (2020)

8. **Dow, L.P.**, Engel, L., Garcia, M.A., et al., High Resolution Imaging of Cytoskeletal Response to Epithelial Mid-Plane Shear, *2020 Biophysical Society Meeting poster presentation* (2020)
9. **Dow, L.P.**, Engel, L., Garcia, M.A., et al., “Utilizing a MEMS Platform for Characterizing Epithelium Response to Shear”. *Presented at the 2019 BMES Annual Meeting, Philadelphia, PA* (2019).
10. Engel, L., Gaietta, G., **Dow, L.P.**, “Extracellular matrix protein micropatterning for whole-cell cryo-electron microscopy studies.” *Presented at the American Society for Cell Biology and European Molecular Biology Organization, San Diego, CA* (2018)
11. **Dow, L.P.**, Dragovich, M., Gavey, M., et al., “Characterization of the Primary Binding Interactions in CAR-T Therapy Using Atomic Force Microscopy.” *2018 Annual Northeast Bioengineering Conference, Drexel University, PA* (2018) AND *2017 BMES Annual Meeting, Phoenix, AZ* (2017)

SELECT PUBLICATIONS

1. **Dow, L.P.***, Surace, S.*, Morozov, K., et al. Cyclic stretch regulates epithelial cell migration in a frequency dependent manner via vinculin recruitment to cell-cell contacts” *BioRxiv*, 2023, doi: 10.1101/2023.08.19.553915
2. **Dow, L.P.**, Parmar, T., Kennedy, R., et al. “A linear micropatterned epithelial model to study force induced collective behavior” (*in preparation, to be submitted Fall 2023*)
3. Lane, K.V.*, **Dow, L.P.***, et. al. “Dual-Protein Patterning to Investigate Effects of Cell-Cell Adhesions on hiPSC-CM Maturity” (*in review, Lab on a Chip, 2023*)
4. **Dow, L.P.**, Parmar, T., Marchetti, C., Pruitt B.L. “Engineering tools for quantifying and manipulating forces in epithelia”, *Biophysics Reviews*, 2022, doi: 10.1063/5.0142537. Promoted as a Featured Article, chosen by editorial staff as “one of the journal’s best”.
5. **Dow, L.P.**, Gaietta, G., Kaufman, Y., et al. “Morphological control enables nanometer-scale dissection of cell-cell signaling complexes” *Nature Communications*, 2022, doi: 10.1038/s41467-022-35409-9
6. **Dow, L.P.**, Khankhel, A. H., Abram, J., et al. “3D-printable cell crowding device enables imaging of live cells in compression” *BioTechniques*, 2020, doi: 10.2144/btn-2019-0160
7. Peng, H., Borg, R. E., **Dow, L. P.**, et al. “Controlled phage therapy by photothermal ablation of specific bacterial species using gold nanorods targeted by chimeric phages”. *Proceedings of the National Academy of Sciences*, 2020, doi: 10.1073/pnas.1913234117
8. Engel, L., Gaietta, G., **Dow, L.P.**, et al. Extracellular matrix micropatterning technology for whole cell cryogenic electron microscopy studies. *Journal of Micromechanics and Microengineering*, 2020, doi: 10.1088/1361-6439/ab419a

**These authors contributed equally to this work*

Abstract

Reduced-ordered *in vitro* models to study mechanical signaling through cell-cell contacts

by

Liam Paul Dow

Active materials are a collection of self-driven units that independently operate to give a material unique, large-scale, global properties (e.g., flock of birds). Mammalian epithelia, which comprise our skin and provides a barrier layer for all our organs, is one of the best examples of active material. For example, when local regions of epithelial cells within a tissue are damaged, neighboring cells can rearrange via active migration to maintain the integrity of the tissue. As a material, the epithelium offers large potential in advancing synthetic biology for engineering active materials that can locally repair themselves when damaged, or globally alter their mechanical properties to adapt to a particular environment. The goal of my research is to understand how epithelial cells signal in response to mechanical cues, and how these changes influence their collective properties. This work will ultimately guide an approach to create synthetic materials with similar characteristics.

Recent work in our lab has demonstrated that mechanical forces on the epithelium, which occur regularly during development, also influence cell migration. These forces occur through tugging tensile forces between cells (e.g., neural tube development, gastrulation, lung epithelial stretch), sliding shear forces as cells slip past one another (e.g., gastrulation and fruit fly genitalia development), or some combination of the two. However, the molecular and biophysical mechanisms that result from epithelial cell-cell force transmission to drive collective migration are largely unknown. New experimental and computational

models can help answer new questions regarding how epithelial cells transmit mechanical signals. These experiments require external and often custom micromanipulation methods.

This thesis attempts to better understand the relationship between epithelial cell-cell signaling and global epithelium behavior on multiple scales. Each study (i.e., chapter) becomes progressively more reduced, starting at the tissue level and ending at the single cell level. Methods within each study involve designing and developing novel experimental platforms that apply mechanical stresses to epithelial tissue. We utilize a programmable cell stretching platform, protein patterning, high-throughput cell segmentation, direct micromanipulation of cell-cell contacts, among other experimental and computational methods. This multi-hierarchical model introduces new tools to better elucidate cell-cell mechanosignaling across the protein and tissue level.

TABLE OF CONTENTS

Acknowledgements	iv
Curriculum Vitae	viii
Abstract	xiii
TABLE OF CONTENTS	xv
LIST OF FIGURES	xix
LIST OF TABLES	xx
Chapter 1 Introduction	1
1.1 Thesis overview	1
1.2 Preface.....	4
1.3. Introduction.....	4
1.1. Properties of epithelial dynamics	5
Development	6
Homeostasis	7
Dynamic Signaling.....	7
1.2. Mechano-signaling in the dynamic epithelium.....	8
1.3. Choosing an experimental model system.....	10
1.4. Mechanical manipulation of the in vitro epithelium	12
1.4.A. 3-D spheroids and organoids.....	12
1.4.B. 2-D cell sheets	19
1.4.C. 1-D cell lines and cell doublets	31
1.4.D. Single cell micromanipulation systems.....	37
1.5. Biophysical in silico models of epithelial dynamics	40
1.5.A. Cell Edge Network Models.....	41
1.5.B. Continuum models	44
1.5.C. Agent based models.....	46
1.6. Discussion	47
1.6.A. Summary of local vs. global mechanical perturbation	47
1.6.B. Additional variables to consider for mechanical manipulation	49
1.6.C. Applications for synthetic biology and biomimetics	50
1.7. Acknowledgements	51
1.8. Conflict of Interest	51
1.9. Author Contributions.....	51
1.10. References	52
Chapter 2 Cyclic stretch of a 2-D epithelium.....	65
2.1 Preface.....	65
2.2. Abstract	66
2.3. Significance Statement.....	67
2.4. Introduction	67
2.5. Results	70
2.5.A. Cells adjust morphology in response to cyclic stretch	70
2.5.B. Low frequency stretch arrests epithelial migration	73
2.C. Adherens junction regulates arrest of cell movements	76
2.5.D. Cell-cell contacts recruit vinculin in response to low frequency stretch.....	78
2.5.E. High-throughput quantification of vinculin localization	79
2.5.F. Vinculin is necessary to suppress migration in response to cyclic stretch.....	81
2.6. Discussion and future directions	84

2.7. Methods and Materials	87
2.7.A. Cell Culture and Cell Seeding	87
2.7.B. Cyclic stretching experiments	88
2.7.C. High-throughput cell segmentation and ROI filtration	89
2.7.D. Statistics	89
2.7.E. Antibodies.....	89
2.8. Acknowledgements	90
2.9. Author Contributions.....	90
2.9. References	90
2.10. Supplemental Information.....	93
2.10.A. Device construction.....	93
2.10.B. Cyclic stretching experiments and migration	94
2.10.C. Particle Image Velocimetry analysis	95
2.10.D. Immunohistochemistry and imaging of stained devices	96
2.10.E. High-throughput cell segmentation and ROI filtration.....	96
2.10.F. Analysis of vinculin localization at cell-cell contacts.....	97
Chapter 3 Compression of a 2-D epithelium.....	103
3.1. Preface.....	103
3.2. Abstract	104
3.3. Introduction	104
3.4. Results	105
3.4.A. Device requirements.....	105
3.4.B. Device fabrication and assembly.....	106
3.4.C. Quantification of membrane strain.....	108
3.4.D. Uniaxial Compression of MDCK epithelial cells	109
3.5. Methods and Materials	111
3.5.A. Strain mapping analysis	111
3.5.B. Substrate properties and functionalization	112
3.5.C. Device Sterilization	112
3.5.D. Cell Culture	113
3.5.E. Imaging	113
3.5.F. Quantification of cell crowding	114
3.6. Conclusions	114
3.7. Author contributions:	114
3.8. Acknowledgements	115
3.9. Financial and Competing Interests Disclosure	115
3.10. References	115
3.11. Supplemental Information.....	116
3.11.A. Instructions for assembly	118
Chapter 4 Boundary strain of a 2-D epithelium	125
4.1. Preface.....	125
4.2. Abstract	126
4.4. Introduction	126
4.5. Results	130
4.5.A. Development of a high-throughput segmentation approach	130
4.5.B. Analysis of cell shape following shear perturbation	131
4.5.C. Boundary shear strain does not regulate proliferative capacity of the epithelium.....	138
4.5.D. Actomyosin regulates active cell shape response to boundary shear strain	139
4.5.E. F-actin stabilization elasticizes collective properties of the epithelium	141
4.6. Discussion and ongoing work	143
4.6.A. Effect of shear strain on the epithelium	143

4.6.B. Regulation of actomyosin dynamics via perturbation with blebbistatin and jasplakinolide	144
4.6.C. Current work	144
4.7. Methods	145
4.7.A. Image generation	145
4.7.B. Segmentation Analysis	145
4.7.C. Particle Image Velocimetry	146
4.7.D. Statistical analysis	147
4.8. References	147
4.9. Supplementary Information	149
Chapter 5 Boundary strain of a 1-D epithelium	151
5.1. Preface	151
5.2. Abstract	152
5.3. Introduction	153
5.4. Results	155
5.4.A. Development of a 1-D micromanipulation model	155
5.4.B. Boundary step strain promotes collective cell behavior	156
5.4.C. Wave-like oscillations of a 1-D epithelium	158
5.4.D. Distinct responses of cell behavior based on cell-cell contact orientation under mechanical load	159
5.4.E. Modulation of cell-cell contacts via ECM patterning alters collective migration	161
5.5. Methods and Materials	163
5.5.A. Particle Image Velocimetry	163
5.5.B. Assembly of custom probes	164
5.5.C. Probe preparation	165
5.5.D. Micromanipulation and Microscopy	165
5.5.E. Strain Analysis	165
5.5.F. Protein micropatterning	166
5.5.G. Cell culture	167
5.5.H. Calculation of stacked nuclei	167
5.7. Discussion and future directions	168
5.8. Acknowledgements	170
5.9. References	170
Chapter 6 Structural characterization of epithelial doublets	172
6.1. Preface	172
6.2. Abstract	173
6.3. Introduction	174
6.4. Results	177
6.4.A. Contactless grid handling and micropatterning	177
6.4.B. Characterization of protein micropatterns	179
6.4.C. Mechanical characterization of carbon film	181
6.4.D. Confinement of epithelial cell pairs	182
6.4.E. Correlative light and cryo-EM/ET visualization of cell-cell contacts	184
6.4.F. Cryo-FIB milling of cell-cell contacts	186
6.5. Methods and Materials	189
6.5.A. Grid preparation and handling	189
6.5.B. Photopatterning and protein functionalization of EM grids	189
6.5.C. Atomic force microscopy	191
6.5.D. Generation of new cell line stably expressing EGFP-alpha E catenin	192
6.5.E. Preparation of micropatterned grids, cell plating and titration for cryo-ET	193
6.5.F. Vitrification and cryo-EM screening	194

6.5.G. Cryo-FIB Lamella preparation	194
6.5.H. Correlative Light and Cryo-EM, cellular cryo-Tomography	195
6.5.I. Tomographic reconstruction, volume processing and segmentation	196
6.5.J. Optimization of imageable regions on 200-mesh Quantifoil copper/gold grid squares using micropatterning.	197
6.6. Data Availability	198
6.7. Acknowledgements	198
6.8. Conclusions and Discussion	199
6.9. References	203
6.10. Supplemental Information	206
Chapter 7 Mimicking cell-cell interactions in a single cell model	216
7.1. Preface	216
7.2. Abstract	217
7.3. Introduction	218
7.4. Results and discussion	220
7.5. Methods and Materials	222
7.5.A. Protein patterning glass coverslips	222
7.5.B. Preparation of polyacrylamide hydrogels	223
References	225
Chapter 8 Conclusions and future directions	227
8.1. Application of reductionist epithelial models	227
8.2. New methods contributed and expansion of existing methods	228
8.2.A. Experimental tools	229
8.2.B. Analytical tools	231
8.3 Expanding on biology	233
8.3.A. How does mechanical stretch regulate epithelial behavior?	233
8.3.B. <i>In vivo</i> relevance	237
8.4. Future directions and shortcomings	241
2-D epithelial models	241
1-D epithelial models	242
Epithelial doublets	243
Single cell epithelial models	244
8.5. Concluding remarks	244
8.6. References	245
Appendix	248
A.1 Segmentation analysis and segmentation scripts	248
A.2. Particle Image Velocimetry Scripts for 1-D line analysis	251
Averaging X vector displacements for 1-D line data	251
Generating a kymograph from PIV data	252
Determining wave period from 1-D oscillations	253
A.3. Fabrication and preparation of pneumatic uniaxial cell stretching devices	254
A.4. Setting up microfluidic perfusion system for pneumatic cell stretcher	255
A.5. MDCK Cell Culture	256
Recipe for basal medium used for microscopy experiments	257
A.6. Primo micropatterning	258
Sample Preparation	258
Patterning	258
Protein Adsorption	258
A.7. Gluing beads on micropipettes for custom probes	259
List of materials	259
Protocol	259

A.8. Setting up 1-D micromanipulation experiments.....	260
A.9. Immunohistochemistry protocol.....	263
Necessary Solutions:	263
Protocol:	264
A.10. Protocol for custom PDMS stencils	264

LIST OF FIGURES

Figure 1.1. In vitro experimental models of varying complexity used to study collective epithelial mechanics.	5
Figure 1.2. Mechanosignaling at the adherens junction aids in collective cell migration.	9
Figure 1.3. In vivo experimental models.....	11
Figure 1.4. In vitro 3-D experimental models.	16
Figure 1.5. Global and local deformations of epithelia.	20
Figure 1.6. In vitro 2-D experimental models.	30
Figure 1.7. In vitro 1-D experimental models.	36
Figure 1.8. <i>In silico</i> models.	41
Figure 2.1. Demonstration of uniaxial stretch device and segmentation of epithelial cells after cyclic stretch.....	72
Figure 2.2. Low frequency cyclic stretch reduces epithelial migration in a directionally independent manner.	76
Figure 2.3. The extracellular domain of E-cadherin is necessary for reducing migration after 0.1 Hz stretching.	78
Figure 2.4. 0.1 Hz cyclic stretch transiently regulates vinculin recruitment to cell-cell contacts.	80
Figure 2.5. Vinculin regulates migratory response of MDCK cells to cyclic stretch, but not cell morphology.....	83
Figure 3.1. Device design and construction compatible for long-term cell culture and live-cell imaging.	107
Figure 3.2. Digital image correlation demonstrates and quantifies linear strain of substrate.	109
Figure 3.3. Substrate compression successfully crowds cells for live-cell extrusion studies.	110
Figure 4.1. Jammed v.s. unjammed epithelium.	129
Figure 4.2. Workflow for high-throughput cell segmentation.....	131
Figure 4.3. Mechanical shear propagates changes in cell shape that dissipate over time.	136
Figure 4.4. Long-term implications of boundary shear strain on epithelial cell shape.....	137
Figure 4.5. Boundary shear strain does not drive changes in proliferative capacity of epithelium.	138
Figure 4.6. Inhibition of actomyosin isolates passive deformations of boundary shear strain on shape change.	140
Figure 4.7. Actin polymerization drives changing morphology in response to epithelial shear.	142
Figure 5.1. Micromanipulation of epithelial 1-D train model.	156
Figure 5.2. Boundary step strain on 1-D epithelium promotes collective migration.....	158
Figure 5.3. Oscillations of epithelium on lines.....	159
Figure 5.4. Distinct cell migration responses to either tension or shear.....	160
Figure 5.5. Underlying extracellular matrix organization regulates collective migration speed.	163
Figure 6.1. Micropatterning of holey carbon EM grids using photomolecular adsorption.	178
Figure 6.2. Nanoscale characterization of the micropatterning of holey carbon EM grids using photomolecular adsorption.	180
Figure 6.3. Mechanical characterization of carbon film cell substrate.	182

Figure 6.4. Confinement of epithelial cell pairs on patterned holey carbon electron microscopy grids.	183
Figure 6.5. Correlative light and cryo-EM/ET visualization of cell-cell contacts in PTK-1 cells adhering to micropatterns.	185
Figure 6.6. In situ cellular tomography of shape-guided thinned region of micropatterned adhering PTK-1 cell-cell contacts.	188
Figure 7.1. Dual-protein patterning of PA hydrogels.	221
Figure A.0.1. Perfusion setup for cyclic cell stretching experiments	256

LIST OF TABLES

Table 1.1. Engineered approaches used to probe and infer mechanics of epithelia.	48
Table 3.1. Materials List and Assembly Instructions: 3-D printed parts.....	117
Table 3.2. McMaster-Carr Parts	117

Chapter 1

Introduction

1.1 Thesis overview

This thesis attempts to elucidate the relationship between epithelial cell-cell signaling and epithelia behavior on multiple scales. Each study (i.e., chapter) becomes progressively more reduced, starting with 2-D cell sheets and ending at the single cell level. Methods within each study involve designing and developing novel experimental platforms that apply mechanical stresses to epithelial tissue. Experimentally, I used several different tools to exert these strains in different forms across different studies (e.g., a pneumatically regulated elastomeric cell stretcher, a 3-D printed cell compression device, micromanipulation with custom probes, and ECM protein patterning). From my experiments, I have also integrated several modes of automated and quantitative image analysis. A brief description of each chapter is included below.

Chapter 1: Introduction

We highlight the importance of cellular migration, the role of mechanosignaling in its regulation, and the need for mapping *in silico* biophysical models onto *in vivo* and *in vitro* experiments. Furthermore, we introduce a range of *in vitro* reduced order models from 3-D tissues to single cells in controlled environments and how we can obtain new insights at these different scales. These *in vitro* epithelial models provide context for the remaining chapters of this thesis.

Chapter 1 is reproduced from: Dow, Liam P., et al. "Engineering tools for quantifying and manipulating forces in epithelia." *Biophysics Reviews* 4.2 (2023). Doi: 10.1063/5.0142537 with the permission of AIP Publishing.

Chapter 2: Cyclic stretch of a 2-D epithelium

While cyclic cell stretching platforms have revealed responses of the epithelium such as cell reorientation and gap formation, few studies have investigated the long-term effects of cyclic stretch on cell migration. We measured the migratory response of the epithelium to a range of physiologically relevant frequencies and stretch. This work demonstrates a critical role for frequency dependence in epithelial response to mechanical stretch.

Chapter 3: Compression of a 2-D epithelium

We designed and fabricated, using low-cost 3D printing technologies, a device that enables direct control of cell density in epithelial monolayers. This device allows long-term culturing of cells on pre-tensioned substrates until the user decreases the tension, thereby inducing compressive forces in plane and subsequent instantaneous cell crowding. Moreover, the low-profile device is completely portable and can be directly mounted onto an inverted optical microscope

Chapter 3 is reprinted and reformatted with permission from the following:

Dow, L. P., Khankhel, A. H., Abram, J., & Valentine, M. T. (2020). 3D-printable cell crowding device enables imaging of live cells in compression. *BioTechniques*, 68(5), 275-278.

Chapter 4: Boundary strain of a 2-D epithelium

Recently, we have demonstrated local shear perturbation to induce specific modes of collective, global epithelial migration via actomyosin dependent intercellular signaling.

However, it is unclear how morphological changes in cells contribute to these migration responses. By developing high-throughput and automated segmentation methods, we conducted a spatiotemporal analysis connecting cell morphology to cell migration.

Chapter 5: Boundary strain of a 1-D epithelium

In vitro studies of single, adherent epithelial cells lack the force transduction mechanisms of cell-cell contacts, while 2-D epithelial sheets lose information about directional epithelial movements to both the x and y directions. Therefore, we developed an innovative 1-D epithelial model with a custom micromanipulation system that enables boundary strain.

Chapter 6: Structural characterization of epithelial doublets

Protein micropatterning enables robust control of cell positioning on electron-microscopy substrates for cryogenic electron tomography (cryo-ET). However, the combination of defined cell boundaries and the underlying electron-microscopy substrate (EM-grids) provides a poorly characterized microenvironment for cell biology. Because substrate stiffness and morphology affect cellular behavior, we devised protocols to characterize the nanometer-scale details of the protein micropatterns on EM-grids by combining cryo-ET, atomic force microscopy, and scanning electron microscopy. Our protein micropatterning workflow provides the means to control both positioning and morphology of epithelial cell doublets to determine nanometer details of punctate adherens junctions.

Chapter 6 is reprinted and reformatted under Attribution 4.0 International (CC BY 4.0) license from: Dow, L. P., Gaietta, G., Kaufman, Y., Swift, M. F., Lemos, M., Lane, K.,

... & Hanein, D. (2022). Morphological control enables nanometer-scale dissection of cell-cell signaling complexes. *Nature Communications*, 13(1), 7831.

Chapter 7: Mimicking cell-cell interactions in a single cell model

Single cells are abundantly used in *in vitro* models, yet lack cell-cell contacts that are known to have critical roles in cell function. In this work, I developed innovative methods in protein micropatterning to mimic cell-cell interactions for improving the maturity of single cell iPSC cardiomyocytes.

1.2 Preface

All contents from this chapter are fully published and reproduced from: Dow, L.P., Parmar, T., Marchetti M.C., Pruitt, B.L., "Engineering tools for quantifying and manipulating forces in epithelia." *Biophysics Reviews* 4.2 (2023). Doi: 10.1063/5.0142537 with the permission of AIP Publishing. Adaptations have been made to section headings to be consistent with the formatting of this thesis. Within this reproduced manuscript, I led the conceptualization, visualization, and writing of the original draft, specifically for all experimental studies. Toshi Parmar supported the conceptualization and writing of the original draft by leading the discussion of *in silico* studies (section 1.5). Cristina Marchetti and Beth Pruitt obtained funding for the study and supervised the project, while also contributing to the writing and editing of the manuscript.

1.3. Introduction

This paper reviews approaches for inferring and applying mechanical forces while observing epithelial dynamics. Our ultimate goal is to help researchers close the loop between *in silico* and experimental (*in vivo* and *in vitro*) biophysical models for both

understanding and predicting collective epithelial cell behaviors. Sections 1.1-1.3 motivate the need to understand cellular migration, the role of mechanosignaling in its regulation, and the need for mapping *in silico* biophysical models onto *in vivo* and *in vitro* experiments. Section 1.4. introduces a range of *in vitro* reduced order models from 3-D tissues to single cells in controlled environments and how we can obtain new insights at these different scales (Figure 1.1). Section 1.5 reviews the three most common classes of *in silico* biophysical models and their benefits and limitations. Finally, Section 1.6 discusses how these experimental and *in silico* biophysical models can be integrated and inform each other.

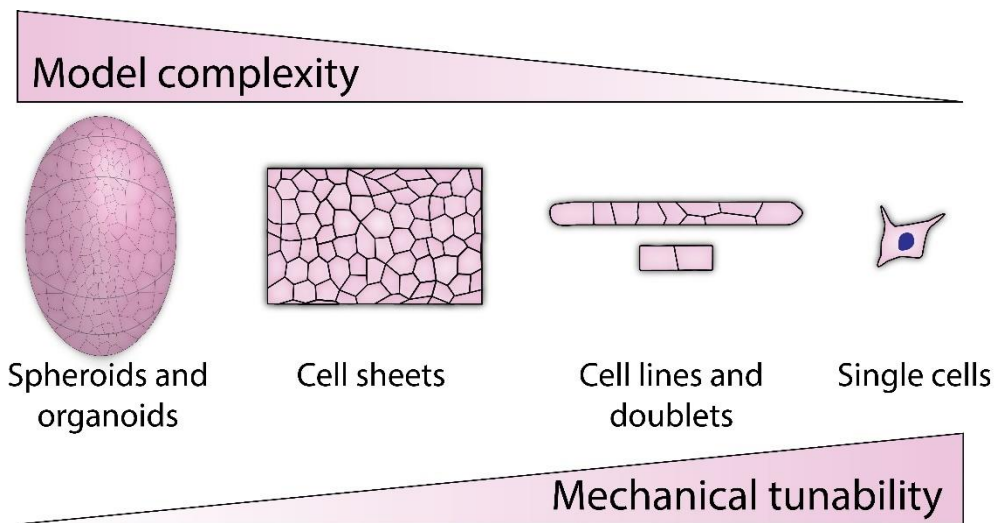


Figure 1.1. In vitro experimental models of varying complexity used to study collective epithelial mechanics.

(left) Spheroids and organoids are the most complex in vitro models. Cell sheets and cell lines are amenable to engineering interventions that allow researchers to investigate the impact of external forces on the epithelium. (right) The simplest model, a single cell, can also be useful to infer properties of collective cell behavior.

1.1. Properties of epithelial dynamics

The collective properties of epithelia define their abilities to perform tasks integral to life including tissue growth and development¹⁻¹⁰, wound repair¹¹⁻¹⁴, nutrient absorption¹⁵, and preventing pathogenic invasion¹⁶. As an active material, the epithelium and its collective

properties are defined by changes at the cellular level. These collective properties are a combination of cellular movements within the tissue, cell renewal, cell death, and inter/intracellular tensions¹⁷⁻²⁰. For example, epithelial migration patterns facilitate changes in cell division and cell death necessary for tissue morphogenesis^{14,21,22}. In the healthy intestinal epithelium, migration from the intestinal crypt drives cellular extrusion at the top of the villus²². In zebrafish injury, significant cell migration, proliferation, and extrusion are observed to occur simultaneously during wound repair¹⁴. For many processes that dictate epithelial dynamics, collective cell migration is a reoccurring trait that defines the physical state of the epithelium.

Development

The controlled collective movements of epithelial cells are necessary for the growth and formation of tissues during development¹⁻¹⁰. Embryonic processes including gastrulation, epiboly, oogenesis, and convergent extension that require epithelial migration are seen ubiquitously across different model organisms. During gastrulation, the migration of cells drives furrow formation and creation of germ layers^{2,3}. During epiboly, epithelial cells spread in a coordinated manner to cover the entire embryo⁵. During convergent extension as portions of the embryo change shape or elongate, cells must actively migrate and rearrange to mitigate tissue deformation and maintain tissue integrity⁶⁻¹⁰. Even after development, epithelial migration continues to be essential for the homeostasis of mature tissues across all organisms.

Homeostasis

Adult tissue is often thought of as an immobile epithelium that provides functions like filtration of waste products or nutrients while also acting as a barrier to infectious agents. However, continuous cell renewal and collective epithelial movements are critical for regulating many aspects of adult tissue. The repair of epithelial damage (i.e., wounds) occurs both internally (e.g., lungs, gut) and externally (e.g., skin) and requires the coordinated movement of epithelial cells¹¹⁻¹⁴. Without proper epithelial homeostasis and wound repair, our organs are at risk of pathogenic invasion, poor nutrient absorption, and ultimately organ failure.

Dynamic Signaling

Collective cell migration can be prompted by various cues: directional fluid flow²³, chemical (chemotaxis)²⁴, physical (plithotaxis)^{25,26}, bio-interface (haptotaxis)²⁷, substrate stiffness (durotaxis)²⁸, and even electrical (galvanotaxis)²⁹. These migratory regulators, or taxis processes, have been extensively reviewed^{27,28,30-33}. However, existing studies on the relationships between mechanosignaling pathways and epithelial migration at the tissue level often neglect localized, intercellular mechanical forces and long range dynamic changes that can influence migration³⁴⁻³⁶. Whether in a developing tissue or adult tissue, the epithelial environment is not static. It is incredibly dynamic. Many mechanical forces occur within these environments in a localized or regionalized context via local tissue deformation. Developing tissues continuously bend, fold, constrict, or stretch, imposing local forces on groups of cells^{8,22,37-45}. An open question is to what extent mechanical perturbations regulate cell migration, and if these resulting cellular movement patterns can be predicted *in silico*. An increased understanding of epithelial cell migration will be critical to predicting and

controlling deviations from normal development and adult epithelial tissue homeostasis. Testing and validating these models requires new controlled techniques for applying mechanical perturbations *in vitro*.

1.2. Mechanosignaling in the dynamic epithelium

At the cellular level, epithelial cells exert forces on neighboring cells as well as on the extracellular matrix (ECM). Neighboring cells are "stitched" together by cell-cell adhesions, where homotypic binding of E-cadherins is thought to initiate binding of like cells. E-cadherins then indirectly link to junction-supporting F-actin bundles via intracellular intermediate proteins such as β -catenin and α -catenin⁴⁶, making up adherens junctions (Figure 1.2.a). Cadherin complexes are further stabilized by other proteins such as vinculin and p-120 catenin^{47,48}. Mechanical cues can either release the catenin proteins from the adherens junction or recruit them, which have implications on the stability of cell-cell adhesion and cell behavior⁴⁹⁻⁵². Cell-cell contacts are then stabilized by other junctions, e.g., tight junctions and desmosomes, which further reinforce or regulate cell-cell adhesion^{53,54}. Mechanically linked cells also bind to the ECM via focal adhesion complexes and hemidesmosomes⁵⁵. These complexes anchor to F-actin and other cytoskeletal filaments^{56,57}. During migration, branching F-actin pushes the cell membrane forward within protrusions known as lamellipodia. The adhesion sites between cells and their substrate that guide lamellipodia formation are known to experience mechanical cross-talk. For example, the number of adhesion sites, types of integrin mediated adhesions (via different ECM proteins), or viscoelastic relaxation can all influence the persistence and speed of cell migration^{27,28,58}. Many of these mechanisms operate through mechanotransduction pathways to indirectly modulate intracellular signaling. For example, branching F-actin can be regulated by

rhoGTPases, including *cdc42* and *Rac1*^{59,60}. Lamellipodia at the front of the cell work in unison with actomyosin driven contractions at the rear to propel the cell forward with a lateral front-rear polarity (Figure 1.2.b). While lamellipodia are most commonly observed on leader cells at the edge of an expanding epithelium, cryptic lamellipodia are produced by follower cells to chase leader cells^{61,62}. As leader cells migrate, they can induce tension on follower cells to guide follower cell polarization via E-cadherin and Merlin^{4,34}. However, cells behind leader cells can help determine leader cell migration^{63,64}. Therefore, there exists an intricate network of mechanical regulation among cell-cell and cell-ECM interactions to guide cell migration.

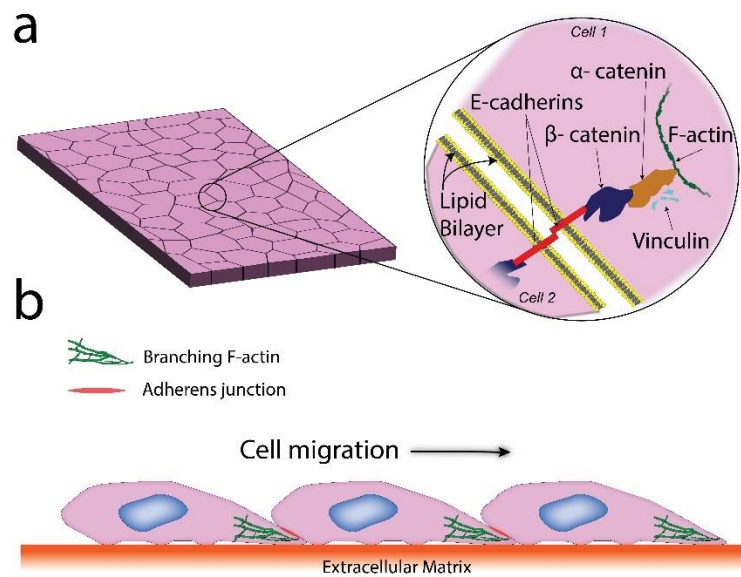


Figure 1.2. Mechanosignaling at the adherens junction aids in collective cell migration.

(a) The force-sensitive adherens junction has been shown to regulate mechanical forces between cells and dissipate them via intercellular signaling. (b) Cross-section of collectively migrating epithelial cells, which rely on adherens junction to mechanically link cells together and transduce signals.

Many of these mechanical complexes (e.g., intercellular tension, cell contractility and cell traction), along with shape descriptors (e.g., cell area and perimeter) can be used as inputs within *in silico* biophysical models. For example, factors that affect cell-cell and cell-

ECM adhesion (e.g., cadherins, integrins, desmosomes, and hemidesmosomes) can be modeled as frictional forces^{65,66}; cells must overcome these adhesions to migrate along the substrate. By manipulating these different variables experimentally, experiments and theoretical models can help inform one another to help researchers both understand and predict intercellular signaling and force propagation.

1.3. Choosing an experimental model system

In vivo epithelial models have illustrated the necessary role for collective migration in tissue repair and development. These models most commonly include zebrafish (e.g., epiboly, gastrulation) and *Drosophila* (e.g., germ band extension, gastrulation, border cell migration, wing development) though other systems exist⁶⁷. To isolate mechanistic elements associated with cell migration, observational studies often rely on genetic knockouts and pharmacological approaches combined with imaging techniques. Light microscopy has been particularly valuable. For example, fluorescent labels have helped researchers understand protein localization during specific developmental events, including the distribution of myosin during cellular movements in *Drosophila*⁶⁸. More recently, several engineered interventions have helped identify the role of mechanical forces in *in vivo* epithelia⁶⁹. For example, Förster Resonance Energy Transfer (FRET) sensors encoded into *Drosophila* revealed that mechanical tension through cell-cell contacts is critical in directing cell movement^{4,70,71}. Oil and actuated ferrofluid droplets have been used to infer tissue forces in zebrafish using known mechanical properties of the droplets^{72,73}. Recent advances in cell segmentation (i.e., reducing cell-cell borders to a polygonal packing structure) have offered a non-invasive method to infer forces between cells within *Drosophila* and quail⁷⁴⁻⁷⁷. Laser ablation, a more invasive technique, has helped validate these force inferences⁷⁷ (Figure

1.3.b). Laser ablation can also be used to induce wounds to study collective cell dynamics during wound healing of the *Drosophila* pupae⁷⁸. More recently, "synthetic mechanosignaling" tools (i.e., optogenetics) have been expanded to inhibit or facilitate protein function in a spatiotemporal manner. For example, optogenetically controlled RhoA has been used to manipulate mechanical forces during *Drosophila* tissue folding and morphogenesis^{79,80} (Figure 1.3.a).

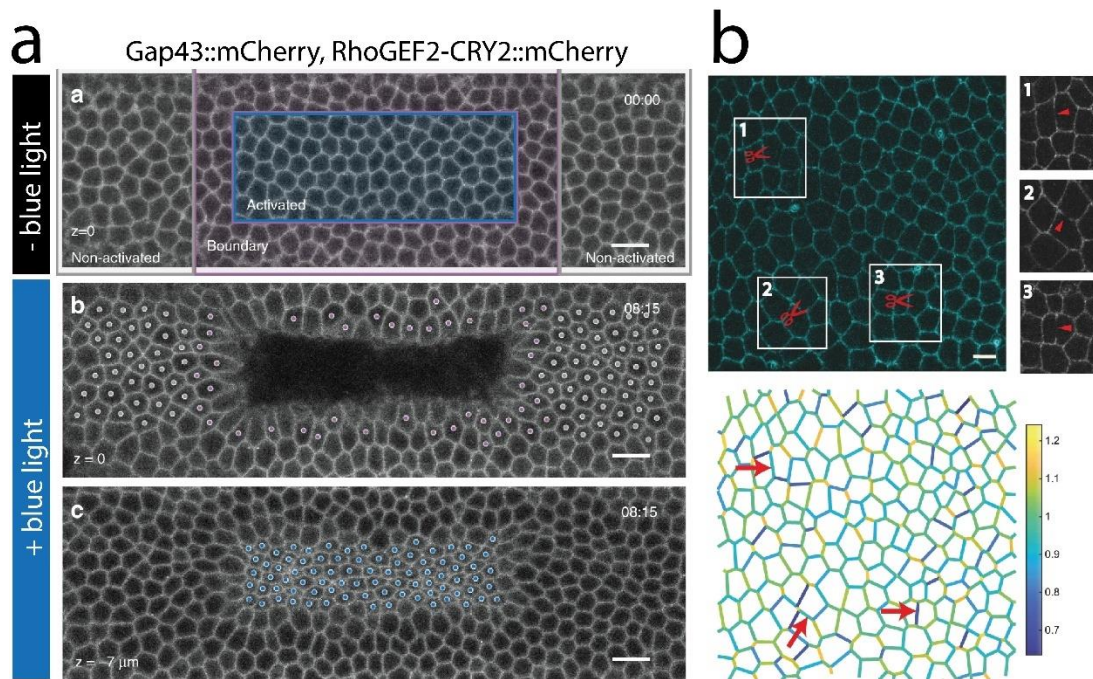


Figure 1.3. In vivo experimental models.

(a) Optogenetic RhoGEF2 can be used to trigger apical constriction of specific cells in the *Drosophila* embryo. (b-top) Laser ablation of cell-cell junctions in the *Drosophila* notum has validated (b-bottom) segmentation inferred intercellular tension levels. Figures adapted from (a) Izquierdo, Quinkler, and De Renzis, *Nature Communications*. 9, 1-13 (2018)⁷⁹ and (b) Kong et al., *Scientific Reports*. 9, 1-12 (2019)⁷⁷ under Creative Commons Attribution 4.0 International (CC BY 4.0). Scale bars: a= 10 μm, b= 5 μm.

Despite the physiological relevance of *in vivo* models, they are complex. Numerous interacting variables in the *in vivo* environment make it difficult to isolate the effect of mechanical forces on epithelial growth and migration. Specifically, it is difficult to directly

connect cell-cell mechanics and local mechanical tissue deformations to tissue rheology (i.e., migration). Furthermore, *in vivo* biophysical studies are often expensive with experimental setups that may be difficult or elaborate. *in vitro* studies can supplement those done *in vivo* by providing information under more controlled conditions where single variables (e.g., traction force) are manipulated. Biophysical *in silico* models can then help by providing continuous feedback between theory and experiments.

In this introduction, we describe micromanipulation tools available to probe collective epithelial dynamics (with a focus on migration) in four scales of *in vitro* models: spheroids/organoids, tissue sheets, cell lines/doublets, and single cells. For each of these cellular structures, we review the following themes: i) methods to infer forces, ii) methods to apply forces (including controlling the biophysical environment and local vs. global mechanical manipulation), and iii) limitations/advantages of the model system. Finally, we discuss biophysical *in silico* models that can inform and guide our understanding of the experiments.

1.4. Mechanical manipulation of the *in vitro* epithelium

In vitro experiments allow control of boundary conditions and tissue geometry while quantitatively describing the relationship between spatiotemporal mechanical inputs and epithelial migration. A number of devices that allow the application of mechanical perturbations to an epithelium *in vitro* have been proposed and will be reviewed below.

1.4.A. 3-D spheroids and organoids

Spheroids and organoids are powerful 3-D *in vitro* models that offer the possibility of carrying out high-throughput assays in a controlled microenvironment. Many 3-D *in vitro*

models are valuable for answering questions related to disease or understanding tumor invasion (i.e., metastasis), phenomena extensively reviewed elsewhere⁸¹⁻⁸³. Our interest is in how organoids have been used to study epithelial collective dynamics (i.e., migration and mechanosignaling)⁸⁴.

In vitro organoids are most commonly generated from stem cells that differentiate into clusters representative of the cell types found in organs, typically on glass or gel substrates (sometimes referred to as "bottom-up" assembly)⁸⁵⁻⁸⁷. Alternatively, spheroids are manufactured "top-down" either by mixing multiple cell types in a mold or by allowing a sheet of a single cell type to fold or aggregate into a 3-D structure⁸⁸⁻⁹⁰. Spheroid and organoid models have both been deployed to mimic healthy and pathological tissue microenvironments, reviewed here⁹¹. For example, stem cells can differentiate in 3-D to form an intestinal epithelium for disease modeling⁸⁵ or be directed to form an intestinal lumen through biofabrication methods^{92,93}.

Methods to infer force from 3-D spheroids and organoids

Inferring forces exerted or transmitted by epithelia help researchers connect mechanical cues to epithelia behavior. When considering how engineering tools can be implemented for 3-D *in vitro* studies to measure migration and mechanosignaling, we do not need to look much further than methods used *in vivo*. These shared methods for *in vitro* applications have answered a variety of questions on epithelial cell behavior. Additionally, they have utilized human derived cells. For example, cell segmentation via image analysis has been used to discover an increase in fluidity of human carcinoma epithelial cells during tumor progression⁸⁸ (Figure 1.4.a). Other methods referenced earlier, including FRET

molecular tension sensors⁹⁴ and oil droplets embedded in the tissue⁹⁰ (1.4.b.) are amenable to *in vitro* 3-D systems as well.

While both *in vivo* and 3-D *in vitro* epithelia consist of large multi-cellular tissues, *in vitro* environments offer several additional approaches for inferring cellular forces. Since organoids or spheroids can exist on a substrate or within an extracellular medium⁹⁵, traction force microscopy (TFM) or monolayer stress microscopy can be used to infer local cellular stresses to help researchers understand the forces that drive migration⁹⁶. To perform TFM, gels such as polyacrylamide (PA) or polydimethylsiloxane (PDMS) are fabricated with embedded fluorescent microbeads^{96,97}. Cells exert traction on the gels, resulting in measurable displacements of the beads, from which one can infer the forces or traction stresses that generate the corresponding displacements⁹⁸. TFM is a particularly powerful force inference technique as it can be used to dissect the temporal and spatial variations of tractions associated with collective cell movements in different environments. For example, studies of ovarian tumor spheroids have shown that cancer cell clusters generate force to gain access to the submesothelial environment. By blocking force transmitting proteins (i.e., $\alpha 5\beta 1$ integrin, talin I and myosin II), researchers were able to block metastatic escape of ovarian cancer cells⁹⁹. Furthermore, TFM can be combined with protein dysregulation methods to determine how specific proteins regulate epithelia traction and migration. For example, suppression of E-cadherin and induction of basement membrane expression influenced branching morphogenesis (i.e., migration) of stratified epithelia in a 3-D spheroid model¹⁰⁰. An alternative form of TFM involves individual cells or whole spheroids grown on fabricated elastic micropillars^{101,102}, where pillar deflection provides a direct measurement of traction force. Additional methods include elastically compressed PA "force sensors" embedded

within the tissue itself, which can connect local mechanical forces to changes in cell behavior. This method has shown that increased pressure near the core of a carcinoma spheroid is accompanied by cell shape anisotropy and minimal cell proliferation¹⁰³. Custom tools have also been built, such as microtweezers, to measure the stiffness of organoids^{102,104}. Methods that can quantify and measure mechanical stresses within 3-D epithelial models can help researchers understand the complicated relationship between intercellular forces and migration. Direct manipulation of the microenvironment can also provide information on causal relationships, as discussed in the next section.

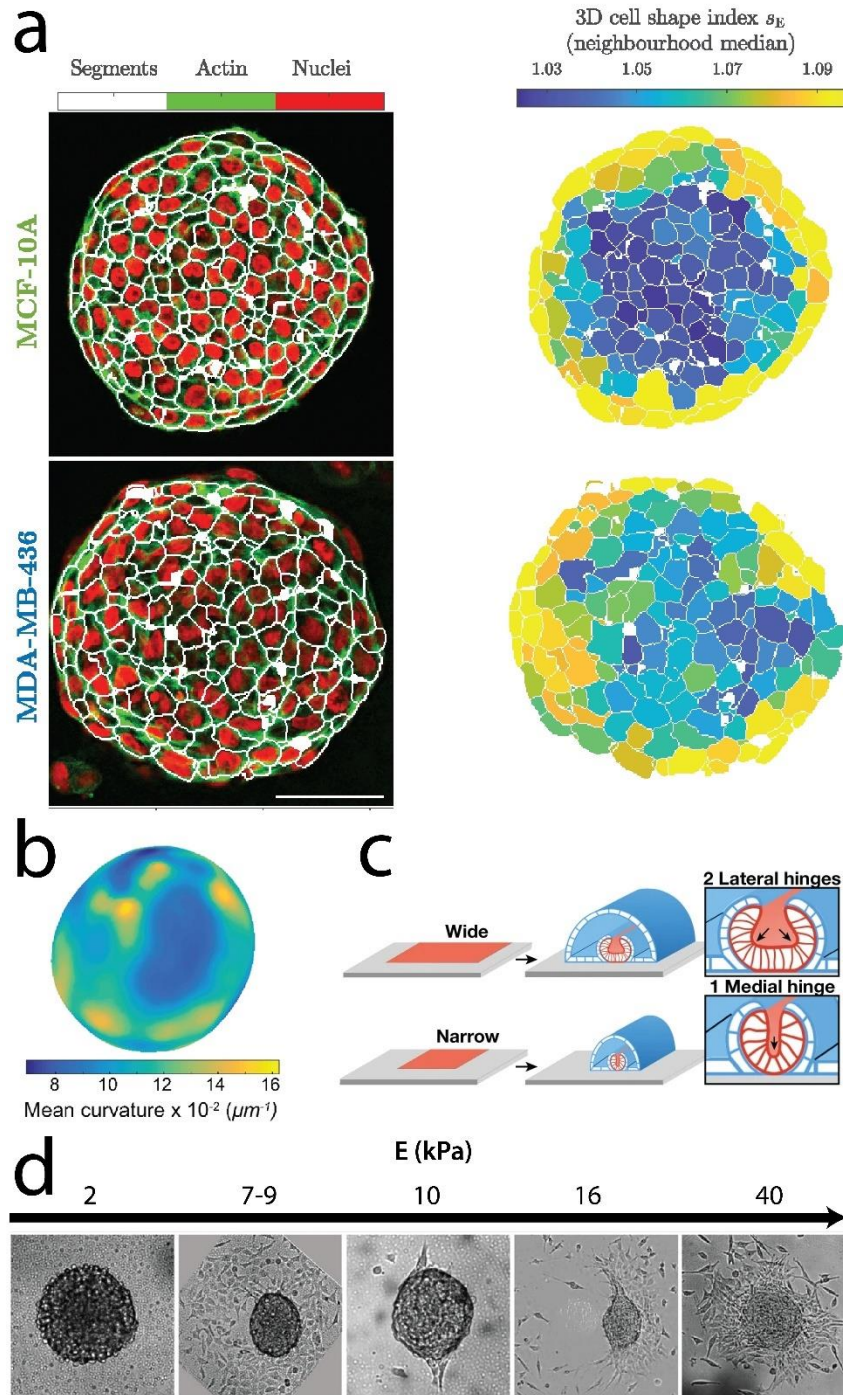


Figure 1.4. In vitro 3-D experimental models.

(a) Cell segmentation has been used to quantify cell shape and subsequent increase in tissue fluidity for cancerous (MDA-MB-436) compared to noncancerous (MCF-10A) breast epithelial spheroids⁸⁸. (b) 3-D fluorocarbon oil droplets embedded in mesenchymal cell aggregates can map out the internal forces exerted by cells⁹⁰. (c) To control organoid development, the underlying geometry of the ECM can be controlled⁴³ or (d) the stiffness to regulate tissue organization and cell migration¹⁰⁵. Figures adapted from (a) Grosser et al., Phys. Rev. X. 11, (2021)⁸⁸ and Lucio et al., Scientific Reports 7, 1-11

(2017)⁹⁰ under Creative Commons Attribution 4.0 International (CC BY 4.0). Figure (c) adapted with permission from Karzbrun et al., Nature 599, 268-272 (2021)⁴³. Copyright 2021 Springer Nature. Figure (d) adapted from Beaune et al., Proc. Natl. Acad. Sci. U.S.A 115, 12926-12931 (2018)¹⁰⁵. Copyright 2021 National Academy of Sciences of the United States of America. Scale bars: a=100 μm

Methods to apply force to 3-D spheroids and organoids

Engineering the biophysical microenvironment

There are several methods to engineer the microenvironment of a spheroid or organoid, including altering substrate stiffness, ECM composition, or geometric confinement. Each method may be used to mimic specific conditions (e.g., disease states) and connect these inputs to changes in collective epithelia behavior.

Tailoring substrate stiffness is one method that enables researchers to measure changes in tissue fluidity under specific pathological conditions. For example, altering the substrate rigidity of murine sarcoma spheroids resulted in different forms of motile behavior, ranging from a “running spheroid” to a flattened spheroid moving as a film¹⁰⁵ (Figure 1.4.d.). In other studies, tunable substrate stiffness can regulate collective migration via changes in tissue folding¹⁰⁶.

Changing the ECM is another minimally invasive way to alter the collective dynamics of a spheroid. Some studies have shown that the concentration of ECM can change the degree of migration of tumor spheroids¹⁰⁷. In collagen for example, human mammary gland organoids show increased branching and migration¹⁰⁸.

Spheroids or organoids can be subjected to varying degrees of geometric confinement as well. By varying the spatial constraints, researchers can recapitulate a diseased or developmental microenvironment. For example, patterned substrates of different geometries have been used to regulate the tube size and folding architecture in the development of neural

tube organoids⁴⁴ (Figure 1.4.c.). Tailoring geometric confinement is commonly done using pre-determined geometric patterns of ECM for cell growth and migration. These shapes can be sized and designed for diverse studies ranging from single cells^{109–111} to entire monolayers and tissues^{25,112}. Several methods can be used to fabricate specific shapes or patterns of ECM. Popular methods include microcontact printing¹¹³, co-polymerization via hydrogel “lift-off”¹⁰⁹, and light-induced photomolecular adsorption of proteins^{114–116}.

Beyond changing the substrate stiffness or the geometry of the microenvironment, cellular biomechanics can also be tuned by introducing biochemical reagents, pharmacological approaches, or gene editing^{94,95}. For example, genetic mutation of force sensitive α -catenin revealed that tension at the adherens junction is critical to the formation of multi-cellular structures during epithelial spheroid development¹¹⁷.

Organoid and spheroid models have largely focused on engineering the microenvironment of 3-D *in vitro* systems and measuring force generation, deformations, or fluidity. Thus far, there are limited engineered devices (e.g., cell stretchers) applied to loading or deforming epithelial spheroid or organoids^{118,119}.

Local force application

In vitro spheroids and organoids are also advantageous in that they allow local force gradients to occur naturally as they would *in vivo*. Relating local mechanical deformations to global cell migration or tissue rheology remains, however, challenging. The methods used to apply local forces to 3-D cellular structures are largely the same *in vivo* and *in vitro*. Optogenetic "synthetic mechanosignaling" has for instance been used to demonstrate the role of the WNT pathway in embryonic dynamics¹²⁰ and that of the Notch1 pathway in breast

cancer cells¹²¹. Laser ablation has been used to relax tension on ECM fibers and reduce tumor invasion⁸⁹.

Advantages and limitations of 3-D spheroids and organoids

3-D *in vitro* multi-cellular structures provide important models for the study of *in vivo* mechanosignaling. They are advantageous in several ways. They are cost-effective, relatively high-throughput, and offer control over cell types and the microenvironment. They retain, however, substantial complexity. Multiple cell types or self-organizing structures can make it difficult to introduce and isolate mechanical variables. Their large size can also hinder imaging accessibility and dissection at the molecular level. Overall, spheroid and organoid models are largely advantageous for modeling disease or cancer invasiveness, but don't often re-capitulate collective migration seen in developing embryos or wound repair.

1.4.B. 2-D cell sheets

The reduced dimensionality of 2-D cell sheets allows researchers to introduce mechanical perturbations that control, limit, or enhance cellular movements (Figure 1.5.). Within an *in vitro* 2-D environment, cells explore the XY plane typically on an ECM coated substrate made from a hydrogel, plastic, or glass. 2-D epithelial sheets also exist *in vivo* (e.g., lungs, kidneys, intestines), though may have different regions of folding and diverse topologies depending on the organ.

Methods to infer force from 2-D cell sheets

Just as in other experimental models, extensive information about cellular behavior can be extrapolated through time-lapse or video microscopy. In a 2-D system, however, researchers can answer questions about collective cell behavior in a more controlled

environment with specific mechanical inputs. For example, wound healing assays are a common method to better understand cell migration. Open gaps or “wounds” in an otherwise confined system are most commonly created using physical barriers^{34,122,123} or scratch assays^{124,125}. Cellular migration in these 2-D systems can be imaged by wide-field fluorescence and bright-field imaging modalities (Figure 1.6.a)⁶³. Fluorescence microscopy combined with wound healing assays and genetic knockdown experiments has matched transcription factor (TF) regulation or activation of pathways to migration of cells. For example, mechanical tension between cell-cell contacts causes the release of junctional merlin to the cytoplasm, which activates Rac1 and subsequent lamellipodium formation for cell migration³⁴.

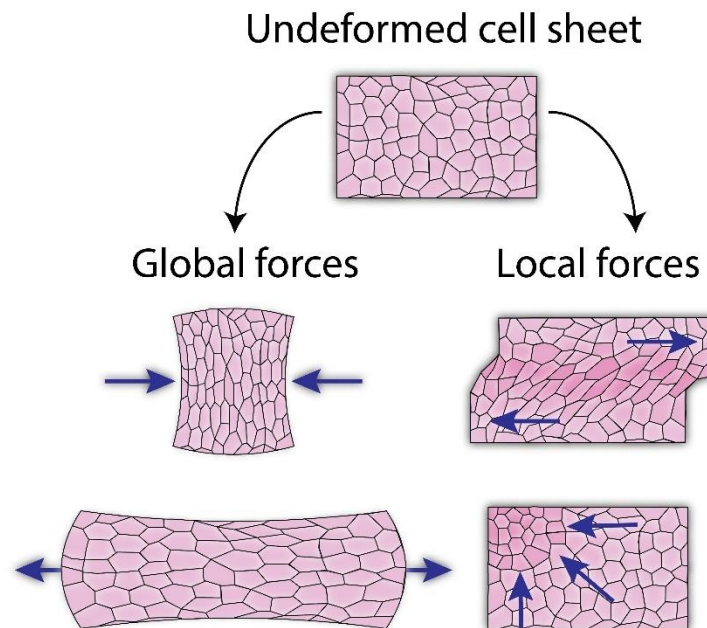


Figure 1.5. Global and local deformations of epithelia.

Epithelial tissues experience a range of mechanical forces, some of which are (left) global and (right) local. Most engineered devices, including cell stretchers, have mimicked global forces (e.g., compression and tension) by applying a more evenly distributed strain field throughout the tissue using elastomeric substrates. Few studies have focused on local forces and their impact on epithelial collective behavior. These forces can originate from local regions of deformation (e.g., shear forces, tissue bending, or apical constriction).

Time-lapse image stacks can be used to quantify cell migration and can also be combined with multiple force inference techniques that are more difficult in 3-D systems. Particle image velocimetry (PIV) is a widely used tool to quantify cellular movements by capturing the migratory "flow" of cells across the XY plane^{35,126,127}. Images are broken down into an array of windows, each with a distinct arrangement of pixels that can be tracked between frames. PIV is especially useful in quantifying migration directionality and velocity. Combining migration tracking with TFM in expanding cell monolayers has revealed a highly heterogeneous spatio-temporal distribution of traction forces that extend throughout an epithelial sheet⁶⁴. TFM combined with fluorescent live-cell imaging can further reveal how cytoskeletal filaments influence cell migration¹²⁸ or change structure as a function of mechanical tension at cell-cell contacts^{129–131}.

Beyond video microscopy used for TFM or PIV, segmentation tools are increasingly deployed to relate cellular structure to epithelia mechanics^{76,132,133}. For example, cell morphology obtained from segmentation of tissue imaging has helped predict changes in cell tractions or cell movements during cell migration⁶³. Shape descriptors derived from epithelial cells (e.g., area, perimeter, mean cell shape) can then be used as useful inputs for *in silico* biophysical models. Since segmentation can also be used to infer intercellular tension¹³⁴, combining tools such as segmentation and PIV provides powerful opportunities to connect the mechanical state of the cell-edge network and epithelial migratory behavior.

With imaging methods on an even smaller spatial scale, researchers can start to determine the proteins responsible for transmitting mechanical load during traction and migration. For example, E-cadherin FRET probes have shown E-cadherin is under tension as cell-cell contacts are actively stretched¹³⁵. Interestingly, this tension seems to relax over

time¹²⁹. These same sensors have also shown E-cadherin tension is highest inside expanding monolayers compared to the leading edge, corroborating TFM data^{64,128}.

A more invasive method to infer force properties of cell-cell contacts is laser ablation. Laser ablation can also be used to induce wound closure for single cells (e.g., apoptotic induced extrusion), which can be used to assess the mechanics behind localized wound closure^{21,136}. However, as mentioned in the previous section, laser ablation is invasive, requires specific equipment, and single cuts can affect the tension states of other regions of the tissue.

Methods to apply force to 2-D cell sheets

Engineering the biophysical microenvironment

Many methods exist to manipulate the microenvironment of epithelial sheets for the purpose of connecting mechanical inputs to collective epithelia behavior: geometric confinement, substrate stiffness, substrate topography, and ECM composition.

Geometric confinement within a 2-D environment provides a passive way to constrain a tissue and thereby manipulate interfacial tension on specific regions of cells. Geometric confinement via protein micropatterning indirectly applies edge tensions and intercellular tensions to cells which can influence their collective dynamics. For example, protein shapes designed for higher amounts of interfacial tension (e.g., star vs. circle) have been shown to control locations of cellular extrusion events within the tissue via changes in nematic order²¹. Furthermore, protein patterns have regulated migratory oscillations and proliferation patterns as a function of geometric confinement^{112,137,138}.

Beyond regulating the geometric confinement to control the collective motion of cellular sheets, the stiffness of the underlying substrate can also be tuned by creating hydrogels of varying polymerization parameters^{39,139}. Different stiffnesses can be used to mimic specific disease states and correlate these conditions to changes in the expansion of an epithelium. Physiological stiffnesses of epithelia are generally reported in the range of 1-500 kPa (depending on the tissue or if malignant)^{140,141} accompanied by changes in collective cell dynamics (e.g., stiffness and migration¹⁴²). Stiffer substrate conditions can also regulate the rate of wound closure by increasing actomyosin dynamics, YAP activation, and subsequent migration rates^{143–145}.

One can additionally engineer substrates with nanofabricated topography to investigate substrate based mechanotransduction (e.g., microgrooves¹⁴⁶) of expanding or confluent epithelial sheets. Substrate topography has been shown to increase the persistence of migration of MCF10A epithelial cells¹⁴⁷, which is likely influenced by their ability to re-orient and elongate along the direction of the groove¹⁴⁸. On a larger scale, the topography of the ECM has been altered to have curvature (i.e., hills and valleys) on the order of microns¹⁴⁹, which has implications for tissue thickness and nuclear morphology.

Studies have also manipulated collective cell migration by tuning the underlying ECM. Different ECM proteins (e.g., laminin, fibronectin, collagen, and their various subtypes) have different binding domains that connect to various integrin α and β subunits of cells. These integrin sub-units subsequently regulate cell migration differently, as quantified in an expanding 2-D epithelium. For example, fibronectin has been shown to enhance migration and alter epithelial organization in both developing and adult tissues^{150–152}. In another study, fibronectin *gradients* have been attributed to directional cell migration, with

implications for cellular collectives¹⁵³. ECM concentration has also been shown to affect migration speed of epithelial keratocytes, where cell collectives had a lower velocity on denser collagen networks¹⁵⁴.

The way in which researchers modify the biophysical environment, whether it be via ECM modification or altering substrate stiffness, will largely depend on the questions at hand. 2-D epithelial models enable a large combination of force inference techniques such as traction force microscopy or migration analysis within a confined or expanding sheet.

Global force application

To directly study the effect of cell-cell mechanics on collective cell migration, engineers have designed and utilized novel systems such as elastomeric cell stretchers. These polymer stretching devices are made from commonly used elastomers (i.e., PDMS or silicone rubber) and when stretched are assumed to apply a homogeneous, global strain field across the *entire* tissue. Cell stretchers can provide a useful approach for tackling several open questions in epithelia mechanics. Future studies may for instance examine temporal variations, downstream effects on cell migration, or employ different substrates, such as ones based on viscoelastic materials.

Cell stretchers can vary in several ways, starting with their actuation methods. Stretch actuation can be induced pneumatically via vacuum^{155–157}, mechanically^{158–160}, or through a dielectric elastomer actuator^{161,162} (Figure 1.6.b. and 1.6.c.). Furthermore, cell stretchers can induce either uniaxial or biaxial strain on a tissue in a static or cyclic dependent manner. Some have been 3-D printed^{159,163} or have been easily fabricated^{133,158} to improve accessibility. They have even been commercialized (*Flexcell International Corporation, Red Dog Research, Strex Cell*). Several reviews have been written solely on cell stretching

devices^{164,165}. Here we will focus on studies that have examined the role of stretch in regulating epithelia organization and intercellular signaling within a 2-D sheet.

Uniaxial tension: The simplest uniaxial stretchers apply a static stretch to the substrate and enable the observation of the tissue response. These methods may be useful to gain fundamental insight into how epithelial cells handle mechanical load. For example, uniaxial tension has connected force sensitive proteins at cell-cell contacts to mitotic activity and division along the axis of stretch¹⁵⁵. It has also shown that mechanical strain on E-cadherin drives the initial stages of the cell cycle via β -catenin and YAP activation^{156,166}. In addition to demonstrating the importance of direct cell-cell linkages, such experiments have established that stretch activated ion channels such as Piezo1 influence cell division, causing phosphorylation of the ERK pathway and driving cells into mitosis¹⁶⁷. Intercellular tension can also orient the mitotic spindle during cell division^{155,168}. Taken together, preferential division along the long axis of stretched cells¹⁵⁵ may be an adaptive mechanism for epithelial cells to combat external mechanical stresses¹⁶⁹ and facilitate tissue elongation and renewal. Beyond the role of static stretch in epithelial cell division, static stretch has been shown to limit epithelial cell migration¹³³. However, this migratory response can depend on the cell type, as stretch increased directed migration of fibroblasts¹⁷⁰. Additional experiments will help elucidate the mechanisms of static stretch in collective epithelial behavior.

Devices with more complex actuation methods (e.g., vacuum controllers¹⁷¹ or innovative systems built from LEGOsTM¹⁵⁸ have been engineered to study the role of cyclic stretch on epithelial behavior. Studies have shown that during cyclic uniaxial stretch, cell orientation changes periodically in intestinal epithelial cells¹⁷² and endothelial cells^{173,174}. This phenomenon has been observed in fibroblasts as well^{175,176}. On a molecular level,

changes in cellular reorientation have been correlated with restructuring of the cytoskeleton^{173,177} or to the growth of focal adhesions in osteosarcoma epithelial cells¹⁷⁸. Interestingly, cyclic stretch has shown minimal effect on nuclei positioning or nuclei orientation¹⁵⁸. Stretch-induced reinforcement mechanisms, including cell division and cytoskeletal restructuring, are, however, limited in their capacity to maintain epithelia integrity, as the tissue eventually ruptures when subjected to high stretch amplitudes and frequencies¹⁷⁹.

Biaxial tension: Biaxial cell stretchers can apply uniform strains resulting in uniform tissue growth and may be more physiologically relevant for certain tissue types (e.g., lung). Most studies employing biaxial stretch have focused on cyclic protocols. It was found that, while both cyclic uniaxial and biaxial stretch induce gap formation^{179,180}, biaxial cyclic stretch can also increase the ability of epithelial monolayers to withstand chemical disruption, as seen with human pulmonary artery endothelial cells¹⁸⁰. Cyclic stretch under physiologically relevant stretch also induced a quicker recovery of gaps/wounds compared to higher pathological stretch, potentially due to increased activation of Rac¹⁸¹. The variations in the ability of epithelial wounds to form or repair may also be associated with the magnitude of applied stretch or the density of the epithelium itself¹⁷⁹.

Cell stretchers continue to be optimized for higher imaging resolution¹⁶⁰ and fabrication accessibility^{133,158,159,182}. In addition to cell stretchers that exert tension, devices that apply both uniaxial and biaxial compression to manipulate cell packing and extrusion have also been developed^{158,159,183}. Devices have been custom engineered to probe the mechanics of suspended epithelia¹⁸⁴ in either compression¹⁸⁵ or tension¹⁸⁴. Unlike traditional cell stretching studies, suspended monolayers are devoid of cell-ECM interactions and can be

used to isolate the effect of cell-cell interactions on epithelia behavior. Mechanical stretch of a suspended epithelium has validated that stretch causes division along the long axis rather than along the monolayer stress axis¹⁸⁶. When subjected to compression, a suspended epithelium buckles in a manner reminiscent of an elastic material, but recuperates tension in an actomyosin dependent manner¹⁸⁵. Of course, the limitation of studying suspended epithelia is its lack of cell migration. An open question moving forward is how observed changes at cell-cell contacts correlate to changes in collective cell migration throughout the tissue.

Devices that apply global forces to epithelia have been instrumental in unlocking how cell-cell contacts respond to mechanical load, but more local approaches are needed to dissect how these mechanical loads are propagated through an epithelium.

Local force application

Engineering a method to apply local forces to an epithelium can be difficult, though necessary to recapitulate local forces *in vivo* that regulate epithelia behavior. Existing strategies to apply local forces to an epithelium have utilized tunable substrate stiffness, protein micropatterning, high precision micromanipulation tools, and more recently "synthetic mechanosignaling" approaches. These strategies have been used, and continue to be innovated, to answer questions around how local mechanics influence epithelial force transmission and collective migration.

In a transition from global to local mechanical inputs, gradients of substrate stiffness can be applied to cell collectives using methods such as light-induced gel polymerization^{187–189}. Such stiffness gradients exist *in vivo*, for example in tumor development¹⁹⁰. By mimicking these mechanical gradients *in vitro*, researchers can determine how regional cues

transmit signals to influence intercellular signaling. For example, controlled *in vitro* studies have revealed that cell migration can occur in a stiffness dependent fashion¹⁹¹, the basis for durotaxis. Cells migrate towards regions of higher stiffness but can also influence long-range intercellular force transmission¹⁹². There are several helpful reviews of migration on stiffness gradients^{28,30,33,193}.

Protein micropatterns with defined gaps may be used^{194–196} to answer questions surrounding protrusion dynamics of lamellipodia or to understand epithelial gap closure (i.e., wound healing). Though, there are limited studies using this method to explore local stretch on regulating collective migration. Other local stretch methods have been attempted for epithelial sheets using elastomeric substrates with “trenches”⁶³ on an expanding (i.e., nonconfluent) epithelium.

Micromanipulation tools, including microfabricated platforms, have also been engineered to directly apply local boundary forces to an epithelium. By adjusting the mechanical inputs (e.g., strain) and subsequently observing epithelial behavior (e.g., signaling or migration), researchers can understand how mechanical forces are transmitted between cells. Many of these tools are exclusively compatible with 2-D epithelial sheets. For example, microfabricated silicon devices have been used to exert a local shear or tension on an epithelium as observed in tissue morphogenesis^{35,197} (Figure 1.6.d.). Following local shear strain, cell collectives actively migrate towards the shear zone in an oscillatory manner for several hours after the mechanical perturbation. To understand which protein complexes facilitated the collective migratory response, the authors combined their micromanipulation methods with an E-cadherin mutant cell line and pharmacological approaches. Unlike the global mechanical strain induced by cell stretchers that have caused epithelial cells to re-

orient or divide, local boundary mechanical strain has found that the epithelium may dissipate mechanical stresses via collective and directed cell migration. Other micromanipulation methods have investigated the importance of local mechanics in more specific applications (e.g., disease). For example, pneumatically actuated PDMS chambers were used to apply a local mechanical stress on regions of a retinal pigment epithelium¹⁹⁸ to assess changes in the progression of choroidal neovascularization. Various other micromanipulation methods exist that can apply local forces to epithelial sheets, (e.g., micropipette aspiration, magnetic twisting cytometry, and atomic force microscopy) though are largely confined to single-cell force applications and rarely used to investigate downstream collective epithelial migration or other dynamics. Furthermore, many of these techniques have been exclusively used to characterize mechanical properties of the *static* epithelium and not to study the *dynamic* epithelium.

The last form of manipulating mechanical inputs on an epithelial sheet involves local "synthetic mechanosignaling" via optogenetics. Optogenetics advances in the last decade allow both spatial and temporal activation of force-sensitive proteins within epithelial sheets¹⁹⁹, which are more amenable to quantifying migration. These experiments allow researchers to cross new mechanical inputs between experimental and *in silico* models and determine their effects on collective epithelial behavior. For example, local control of RhoA has been shown to remodel cell-cell junctions⁸⁰ and alter cell shape²⁰⁰. Light-activated RhoA can also control cell traction and subsequent activation of transcriptional regulator YAP¹⁹⁹, a key player in both cell proliferation and migration. Other proteins that induce apical constriction (e.g., Shroom) can induce folding of an epithelial sheet²⁰¹. Aside from contractility based optogenetic tools used in epithelial sheets, optogenetic tools have also

been developed for the migration regulating proteins *cdc42* and *Rac1*^{202–204}. While still in its infancy, future studies in optogenetics have the potential to exert unique, tunable control over cell migration and tissue behavior by regulating force propagation from specific cellular regions. By utilizing optogenetics in epithelial sheets, local synthetic signaling can be combined with highly quantifiable cell migration methods.

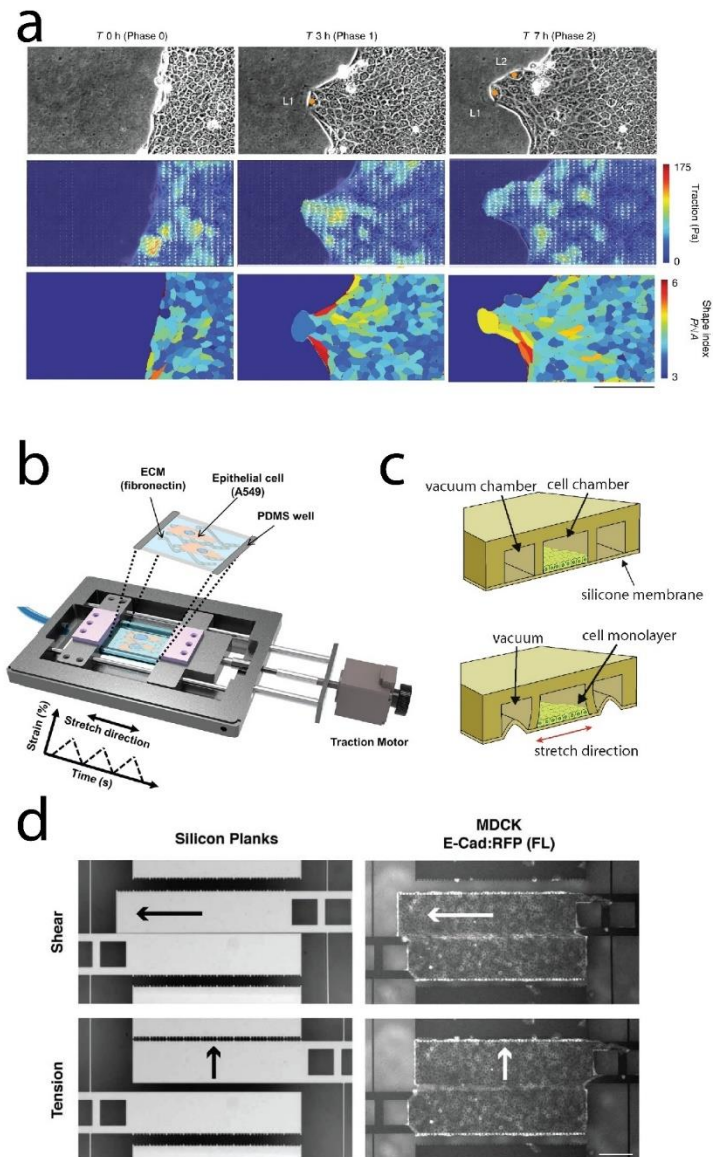


Figure 1.6. In vitro 2-D experimental models.

Several techniques have been used in conjunction with light microscopy to quantify migration and force exertion by migrating epithelial sheets. (a) An expanding MDCK epithelium in brightfield (top)

can be combined with TFM (middle) and segmented (bottom) to correlate changes in physical changes in cell shape with cell migration⁶³. When applying external forces to epithelia, cell stretcher can be actuated (b) mechanically via motors¹⁷⁴ or pneumatically¹³³. (d) More limited studies of local actuation include an MDCK epithelia grown on a microfabricated silicon platform, where the center of the epithelium can be subjected to either a mid-plane tension or shear strain to induce collective migration³⁵. Figures adapted from (a) Vishwakarma et al., Nature Communications 9, 1-12 (2018)⁶³, (b) Roshanzadeh et al., Scientific Reports 10, 1-14 (2020)¹⁷⁴, and (c) Hart et al., Cell. Mol. Bioeng. 14, 569-581 (2021)¹³³ under Creative Commons Attribution 4.0 International (CC BY 4.0). Figure (d) adapted with permission from Garcia et al., J. Micromech. Microeng. 30, (2020)¹⁹⁷. Scale bar: a= 100 μm , d= 200 μm

Advantages and limitations of 2-D cell sheets

2-D epithelial sheets importantly preserve the relevance of cell-cell contacts, a key component of collective migration. Unlike complex *in vitro* 3-D systems, 2-D epithelial sheets are easily accessible for cell migration experiments and analysis. Furthermore, they are tunable with respect to ECM modification, substrate stiffness, and amenable to culture on microfabricated devices^{35,158,171}. Since the 2-D epithelium is a more general model, it also allows researchers to control the uncontrollable endogenous factors that are unique to specific *in vivo* or organoid environments (e.g., the effect of cell packing density or cell confluency on collective cell migration). Such biophysical parameters can then be translated more easily into *in silico* models. However, mechanical forces applied to 2-D *in vitro* systems can be outside the context of the forces that occur *in vivo*. Therefore, force application methods within these simplified systems should be considered carefully.

1.4.C. 1-D cell lines and cell doublets

Even more spatially reduced models than cell sheets are linear epithelial models (1-D). Within 1-D models, both force transmission and migration is confined along the direction of a single axis. These "cell train" models are not just limited to 1-D cell lines or cell rings (Figure 1.7.a.) but can include cell doublets which are 1-D by nature. Cell lines are commonly used to study migration, which can be created through either spatial confinement

or protein micropatterning. Cell doublets can also be spatially confined but are more commonly used to isolate force transmission at single cell-cell contacts.

Methods to infer force from 1-D cell lines and cell doublets

As in other models we've discussed, TFM is a powerful inference tool for cellular traction stresses. Between cell lines and cell doublets, TFM has been more widely used for cell doublets to assess how cell-ECM tension influences stability and strength of a cell-cell interaction^{129,205,206}. TFM studies on epithelial cell pairs may be advantageous for dissecting the relationship between geometric confinement and cell contractility or manipulating mechanical regulation at a single cell-cell contact. The mechanical regulation of single cell-cell contacts can also be combined with FRET to return semi-quantitative feedback on intercellular molecular mechanics. For example, changing tension at cell-cell contacts of micropatterned cell doublets showed no change in E-cadherin tension¹²⁹, suggesting that tension over long time-scales may be supported by junction reinforcement from the cytoskeleton.

Image analysis, including video microscopy, is again a useful tool for force inference and quantifying cellular migration. While PIV is commonly used for 2-D epithelial sheets, analysis can be simplified when cells are confined to moving in a single direction. PIV has pointed to increased speed and persistence when confining either breast or kidney epithelial cells to a 1-D style of movement^{25,147}, which can be explained by a simple random walk diffusion anisotropy model. Cells have less room to migrate in the y direction and therefore redistribute that migration to the x direction. When these migration studies were distilled to a cell doublet experimental model, the mode of contact dissociation influenced how cells migrated away from one another via change in the protrusion angle²⁰⁷. Taken together, these

results from 1-D model systems have brought new insight regarding how the orientation of force at cell-cell contacts influences migration direction.

At the subcellular level, immunohistochemistry (IHC) can answer questions surrounding protein localization and concentrations that may be more difficult to observe in larger tissues. For example, IHC has been used to determine protein localization at cell-cell contacts during single direction movement, including how cryptic lamellipodia form under epithelial kidney cell-cell contacts. Further examination of Rac1 activity has helped determine the relationship between adherens junctions and downstream signaling to influence cell polarity⁶¹. For cell doublets, IHC has shown that E-cadherin and F-actin bundle together at cell-cell contacts²⁰⁸, where tension is localized to edges of the cell-cell contact²⁰⁵. These studies also show that increasing tension at cell-cell contacts does not change E-cadherin localization or intensity¹²⁹. Even though IHC is just a snapshot of cellular and protein structure, positioning of the centrosome and other organelles can be used as an indicator of cell polarity during dynamic processes (i.e., migration direction)²⁰⁹.

Methods to apply force to 1-D cell lines and cell doublets

Engineering the biophysical microenvironment

Cell lines are commonly created through either spatial confinement or protein micropatterning. Alternative methods have also been utilized, such as migration across a cylindrical wire²¹⁰. In spatial confinement, cells are trapped in microfabricated glass or polymer channels anywhere from 5-30 microns wide^{211,212}. Protein micropatterns can be fabricated on similar dimensions, but rely on biopassivation techniques to restrict the

spreading of cells^{25,61,114,213,214}. These same techniques can also be used for cell doublets^{129,206,215,216}.

Several modifications to the protein microenvironment for 1-D cell models can be implemented to answer new questions regarding how cells collectively migrate. For example, researchers have made new conclusions regarding how colliding cells interact to overcome contact inhibition^{61,217} (Figure 1.7.a. and 1.7.c). Protein micropatterns can also guide directional migration of melanoma cells using asymmetric “ratcheted” micropatterns²¹⁸. There is also evidence that increasing cell-ECM tension via substrate stiffness proportionally increases cell-cell tension²⁰⁵. Furthermore, varying the collagen gradient can impact the migratory behavior²¹⁹ in corroboration with haptotaxis.

Protein micropatterning has been used to regulate cell-cell junctions for 1-D cell doublets in various ways. For example, rectangles of increasing aspect ratios can be used to alter the forces at cell-cell contacts¹²⁹. Specific shapes for cell doublets, including I-shapes or bowties, can alter the location or stabilization of the cell-cell contact^{206,216}. Other geometric shapes (e.g., circle, triangle, or square) of cell doublets have shown changes in junction maturation which has implications for cell-cell signaling and properties of collective migration²²⁰ (Figure 1.7.b).

Global force application

Several studies have globally stretched cell doublets^{36,216} to determine how single cell-cell contacts respond to different mechanical inputs. For example, stretch of a mesendoderm cell doublet on a uniaxial stretcher showed lamellipodia extension away from the cell-cell contact³⁶. This experimental finding supports a biophysical model in which intercellular tension directs migration away from the direction of mechanical pull. Beyond

elastomeric cell stretchers for cell doublets, a recently printed two-photon polymerization device showed strain rate dependent rupture of cell-cell contacts²¹⁶. Even more recently, a method using a DNA E-cadherin hybrid linker was engineered to tune the cell-cell adhesion strength in cell doublets²²¹. Tuning the adhesion properties of cell-cell contacts may have significant applications for migrating cell collectives.

Local force application

In a cell train, a local force would imply mechanically perturbing one region of the train. For a cell doublet, a local force would imply perturbing only one of the cells. Optogenetics has been useful so far in locally perturbing 1-D epithelial models. For example, an Opto-Rac1 tool was used to locally perturb migration⁶¹ within a cell line. Less common methods have been used to dissect cell doublets, though in one study a mechanical probe was used to pull at the cell-cell contact and induce E-cadherin tension¹³⁵.

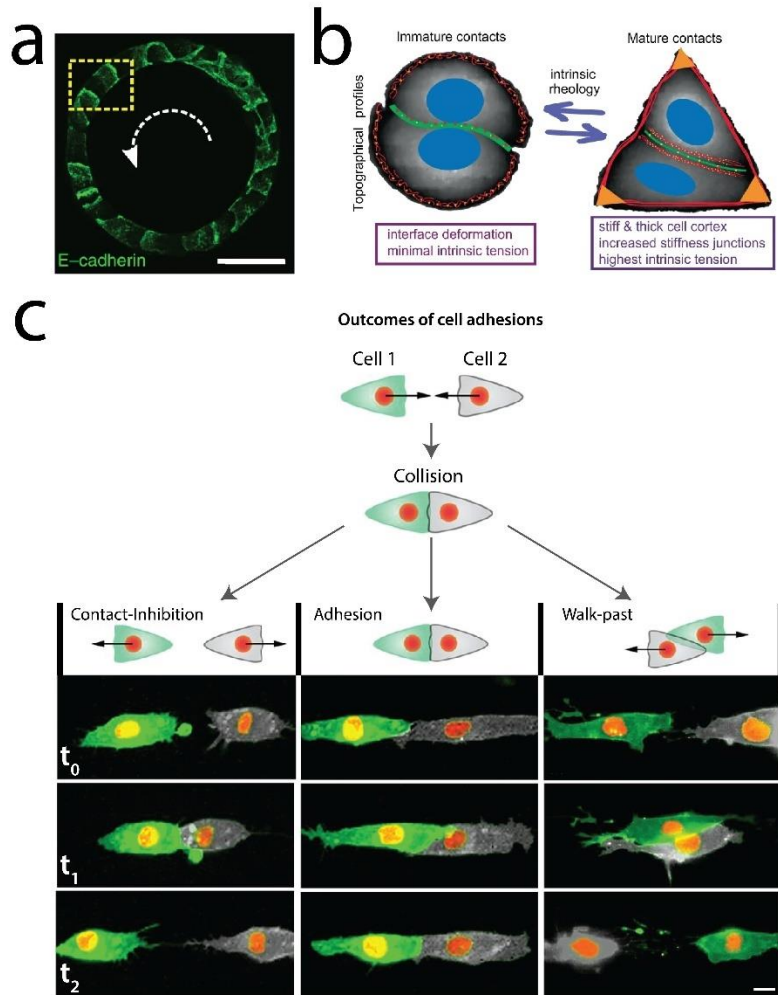


Figure 1.7. In vitro 1-D experimental models.

(a) MDCK epithelial cells have been grown on micropatterned ECM rings to direct their single-file motion in a circle⁶¹. (b) Alternatively, linear tracks have also been used to force cell-cell collisions which can have different implications for cell migration depending on how they interact²¹⁷. Figure (a) adapted with permission from Jain et al., *Nature Physics* 16, 802-809 (2020)⁶¹. Copyright 2020 Springer Nature. Figure (b) adapted from Sri-Ranjan et al., *Nature Communications* 13, 1-20 (2022)²¹⁹ under Creative Commons Attribution 4.0 International (CC BY 4.0). Figure (c) adapted from Scarpa et al., *Biol. Open* 2, 901-906 (2013)²¹⁷ under Creative Commons Attribution 3.0 Unported (CC BY 3.0). Scale bars: a= 50 μm c= 10 μm .

Advantages and limitations of 1-D cell lines and cell doublets

The 1-D model simplifies the mechanical forces acting on cell-cell contacts by reducing the number of cell-cell contacts per cell. Force exchanges can be directly in line with cell migration and can make the relationship between cell-cell signaling and migration

easier to understand and analyze. Cell doublets allow researchers to more easily calculate forces acting at single cell-cell contacts with more certainty compared to larger clusters or collectives¹³². Both lines and doublets also offer high control and tunability and are useful with high resolution microscopy.

The largest limitation of these reduced 1-D models is their lack of physiological relevance compared to *in vivo* systems or more complex *in vitro* systems.

1.4.D. Single cell micromanipulation systems

The most reduced cellular system for studying cell migration and force transmission is the single cell. However, fewer single cell epithelial studies exist since cell-cell contacts are so critical to epithelial behavior. Most studies with single epithelial cells primarily focus on either single cell mechanics (e.g., stiffness) or single cell migration. Some cleverly designed studies use single cell epithelial models to connect intercellular forces to cell migration.

Methods to infer force from single cell systems

For single cells, TFM is a common method to infer force of a moving cell as a way to understand how its microenvironment influences migration²²²⁻²²⁴. Other methods for single cell force inference are not necessarily unique from other models, which include tools such as FRET²²⁵, atomic force microscopy²²³, IHC²²⁴, and live cell imaging³⁶. Since the focus of this introduction is on collective cell mechanics, we will not go in depth into many single cell force inference studies.

Methods to apply force to single cell systems

Engineering the biophysical microenvironment

As covered previously in this introduction, a basic component of the microenvironment for epithelial cells is substrate composition and mechanics (e.g., the ECM and stiffness), which is easily tuned for single cell environments *in vitro*. With innovative experimental design, many conclusions regarding collective cell mechanics have been extrapolated from these findings. For example, cell culture substrates functionalized with cell contact mimicking E-cadherin has shown stiffness dependent adhesion regulation²²².

More complex methods to tailor the microenvironment for single cells involve protein micropatterning, which offer controlled physical pathways for single cell migration. Many of these studies involve 1-D tracks or channels where only single cells are allowed to move in the tracks^{211,213}. For example, microfabricated tapered channels helped determine how cancerous vs. noncancerous breast epithelial cells navigate something akin to a tumor microenvironment during metastasis²¹¹.

Global/local force application

In contrast to using protein micropatterns to create migration tracks for single cells, numerous studies have used protein micropatterns to regulate various aspects of cytoskeletal dynamics (e.g., actin orientation, interfacial tension, chirality, and overall traction force^{110,111,226,227}). More active approaches have utilized cyclic cell stretchers, where reorientation of NRK epithelial cells occurred through microtubule extension during the relaxation phase¹⁷⁷. Interestingly, many single cell epithelial studies using cell stretchers have

mainly focused on changes in focal adhesion and cytoskeletal dynamics, rather than changes in migratory activity^{160,177,178,225}.

There are few single cell studies that combine an applied force and the subsequent effect on cellular migration. Limited studies exist in part because there are few tools (besides TFM) that can apply force and measure migration. Techniques like atomic force microscopy, magnetic or optical tweezers, and micropipette aspiration apply and quantify forces on cells, but often do not look at actively migrating cells or how such forces have differing impacts on cell migration. However, one study utilized magnetic tweezers to connect force to migration, where E-cadherin coated magnetic beads were pulled against single mesendoderm cells to measure cell polarization (i.e., migration)³⁶.

Advantages and limitations of single cell systems

Unlike *in vitro* models that utilize cell collectives, observational studies of the fundamental single cell can reveal more information about cell morphology. For example, the lamellipodia can be easily visualized, unlike the cryptic lamellipodia of moving cells in a sheet.

However, while many single cell epithelial studies attempt to extrapolate collective behavior, epithelial cell-cell contacts are integral to both migration and tissue integrity. The lack of this additional complexity should be considered in single cell studies aiming to make conclusions about collective cell properties. Furthermore, many tools that study single cell mechanics largely investigate non-moving cells outside the dynamic nature of epithelia.

1.5. Biophysical *in silico* models of epithelial dynamics

The physical state of epithelia has important consequences for how cells communicate and how biological tissues respond to force and deformation. Confluent epithelia can exist in a solid-like (jammed) state or a liquid-like (unjammed) state. A jammed state is characterized by compact, roughly isotropic cells with reduced motility. Cell-cell adhesions are highly mature with few to no neighbor exchanges. The unjammed state is characterized by a disordered configuration of anisotropic cells with frequent neighbor exchanges. Neighbor exchanges lead to tissue level rearrangements which allow the tissue to "flow" and remodel, thus affecting the tissue's response to forces and deformations^{17,228,229}. A physical property that distinguishes between the two states is the mean cell shape, as quantified for instance by:

$$q = P_i / \sqrt{A_i}$$

Where P_i and A_i are the perimeter and area of the i -th cell and the brackets denote an average over all cells in the tissue²³⁰. Theoretical work²³⁰ supported by experiments²³¹ has indicated that a threshold value $q^* \simeq 3.81$ separates jammed ($q < q^*$) from unjammed ($q > q^*$) tissue.

Confluent epithelia can undergo jamming-unjamming transition by tuning cell-edge tension, cell motility, and the rate of cell division¹⁷. The tissue jamming transition has been predicted theoretically^{232,233} and has been observed *in vivo* in the body axis elongation of Zebrafish embryos¹⁸ where unjamming drives morphogenetic flows¹⁸⁻²⁰. Unjamming is also thought to play a major role in cancer cell invasion^{107,234}.

The iterative back and forth between *in silico*, *in vitro*, and *in vivo* studies has brought forth new understanding of collective cell motion in epithelia. *In silico* models are useful to quantify the role of distinct mechanisms that cannot be disentangled experimentally.

For example, they have provided quantitative understanding of a number of processes that affect the onset of cell jamming/unjamming, such as cell motility^{107,232}, cell-cell adhesion and cortex contractility^{234,235}, the interaction of cells with their environment^{107,234}, and the rate of cell division^{236,237}.

We can classify existing models of epithelia in three groups: Cell Edge Network models, continuum models, and agent based models^{238,239}.

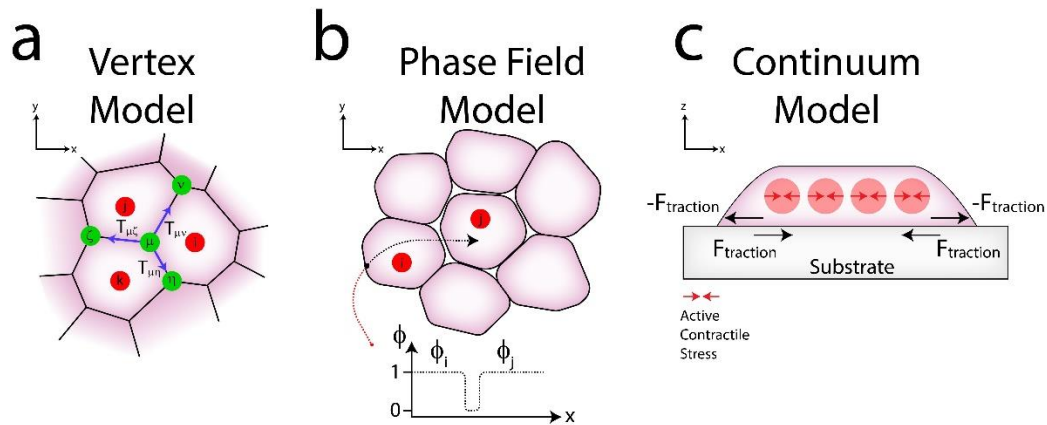


Figure 1.8. *In silico* models.

(a) Vertex model of cells i , j , and k sharing a vertex μ under tension from three edges. (b) Multi-phase field model of deformable cells. The bottom graph shows how the total phase field $\Phi = \sum_i \phi_i(x, t)$ varies in the x direction as we move along the arrow. (c) An example of a continuum picture, where an epithelial monolayer sits atop a substrate with the edges free to move. Contractile elements generate active contractile stress and cells move by generating traction with the substrate. Figure (c) adapted from Banerjee et al., Phys. Rev. Lett. 114, 228101²⁴⁰. Copyright 2015 American Physical Society.

1.5.A. Cell Edge Network Models

Under the heading of Cell Edge Network models we group a number of 2-D models that describe cells in confluent tissues as irregular polygons covering the plane, with no gaps between cells and shared edges representing the network of adherens junctions that connect

neighboring cells^{241–243}. This 2-D representation models a cross section (e.g., apical or basal surface) of the epithelial tissue layer^{244,245}.

The most popular models of this type are vertex models that describe the tissue as a network of N polygonal cells labelled by $i = 1, 2, \dots, N$, each with area A_i and perimeter P_i . The mechanical and structural properties of the tissue are described by an energy:

$$\mathcal{E}_{\mathcal{VM}} = \sum_i \frac{K_i}{2} (A_i - A_i^0)^2 + \sum_{\langle \mu, \nu \rangle} \Lambda_{\mu\nu} l_{\mu\nu} + \sum_i \frac{\Gamma_i}{2} P_i^2$$

The first term of the equation quantifies the energy cost for deviation of the i – th cell area from its target value A_i^0 and capture cell area elasticity, with associated stiffness K_i .

Although tissues are generally practically incompressible, this term accounts for the fact that cells can change their 2-D cross-sectional area by changing their height. The second term describes line tension $\Lambda_{\mu\nu}$ along cell edges connecting vertices μ and ν , with $l_{\mu\nu}$ the corresponding cell-edge length, and is summed over all neighboring cell edges ($\langle \mu, \nu \rangle$).

The line tension is positive when cortical tension dominates inter-cellular adhesion and negative otherwise. The last term describes contractility of the cell perimeter of strength Γ_i , which is set by various processes in the cell, such as acto-myosin ring contraction²⁴².

Vertex models have been widely successful in studies of morphogenetic tissue remodeling and deformations *in vitro* in 2-D^{20,245–247} and in 3-D epithelial layers and organoids^{106,248–251}. They have been modified to include a variety of active processes, such as cell motility, as in Active Vertex Models²⁵², cell-edge tensions fluctuations²⁵³, cell proliferation and death^{169,236}, and even to allow for local tearing of the tissue²⁵⁴.

A related class of models consists of Voronoi models, where the cell energy is written entirely in terms of cell area and perimeter as:

$$\mathcal{E}_{\mathcal{V}\sigma} = \frac{1}{2} \sum_i [K_i (A_i - A_i^0)^2 + K_i^P (P_i - P_i^0)^2]$$

The Voronoi energy can be obtained from the vertex model energy by assuming uniform cell edge tensions $\Lambda_{\mu\nu} = \Lambda$. An important distinction between the two models is that in vertex models the degrees of freedom are the cell vertices, while in the Voronoi model the degrees of freedom are the centroids of the polygonal cells. This makes Voronoi models more directly suitable for including cell motility, as implemented in the Self Propelled Voronoi (SPV) model^{232,252}. In the SPV the cell centers have a noisy self-propulsion velocity and are acted upon by forces derived from the energy given in the above equation. This model has been used to study the effect of cell motility on the tissue jamming-unjamming transition²³². The further addition of alignment interactions has revealed the possibility of flocking liquid and solid states, with possible relevance to collective cell migration^{255,256}.

A related model is the Active Tension Model (ATN) that neglects area elasticity, but includes the mechanical feedback between cell-edge tension and myosin activation²⁵⁷. This model can explain the variable apical areas of ventral cells in early stages of gastrulation in the fruit fly embryo. Another modified vertex model study links contraction pulses acting like mechanical ratchets to tissue-scale deformations during morphogenesis⁸⁰.

The idea of representing tissues as networks has been shown to be useful even in the analysis of *in vivo* experimental data. Using networks of cell centers, called cell connectivity networks, a recent study linked changes in tissue rigidity and tissue viscosity to variation in cell packing fraction²³⁵.

Cell Edge Network models are generally appropriate for confluent tissue. They have been adapted to allow for the creation of extra-cellular spaces in vertex models^{258,259}. Like vertex models, the “active foam” model²⁵⁹ predicts that edge tension fluctuations control

stress relaxation and tissue fluidization, which is corroborated by *in vivo* studies²⁵⁹. In spite of these adaptations, Cell Edge Network models may not be ideal for systems that can develop inter-cellular gaps, as for instance near the transition from epithelial to mesenchymal behavior. In such cases agent based models, such as active particles or multi-phase field models may be more appropriate (see section 1.6.C.).

1.5.B. Continuum models

Continuum models describe epithelial tissues on scales much larger than the size of individual cells^{260,261}. In a continuum model the tissue is described in terms of a few coarse-grained fields that vary in space and time, such as the mean cell density, velocity, and polarity. The tissue dynamics is then controlled by conservation laws and constitutive equations that capture the system's symmetries and mechanical state. Epithelial monolayers are often modeled as active viscoelastic²⁶² fluids or viscoplastic elastic sheets, with couplings to internal degrees of freedom that account for active processes, such as contractility and cellular polarization. Continuum models have been shown to account for the heterogeneous spatial distribution of cellular stresses inferred from TFM in both expanding^{64,130} and confined²⁶³ monolayers, and even at the level of cell clusters¹³² and individual cells²⁰⁵. They have also captured collective waves in migrating monolayers²⁴⁰ as observed in *in vitro* experiments²⁶⁴. Continuum models have also been used in conjunction with *in vitro* studies to explain cell extrusion and apoptosis²¹, intercellular force transmission during migration⁶³, long range force transmission leading to durotaxis¹⁹², and curvature dependent mechanics of purse-string contraction during gap-closure¹⁹⁶.

They have also been used to predict the causal relation between stress patterns induced by myosin contractility and cell flow in *in vivo* morphogenesis in *Drosophila*

gastrulation⁶⁸ and ventral furrow formation²⁶⁵, as well as viscosity and cell ingression rates in Zebrafish body axis elongation¹⁹ and surface displacements in early starfish oocyte development²⁶⁶.

Continuum approaches do not attempt to faithfully incorporate intracellular processes, but rather aim at characterizing quantitatively the modes of organization and the materials properties of cell collectives in terms of a few macroscopic parameters, such as cell density and shape, cell-cell adhesiveness, contractility, polarization and division/death rates. Each of these quantities may describe the combined effect of a number of molecular processes and signaling pathways. An important open challenge is relating the coefficients of continuum models to both the parameters of mesoscopic (e.g., Vertex) models and to quantities controlled in experiments.

Another key limitation of the most current continuum modeling approaches lies in the assumption of fixed materials properties of tissues, which is encoded in the choice of a particular constitutive law. Tissues are able to adapt their mechanical response to perturbations (both external and internal) and are characterized by multiple relaxation times. This demands a rheological model capable of capturing both active solid-like and fluid-like behavior in different regimes of stress response and to dynamically transition between the two. In other words one needs to incorporate the feedbacks between cellular mechanics, polarized motility, and the regulatory biochemistry of actomyosin contractility^{260,267}. These couplings play an essential role in the transmission of spatial information in large cell monolayers, mediated by waves, pulses, and a tug of war between cell-cell and cell-substrate forces.

1.5.C. Agent based models

Agent based models describe each individual cell as a discrete agent with its own biophysical properties and interaction forces with other cells and with the surrounding environment²⁶⁸. Agent based models can be defined on a lattice with cells constrained to occupy spaces on a discrete grid, as for instance in Cellular Potts models^{269–271} or Cellular Automaton type models^{123,234}. They can also be defined off-lattice as multi-phase field models^{272,273}, deformable particle models^{179,274}, various Spring link models^{275,276} or 1-D train models^{61,277,278}. Recently a Cellular Potts model was used to study the role of ECM confinement on collective and single-cell dynamics²³⁴. Phase field models were originally developed to study multi-component micro-structure materials²⁷⁹ and have been adapted to represent epithelial cells as deformable active particles^{272,273,280–285}. Each cell (i) is represented by a phase field ($\phi_i(\mathbf{x}, t)$) defined to have value 1 in the region occupied by the cell and 0 otherwise (Figure 1.8). Cell-cell interactions and cell shape are controlled by a Cahn-Hilliard phase field free energy, whose minimum determines the ground state configuration of the tissue²³⁹. Phase field models can then be augmented to include cell-individual properties like polarization, contractility, self-propulsion, as well as cell-cell interactions and active stresses^{282,284}. Phase field models additionally allow for variations in both cell density and cell shape and can resolve arbitrary cell shapes. These models have been used to explore many behaviors of biological tissue, such as liquid-solid transitions²⁸³, spontaneous emergence of collective cell migration²⁷³, collective sustained oscillations¹¹², emergent nematic behavior and defects on mesoscopic scales²⁸⁴, differential elasticity of cancerous versus healthy cells^{272,286}, and how contractile cells can yield tissue scale extensile behavior²⁸⁴.


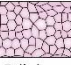
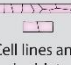

Many more modeling approaches exist²³⁹ beyond the ones described above, such as hybrid multiscale models linking continuum description to agent based description^{271,287}. *In silico* modeling is a powerful tool for filling in gaps in both *in vivo* and *in vitro* experiments, and can motivate new directions of experimental inquiry.

1.6. Discussion

1.6.A. Summary of local vs. global mechanical perturbation

There is a broad spectrum of devices that can be used to exert forces on epithelia for the purpose of understanding collective cell behavior. These devices can be soft or rigid, transparent or opaque, low-throughput or high-throughput, etc. However, an important distinction we want to highlight is the ability for a device to apply a local force (i.e., region of cells within the tissue) or global force (i.e., the entire tissue) (Table 1.1). Epithelial tissues *in vivo* experience a range of mechanical deformations that are not always uniform across the tissue. Tissue forces and strains are often regionalized with high variability across different parts of the tissue depending on the microenvironment or biochemical gradients. So far, most devices in the literature apply mechanical deformation across all cells (e.g., cell stretchers) or on a single cell (e.g., atomic force microscopy, optical tweezers, micropipette aspiration). Future studies focused on applying regional or local strains to epithelia will help elucidate how mechanical cues propagate through the epithelium.

Table 1.1. Engineered approaches used to probe and infer mechanics of epithelia.

	Local mechanical manipulation methods to study collective cell behavior	Global mechanical manipulation methods to study collective cell behavior	Methods to <i>infer</i> force and collective cell behavior
 <p>Spheroids and organoids</p>	<ul style="list-style-type: none"> • Optogenetics • Actuatable droplets 	<ul style="list-style-type: none"> • Biochemical reagents, pharmacological approaches, or gene editing • Substrate modifications • Geometric confinement 	<ul style="list-style-type: none"> • Traction Force Microscopy (via beads and micropillars) • Segmentation and shape analysis • Molecular tension sensors • Laser ablation • Incompressible droplets • Time-lapse microscopy (including particle image velocimetry) • Immunohistochemistry and fluorescence microscopy • Micropipette aspiration
 <p>Cell sheets</p>	<ul style="list-style-type: none"> • Optogenetics • MEMS platforms and custom micromanipulation setups • ECM or stiffness gradients • ECM shapes • Atomic Force Microscopy 	<ul style="list-style-type: none"> • Biochemical reagents, pharmacological approaches, or gene editing • Substrate modifications • Geometric confinement • Cell stretchers (static or cyclic) • Suspended epithelia • Shear flow 	<ul style="list-style-type: none"> • Traction Force Microscopy (via beads and micropillars) • Segmentation and shape analysis • Molecular tension sensors • Laser ablation • Time-lapse microscopy (including particle image velocimetry) • Wound healing assays • Immunohistochemistry and fluorescence microscopy • Atomic Force Microscopy
 <p>Cell lines and doublets</p>	<ul style="list-style-type: none"> • Optogenetics • MEMS platforms and custom micromanipulation setups • ECM or stiffness gradients • ECM shapes • Atomic Force Microscopy 	<ul style="list-style-type: none"> • Biochemical reagents, pharmacological approaches, or gene editing • Substrate modifications • Geometric confinement • Cell stretchers (static or cyclic) 	<ul style="list-style-type: none"> • Traction Force Microscopy (via beads and micropillars) • Molecular tension sensors • Time-lapse microscopy (including particle image velocimetry) • Immunohistochemistry and fluorescence microscopy • Atomic Force Microscopy
 <p>Single cells</p>	<ul style="list-style-type: none"> • Optogenetics • Atomic Force Microscopy 	<ul style="list-style-type: none"> • Biochemical reagents, pharmacological approaches, or gene editing • Substrate modifications • Geometric confinement • Micropipette aspiration • Magnetic bead trap • Cell stretchers (static or cyclic) 	<ul style="list-style-type: none"> • Traction Force Microscopy (via beads and micropillars) • Molecular tension sensors • Time-lapse microscopy (including particle image velocimetry) • Immunohistochemistry and fluorescence microscopy • Magnetic Twisting Cytometry • Tweezers • Atomic Force Microscopy • Micropipette aspiration

Our limited understanding of how forces propagate through epithelia subsequently hinders our understanding of how local forces influence migration. Currently in the literature, there are conflicting models with respect to how intercellular forces direct migration. Many biological models suggest that cells follow local force^{4,34}, corroborating the theory that leader cells pull on follower cells to direct them forward. However, some biophysical models suggest that cells move *away* from increasing tension^{36,64,130}. These models are reminiscent of contact inhibition, where collision of cell-cell contacts cause cells to polarize in the opposite direction and turnaround^{217,277,288}. Perhaps these different models can be explained by differences in cell-cell contact regulation for leader-follower cells vs. neighboring cells moving within a confluent epithelium.

To elucidate the discrepancies between these migration models, a new class of *in vitro* studies would be beneficial. Many studies regarding force-induced repolarization have been modeled through simulations and theory^{277,288}, but few have experimentally taken into

account the complex variables of the cell-cell contact. Even experimental studies that have made conclusions about intercellular forces are often based on TFM without external mechanical manipulation^{26,129}. *In vitro* models will be a useful platform to dissect these complex variables that exist in biology, but require micromanipulation techniques to directly probe and manipulate intercellular cues.

1.6.B. Additional variables to consider for mechanical manipulation

Beyond devices and tools that mechanically manipulate *regions* of tissue, there are also limited studies on the impact of different *kinds* of mechanical strain (e.g., strain rate, magnitude, frequency, or directionality) of mechanical force and subsequent effects on collective dynamics. Many different forces exist at cell-cell contacts and these changes are likely to influence force propagation and subsequent changes in collective cell behavior.

For example, several studies have shown the physiological significance of oscillatory strains as they are needed to drive tissue deformations or junction remodeling⁸⁰. However, many studies apply either step or single strains to the epithelium. Beyond step vs. cyclic strain application, the rate of strain is another important variable that can be implemented in future studies²⁸⁹.

Mechanical forces can also vary with respect to their orientation on cell-cell contacts (e.g., tension and shear). Tugging at cell-cell contacts of different orientations may have implications for junction adhesion and downstream signaling²⁹⁰. Tensile tugging forces, where force is exerted perpendicular to the cell-cell contact, occur regularly in developmental events such as invagination, neural tube development, and routinely in lung epithelial stretch or in intestinal crypts^{37,40,42,51,291–293}. Shear forces, where cell membranes are pulled laterally past one another, also occur regularly in development (e.g., gastrulation and *Drosophila*

genitalia development)^{40,290,294}. Beyond potential downstream signaling for cellular function, the orientation of cell-cell contacts under mechanical load may influence their molecular interactions and ability to collectively migrate. This spectrum of molecular interactions at cell-cell contacts could help explain how different stages of embryo development utilize different modes of cell migration with regard to retaining cell neighbors. In zebrafish eyelid closure, cell monolayers utilize collective cell movements while retaining neighbors²⁹² via cell-cell adhesion. In germband extension, cells actively migrate past one another by breaking and reforming transmembrane binding proteins in a process known as intercalation⁹. Alternatively, cell-cell contacts under tension may promote adhesion reinforcement.

Whether cell junctions experience predominantly shear or tension depends on the dynamics of the local microenvironment (e.g., bending, folding, or constriction events)^{37,42,295}. Other cell-cell mechanics can include compression, which has been shown to lead to extrusion and subsequent gap closure²⁹⁶⁻²⁹⁸.

1.6.C. Applications for synthetic biology and biomimetics

Epithelia are biological tissues that create and maintain life. At the core of these studies researchers stand to gain fundamental understanding of how tissues develop, regenerate, and provide protection for our organs. However, epithelia are also nature's best examples of active matter. Understanding the collective and regenerative dynamics of epithelia will enable the advancement of synthetic materials with far reaching applications in society. For example, synthetic membranes could be engineered to alter filtration specificity as a function of environmental inputs (e.g., mechanical stress). Other materials could self-repair when "wounded" from a rip or tear.

Several other reviews focus on additional aspects of collective cell migration and engineered platforms that have been used for *in vitro* cell studies^{84,298–301}. Several methods in mechanobiology have also been commercialized in recent years beyond cell stretchers mentioned earlier (*Forcyte Biotechnologies, CYTOO, Alvéole, 4D-Cell*). These commercialized platforms will help to accelerate mechanobiology studies in both academia and industry.

1.7. Acknowledgements

This work was funded by the Institute for Collaborative Biotechnology and the NSF (1834760). The authors would also like to acknowledge helpful feedback from members of the Pruitt Lab.

1.8. Conflict of Interest

The authors have no conflicts of interest to disclose.

1.9. Author Contributions

Liam P. Dow: Conceptualization (lead); Visualization (lead); Writing - original draft (lead); Writing - review and editing. Toshi Parmar: Conceptualization (supporting); Visualization (supporting); Writing - original draft (supporting); Writing - review and editing. M. Cristina Marchetti: Conceptualization (supporting); Funding acquisition; Writing -review and editing. Beth L. Pruitt: Conceptualization (supporting); Funding acquisition; Writing - original draft (supporting); Writing - review and editing. Liam P. Dow and Beth L. Pruitt led discussion on biophysical experimental models, while Toshi Parmar and M. Cristina Marchetti led discussion on *in silico* biophysical models.

1.10. References

1. Nishimura, T., Honda, H. & Takeichi, M. Planar cell polarity links axes of spatial dynamics in neural-tube closure. *Cell* **149**, 1084–1097 (2012).
2. Fuse, N., Yu, F. & Hirose, S. Gprk2 adjusts Fog signaling to organize cell movements in *Drosophila* gastrulation. *Dev.* **140**, 4246–4255 (2013).
3. Warga, R. M. & Kimmel, C. B. Cell movements during epiboly and gastrulation in zebrafish. *Development* **108**, 569–580 (1990).
4. Cai, D. *et al.* Mechanical feedback through E-cadherin promotes direction sensing during collective cell migration. *Cell* **157**, 1146–1159 (2014).
5. Panousopoulou, E., Hobbs, C., Mason, I., Green, J. B. A. & Formstone, C. J. Epiboly generates the epidermal basal monolayer and spreads the nascent mammalian skin to enclose the embryonic body. *J. Cell Sci.* **129**, 1915–1927 (2016).
6. Davidson, L. A. & Keller, R. E. Neural tube closure in *Xenopus laevis* involves medial migration, directed protrusive activity, cell intercalation and convergent extension. *Development* **126**, 4547–4556 (1999).
7. Keller, R. *et al.* Mechanisms of convergence and extension by cell intercalation. *Philos. Trans. R. Soc. London. Ser. B Biol. Sci.* **355**, 897–922 (2000).
8. Munro, E. M. & Odell, G. M. Polarized basolateral cell motility underlies invagination and convergent extension of the ascidian notochord. *Development* **129**, 13–24 (2002).
9. Tada, M. & Heisenberg, C. P. Convergent extension: using collective cell migration and cell intercalation to shape embryos. *Development* **139**, 3897–3904 (2012).
10. Trinkaus, J. P., Trinkaus, M. & Fink, R. D. On the convergent cell movements of gastrulation in *Fundulus*. *J. Exp. Zool.* **261**, 40–61 (1992).
11. Begnaud, S., Chen, T., Delacour, D., Mège, R. M. & Ladoux, B. Mechanics of epithelial tissues during gap closure. *Curr. Opin. Cell Biol.* **42**, 52–62 (2016).
12. Sonnemann, K. J. & Bement, W. M. Wound repair: toward understanding and integration of single-cell and multicellular wound responses. *Annu. Rev. Cell Dev. Biol.* **27**, 237–263 (2011).
13. Zulueta-Coarasa, T. & Fernandez-Gonzalez, R. Dynamic force patterns promote collective cell movements during embryonic wound repair. *Nat. Phys.* **14**, 750–758 (2018).
14. Franco, J. J., Atieh, Y., Bryan, C. D., Kwan, K. M. & Eisenhoffer, G. T. Cellular crowding influences extrusion and proliferation to facilitate epithelial tissue repair. *Mol. Biol. Cell* **30**, 1890 (2019).
15. Ballard, S. T., Hunter, J. H. & Taylor, A. E. Regulation of Tight-Junction Permeability During Nutrient Absorption Across the Intestinal Epithelium. <https://doi.org/10.1146/annurev.nu.15.070195.000343> **15**, 35–55 (2003).
16. Hartland, E. L., Ghosal, D. & Giogha, C. Manipulation of epithelial cell architecture by the bacterial pathogens *Listeria* and *Shigella*. *Curr. Opin. Cell Biol.* **79**, 102131 (2022).
17. Lawson-Keister, E. & Manning, M. L. Jamming and arrest of cell motion in biological tissues. *Curr. Opin. Cell Biol.* **72**, 146–155 (2021).
18. Mongera, A. *et al.* A fluid-to-solid jamming transition underlies vertebrate body axis elongation. *Nature* **561**, 401–405 (2018).
19. Banavar, S. P. *et al.* Mechanical control of tissue shape and morphogenetic flows during vertebrate body axis elongation. *Sci. Rep.* **11**, 8591 (2021).
20. Wang, X. *et al.* Anisotropy links cell shapes to tissue flow during convergent extension. *Proc. Natl. Acad. Sci. U. S. A.* **117**, 13541–13551 (2020).
21. Saw, T. B. *et al.* Topological defects in epithelia govern cell death and extrusion. *Nat.* **544**, 212–216 (2017).
22. Krndjija, D. *et al.* Active cell migration is critical for steady-state epithelial turnover in the gut. *Science* (80-.). **365**, 705–710 (2019).

23. Vasilyev, A. & Drummond, I. A. Fluid flow and guidance of collective cell migration. *Cell Adh. Migr.* **4**, 353 (2010).
24. Blay, J. & Brown, K. D. Epidermal growth factor promotes the chemotactic migration of cultured rat intestinal epithelial cells. *J. Cell. Physiol.* **124**, 107–112 (1985).
25. Vedula, S. R. K. *et al.* Emerging modes of collective cell migration induced by geometrical constraints. *Proc. Natl. Acad. Sci. U. S. A.* **109**, 12974–12979 (2012).
26. Trepap, X. & Fredberg, J. J. Plithotaxis and emergent dynamics in collective cellular migration. *Trends Cell Biol.* **21**, 638–646 (2011).
27. StefanooZapperi Editors, C. *Advances in Experimental Medicine and Biology 1146 Cell Migrations: Causes and Functions.*
28. Espina, J. A., Marchant, C. L. & Barriga, E. H. Durotaxis: the mechanical control of directed cell migration. *FEBS J.* **289**, 2736–2754 (2022).
29. Cohen, D. J., Nelson, W. J. & Maharbiz, M. M. Galvanotactic control of collective cell migration in epithelial monolayers. *Nat. Mater.* **2014 134 13**, 409–417 (2014).
30. Haeger, A., Wolf, K., Zegers, M. M. & Friedl, P. Collective cell migration: guidance principles and hierarchies. *Trends Cell Biol.* **25**, 556–566 (2015).
31. Mycielska, M. E. & Djamgoz, M. B. A. Cellular mechanisms of direct-current electric field effects: galvanotaxis and metastatic disease. *J. Cell Sci.* **117**, 1631–1639 (2004).
32. Roca-Cusachs, P., Sunyer, R. & Trepap, X. Mechanical guidance of cell migration: lessons from chemotaxis. *Curr. Opin. Cell Biol.* **25**, 543–549 (2013).
33. Shellard, A. & Mayor, R. Durotaxis: The Hard Path from In Vitro to In Vivo. *Dev. Cell* **56**, 227–239 (2021).
34. Das, T. *et al.* A molecular mechanotransduction pathway regulates collective migration of epithelial cells. *Nat. Cell Biol.* **2014 173 17**, 276–287 (2015).
35. Sadeghipour, E., Garcia, M. A., Nelson, W. J. & Pruitt, B. L. Shear-induced damped oscillations in an epithelium depend on actomyosin contraction and E-cadherin cell adhesion. *Elife* **7**, (2018).
36. Weber, G. F., Bjerke, M. A. & DeSimone, D. W. A mechanoresponsive cadherin-keratin complex directs polarized protrusive behavior and collective cell migration. *Dev. Cell* **22**, 104–115 (2012).
37. Gayer, C. P. & Basson, M. D. The effects of mechanical forces on intestinal physiology and pathology. *Cell. Signal.* **21**, 1237–1244 (2009).
38. Blonski, S. *et al.* Direction of epithelial folding defines impact of mechanical forces on epithelial state. *Dev. Cell* **56**, 3222-3234.e6 (2021).
39. Díaz-Bello, B. *et al.* Method for the Direct Fabrication of Polyacrylamide Hydrogels with Controlled Stiffness in Polystyrene Multiwell Plates for Mechanobiology Assays. *ACS Biomater. Sci. Eng.* **5**, 4219–4227 (2019).
40. Etournay, R. *et al.* Interplay of cell dynamics and epithelial tension during morphogenesis of the *Drosophila* pupal wing. *Elife* **4**, (2015).
41. Goodwin, K. & Nelson, C. M. Mechanics of Development. *Dev. Cell* **56**, 240–250 (2021).
42. Schroeder, T. E. Mechanisms of morphogenesis: the embryonic neural tube. *Int. J. Neurosci.* **2**, 183–197 (1971).
43. Aigouy, B. *et al.* Cell flow reorients the axis of planar polarity in the wing epithelium of *Drosophila*. *Cell* **142**, 773–786 (2010).
44. Karzbrun, E. *et al.* Human neural tube morphogenesis in vitro by geometric constraints. *Nat.* **2021 5997884 599**, 268–272 (2021).
45. Roellig, D. *et al.* Force-generating apoptotic cells orchestrate avian neural tube bending. *Dev. Cell* **57**, 707-718.e6 (2022).
46. Meng, W. & Takeichi, M. Adherens junction: molecular architecture and regulation. *Cold Spring Harb. Perspect. Biol.* **1**, (2009).
47. Le Duc, Q. *et al.* Vinculin potentiates E-cadherin mechanosensing and is recruited to actin-

- anchored sites within adherens junctions in a myosin II-dependent manner. *J. Cell Biol.* **189**, 1107–1115 (2010).
48. Menke, A. & Giehl, K. Regulation of adherens junctions by Rho GTPases and p120-catenin. *Arch. Biochem. Biophys.* **524**, 48–55 (2012).
 49. Seddiki, R. *et al.* Force-dependent binding of vinculin to α -catenin regulates cell-cell contact stability and collective cell behavior. *Mol. Biol. Cell* **29**, 380–388 (2018).
 50. Harris, T. J. C. & Peifer, M. Decisions, decisions: β -catenin chooses between adhesion and transcription. *Trends Cell Biol.* **15**, 234–237 (2005).
 51. Pannekoek, W. J., de Rooij, J. & Gloerich, M. Force transduction by cadherin adhesions in morphogenesis. *F1000Research* **8**, (2019).
 52. Thoreson, M. A. *et al.* Selective uncoupling of p120(ctn) from E-cadherin disrupts strong adhesion. *J. Cell Biol.* **148**, 189–201 (2000).
 53. Runswick, S. K., O’Hare, M. J., Jones, L., Streuli, C. H. & Garrod, D. R. Desmosomal adhesion regulates epithelial morphogenesis and cell positioning. *Nat. Cell Biol.* **2001 39 3**, 823–830 (2001).
 54. Hartsock, A. & Nelson, W. J. Adherens and tight junctions: structure, function and connections to the actin cytoskeleton. *Biochim. Biophys. Acta* **1778**, 660–669 (2008).
 55. Borradori, L. & Sonnenberg, A. Structure and Function of Hemidesmosomes: More Than Simple Adhesion Complexes. *J. Invest. Dermatol.* **112**, 411–418 (1999).
 56. Alberts, B. *et al.* Integrins. (2002).
 57. Rafiq, N. B. M. *et al.* A mechano-signalling network linking microtubules, myosin IIA filaments and integrin-based adhesions. *Nat. Mater.* **2019 186 18**, 638–649 (2019).
 58. Clark, A. G. *et al.* Self-generated gradients steer collective migration on viscoelastic collagen networks. *Nat. Mater.* **2022 2110 21**, 1200–1210 (2022).
 59. Chauhana, B. K., Louc, M., Zhengd, Y. & Langa, R. A. Balanced Rac1 and RhoA activities regulate cell shape and drive invagination morphogenesis in epithelia. *Proc. Natl. Acad. Sci. U. S. A.* **108**, 18289–18294 (2011).
 60. Mythreye, K. & Blobel, G. C. The type III TGF- β receptor regulates epithelial and cancer cell migration through β -arrestin2-mediated activation of Cdc42. *Proc. Natl. Acad. Sci. U. S. A.* **106**, 8221–8226 (2009).
 61. Jain, S. *et al.* The role of single-cell mechanical behaviour and polarity in driving collective cell migration. *Nat. Phys.* **2020 167 16**, 802–809 (2020).
 62. Ozawa, M. *et al.* Adherens junction regulates cryptic lamellipodia formation for epithelial cell migration. *J. Cell Biol.* **219**, (2020).
 63. Vishwakarma, M. *et al.* Mechanical interactions among followers determine the emergence of leaders in migrating epithelial cell collectives. *Nat. Commun.* **2018 91 9**, 1–12 (2018).
 64. Trepap, X. *et al.* Physical forces during collective cell migration. *Nat. Phys.* **2009 56 5**, 426–430 (2009).
 65. Vazquez, K., Saraswathibhatla, A. & Notbohm, J. Effect of substrate stiffness on friction in collective cell migration. *Sci. Reports* **2022 121 12**, 1–13 (2022).
 66. D’Angelo, A., Dierkes, K., Carolis, C., Salbreux, G. & Solon, J. In Vivo Force Application Reveals a Fast Tissue Softening and External Friction Increase during Early Embryogenesis. *Curr. Biol.* **29**, 1564-1571.e6 (2019).
 67. Prakash, V. N., Bull, M. S. & Prakash, M. Motility-induced fracture reveals a ductile-to-brittle crossover in a simple animal’s epithelia. *Nat. Phys.* **2020 174 17**, 504–511 (2021).
 68. Streichan, S. J., Lefebvre, M. F., Noll, N., Wieschaus, E. F. & Shraiman, B. I. Global morphogenetic flow is accurately predicted by the spatial distribution of myosin motors. *Elife* **7**, (2018).
 69. Herrera-Perez, R. M. & Kasza, K. E. Biophysical control of the cell rearrangements and cell shape changes that build epithelial tissues. *Curr. Opin. Genet. Dev.* **51**, 88–95 (2018).
 70. Wang, X., He, L., Wu, Y. I., Hahn, K. M. & Montell, D. J. Light-mediated activation reveals a

- key role for Rac in collective guidance of cell movement in vivo. *Nat. Cell Biol.* **12**, 591–597 (2010).
71. Eder, D., Basler, K. & Aegerter, C. M. Challenging FRET-based E-Cadherin force measurements in Drosophila. *Sci. Reports* 2017 71 **7**, 1–12 (2017).
 72. Campàs, O. *et al.* Quantifying cell-generated mechanical forces within living embryonic tissues. *Nat. Methods* 2013 112 **11**, 183–189 (2013).
 73. Serwane, F. *et al.* In vivo quantification of spatially varying mechanical properties in developing tissues. *Nat. Methods* 2016 142 **14**, 181–186 (2016).
 74. Etournay, R. *et al.* TissueMiner: A multiscale analysis toolkit to quantify how cellular processes create tissue dynamics. *Elife* **5**, (2016).
 75. Mashburn, D. N., Lynch, H. E., Ma, X. & Hutson, M. S. Enabling user-guided segmentation and tracking of surface-labeled cells in time-lapse image sets of living tissues. *Cytom. Part A* **81A**, 409–418 (2012).
 76. Stringer, C., Wang, T., Michaelos, M. & Pachitariu, M. Cellpose: a generalist algorithm for cellular segmentation. *Nat. Methods* 2020 181 **18**, 100–106 (2020).
 77. Kong, W. *et al.* Experimental validation of force inference in epithelia from cell to tissue scale. *Sci. Reports* 2019 91 **9**, 1–12 (2019).
 78. O’Connor, J., Akbar, F. B., Hutson, M. S. & Page-McCaw, A. Zones of cellular damage around pulsed-laser wounds. *PLoS One* **16**, e0253032 (2021).
 79. Izquierdo, E., Quinkler, T. & De Renzis, S. Guided morphogenesis through optogenetic activation of Rho signalling during early Drosophila embryogenesis. *Nat. Commun.* 2018 91 **9**, 1–13 (2018).
 80. Staddon, M. F., Cavanaugh, K. E., Munro, E. M., Gardel, M. L. & Banerjee, S. Mechanosensitive Junction Remodeling Promotes Robust Epithelial Morphogenesis. *Biophys. J.* **117**, 1739–1750 (2019).
 81. Kelava, I. & Lancaster, M. A. Dishing out mini-brains: Current progress and future prospects in brain organoid research. *Dev. Biol.* **420**, 199–209 (2016).
 82. Miyamoto, M., Nam, L., Kannan, S. & Kwon, C. Heart organoids and tissue models for modeling development and disease. *Semin. Cell Dev. Biol.* **118**, 119–128 (2021).
 83. Balak, J. R. A., Juksar, J., Carlotti, F., Lo Nigro, A. & de Koning, E. J. P. Organoids from the Human Fetal and Adult Pancreas. *Curr. Diab. Rep.* **19**, 1–10 (2019).
 84. Yang, Q. & Liberali, P. Collective behaviours in organoids. *Curr. Opin. Cell Biol.* **72**, 81–90 (2021).
 85. Sato, T. & Clevers, H. Growing self-organizing mini-guts from a single intestinal stem cell: mechanism and applications. *Science* **340**, 1190–1194 (2013).
 86. Karzbrun, E. & Reiner, O. Brain Organoids—A Bottom-Up Approach for Studying Human Neurodevelopment. *Bioeng. 2019, Vol. 6, Page 9* **6**, 9 (2019).
 87. Skylar-Scott, M. A. *et al.* Orthogonally induced differentiation of stem cells for the programmatic patterning of vascularized organoids and bioprinted tissues. *Nat. Biomed. Eng.* 2022 64 **6**, 449–462 (2022).
 88. Grosser, S. *et al.* Cell and Nucleus Shape as an Indicator of Tissue Fluidity in Carcinoma. *Phys. Rev. X* **11**, (2021).
 89. Kopanska, K. S., Alcheikh, Y., Staneva, R., Vignjevic, D. & Betz, T. Tensile Forces Originating from Cancer Spheroids Facilitate Tumor Invasion. *PLoS One* **11**, e0156442 (2016).
 90. Lucio, A. A. *et al.* Spatiotemporal variation of endogenous cell-generated stresses within 3D multicellular spheroids. *Sci. Reports* 2017 71 **7**, 1–11 (2017).
 91. Hofer, M. & Lutolf, M. P. Engineering organoids. *Nat. Rev. Mater.* 2021 65 **6**, 402–420 (2021).
 92. Nikolaev, M. *et al.* Homeostatic mini-intestines through scaffold-guided organoid morphogenesis. *Nat.* 2020 5857826 **585**, 574–578 (2020).
 93. Wang, Y. *et al.* Formation of Human Colonic Crypt Array by Application of Chemical Gradients Across a Shaped Epithelial Monolayer. *Cell. Mol. Gastroenterol. Hepatol.* **5**, 113–

- 130 (2018).
94. Narayanan, V. *et al.* Osmotic Gradients in Epithelial Acini Increase Mechanical Tension across E-cadherin, Drive Morphogenesis, and Maintain Homeostasis. *Curr. Biol.* **30**, 624-633.e4 (2020).
 95. Fang, G. *et al.* Mammary Tumor Organoid Culture in Non-Adhesive Alginate for Luminal Mechanics and High-Throughput Drug Screening. *Adv. Sci.* **8**, 2102418 (2021).
 96. Ribeiro, A. J. S., Denisin, A. K., Wilson, R. E. & Pruitt, B. L. For whom the cells pull: Hydrogel and micropost devices for measuring traction forces. *Methods* **94**, 51–64 (2016).
 97. Wang, J. H. C. & Lin, J. S. Cell traction force and measurement methods. *Biomech. Model. Mechanobiol.* **6**, 361–371 (2007).
 98. Plotnikov, S. V., Sabass, B., Schwarz, U. S. & Waterman, C. M. High-Resolution Traction Force Microscopy. *Methods Cell Biol.* **123**, 367–394 (2014).
 99. Iwanicki, M. P. *et al.* Ovarian cancer spheroids use myosin-generated force to clear the mesothelium. *Cancer Discov.* **1**, 144–157 (2011).
 100. Wang, S., Matsumoto, K., Lish, S. R., Cartagena-Rivera, A. X. & Yamada, K. M. Budding epithelial morphogenesis driven by cell-matrix versus cell-cell adhesion. *Cell* **184**, 3702-3716.e30 (2021).
 101. Saez, A. *et al.* Traction forces exerted by epithelial cell sheets. *J. Phys. Condens. Matter* **22**, 194119 (2010).
 102. Aoun, L. *et al.* Measure and characterization of the forces exerted by growing multicellular spheroids using microdevice arrays. *PLoS One* **14**, e0217227 (2019).
 103. Dolega, M. E. *et al.* Cell-like pressure sensors reveal increase of mechanical stress towards the core of multicellular spheroids under compression. *Nat. Commun.* **2017 81** **8**, 1–9 (2017).
 104. Jaiswal, D. *et al.* Stiffness analysis of 3D spheroids using microtweezers. *PLoS One* **12**, e0188346 (2017).
 105. Beaune, G. *et al.* Spontaneous migration of cellular aggregates from giant keratocytes to running spheroids. *Proc. Natl. Acad. Sci. U. S. A.* **115**, 12926–12931 (2018).
 106. Pérez-González, C. *et al.* Mechanical compartmentalization of the intestinal organoid enables crypt folding and collective cell migration. *Nat. Cell Biol.* **2021 237** **23**, 745–757 (2021).
 107. Kang, W. *et al.* A novel jamming phase diagram links tumor invasion to non-equilibrium phase separation. *iScience* **24**, 103252 (2021).
 108. Buchmann, B. *et al.* Mechanical plasticity of collagen directs branch elongation in human mammary gland organoids. *Nat. Commun.* **2021 121** **12**, 1–10 (2021).
 109. Moeller, J. *et al.* Controlling cell shape on hydrogels using lift-off protein patterning. *PLoS One* **13**, e0189901 (2018).
 110. Tee, Y. H. *et al.* Cellular chirality arising from the self-organization of the actin cytoskeleton. *Nat. Cell Biol.* **2014 174** **17**, 445–457 (2015).
 111. Thé, M. *et al.* Anisotropy of cell adhesive microenvironment governs cell internal organization and orientation of polarity. *Proc. Natl. Acad. Sci. U. S. A.* **103**, 19771–19776 (2006).
 112. Peyret, G. *et al.* Sustained Oscillations of Epithelial Cell Sheets. *Biophys. J.* **117**, 464–478 (2019).
 113. Alom Ruiz, S. & Chen, C. S. Microcontact printing: A tool to pattern. *Soft Matter* **3**, 168–177 (2007).
 114. Engel, L. *et al.* Extracellular matrix micropatterning technology for whole cell cryogenic electron microscopy studies. *J. Micromechanics Microengineering* **29**, 115018 (2019).
 115. Nakanishi, J. *et al.* Spatiotemporal control of cell adhesion on a self-assembled monolayer having a photocleavable protecting group. *Anal. Chim. Acta* **578**, 100–104 (2006).
 116. Strale, P. O. *et al.* Multiprotein Printing by Light-Induced Molecular Adsorption. *Adv. Mater.* **28**, 2024–2029 (2016).
 117. Nishimura, R. *et al.* Appropriate tension sensitivity of α -catenin ensures rounding morphogenesis of epithelial spheroids. *Cell Struct. Funct.* **47**, 55–73 (2022).

118. Cassereau, L., Miroshnikova, Y. A., Ou, G., Lakins, J. & Weaver, V. M. A 3D tension bioreactor platform to study the interplay between ECM stiffness and tumor phenotype. *J. Biotechnol.* **193**, 66–69 (2015).
119. Mekhdjian, A. H. *et al.* Integrin-mediated traction force enhances paxillin molecular associations and adhesion dynamics that increase the invasiveness of tumor cells into a three-dimensional extracellular matrix. *Mol. Biol. Cell* **28**, 1467–1488 (2017).
120. Repina, N. A. *et al.* Optogenetic control of Wnt signaling for modeling early embryogenic patterning with human pluripotent stem cells. *bioRxiv* 665695 (2019) doi:10.1101/665695.
121. Kałafut, J. *et al.* Optogenetic control of NOTCH1 signaling. *Cell Commun. Signal.* **2022** *201* **20**, 1–14 (2022).
122. Van Horsen, R. & Ten Hagen, T. L. M. Crossing barriers: the new dimension of 2D cell migration assays. *J. Cell. Physiol.* **226**, 288–290 (2011).
123. Fong, E., Tzllil, S. & Tirrell, D. A. Boundary crossing in epithelial wound healing. *Proc. Natl. Acad. Sci. U. S. A.* **107**, 19302–19307 (2010).
124. Bürk, R. R. A Factor from a Transformed Cell Line That Affects Cell Migration. *Proc. Natl. Acad. Sci. U. S. A.* **70**, 369 (1973).
125. Coomber, B. L. & Gotlieb, A. I. In vitro endothelial wound repair. Interaction of cell migration and proliferation. *Arterioscler. An Off. J. Am. Hear. Assoc. Inc.* **10**, 215–222 (1990).
126. Petitjean, L. *et al.* Velocity Fields in a Collectively Migrating Epithelium. *Biophys. J.* **98**, 1790 (2010).
127. Poujade, M. *et al.* Collective migration of an epithelial monolayer in response to a model wound. *Proc. Natl. Acad. Sci. U. S. A.* **104**, 15988–15993 (2007).
128. De Pascalis, C. *et al.* Intermediate filaments control collective migration by restricting traction forces and sustaining cell-cell contacts. *J. Cell Biol.* **217**, 3031–3044 (2018).
129. Sim, J. Y. *et al.* Spatial distribution of cell-cell and cell-ECM adhesions regulates force balance while main-taining E-cadherin molecular tension in cell pairs. *Mol. Biol. Cell* **26**, 2456–2465 (2015).
130. Tambe, D. T. *et al.* Collective cell guidance by cooperative intercellular forces. *Nat. Mater.* **10**, 469–475 (2011).
131. Zaritsky, A. *et al.* Seeds of Locally Aligned Motion and Stress Coordinate a Collective Cell Migration. *Biophys. J.* **109**, 2492 (2015).
132. Ng, M. R. os., Besser, A., Brugge, J. S. & Danuser, G. Mapping the dynamics of force transduction at cell-cell junctions of epithelial clusters. *Elife* **3**, e03282 (2014).
133. Hart, K. C. *et al.* An Easy-to-Fabricate Cell Stretcher Reveals Density-Dependent Mechanical Regulation of Collective Cell Movements in Epithelia. *Cell. Mol. Bioeng.* **14**, 569–581 (2021).
134. Brodland, G. W. *et al.* CellFIT: A Cellular Force-Inference Toolkit Using Curvilinear Cell Boundaries. *PLoS One* **9**, e99116 (2014).
135. Borghi, N. *et al.* E-cadherin is under constitutive actomyosin-generated tension that is increased at cell-cell contacts upon externally applied stretch. *Proc. Natl. Acad. Sci. U. S. A.* **109**, 12568–12573 (2012).
136. Tamada, M., Perez, T. D., Nelson, W. J. & Sheetz, M. P. Two distinct modes of myosin assembly and dynamics during epithelial wound closure. *J. Cell Biol.* **176**, 27 (2007).
137. Silver, B. B., Wolf, A. E., Lee, J., Pang, M. F. & Nelson, C. M. Epithelial tissue geometry directs emergence of bioelectric field and pattern of proliferation. *Mol. Biol. Cell* **31**, 1691–1702 (2020).
138. Yu, J. *et al.* Spatiotemporal Oscillation in Confined Epithelial Motion upon Fluid-to-Solid Transition. *ACS Nano* **15**, 7618–7627 (2021).
139. Simmons, C. S., Ribeiro, A. J. S. & Pruitt, B. L. Formation of composite polyacrylamide and silicone substrates for independent control of stiffness and strain. *Lab Chip* **13**, 646–649 (2013).
140. Butcher, D. T., Alliston, T. & Weaver, V. M. A tense situation: forcing tumour progression. *Nat. Rev. Cancer* **2009** *92* **9**, 108–122 (2009).

141. Kolahi, K. S. *et al.* Effect of Substrate Stiffness on Early Mouse Embryo Development. *PLoS One* **7**, 41717 (2012).
142. Ondeck, M. G. *et al.* Dynamically stiffened matrix promotes malignant transformation of mammary epithelial cells via collective mechanical signaling. *Proc. Natl. Acad. Sci. U. S. A.* **116**, 3502–3507 (2019).
143. Ng, M. R., Besser, A., Danuser, G. & Brugge, J. S. Substrate stiffness regulates cadherin-dependent collective migration through myosin-II contractility. *J. Cell Biol.* **199**, 545–563 (2012).
144. Pelham, R. J. & Wang, Y. L. Cell locomotion and focal adhesions are regulated by substrate flexibility. *Proc. Natl. Acad. Sci. U. S. A.* **94**, 13661–13665 (1997).
145. Nasrollahi, S. *et al.* Past matrix stiffness primes epithelial cells and regulates their future collective migration through a mechanical memory. *Biomaterials* **146**, 146–155 (2017).
146. Dalton, B. A. *et al.* Modulation of epithelial tissue and cell migration by microgrooves. (2001) doi:10.1002/1097-4636.
147. Nam, K. H. *et al.* Multiscale Cues Drive Collective Cell Migration. *Sci. Rep.* **6**, (2016).
148. Leggett, S. E., Hruska, A. M., Guo, M. & Wong, I. Y. The epithelial-mesenchymal transition and the cytoskeleton in bioengineered systems. *Cell Commun. Signal.* **2021 191** **19**, 1–24 (2021).
149. Luciano, M. *et al.* Cell monolayers sense curvature by exploiting active mechanics and nuclear mechanoadaptation. *Nat. Phys.* **2021 1712** **17**, 1382–1390 (2021).
150. Hocking, D. C. & Chang, C. H. Fibronectin matrix polymerization regulates small airway epithelial cell migration. *Am. J. Physiol. Lung Cell. Mol. Physiol.* **285**, (2003).
151. Trinh, L. A. & Stainier, D. Y. R. Fibronectin regulates epithelial organization during myocardial migration in zebrafish. *Dev. Cell* **6**, 371–382 (2004).
152. Zhang, J., Owen, C. R., Sanders, M. A., Turner, J. R. & Basson, M. D. The Motogenic Effects of Cyclic Mechanical Strain on Intestinal Epithelial Monolayer Wound Closure Are Matrix Dependent. *Gastroenterology* **131**, 1179–1189 (2006).
153. Smith, J. T., Elkin, J. T. & Reichert, W. M. Directed cell migration on fibronectin gradients: effect of gradient slope. *Exp. Cell Res.* **312**, 2424–2432 (2006).
154. Mohammed, D. *et al.* Producing Collagen Micro-stripes with Aligned Fibers for Cell Migration Assays. *Cell. Mol. Bioeng.* **13**, 87–98 (2020).
155. Hart, K. C. *et al.* E-cadherin and LGN align epithelial cell divisions with tissue tension independently of cell shape. *Proc. Natl. Acad. Sci. U. S. A.* **114**, E5845–E5853 (2017).
156. Benham-Pyle, B. W., Pruitt, B. L. & Nelson, W. J. Mechanical strain induces E-cadherin-dependent Yap1 and β -catenin activation to drive cell cycle entry. *Science (80-.)*. **348**, 1024–1027 (2015).
157. Roye, Y. *et al.* A Personalized Glomerulus Chip Engineered from Stem Cell-Derived Epithelium and Vascular Endothelium. *Micromachines* **2021, Vol. 12, Page 967** **12**, 967 (2021).
158. Mäntylä, E. & Ihalainen, T. O. Brick Strex: a robust device built of LEGO bricks for mechanical manipulation of cells. *Sci. Reports* **2021 111** **11**, 1–14 (2021).
159. Dow, L. P., Khankhel, A. H., Abram, J. & Valentine, M. T. 3D-printable cell crowding device enables imaging of live cells in compression. *Biotechniques* **68**, 275–278 (2020).
160. Huang, L., Mathieu, P. S. & Helmke, B. P. A stretching device for high-resolution live-cell imaging. *Ann. Biomed. Eng.* **38**, 1728–1740 (2010).
161. Li, Z. *et al.* Cell Nanomechanics Based on Dielectric Elastomer Actuator Device. *Nano-Micro Lett.* **2019 111** **11**, 1–19 (2019).
162. Poulin, A. *et al.* An ultra-fast mechanically active cell culture substrate. *Sci. Reports* **2018 81** **8**, 1–10 (2018).
163. Al-Maslamani, N. A., Khilan, A. A. & Horn, H. F. Design of a 3D printed, motorized, uniaxial cell stretcher for microscopic and biochemical analysis of mechanotransduction. *Biol. Open* **10**, (2021).

164. Kamble, H., Barton, M. J., Jun, M., Park, S. & Nguyen, N. T. Cell stretching devices as research tools: engineering and biological considerations. *Lab Chip* **16**, 3193–3203 (2016).
165. Khilan, A. A., Al-Maslamani, N. A. & Horn, H. F. Cell stretchers and the LINC complex in mechanotransduction. *Arch. Biochem. Biophys.* **702**, 108829 (2021).
166. Das, A., Fischer, R. S., Pan, D. & Waterman, C. M. YAP nuclear localization in the absence of cell-cell contact is mediated by a filamentous actin-dependent, Myosin II and Phospho-YAP-independent pathway during extracellular matrix mechanosensing. *J. Biol. Chem.* **291**, 6096–6110 (2016).
167. Gudipaty, S. A. *et al.* Mechanical stretch triggers rapid epithelial cell division through Piezo1. *Nat. 2017 5437643* **543**, 118–121 (2017).
168. Den Elzen, N., Buttery, C. V., Maddugoda, M. P., Ren, G. & Yap, A. S. Cadherin adhesion receptors orient the mitotic spindle during symmetric cell division in mammalian epithelia. *Mol. Biol. Cell* **20**, 3740–3750 (2009).
169. Xu, G. K., Liu, Y. & Zheng, Z. Oriented cell division affects the global stress and cell packing geometry of a monolayer under stretch. *J. Biomech.* **49**, 401–407 (2016).
170. Ao, M. *et al.* Stretching Fibroblasts Remodels Fibronectin and Alters Cancer Cell Migration. *Sci. Reports 2015 51* **5**, 1–9 (2015).
171. Simmons, C. S. *et al.* Integrated strain array for cellular mechanobiology studies. *J. Micromechanics Microengineering* **21**, 054016 (2011).
172. G er emie, L. *et al.* Evolution of a confluent gut epithelium under on-chip cyclic stretching. *Phys. Rev. Res.* **4**, 023032 (2022).
173. Wang, J. H. C., Goldschmidt-Clermont, P., Wille, J. & Yin, F. C. P. Specificity of endothelial cell reorientation in response to cyclic mechanical stretching. *J. Biomech.* **34**, 1563–1572 (2001).
174. Roshanzadeh, A. *et al.* Mechanoadaptive organization of stress fiber subtypes in epithelial cells under cyclic stretches and stretch release. *Sci. Reports 2020 101* **10**, 1–14 (2020).
175. Tremblay, D., Chagnon-Lessard, S., Mirzaei, M., Pelling, A. E. & Godin, M. A microscale anisotropic biaxial cell stretching device for applications in mechanobiology. *Biotechnol. Lett.* **36**, 657–665 (2014).
176. Goldyn, A. M., Rioja, B. A., Spatz, J. P., Ballestrem, C. & Kemkemer, R. Force-induced cell polarisation is linked to RhoA-driven microtubule-independent focal-adhesion sliding. *J. Cell Sci.* **122**, 3644–3651 (2009).
177. Lien, J. C. & Wang, Y. li. Cyclic stretching-induced epithelial cell reorientation is driven by microtubule-modulated transverse extension during the relaxation phase. *Sci. Reports 2021 111* **11**, 1–12 (2021).
178. Chen, Y., Pasapera, A. M., Koretsky, A. P. & Waterman, C. M. Orientation-specific responses to sustained uniaxial stretching in focal adhesion growth and turnover. *Proc. Natl. Acad. Sci. U. S. A.* **110**, (2013).
179. Xu, J. *et al.* Cellular mechanics of wound formation in single cell layer under cyclic stretching. *Biophys. J.* **121**, 288–299 (2022).
180. Dan, A., Huang, R. B. & Leckband, D. E. Dynamic Imaging Reveals Coordinate Effects of Cyclic Stretch and Substrate Stiffness on Endothelial Integrity. *Ann. Biomed. Eng.* **44**, 3655 (2016).
181. Birukova, A. A. *et al.* Differential Regulation of Pulmonary Endothelial Monolayer Integrity by Varying Degrees of Cyclic Stretch. *Am. J. Pathol.* **168**, 1749 (2006).
182. Kah, D. *et al.* A low-cost uniaxial cell stretcher for six parallel wells. *HardwareX* **9**, e00162 (2021).
183. Peussa, H. I. *et al.* Pneumatic equiaxial compression device for mechanical manipulation of epithelial cell packing and physiology. *PLoS One* **17**, e0268570 (2022).
184. Harris, A. R. *et al.* Generating suspended cell monolayers for mechanobiological studies. *Nat. Protoc.* **2013 812** **8**, 2516–2530 (2013).

185. Wyatt, T. P. J. *et al.* Actomyosin controls planarity and folding of epithelia in response to compression. *Nat. Mater.* 2019 191 **19**, 109–117 (2019).
186. Wyatt, T. P. J. *et al.* Emergence of homeostatic epithelial packing and stress dissipation through divisions oriented along the long cell axis. *Proc. Natl. Acad. Sci. U. S. A.* **112**, 5726–5731 (2015).
187. Frey, M. T. & Wang, Y. L. A photo-modulatable material for probing cellular responses to substrate rigidity. *Soft Matter* **5**, 1918–1924 (2009).
188. Mosiewicz, K. A., Kolb, L., Van Der Vlies, A. J. & Lutolf, M. P. Microscale patterning of hydrogel stiffness through light-triggered uncaging of thiols. *Biomater. Sci.* **2**, 1640–1651 (2014).
189. Kloxin, A. M., Kasko, A. M., Salinas, C. N. & Anseth, K. S. Photodegradable hydrogels for dynamic tuning of physical and chemical properties. *Science (80-.)*. **324**, 59–63 (2009).
190. Levental, K. R. *et al.* Matrix crosslinking forces tumor progression by enhancing integrin signaling. *Cell* **139**, 891–906 (2009).
191. Lo, C. M., Wang, H. B., Dembo, M. & Wang, Y. L. Cell movement is guided by the rigidity of the substrate. *Biophys. J.* **79**, 144 (2000).
192. Sunyer, R. *et al.* Collective cell durotaxis emerges from long-range intercellular force transmission. *Science (80-.)*. **353**, 1157–1161 (2016).
193. Plotnikov, S. V. & Waterman, C. M. Guiding cell migration by tugging. *Curr. Opin. Cell Biol.* **25**, 619–626 (2013).
194. Garbett, D. *et al.* T-Plastin reinforces membrane protrusions to bridge matrix gaps during cell migration. *Nat. Commun.* 2020 111 **11**, 1–18 (2020).
195. Vedula, S. R. K. *et al.* Microfabricated environments to study collective cell behaviors. *Methods Cell Biol.* **120**, 235–252 (2014).
196. Vedula, S. R. K. *et al.* Mechanics of epithelial closure over non-adherent environments. *Nat. Commun.* 2015 61 **6**, 1–10 (2015).
197. Garcia, M. A., Sadeghipour, E., Engel, L., Nelson, W. J. & Pruitt, B. L. MEMS device for applying shear and tension to an epithelium combined with fluorescent live cell imaging. *J. Micromech. Microeng.* **30**, (2020).
198. Farjood, F. & Vargis, E. Novel devices for studying acute and chronic mechanical stress in retinal pigment epithelial cells. *Lab Chip* **18**, 3413–3424 (2018).
199. Valon, L., Marín-Llauradó, A., Wyatt, T., Charras, G. & Trepate, X. Optogenetic control of cellular forces and mechanotransduction. *Nat. Commun.* 2017 81 **8**, 1–10 (2017).
200. Cavanaugh, K. E., Staddon, M. F., Munro, E., Banerjee, S. & Gardel, M. L. RhoA Mediates Epithelial Cell Shape Changes via Mechanosensitive Endocytosis. *Dev. Cell* **52**, 152-166.e5 (2020).
201. Martínez-Ara, G. *et al.* Optogenetic control of apical constriction induces synthetic morphogenesis in mammalian tissues. *Nat. Commun.* 2022 131 **13**, 1–13 (2022).
202. Mehidi, A. *et al.* Transient Activations of Rac1 at the Lamellipodium Tip Trigger Membrane Protrusion. *Curr. Biol.* **29**, 2852-2866.e5 (2019).
203. Valon, L. *et al.* Robustness of epithelial sealing is an emerging property of local ERK feedback driven by cell elimination. *Dev. Cell* **56**, 1700-1711.e8 (2021).
204. Meshik, X., O'Neill, P. R. & Gautam, N. Optogenetic Control of Cell Migration. *Methods Mol. Biol.* **1749**, 313–324 (2018).
205. Maruthamuthu, V., Sabass, B., Schwarz, U. S. & Gardel, M. L. Cell-ECM traction force modulates endogenous tension at cell-cell contacts. *Proc. Natl. Acad. Sci. U. S. A.* **108**, 4708–4713 (2011).
206. Tseng, Q. *et al.* Spatial organization of the extracellular matrix regulates cell-cell junction positioning. *Proc. Natl. Acad. Sci. U. S. A.* **109**, 1506–1511 (2012).
207. Maruthamuthu, V. & Gardel, M. L. Protrusive Activity Guides Changes in Cell-Cell Tension during Epithelial Cell Scattering. *Biophys. J.* **107**, 555 (2014).

208. Li, J. X. H., Tang, V. W. & Brieher, W. M. Actin protrusions push at apical junctions to maintain E-cadherin adhesion. *Proc. Natl. Acad. Sci. U. S. A.* **117**, 432–438 (2020).
209. Burute, M. *et al.* Polarity Reversal by Centrosome Repositioning Primes Cell Scattering during Epithelial-to-Mesenchymal Transition. *Dev. Cell* **40**, 168–184 (2017).
210. Yevick, H. G., Duclos, G., Bonnet, I. & Silberzan, P. Architecture and migration of an epithelium on a cylindrical wire. *Proc. Natl. Acad. Sci. U. S. A.* **112**, 5944–5949 (2015).
211. Mak, M., Reinhart-King, C. A. & Erickson, D. Microfabricated Physical Spatial Gradients for Investigating Cell Migration and Invasion Dynamics. *PLoS One* **6**, e20825 (2011).
212. Ros, E. *et al.* Single cell migration profiling on a microenvironmentally tunable hydrogel microstructure device that enables stem cell potency evaluation. *Lab Chip* **20**, 958–972 (2020).
213. Hennig, K. *et al.* Stick-slip dynamics of cell adhesion triggers spontaneous symmetry breaking and directional migration of mesenchymal cells on one-dimensional lines. *Sci. Adv.* **6**, (2020).
214. Yokoyama, S., Matsui, T. S. & Deguchi, S. Microcontact Peeling as a New Method for Cell Micropatterning. *PLoS One* **9**, e102735 (2014).
215. Albert, P. J. & Schwarz, U. S. Dynamics of Cell Ensembles on Adhesive Micropatterns: Bridging the Gap between Single Cell Spreading and Collective Cell Migration. *PLOS Comput. Biol.* **12**, e1004863 (2016).
216. Esfahani, A. M. *et al.* Characterization of the strain-rate-dependent mechanical response of single cell–cell junctions. *Proc. Natl. Acad. Sci. U. S. A.* **118**, (2021).
217. Scarpa, E. *et al.* A novel method to study contact inhibition of locomotion using micropatterned substrates. *Biol. Open* **2**, 901–906 (2013).
218. Mahmud, G. *et al.* Directing cell motions on micropatterned ratchets. *Nat. Phys.* **2009 58** **5**, 606–612 (2009).
219. Li, G. *et al.* Hierarchically aligned gradient collagen micropatterns for rapidly screening Schwann cells behavior. *Colloids Surfaces B Biointerfaces* **176**, 341–351 (2019).
220. Sri-Ranjan, K. *et al.* Intrinsic cell rheology drives junction maturation. *Nat. Commun.* **2022 131** **13**, 1–20 (2022).
221. Schoenit, A. *et al.* Tuning Epithelial Cell-Cell Adhesion and Collective Dynamics with Functional DNA-E-Cadherin Hybrid Linkers. *Nano Lett.* **22**, 302–310 (2022).
222. Collins, C., Denisin, A. K., Pruitt, B. L. & Nelson, W. J. Changes in E-cadherin rigidity sensing regulate cell adhesion. *Proc. Natl. Acad. Sci. U. S. A.* **114**, E5835–E5844 (2017).
223. Schierbaum, N., Rheinlaender, J. & Schäffer, T. E. Combined atomic force microscopy (AFM) and traction force microscopy (TFM) reveals a correlation between viscoelastic material properties and contractile prestress of living cells. *Soft Matter* **15**, 1721–1729 (2019).
224. Rheinlaender, J., Wirbel, H. & Schäffer, T. E. Spatial correlation of cell stiffness and traction forces in cancer cells measured with combined SICM and TFM. *RSC Adv.* **11**, 13951–13956 (2021).
225. Sigaut, L. *et al.* Live cell imaging reveals focal adhesions mechanoresponses in mammary epithelial cells under sustained equibiaxial stress. *Sci. Reports* **2018 81** **8**, 1–15 (2018).
226. Mandal, K., Asnacios, A., Goud, B. & Manneville, J. B. Mapping intracellular mechanics on micropatterned substrates. *Proc. Natl. Acad. Sci. U. S. A.* **113**, E7159–E7168 (2016).
227. Oakes, P. W., Banerjee, S., Marchetti, M. C. & Gardel, M. L. Geometry regulates traction stresses in adherent cells. *Biophys. J.* **107**, 825–833 (2014).
228. Park, J. A., Atia, L., Mitchel, J. A., Fredberg, J. J. & Butler, J. P. Collective migration and cell jamming in asthma, cancer and development. *J. Cell Sci.* **129**, 3375–3383 (2016).
229. Yan, L. & Bi, D. Multicellular Rosettes Drive Fluid-solid Transition in Epithelial Tissues. (2019) doi:10.1103/PhysRevX.9.011029.
230. Bi, D., Lopez, J. H., Schwarz, J. M. & Manning, M. L. A density-independent rigidity transition in biological tissues. *Nat. Phys.* **2015 1112** **11**, 1074–1079 (2015).
231. Park, J. A. *et al.* Unjamming and cell shape in the asthmatic airway epithelium. *Nat. Mater.* **14**, 1040–1048 (2015).

232. Bi, D., Yang, X., Marchetti, M. C. & Manning, M. L. Motility-driven glass and jamming transitions in biological tissues. *Phys. Rev. X* **6**, (2016).
233. Chiang, M. & Marenduzzo, D. Glass transitions in the cellular Potts model. *EPL* **116**, (2016).
234. Ilina, O. *et al.* Cell–cell adhesion and 3D matrix confinement determine jamming transitions in breast cancer invasion. *Nat. Cell Biol.* **22**, 1103–1115 (2020).
235. Petridou, N. I., Corominas-Murtra, B., Heisenberg, C. P. & Hannezo, E. Rigidity percolation uncovers a structural basis for embryonic tissue phase transitions. *Cell* **184**, 1914–1928.e19 (2021).
236. Czajkowski, M., Sussman, D. M., Marchetti, M. C. & Manning, M. L. Glassy dynamics in models of confluent tissue with mitosis and apoptosis. *Soft Matter* **15**, 9133–9149 (2019).
237. Matoz-Fernandez, D. A., Martens, K., Sknepnek, R., Barrat, J. L. & Henkes, S. Cell division and death inhibit glassy behaviour of confluent tissues. *Soft Matter* **13**, 3205–3212 (2017).
238. Tanaka, S. Simulation Frameworks for Morphogenetic Problems. *Comput. 2015, Vol. 3, Pages 197-221* **3**, 197–221 (2015).
239. Alert, R. & Trepat, X. Physical Models of Collective Cell Migration. <https://doi.org/10.1146/annurev-conmatphys-031218-013516> **11**, 77–101 (2020).
240. Banerjee, S., Utuje, K. J. C. & Marchetti, M. C. Propagating Stress Waves during Epithelial Expansion. *Phys. Rev. Lett.* **114**, 228101 (2015).
241. Nagai, T. & Honda, H. A dynamic cell model for the formation of epithelial tissues. *Philos. Mag. B Phys. Condens. Matter; Stat. Mech. Electron. Opt. Magn. Prop.* **81**, 699–719 (2001).
242. Farhadifar, R., Röper, J. C., Aigouy, B., Eaton, S. & Jülicher, F. The Influence of Cell Mechanics, Cell-Cell Interactions, and Proliferation on Epithelial Packing. *Curr. Biol.* **17**, 2095–2104 (2007).
243. Fletcher, A. G., Osborne, J. M., Maini, P. K. & Gavaghan, D. J. Implementing vertex dynamics models of cell populations in biology within a consistent computational framework. *Prog. Biophys. Mol. Biol.* **113**, 299–326 (2013).
244. Alt, S., Ganguly, P. & Salbreux, G. Vertex models: from cell mechanics to tissue morphogenesis. *Philos. Trans. R. Soc. B Biol. Sci.* **372**, (2017).
245. Fletcher, A. G., Osterfield, M., Baker, R. E. & Shvartsman, S. Y. Vertex Models of Epithelial Morphogenesis. *Biophys. J.* **106**, 2291–2304 (2014).
246. Pérez-Verdugo, F., Reig, G., Cerda, M., Concha, M. L. & Soto, R. Geometrical characterization of active contraction pulses in epithelial cells using the two-dimensional vertex model. *J. R. Soc. Interface* **19**, (2022).
247. Honda, H. & Nagai, T. Mathematical Models of Cell-Based Morphogenesis. (2022) doi:10.1007/978-981-19-2916-8.
248. Honda, H., Tanemura, M. & Nagai, T. A three-dimensional vertex dynamics cell model of space-filling polyhedra simulating cell behavior in a cell aggregate. *J. Theor. Biol.* **226**, 439–453 (2004).
249. Bielmeier, C. *et al.* Interface Contractility between Differently Fated Cells Drives Cell Elimination and Cyst Formation. *Curr. Biol.* **26**, 563–574 (2016).
250. Osterfield, M., Du, X. X., Schüpbach, T., Wieschaus, E. & Shvartsman, S. Y. Three-Dimensional Epithelial Morphogenesis in the Developing Drosophila Egg. *Dev. Cell* **24**, 400–410 (2013).
251. Okuda, S., Inoue, Y., Eiraku, M., Sasai, Y. & Adachi, T. Apical contractility in growing epithelium supports robust maintenance of smooth curvatures against cell-division-induced mechanical disturbance. *J. Biomech.* **46**, 1705–1713 (2013).
252. Barton, D. L., Henkes, S., Weijer, C. J. & Sknepnek, R. Active Vertex Model for cell-resolution description of epithelial tissue mechanics. *PLoS Comput. Biol.* **13**, (2017).
253. Duclut, C., Paijmans, J., Inamdar, M. M., Modes, C. D. & Jülicher, F. THE EUROPEAN PHYSICAL JOURNAL E Active T1 transitions in cellular networks. *Eur. Phys. J. E* **45**, 29 (2022).

254. Chen, Y. *et al.* Activation of Topological Defects Induces a Brittle-to-Ductile Transition in Epithelial Monolayers. *Phys. Rev. Lett.* **128**, 018101 (2022).
255. Saraswathibhatla, A., Henkes, S., Galles, E. E., Sknepnek, R. & Notbohm, J. Coordinated tractions increase the size of a collectively moving pack in a cell monolayer. *Extrem. Mech. Lett.* **48**, 101438 (2021).
256. Giavazzi, F. *et al.* Flocking transitions in confluent tissues. *Soft Matter* **14**, 3471–3477 (2018).
257. Noll, N., Mani, M., Heemskerk, I., Streichan, S. J. & Shraiman, B. I. Active tension network model suggests an exotic mechanical state realized in epithelial tissues. *Nat. Phys.* **13**, 1221–1226 (2017).
258. Teomy, E., Kessler, D. A. & Levine, H. Confluent and nonconfluent phases in a model of cell tissue. *Phys. Rev. E* **98**, 042418 (2018).
259. Kim, S., Pochitaloff, M., Stooke-Vaughan, G. A. & Campàs, O. Embryonic tissues as active foams. *Nat. Phys.* **17**, 859–866 (2021).
260. Banerjee, S. & Marchetti, M. C. Continuum Models of Collective Cell Migration. *Adv. Exp. Med. Biol.* **1146**, 45–66 (2019).
261. Doostmohammadi, A. *et al.* Celebrating Soft Matter 's 10th Anniversary: Cell division: a source of active stress in cellular monolayers. *Soft Matter* **11**, 7328–7336 (2015).
262. Corominas-Murtra, B. & Petridou, N. I. Viscoelastic Networks: Forming Cells and Tissues. *Front. Phys.* **9**, 314 (2021).
263. Notbohm, J. *et al.* Cellular Contraction and Polarization Drive Collective Cellular Motion. *Biophys. J.* **110**, 2729–2738 (2016).
264. Serra-Picamal, X. *et al.* Mechanical waves during tissue expansion. *Nat. Phys.* **8**, 628–634 (2012).
265. Fierling, J. *et al.* Embryo-scale epithelial buckling forms a propagating furrow that initiates gastrulation. *Nat. Commun.* **13**, (2022).
266. Klughammer, N. *et al.* Cytoplasmic flows in starfish oocytes are fully determined by cortical contractions. *Plos Comput. Biol.* **14**, e1006588–e1006588 (2018).
267. Marchetti, M. C. *et al.* Hydrodynamics of soft active matter. *Rev. Mod. Phys.* **85**, 1143–1189 (2013).
268. Van Liedekerke, P., Palm, M. M., Jagiella, N. & Drasdo, D. Simulating tissue mechanics with agent-based models: concepts, perspectives and some novel results. *Comput. Part. Mech.* **2**, 401–444 (2015).
269. Graner, F. & Glazier, J. A. *Simulation of Biological Cell Sorting Using a Two-Dimensional Extended Potts Model.* vol. 69.
270. Käfer, J., Hogeweg, P. & Marée, A. F. M. Moving Forward Moving Backward: Directional Sorting of Chemotactic Cells due to Size and Adhesion Differences. *PLOS Comput. Biol.* **2**, e56 (2006).
271. Scianna, M. & Preziosi, L. Multiscale Developments of the Cellular Potts Model. <http://dx.doi.org/10.1137/100812951> **10**, 342–382 (2012).
272. Palmieri, B., Bresler, Y., Wirtz, D. & Grant, M. Multiple scale model for cell migration in monolayers: Elastic mismatch between cells enhances motility. *Sci. Reports* **5**, 1–13 (2015).
273. Löber, J., Ziebert, F. & Aranson, I. S. Collisions of deformable cells lead to collective migration. *Sci. Reports* **5**, 1–7 (2015).
274. Boromand, A., Signoriello, A., Ye, F., O'Hern, C. S. & Shattuck, M. D. Jamming of Deformable Polygons. *Phys. Rev. Lett.* **121**, 248003 (2018).
275. Rejniak, K. A. & Anderson, A. R. A. A Computational Study of the Development of Epithelial Acini: I. Sufficient Conditions for the Formation of a Hollow Structure. *Bull. Math. Biol.* **70**, 677–712 (2008).
276. Madhikar, P., Åström, J., Baumeier, B. & Karttunen, M. Jamming and force distribution in growing epithelial tissue. *Phys. Rev. Res.* **3**, (2021).

277. George, M., Bullo, F. & Campàs, O. Connecting individual to collective cell migration. *Sci. Reports* 2017 71 **7**, 1–10 (2017).
278. Armon, S., Bull, M. S., Moriel, A., Aharoni, H. & Prakash, M. Modeling epithelial tissues as active-elastic sheets reproduce contraction pulses and predict rip resistance. *Commun. Phys.* 2021 41 **4**, 1–9 (2021).
279. Qin, R. S. & Bhadeshia, H. K. Phase field method. <https://doi.org/10.1179/174328409X453190> **26**, 803–811 (2013).
280. Nonomura, M. Study on Multicellular Systems Using a Phase Field Model. *PLoS One* **7**, e33501 (2012).
281. Fogliano, M., Morozov, A. N., Henrich, O. & Marenduzzo, D. Flow of Deformable Droplets: Discontinuous Shear Thinning and Velocity Oscillations. *Phys. Rev. Lett.* **119**, 208002 (2017).
282. Mueller, R., Yeomans, J. M. & Doostmohammadi, A. Emergence of Active Nematic Behavior in Monolayers of Isotropic Cells. *Phys. Rev. Lett.* **122**, 048004 (2019).
283. Loewe, B., Chiang, M., Marenduzzo, D. & Marchetti, M. C. Solid-Liquid Transition of Deformable and Overlapping Active Particles. *Phys. Rev. Lett.* **125**, 038003 (2020).
284. Balasubramaniam, L. *et al.* Investigating the nature of active forces in tissues reveals how contractile cells can form extensile monolayers. *Nat. Mater.* 2021 208 **20**, 1156–1166 (2021).
285. Hopkins, A., Chiang, M., Loewe, B., Marenduzzo, D. & Marchetti, M. C. Yield Stress and Compliance in Active Cell Monolayers. (2022).
286. Ritter, C. M. *et al.* Differential elasticity in lineage segregation of embryonic stem cells. (2022).
287. Aland, S., Hatzikirou, H., Lowengrub, J. & Voigt, A. A Mechanistic Collective Cell Model for Epithelial Colony Growth and Contact Inhibition. *Biophys. J.* **109**, 1347–1357 (2015).
288. Recho, P., Putelat, T. & Truskinovsky, L. Force-induced repolarization of an active crawler. *New J. Phys.* **21**, 033015 (2019).
289. Charras, G. & Yap, A. S. Tensile Forces and Mechanotransduction at Cell-Cell Junctions. *Curr. Biol.* **28**, R445–R457 (2018).
290. Kale, G. R. *et al.* Distinct contributions of tensile and shear stress on E-cadherin levels during morphogenesis. *Nat. Commun.* 2018 91 **9**, 1–16 (2018).
291. Guillot, C. & Lecuit, T. Mechanics of epithelial tissue homeostasis and morphogenesis. *Science* (80-.). **340**, 1185–1189 (2013).
292. Heller, E., Kumar, K. V., Grill, S. W. & Fuchs, E. Forces generated by cell intercalation tow epidermal sheets in mammalian tissue morphogenesis. *Dev. Cell* **28**, 617–632 (2014).
293. Trepat, X. *et al.* Viscoelasticity of human alveolar epithelial cells subjected to stretch. *Am. J. Physiol. - Lung Cell. Mol. Physiol.* **287**, 1025–1034 (2004).
294. Kuranaga, E. *et al.* Apoptosis controls the speed of looping morphogenesis in Drosophila male terminalia. *Development* **138**, 1493–1499 (2011).
295. Sawyer, J. M. *et al.* Apical constriction: a cell shape change that can drive morphogenesis. *Dev. Biol.* **341**, 5–19 (2010).
296. Eisenhoffer, G. T. *et al.* Crowding induces live cell extrusion to maintain homeostatic cell numbers in epithelia. *Nat.* 2012 4847395 **484**, 546–549 (2012).
297. Gu, Y. & Rosenblatt, J. New emerging roles for epithelial cell extrusion. *Curr. Opin. Cell Biol.* **24**, 865–870 (2012).
298. Kocgozlu, L. *et al.* Epithelial Cell Packing Induces Distinct Modes of Cell Extrusions. *Curr. Biol.* **26**, 2942–2950 (2016).
299. Marchetti, M. C. *et al.* Hydrodynamics of soft active matter. *Rev. Mod. Phys.* **85**, 1143–1189 (2013).
300. Bernheim-Groswasser, A. *et al.* Living Matter: Mesoscopic Active Materials. *Adv. Mater.* **30**, 1707028 (2018).
301. Atia, L. *et al.* Geometric constraints during epithelial jamming. *Nat. Phys.* **14**, (2018).

Chapter 2

Cyclic stretch of a 2-D epithelium

2.1 Preface

The contents of this chapter are from a manuscript submitted to BioRxiv and is reproduced from: Dow, L.P. *, Surace S.*, Morozov, K., Kennedy, R., Pruitt, B.L., “Cyclic stretch regulates epithelial cell migration in a frequency dependent manner via vinculin recruitment to cell-cell contacts”, *BioRxiv*, doi: 10.1101/2023.08.19.553915. Per BioRxiv, the copyright is retained by the authors.

In this chapter, I present a study on cyclic strain of the epithelium and its response on both short-term and long-term time scales. The original idea for the project came up in a collaborative meeting between myself, Dr. Beth Pruitt, and Dr. Cristina Marchetti. My contributions included planning and designing experiments, performing experiments, performing data analysis, creating figures, and writing and editing of the manuscript. Specifically, I performed all cell culture work, cell segmentation analysis, immunohistochemistry experiments, in addition to several cell stretching experiments, device construction, and protocol development. I mentored Stace Surace, who contributed the following: most cyclic stretching and migration experiments, device construction, PIV data analysis, aided in protocol development, and contributed to the writing of the manuscript. She serves as co-first author on the study. The base MATLAB script used for PIV analysis was contributed by Reagan Kennedy, while the base Python scripts used for cell segmentation analysis were contributed by another undergraduate I mentored, Katya

Morozov. Beth Pruitt acquired funding for the project, provided supervision, aided in the design of experiments, and contributed to the review and editing of the manuscript.

2.2. Abstract

Epithelial cell migration is critical in regulating wound healing and tissue development. The epithelial microenvironment is incredibly dynamic, subjected to mechanical cues including cyclic stretch. While cyclic cell stretching platforms have revealed responses of the epithelium such as cell reorientation and gap formation, few studies have investigated the long-term effects of cyclic stretch on cell migration. We measured the migratory response of the epithelium to a range of physiologically relevant frequencies and stretch. We integrated our experimental approach with high-throughput cell segmentation to discover a relationship between changes in cell morphology and migration as a function of cyclic stretch. Our results indicate that lower stretch frequencies (i.e., 0.1 Hz) arrest epithelial migration, accompanied by cell reorientation and high cell shape solidity. We found that this response is also accompanied by increased recruitment of vinculin to cell-cell contacts, and this recruitment is necessary to arrest cell movements. This work demonstrates a critical role for frequency dependence in epithelial response to mechanical stretch. These results confirm the mechanosensitive nature of vinculin within the adherens junction, but independently reveal a novel mechanism of low frequency stress response in supporting epithelial integrity by arresting cell migration.

2.3. Significance Statement

Mechanical forces play an integral role in regulating epithelia behavior, including collective cell movements. This work finds frequency is a critical variable in regulating epithelia response to cyclic stretch. We demonstrate that specific morphological changes including shape reorientation and cell solidity are significantly affected at low frequency mechanical stretch. These changes correlate with arrested cell movements and the recruitment of vinculin at cell-cell contacts. We present here a study that both i) offers a role for different mechanical stretch frequencies in regulating collective epithelial behavior and ii) presents a novel role for vinculin in reinforcing cell-cell contacts.

2.4. Introduction

Organ function and tissue development rely on interconnected sheets of epithelial cells. In adult tissue, these cells regulate nutrient absorption, filtration, and act as a mechanical barrier against trauma or pathogenic invasion. During tissue development, they fold and constrict, shaping new tissues. Unlike passive cellular materials such as foams, cork, honeycombs, etc., the epithelium consumes and exerts energy as independent units. This property allows epithelial cells to migrate, rearrange, and alter their cellular shape¹⁻⁴, facilitating their specific functions in dynamic microenvironments⁵.

Epithelial microenvironments exhibit high dynamism, particularly in terms of mechanical stretch and deformation. For example, lung alveolar epithelial cells experience cyclic stretching due to respiratory rhythms⁶, while peristaltic contractions of smooth muscle cyclically stretch regions of the intestinal epithelium⁷. In developing tissues, pulsatile stretches help orchestrate events such as gastrulation and dorsal closure in *Drosophila*^{8,9}.

These cyclic mechanical stretches occur across various epithelial microenvironments but differ significantly in frequency and magnitude. Many diseases also disrupt the natural mechanics of epithelia by altering stretch magnitudes and rates, as seen in irritable bowel syndrome⁷, asthma^{6,10}, and colorectal cancer¹¹.

Several studies have employed *in vitro* mechanical stretching experiments to elucidate the effects of cyclic stretch on epithelial behavior. At higher cyclic stretch amplitudes and frequencies (>20%, >1 Hz), researchers have observed gap formation in epithelia of parental Madin-Darby canine kidney (NBL-2) cells¹² and a decrease in wound healing time compared to an unstretched epithelium¹³. There is also evidence that cyclic stretch mediated wound healing is ECM dependent¹⁴. Researchers have also observed epithelial cell shape reorientation in response to uniaxial cyclic stretch¹⁵⁻¹⁸ which is believed to influence morphogenesis and wound healing^{19,20}. Studies of isolated NRK (normal rat kidney) epithelial cells (stretched from 5-20% at 0.5Hz) found stretch-induced reorientation depended on microtubule remodeling¹⁵, while studies of isolated A549 alveolar epithelial cells (stretched from 5-15% at 0.3 Hz) found this reorientation also required stress fiber remodeling (i.e., F-actin)¹⁷. Stretch frequencies have ranged broadly from study to study (0.1 Hz – 2.15 Hz)^{12,14-18}, which may contribute to different findings. Moreover, comparison across these studies is complicated by the use of different strains of epithelial cells which can have different adhesion and proliferation characteristics²¹. In related experimental studies^{22,23} and single cell theoretical models²⁴, direct comparisons of the effects of stretch frequency on endothelial or fibroblast stress fiber reorientation do suggest a frequency dependent relationship. However, the role of cyclic stretch frequency in regulating collective epithelial behavior is less clear and we sought to address this gap.

Under in-plane mechanical load, epithelial cells exert forces on each other at their cell-cell contacts. These contacts encompass several junctions, including tight junctions, desmosomes, gap junctions, and adherens junctions²⁵⁻²⁷. Among these, the adherens junction plays a mechanosensitive role in guiding cell migration²⁸ and regulating cell proliferation^{29,30}, even responding to static stretches³¹⁻³³. Yet, the role of the adherens junction in regulating responses to cyclic stretch is unknown.

The transmembrane protein E-cadherin serves as the intercellular mechanical linkage in the adherens junction. E-cadherin forms a trimeric complex with cytosolic β -catenin and α -catenin, which binds to F-actin²⁵. Various adapter proteins stabilize the binding of this complex to F-actin under mechanical load. For example, p120-catenin localizes to E-cadherin to block clathrin-mediated endocytosis of E-cadherin and maintain stability of the complex³⁴. Another protein, vinculin, reinforces the α -catenin/F-actin interaction under mechanical load³⁵⁻³⁷ to fortify the adherens junction³⁸. Despite the known mechanosensitive recruitment of vinculin to the adherens junction, it is unclear how it is recruited with cyclic stretch and how that recruitment affects epithelial shape change and migration.

We sought to learn how different frequencies of uniaxial cyclic stretch impacted epithelial behavior and the potential role of vinculin in mediating this behavior. We subjected high density, confluent Madin-Darby canine kidney (MDCK type II) epithelial monolayers to a range of physiological cyclic stretch frequencies (0.1 Hz, 0.5 Hz, and 1 Hz) at a physiological stretch magnitude of $\sim 10\%$ ^{7,39-42}. Observing the effect of cyclic stretch on the epithelium over time is challenging because stretch devices must be amenable to long-term live cell imaging; to overcome this challenge, we integrated a programmable pneumatic cell

stretching device⁴³ with a microfluidic perfusion system to observe cell migration after cyclic stretch.

2.5. Results

2.5.A. Cells adjust morphology in response to cyclic stretch

To investigate the long-term dynamic response of the epithelium to cyclic stretch, we utilized a pneumatic cell stretcher device previously detailed⁴³ (Figure 2.1a). First, we created a polydimethylsiloxane (PDMS) device from a 3-D printed mold and adhered a thin PDMS bottom membrane, forming 2 main channels. The center channel, flanked by inlet and outlet ports, functioned as the substrate for the epithelium. The outer air-filled channel, encircling the center channel, contracted when vacuum was applied. This contraction of the outer channel led to the uniaxial stretching of the membrane of the central channel and the adherent epithelium. By applying a programmable input pressure of 60 kPa, cells were uniaxially stretched^{29,43}, resulting in $\epsilon_{yy} = 10\% \pm 2\%$ as measured by cell membrane elongation (Supplementary Figure 2.S1a). Since this small level of stretch is difficult to observe, stretched cells were labeled with Hoechst to visualize nuclei displacement (Figure 2.1b). To examine the impact of 10% stretch on cell morphology, we performed a high-throughput automated segmentation of the epithelium before and after stretch (Supplementary Figure 2.S1b-d). This method enabled the analysis of numerous cells, offering robust statistical power to identify variations in cell morphology such as average cell area and perimeter.

After validating that a 10% static stretch changed cell morphology, we subjected the epithelium to 1 Hz, 0.5 Hz, or 0.1 Hz cyclic stretch of 10% for 30 minutes (Figure 2.1c). We

imaged the epithelium before and after cyclic stretch, with the membrane fully relaxed (time = 0 hours and 0.5 hours, respectively). We then performed a large-scale segmentation of all images, which was made possible by a stably transfected cell line with a GFP E-cadherin fluorophore⁴⁴. We extracted several shape descriptors from these segmented images, including cell solidity, which is distinct from tissue solidity. Cell solidity is defined as $\frac{A_{cell}}{A_{convex}}$, where A_{cell} is the cell area and A_{convex} is the convex area. Higher cell solidity indicates rounder cells, while lower cell solidity implies more protrusions⁴⁵. This metric has been used to assess cell deformability and is associated with age-related macular degeneration of retinal pigment epithelial cells^{46,47}. Interestingly, we found that cell solidity was highly frequency dependent (Figure 2.1d). Higher frequency (1 Hz) stretch or no-stretch led to decreased average cell solidity. In contrast, lower frequencies (0.5 Hz and 0.1 Hz) did not elicit changes in average cell solidity, with a subtle increase (though not statistically significant). Cell morphological parameters including circularity and shape index ($Perimeter/\sqrt{Area}$) were also disrupted under higher frequency 1 Hz cyclic stretch, but not 0.1 Hz (Supplementary Figure 2.S2).

At the lower frequency of 0.1 Hz, we also observed a reorientation of epithelial cells (Figure 2.1e-g). Cells reduced their length in the direction of uniaxial stretch (y) and extended their length perpendicular to stretch (x). This shape change corroborates previous studies of how cyclic stretch modulates cell shape^{15,18,48}. We did not observe cell reorientation at 0.5 Hz or 1.0 Hz. These investigations extended the analysis of morphological shifts by linking reorientation to the stabilization of cell solidity. These morphological alterations suggested a role for intercellular signaling at cell-cell contacts.

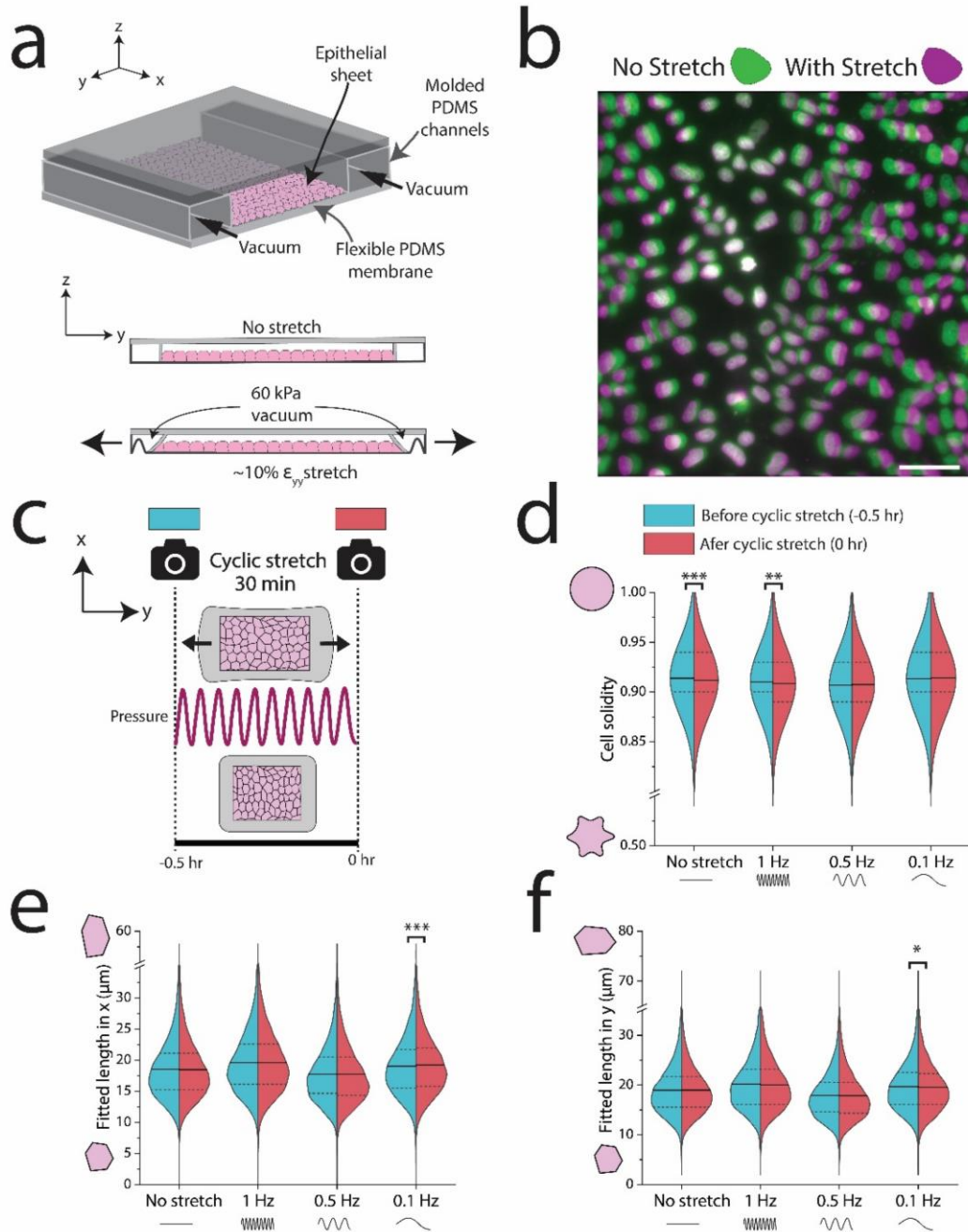


Figure 2.1. Demonstration of uniaxial stretch device and segmentation of epithelial cells after cyclic stretch.

(a) Schematic of PDMS pneumatic cell stretching device. Vacuum in the outer chambers contracts the epithelium $\sim 10\%$ uniaxially. (b) Nuclei were labeled with Hoechst and imaged before and after application of a 60 kPa vacuum to generate a 10% uniaxial stretch. Green nuclei indicate cells without stretch (0 kPa) and magenta denotes displaced nuclei in stretched cells (60 kPa). (c) Schematic of experiment for applying cyclic stretch to an epithelial sheet, where cells were imaged immediately before and after application of a sinusoidal 10% stretch at different frequencies for 30 minutes. (d) At lower frequencies, cells retained their cell solidity. (e and f) At 0.1 Hz, cells elongated perpendicular

to stretch and contracted in the direction of stretch. $n > 10,000$ cells per half of each violin plot. Scale bar in (b) is 50 μm . Statistics were generated from a two-tailed student t-test assuming equal variance. Dotted lines in all violin plots represent the 25th/75th percentiles of data distribution, while the solid lines represent the mean. For segmentation analysis, approximately 8 different regions of the epithelium were imaged across each biological replicate (3 per condition, 9 biological replicates for the no stretch control). P values are denoted as * $p < .05$; ** $p < .005$; *** $p < .0005$.

2.5.B. Low frequency stretch arrests epithelial migration

After cyclic stretching the epithelium for 30 minutes (time = 0.5 hours), we observed how the epithelium changed its collective migration over the next 6 hours (Figure 2.2a).

Comprehensive studies of how cyclic stretch governs the collective epithelium are limited, partly due to the challenges inherent in such investigations. Conducting live cell imaging for prolonged periods on a cell stretcher platform is demanding. The bottom membrane must be both transparent and thin enough for imaging, and many cell stretcher setups are not fully enclosed. Open systems are susceptible to media evaporation within hours and cannot be continuously imaged on a microscope. To counteract this challenge, we integrated a microfluidic based perfusion system within our device to prevent evaporation (Figure 2.2b). A syringe pump sustained a slow media flow rate of 300 $\mu\text{L/hr}$, resulting in minimal shear stress of approximately 1×10^{-6} dyne/cm² on the apical epithelium (Supplementary Figure 2.S3). Furthermore, we eliminated out of plane drift during imaging by mounting the device on a thin glass coverslip.

We utilized particle image velocimetry (PIV) to track displacement of cells during this 6-hour period and confirm collective cell migration (Supplementary Figure 2.S4). Cells within the monolayer moved as large cohesive clusters, corroborating previous studies of collective cell migration. This method facilitated the calculation of migration parameters including average speed, total distance traveled, and specific x and y movements.

Average speeds for the no-stretch control, 1 Hz, and 0.5 Hz conditions were approximately 5-6 $\mu\text{m/hr}$. Notably, the slowest frequency condition (0.1 Hz) displayed a significant reduction in average speed to around 3.8 $\mu\text{m/hr}$ (Figure 2.2c). The total distance traveled aligned closely with the average speed results, with 0.1-Hz stretched cells covering nearly half the distance of cells in the other conditions (Figure 2.2d).

To discern whether the migratory responses occurred over different timeframes, potentially masking variations in speed averages, we plotted migration speed against time (Figure 2.2e). Notably, the speed was most significantly disrupted immediately following a 0.1 Hz cyclic stretch. After 6 hours the speed equalized across all frequencies, resembling the no-stretch control. Surprisingly, the migratory response of cells in the 0.5 Hz and 1 Hz conditions closely matched the migration timescales of the control condition. In all cases, we observed a sigmoidal response in speed fluctuation over time, with initial deceleration, brief acceleration, and subsequent deceleration towards the end of the observation period.

Given the uniaxial nature of the applied stretch (ϵ_{yy}), we also explored the possibility of direction-specific migration dysregulation. However, migration was slowed in *both* the direction of stretch (y) and perpendicular to stretch (x) (Figure 2.2f-i).

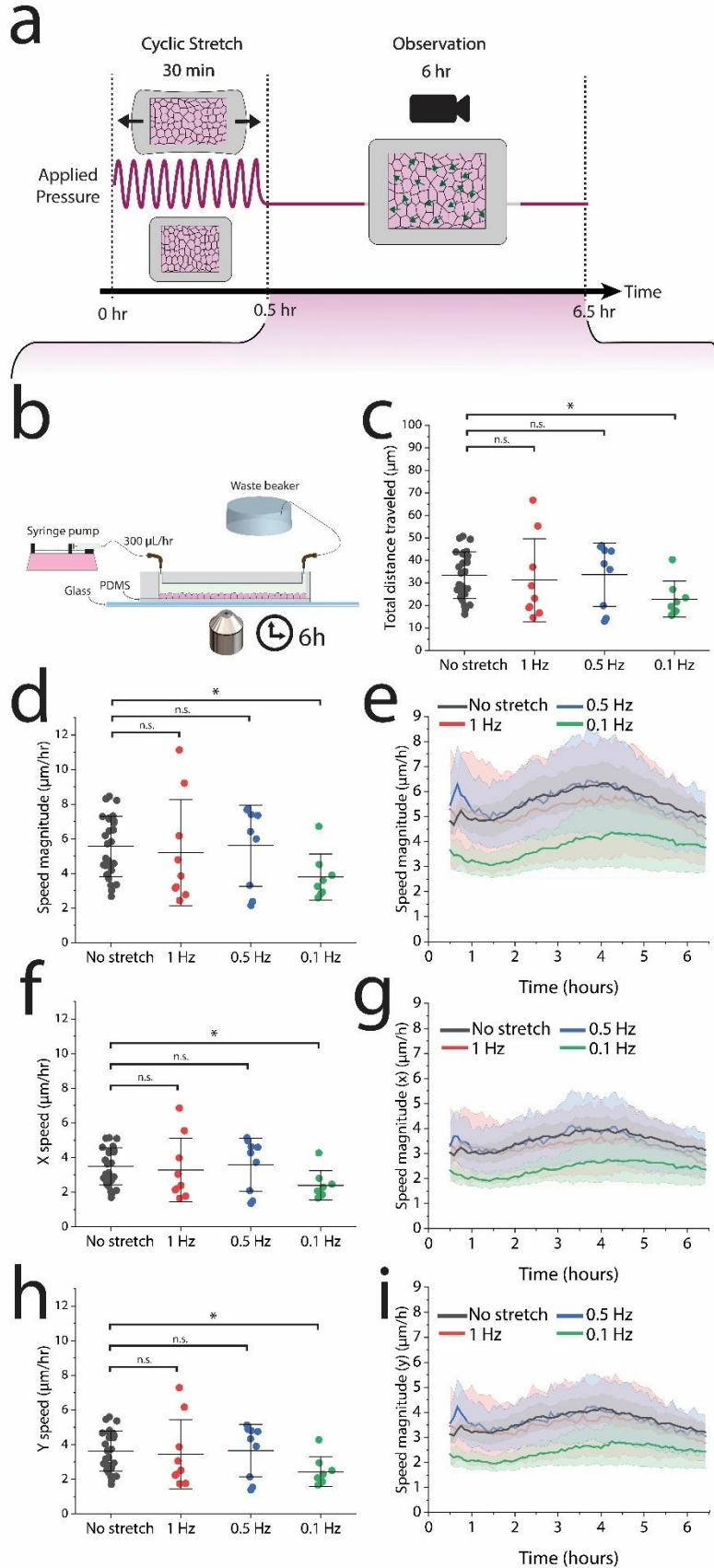


Figure 2.2. Low frequency cyclic stretch reduces epithelial migration in a directionally independent manner.

(a) PIV analysis was conducted in the observation period, the 6 hours following 30 minutes of cyclic stretch. (b) After cyclic stretch, the device was integrated with a perfusion system and imaged on a glass slide to remove out-of-plane drift. (c) Cells traveled the shortest distance in response to 0.1 Hz, with no significant differences among the higher frequencies. (d) The average cell speed diminished significantly in response to a 0.1 Hz frequency. (e) The reduced migratory effect predominantly lasted ~2 hours. (f-i) Both the x and y speeds are reduced in response to 0.1 Hz uniaxial stretch. No-stretch control: n=27 across 9 independent experiments, 1 Hz: n=9 across 3 independent experiments, 0.5 Hz n=9 across 3 independent experiments, 0.1 Hz: n=8 across 3 independent experiments. For each independent experiment, we imaged 2-4 different regions across the epithelium when observing migration. For data that exhibited a normal distribution as determined by the Shapiro-Wilk test, statistics were generated from a two-tailed student t-test assuming equal variance. For data that exhibited a non-normal distribution, we used a Mann-Whitney U test. Shaded regions in all 6-hour migration observation plots represent the 95% CI. I-bars in all scatter plots represent the mean \pm SD. P values are denoted as * $p < .05$; ** $p < .005$; *** $p < .0005$.

2.C. Adherens junction regulates arrest of cell movements

After establishing that slow frequencies disrupted collective epithelial migration speed, we investigated the role of an intact adherens junction in regulating this migration reduction. Therefore, we utilized MDCK cells expressing a mutant E-cadherin protein (T151 cells, made in an MDCK GII background), lacking the extracellular domain of E-cadherin, thus inhibiting adherens junction interaction⁴⁹. The T151 MDCK cells have a doxycycline (DOX) repressible promoter⁴⁹; they maintain a wild-type (WT) E-cadherin ectodomain when cultured with DOX. Removal of DOX from the media causes the E-cadherin to mutate, leading to the absence of the outer ectodomain⁴⁹. The presence of the mutated E-cadherin inhibits mechanical linkages at the adherens junction (Figure 2.3a), though cells are still able to attach via desmosomes and tight junctions.

We noted distinctive characteristics of the T151 epithelium compared to WT MDCK epithelium. First, in our hands the epithelium did not grow as dense. Second, small holes can form in the epithelium over time, a phenomenon which has been previously reported⁴⁹.

Overall, we found that T151 cells were more migratory and maintained a faster average migration speed of approximately 25 $\mu\text{m/hr}$. Despite the increase in migration speed compared to the wild-type MDCK cells, we observed no significant differences in migration between T151 cells subjected to 0.1 Hz or cyclic stretch and those without cyclic stretch (Figure 2.3b). Interestingly, as a function of time, we observed a brief (1.5 hour) increase in migration speed for cells subjected to 0.1 Hz cyclic stretch (Figure 2.3c). We incorporated a high frequency control (1.0 Hz), which also had no significant difference in migration speed compared to the no stretch control. There were no differences between the no stretch control and stretched cells with respect to total distance traveled as well as x and y migration speeds (Figure 2.3d-f). Immunohistochemistry (IHC) staining of the cells confirmed the lack of an adherens junction complex, as evidenced by minimal p120-catenin and vinculin expression at cell-cell contacts (Supplementary Figure 2.S5). Together, these results indicate that an intact adherens junction is necessary for reduced migration following 0.1 Hz cyclic stretch.

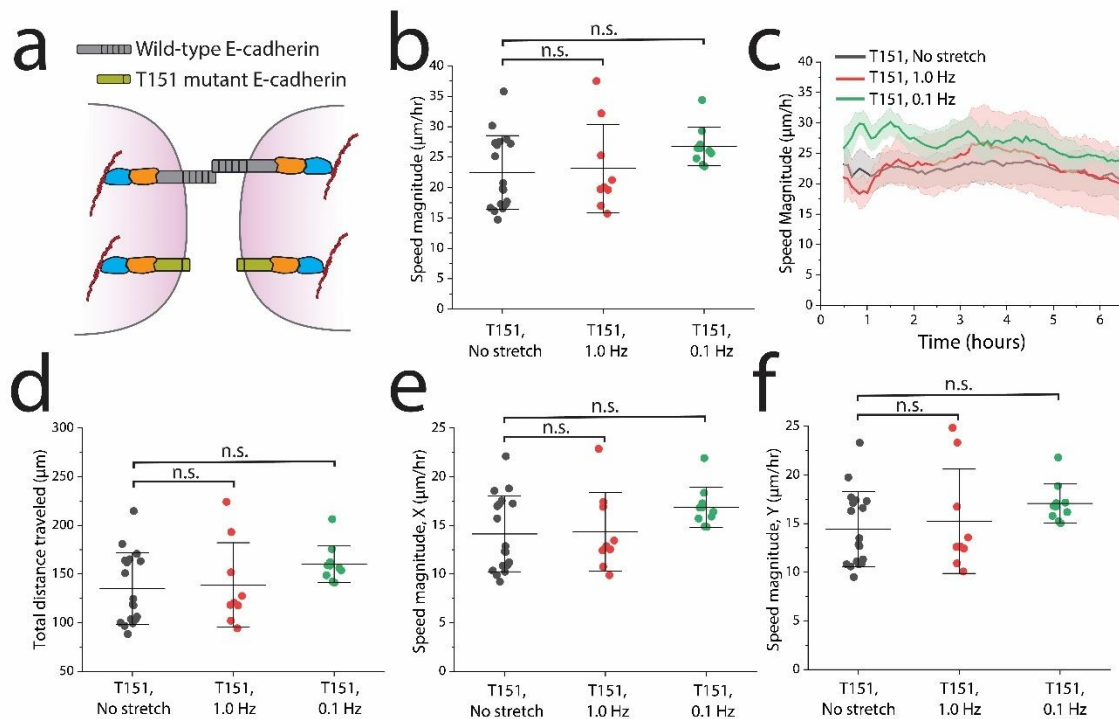


Figure 2.3. The extracellular domain of E-cadherin is necessary for reducing migration after 0.1 Hz stretching.

(a) The extracellular domains of E-cadherin are truncated on the T151 MDCK cells, preventing formation of the adherens junction while allowing formation of other cell-cell adhesions. (b) T151 MDCK cells showed no significant differences in collective average speed magnitude from 1.0 or 0.1 Hz stretch (c) despite an initial increase in migration speed immediately following 0.1 Hz cyclic stretch. (d) No significant differences were observed between conditions in total distance traveled over the course of 6 hours following 0.1 Hz cyclic stretch (green) or 1.0 Hz cyclic stretch (red). (e,f) The migratory response showed no directional dependence. No stretch control: n=9 across 9 independent experiments, 0.1 Hz: n=10 across 4 independent experiments. For each independent experiment, we imaged 2-4 different regions across the epithelium when observing migration. For data that exhibited a normal distribution as determined by the Shapiro-Wilk test, statistics were generated from a two-tailed student t-test assuming equal variance. For data that exhibited a non-normal distribution, we used a Mann-Whitney U test. Shaded regions in all 6-hour migration observation plots represent the 95% CI. I-bars in all scatter plots represent the mean \pm SD. P values are denoted as * $p < .05$; ** $p < .005$; *** $p < .0005$.

2.5.D. Cell-cell contacts recruit vinculin in response to low frequency stretch

After establishing the stretch dependent migratory response of the adherens junction, we looked at the role of vinculin further downstream within the complex. Vinculin is known to support the adherens junctions by stabilizing the α -catenin and F-actin interaction in a force sensitive manner⁵⁰. While vinculin's mechanosensitive role within the adherens junction is acknowledged^{35,36}, its involvement in supporting cell-cell contacts under cyclic stretch, as well as its duration of action in reinforcing the adherens junction, remain less clear.

We conducted a new set of experiments to test the effect of 0.1 Hz cyclic stretch on localization of vinculin. We also included high frequency controls at 0.5 Hz and 1.0 Hz to determine if there was a possible frequency dependence. These experiments were conducted under two different time conditions: cells were fixed immediately after 0.1 Hz cyclic stretch (0.5 hr) or allowed to relax for 30 minutes before fixing and staining (1.0 hr) (Figure 2.4a). No-stretch control devices were fixed and stained following the same time intervals.

2.5.E. High-throughput quantification of vinculin localization

We quantified vinculin recruitment to cell-cell contacts using a unique cell segmentation approach. Traditional fluorescence intensity measurements for quantifying protein recruitment at cell-cell contacts are often low-throughput and subject to user bias. In contrast, cell segmentation offers increased throughput, enhanced statistical power, and reduces user bias. E-cadherin GFP labeled MDCK cells were segmented, and their shape outlines were then overlaid onto the corresponding vinculin-stained images of the same cells (Figure 2.4b). The outlines were eroded either 0 or 3 pixels to encompass the entire cell or isolate the cytoplasmic region, respectively (Figure 2.4c). By measuring the mean fluorescence intensity of both the entire cell and the cytoplasmic region (I_{total} and I_{cyto} , respectively), then calculating the area fraction of the eroded region (Supplementary Figure 2.S6), we calculated the mean fluorescence intensity of vinculin at the cell-cell contact (I_{AJ}) for nearly every cell across all images. We normalized the data on a single cell basis by comparing the ratio of I_{AJ} to I_{cyto} for each cell.

Immediately following 0.1 Hz cyclic stretch ($t=0.5$ hr), I_{AJ}/I_{cyto} significantly increased from the no stretch control condition ($\sim 4.5\%$), signifying a recruitment of vinculin to cell-cell contacts (Figure 2.4d). Notably, vinculin recruitment was transient, with a significant reduction in I_{AJ}/I_{cyto} (3.4%) after just 30 minutes of cell relaxation. However, I_{AJ}/I_{cyto} vinculin levels remained significantly higher than in the no stretch control condition. We also compared the effect of higher frequencies (0.5 Hz and 1.0 Hz) on vinculin localization at cell-cell contacts to test the hypothesis that it was frequency dependent. We observed a significant increase in I_{AJ}/I_{cyto} from 0.5 Hz stretch of approximately 2.5% (Figure 2.4e), which remained elevated after 30 minutes of monolayer relaxation. Lastly, the 0.5% increase

in I_{AJ}/I_{cyto} from 1.0 Hz compared to the no stretch control condition was not significant (Figure 2.4f), which did not significantly change after 30 minutes of monolayer relaxation. By plotting the percent increase in I_{AJ}/I_{cyto} immediately after cyclic stretch (time $t=0.5$ hours), we observed a steady decrease in vinculin recruitment to cell-cell contacts with increasing stretch frequency (Figure 2.4g).

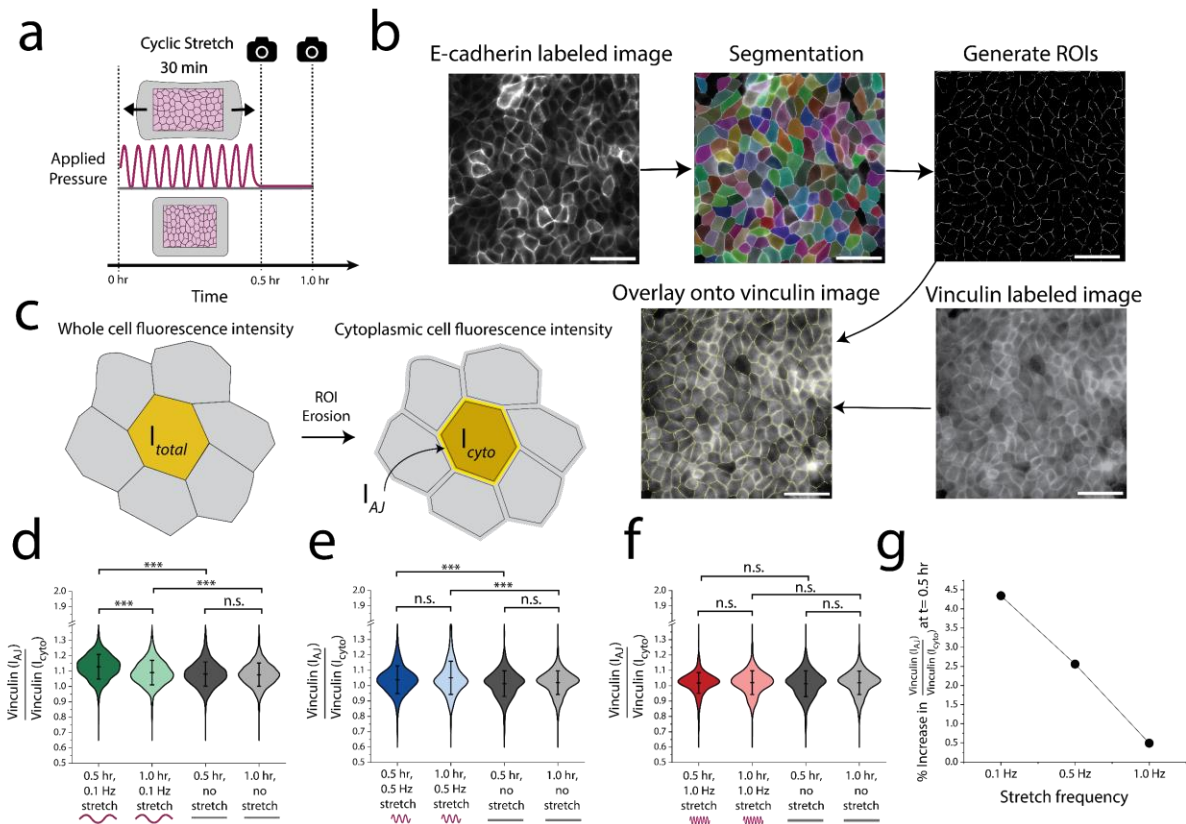


Figure 2.4. 0.1 Hz cyclic stretch transiently regulates vinculin recruitment to cell-cell contacts.

(a) Epithelial sheets were cyclically stretched for 30 minutes at ~10% stretch and either fixed immediately ($t=0.5$ hr) or fixed after 30 minutes (i.e., 1 hour after the onset of stretch) and then stained for vinculin. (b) Vinculin quantification: E-cadherin labeled images were segmented and the resulting ROIs were overlaid onto the corresponding vinculin labeled images. (c) All ROIs were then eroded 3 px to isolate the cytoplasmic region of the cell from the edges of the cell. By obtaining the fluorescence intensity of vinculin in the total cell (I_{total}) as well as the fluorescence intensity of vinculin in the cytoplasm for the eroded cell (I_{cyto}), we computed the fluorescence intensity of vinculin at the cell-cell contact (I_{AJ}) using the area fraction of the cytoplasm (see Supplementary Figure 2.S6). (d) Following 0.1 Hz cyclic stretch, I_{AJ}/I_{cyto} significantly increased from the no stretch control, though diminished approximately after 30 minutes. n for violin plots left to right: 1273, 1000, 1064, 986. (e) Following 0.5 Hz cyclic stretch, I_{AJ}/I_{cyto} significantly increased from the no stretch

control and remained elevated after 30 minutes. n for violin plots from left to right: 396, 337, 378, 422. (f) I_{AJ}/I_{cyto} did not significantly increase in response to 1.0 Hz cyclic stretch from the no stretch control. n for violin plots from left to right: 402, 404, 378, 422. Scale bars are 50 μ m. IHC images shown here were contrast enhanced to help visualize the proteins of interest, but not altered for segmentation analysis. Statistics were generated from a two-tailed student t-test assuming equal variance. I-bars in all violin plots represent the mean \pm SD. 3 separate regions were imaged across each of 2 independent biological replicates per condition. P values are denoted as * $p < .05$; ** $p < .005$; *** $p < .0005$.

2.5.F. Vinculin is necessary to suppress migration in response to cyclic stretch

With evidence of vinculin recruitment to cell-cell contacts at 0.1 Hz cyclic stretch, we tested whether vinculin was necessary for this mechanically regulated migration change. We repeated migration studies using a vinculin knock-out (KO) cell line, made in the MDCK GII background and KO confirmed via western blot⁵¹. Vinculin KO cells were observed after 30 minutes of 0.1 Hz cyclic stretch, as well as in a no-stretch control and 1.0 Hz control. We noted that the no-stretch control Vinculin KO cells moved slightly quicker (18-20 μ m/hr) than the WT MDCK cells, consistent with other studies^{52,53}. Interestingly, Vinculin KO cells observed after 0.1 Hz uniaxial mechanical stretch slightly increased in migratory speed (Figure 2.5b). When plotted as a function of time, the migration speed did not increase initially, but only after about 3 hours were there distinct differences (Figure 2.5c). These changes were also reflected in the total distance traveled, where 0.1 Hz stretched cells moved significantly further (Figure 2.5d). This trend contrasted with the migration reduction in the MDCK WT cells after cyclic stretch. We did not observe this significant increase in migration speed in the 1.0 Hz stretch condition. For all conditions, we observed a similar sigmoidal band of migration speed, similar to the migration response for the WT MDCK cells. Just as with the WT MDCK cells, the change in migration speeds were independent of

direction (Figure 2.5e, f). IHC staining of devices after the 6-hour observation period confirmed low vinculin expression. (Supplementary Figure 2.S8).

We also labeled plasma membranes prior to cyclic stretch to observe changes in cell morphology (Figure 2.5g—i). Strikingly, the morphological changes in the Vinculin KO cells were similar to the changes observed in the WT MDCK cells. 0.1 Hz stretched Vinculin KO cells retained their cell solidity similarly to WT MDCK cells in response to 0.1 Hz cyclic stretch (Figure 2.5g). Meanwhile, the 1.0 Hz and no stretch control cells had significant decreases in cell solidity. Vinculin KO cells stretched at either 1.0 Hz or 0.1 Hz significantly shortened their average length in *both* the (x) and (y) directions (Figure 2.5h,i). In response to 0.1 Hz, cells reduced their width (x) approximately 4.4% and their height (y) approximately 7.1%. In response to 1.0 Hz, cells reduced their width approximately 2.8% and their height (y) approximately 4.5%. These changes are unique for the 1.0 Hz stretched cells, considering the WT cells did not change their lengths after 1.0 Hz stretch. Interestingly, the no stretch control Vinculin KO cells did not have a reduction of length nor width to nearly the same degree (~1% reduction for both width and height).

In conclusion, these findings support vinculin's role in regulating epithelial migration and cell length changes in response to different frequencies of cyclic stretch. However, vinculin's role in regulating cell solidity was not significant.

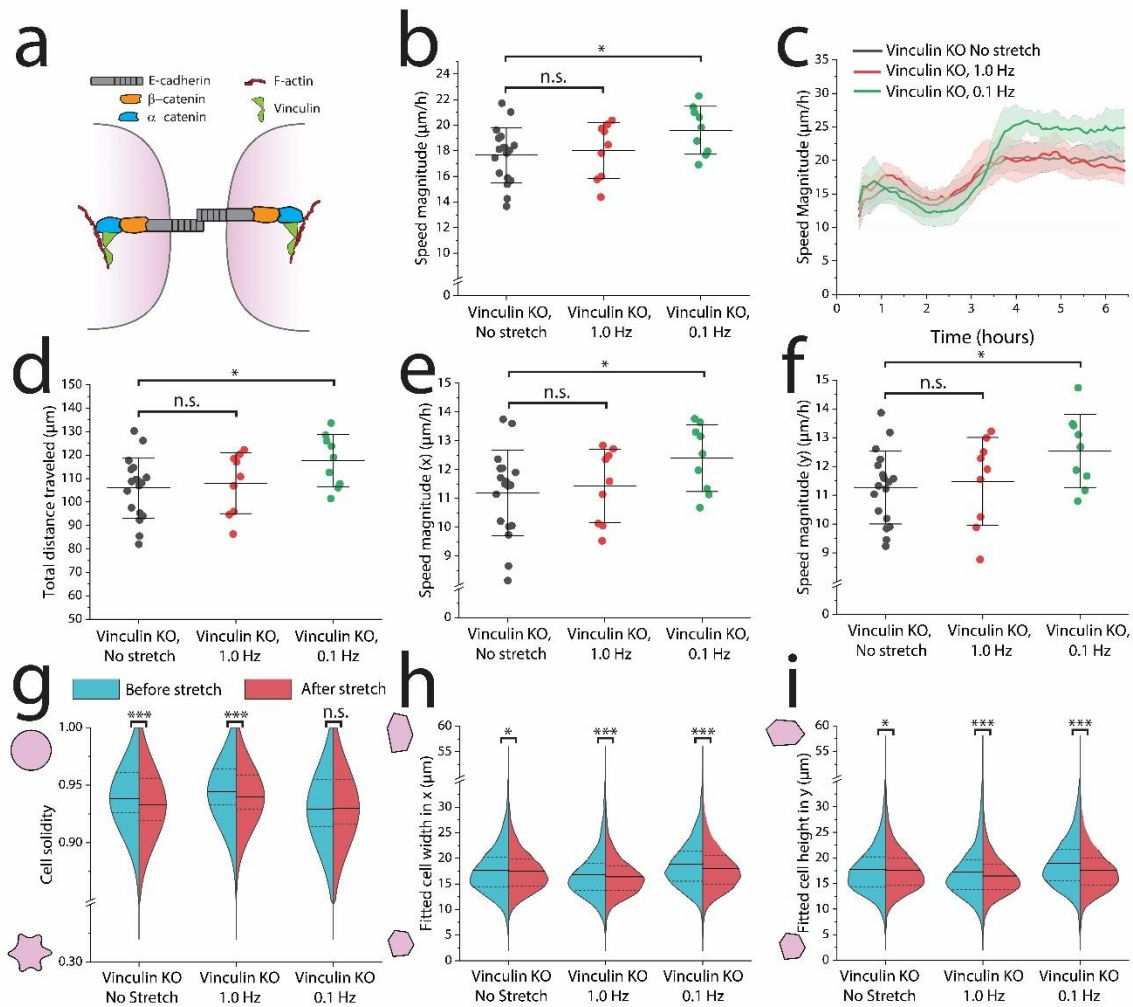


Figure 2.5. Vinculin regulates migratory response of MDCK cells to cyclic stretch, but not cell morphology.

(a) Vinculin reinforces the α -catenin/F-actin complex during mechanical load. (b) Migration speed averaged across 6 hours following 30 minutes of cyclic stretch indicates an increase in migration speed from 0.1 Hz stretch, but not 1.0 Hz stretch. (c) When plotted as a function of time, 0.1 Hz stretched Vinculin KO cells increase their speed after ~3 hours, which (d) allows them to overall travel further compared to the 1.0 Hz and no stretch controls. (e,f) There is no difference in migration speed as a function of direction. (g-h) Across all experiments, 5,000-10,000 cells were segmented immediately before and after 30 minutes of 0.1 Hz cyclic stretch. (g) Immediately after cyclic stretch, 0.1 Hz stretched Vinculin KO cells retain their cell solidity while the cell solidity significantly decreased in the no-stretch and 1.0 Hz controls. (h, i) Vinculin KO cells stretched from either 1.0 Hz or 0.1 Hz shortened their lengths in both x and y directions. No-stretch control: n=9 across 3 independent experiments, 0.1 Hz: n=9 across 3 independent experiments. 1.0 Hz: n=9 across 3 independent experiments.

independent experiments. For each independent experiment, we imaged 2-4 different regions across the epithelium when observing migration. Statistics were generated from a two-tailed student t-test assuming equal variance. For PIV migration data that exhibited a non-normal distribution as determined by the Shapiro-Wilk test, we used a Mann-Whitney U test. Shaded regions in all 6-hour migration observation plots represent the 95% CI. I-bars in all scatter plots represent the mean \pm SD. Dotted lines in all violin plots represent the 25th/75th percentiles of data distribution, while the solid lines represent the mean. For segmentation analysis, approximately 8 different regions of the epithelium were imaged across each biological replicate (3 per condition). n>5,000 cells per half of each violin plot. P values are denoted as * $p < .05$; ** $p < .005$; *** $p < .0005$.

2.6. Discussion and future directions

After discovering that slower frequencies (0.1 Hz) regulated cell shape and migration, we investigated the adherens junction as a mechanosignaling center. Using E-cadherin T151 mutants, Vinculin KO lines, and immunohistochemistry, we confirm 3 unique findings: i) vinculin is recruited to cell-cell contacts in a frequency dependent manner, ii) this vinculin recruitment from 0.1 Hz stretch is transient and reduces after 30 minutes, iii) and the migratory response of the epithelium at 0.1 Hz depends on vinculin.

Our work extends prior studies on cyclic cell stretching by focusing on how different frequencies impact epithelial cell morphology and migration. While higher frequencies (1 Hz and 0.5 Hz) did not significantly alter epithelial cell migration speeds, subjecting cells to 0.1 Hz cyclic stretch for 30 minutes significantly decelerated epithelial movements over a 6-hour observation period.

By quantifying changes in cell morphology and migration, we obtained new information about collective epithelial behavior during cyclic stretch. Previous studies reported that epithelial cells reorient their shapes in response to cyclic stretch, even among different conditions^{15,17}. Our results corroborate this effect, but also demonstrate a frequency dependence. Previous studies have observed a strain rate dependent response of cytoskeletal remodeling, where stress fibers have increased reorientation under increased strain and increased strain rate^{22,23,24}. Many of these studies have utilized highly adherent cells (e.g.,

fibroblasts) and were stretched for longer than 30 minutes. In our hands, we observed apical shape reorientation under slower strain rates. A critical feature of our study is that we utilized a densely packed epithelium with mature cell-cell contacts, which was uniaxially cyclically stretched approximately 10% for only 30 minutes. Furthermore, we did not observe stress fibers, which do not necessarily orient with cell shape. This difference suggests that there are unique roles for strain dependent remodeling at the cell-ECM interface and the cell-cell interface. For example, perhaps the cell-cell interface is more responsive to lower rates while the cell-ECM interface is more responsive to faster rates. In a physiological context, these differences may be responsible for regulating processes such as wound repair or specific steps during tissue development. For example, stress fiber remodeling in heavily adherent cells (e.g., fibroblasts) are generally associated with wound healing⁶⁰, which may experience higher rates or magnitudes of strain associated with injury. These responses may also be affected by strain magnitudes, which we did not investigate in our study. Therefore, we encourage researchers use caution when comparing the results in cell shape between this study and other cyclic stretch studies.

We also found that cells retained their cell solidity at 0.1 Hz, while cell solidity decreased in the no-stretch control and higher frequency stretch conditions. Increased cell solidity is generally associated with more solid-like epithelia⁵⁴, making the reduced epithelial movements following 0.1 Hz stretch consistent with the retention of high cell solidity. Furthermore, we conclude that vinculin does not regulate the change in cell solidity. We noted that cells also experienced unique shape changes at 1 Hz that did not occur in other frequencies (Supplementary Figure 2.S2). These changes included increased cell circularity and increased cell shape index, suggesting increased cell fluidity. However, cell solidity

cannot be used to independently make conclusions on tissue solidity. Future studies on tissue fluidity/solidity should be corroborated with dynamical metrics, including mean square displacement and frequency of T1 transitions.

By conducting experiments with cells expressing a mutant E-cadherin protein (T151 cells), we demonstrated that cell migration arrest following 0.1 Hz depends on intact E-cadherin interactions at the adherens junction. Previous studies have shown that E-cadherin regulates force transfer between cells to regulate directed migration^{31,55}. We build on these studies by extending its necessity for a response to cyclic stretch via reducing cell migration.

To understand this finding, we characterized the role of vinculin in response to cyclic stretching. Using IHC, we observed increased vinculin recruitment to cell-cell contacts under low frequency stretch (i.e., slower strain rates) and reduced vinculin recruitment under high frequency stretch (i.e., faster strain rates). This trend may help explain studies of strained cell-cell contacts; higher strain rate led to junction failure while cell-cell contacts withstood higher stresses in response to slower strain rates⁵⁶. We suggest that vinculin plays a role in reinforcing junctions at slower strain rates.

While vinculin plays a role in stabilizing the adherens junction, it also helps stabilize the focal adhesions of cell-ECM contacts⁵⁷. Recently, vinculin has been found to have an antagonistic relationship between the two regions of the cell³⁵, i.e., by perturbing vinculin expression at cell-cell contacts, vinculin at cell-ECM contacts can be disrupted. Therefore, vinculin recruitment to cell-cell contacts observed after 0.1 Hz cyclic stretch may dysregulate vinculin at cell-ECM contacts and helps arrest cell movements. Not only was migration speed restored in the Vinculin KO cells stretched under 0.1 Hz, but subtly increased compared to the no stretch and 1.0 Hz controls. This response potentially points towards

other junctions (e.g., desmosomes) besides the adherens junction in regulating epithelial migration speed, though in a contradictory manner. Another possibility is that cytoskeletal remodeling induced by cyclic stretch promoted an increase in cell migration, which is normally inhibited by vinculin.

An important tool we leveraged for this study was high-throughput cell segmentation. Not only did this approach significantly boost our statistical power in morphology measurements, but offered a robust method to quantify vinculin expression at cell-cell contacts with minimal user bias. For future studies (by us or others), we recommend a similar approach for quantifying expression of proteins at cell-cell contacts. The user only needs a membrane label for cell segmentation. Several computational and analytical tools (e.g., Cellpose, ImageJ, etc.) are open source.

We present here a study that i) confirms a role for different mechanical stretch frequencies in regulating collective epithelial behavior and ii) presents a novel role for vinculin in reinforcing cell-cell contacts under cyclic stretch. These results help elucidate differences observed across other cyclic stretch studies while helping understand the role of mechanical cues in regulating epithelial function.

2.7. Methods and Materials

2.7.A. Cell Culture and Cell Seeding

We used MDCK GII cells, Vinculin KO, and T151 mutant cells lacking the extracellular domain of E-cadherin both in the same MDCK GII background, as reported previously^{44,49,51}. GFP E-cadherin MDCK and Vinculin KO cells were cultured in low glucose DMEM (*ThermoFisher, 11885084*) supplemented with 10% fetal bovine serum and

1% penicillin-streptomycin at 37° C with 5% CO₂. Approximately 400,000 cells in 400 μL of cell culture media were seeded in the device 36-48 h prior to experiments to create densely packed confluent monolayers. Approximately 15 hours prior to experiments, culture media was replaced with phenol-red-free homemade basal medium (see full reagent list in SI) supplemented with 10% fetal bovine serum, 1% penicillin-streptomycin, and 50 mM HEPES to buffer the cell culture media during long-term microscopy.

T151 MDCK E-cadherin mutant cells were cultured under the same conditions, except for the addition of 20 ng/mL of doxycycline to the culture media. Addition of doxycycline represses the genetically modified promoter region of the mutant gene to maintain a wild-type phenotype in culture conditions⁴⁹. For experiments, doxycycline was removed from the media during device seeding, approximately 36 hours before the experiment.

2.7.B. Cyclic stretching experiments

The MDCK epithelium was imaged and cyclically stretched in a temperature-controlled chamber (37°C) of a Zeiss AxioObserver 7 inverted microscope. To cyclically stretch the epithelium, a vacuum tube connected to an electronic pressure controller (from *Red Dog Research*) was inserted into the hole in the vacuum chamber of the device. The controller is programmed to apply 0 to 60 kPa of pressure in a sinusoidal wave at variable frequencies (0.1 Hz, 0.5 Hz, or 1 Hz depending on the experiment). Immediately after cyclic stretch, the device was briefly imaged and integrated with a perfusion system for a 6-hour imaging period (see SI for details).

2.7.C. High-throughput cell segmentation and ROI filtration

All images used for cell segmentation were taken using a 20x air objective (NA=0.8) and were labeled with a fluorescently tagged for E-cadherin to denote the cell-cell boundary. We utilized the CellPose “cyto” model⁵⁸ with a calibration of 50 pixels per image while excluding cells on edges. ImageJ’s LabelsToROIs plugin was used for shape analysis. See SI for additional post-processing details.

2.7.D. Statistics

Statistics were generated from a two-tailed student t-test assuming equal variance. For PIV migration data that exhibited a non-normal distribution as determined by the Shapiro-Wilk test, we used a Mann-Whitney U test (*OriginPro 2022b, OriginLab*). P values are denoted as $*p < .05$; $**p < .005$; $*** p < .0005$. Dotted lines in all violin plots represent the 25th/75th percentiles of data distribution, while the solid lines represent the mean. Shaded regions in all 6-hour migration observation plots represent the 95% CI. I-bars in all scatter plots represent the mean \pm SD. For each independent experiment, we imaged 2-4 different regions across the epithelium when observing migration. For segmentation analysis, approximately 8 different regions of the epithelium were imaged.

2.7.E. Antibodies

The following primary antibodies were used as previously demonstrated in MDCK cells: purified mouse anti-p120 catenin⁵⁹ (*BD Biosciences, 610133*) at a dilution of 1:200 and recombinant rabbit monoclonal anti-vinculin³⁵ (*abcam, ab129002*) at a dilution of 1:100. The following secondary antibodies were used, both at a 1:500 dilution: Goat anti-Mouse IgG

Alexa Fluor 647 (*Invitrogen*, A32728) and Goat anti-Rabbit IgG Alexa Fluor 405 (*Invitrogen*, A-31556). Antibodies were diluted in PBS + 0.1% Tween20 (1X) + 1% BSA.

2.8. Acknowledgements

The authors acknowledge funding from the NSF (1834760) and the cooperative agreement W911NF-19-2-0026 from the U.S. Army Research Office for the Institute for Collaborative Biotechnologies. LPD acknowledges the BioPACIFIC Materials Innovation Platform of the National Science Foundation (Award No. DMR-1933487) as well as useful discussions with Pruitt Lab members and M. Cristina Marchetti. The authors are also thankful to So Yomada and Sanjeevi Sivasankar (UC Davis) who gifted the Vinculin KO cells, as well as W. James Nelson who gifted the T151 and E-cadherin GFP MDCK cells. The authors acknowledge the use of the Microfluidics Lab within the California NanoSystems Institute, supported by the University of California, Santa Barbara and the University of California, Office of the President.

2.9. Author Contributions

LPD and BLP conceived of study. LPD and BLP designed experiments. LPD and SS performed experiments and analyzed data. KM and RK contributed analytical tools for cell segmentation and PIV, respectively. LPD and SS wrote the original manuscript draft, which was reviewed and edited by LPD, SS, and BLP. BLP provided project funding and supervision.

2.9. References

1. Marchetti, M. C. *et al.* Hydrodynamics of soft active matter. *Rev. Mod. Phys.* **85**, 1143–1189 (2013).

2. Bernheim-Groswasser, A. *et al.* Living Matter: Mesoscopic Active Materials. *Adv. Mater.* **30**, 1707028 (2018).
3. Atia, L. *et al.* Geometric constraints during epithelial jamming. *Nat. Phys.* **14**, (2018).
4. Nelson, C. M., Khauv, D., Bissell, M. J. & Radisky, D. C. Change in cell shape is required for matrix metalloproteinase-induced epithelial-mesenchymal transition of mammary epithelial cells. *J. Cell. Biochem.* **105**, 25–33 (2008).
5. Armon, S., Bull, M. S., Moriel, A., Aharoni, H. & Prakash, M. Modeling epithelial tissues as active-elastic sheets reproduce contraction pulses and predict rip resistance. *Commun. Phys.* **2021 41 4**, 1–9 (2021).
6. Savla, U., Sporn, P. H. S. & Waters, C. M. Cyclic stretch of airway epithelium inhibits prostanoid synthesis. *Am. J. Physiol. - Lung Cell. Mol. Physiol.* **273**, (1997).
7. Gayer, C. P. & Basson, M. D. *The effects of mechanical forces on intestinal physiology and pathology. Cellular Signalling* vol. 21 1237–1244 (Pergamon, 2009).
8. Miao, H. & Blankenship, J. T. The pulse of morphogenesis: Actomyosin dynamics and regulation in epithelia. *Dev.* **147**, (2020).
9. Kim, H. Y. & Davidson, L. A. Punctuated actin contractions during convergent extension and their permissive regulation by the non-canonical Wnt-signaling pathway. *J. Cell Sci.* **124**, 635–646 (2011).
10. Park, J.-A. A. *et al.* Unjamming and cell shape in the asthmatic airway epithelium. *Nat. Mater.* **14**, 1040–1048 (2015).
11. Ciasca, G., Papi, M., Minelli, E., Palmieri, V. & De Spirito, M. Changes in cellular mechanical properties during onset or progression of colorectal cancer. *World J. Gastroenterol.* **22**, 7203 (2016).
12. Xu, J. *et al.* Cellular mechanics of wound formation in single cell layer under cyclic stretching. *Biophys. J.* **121**, 288–299 (2022).
13. Xu, J., Wang, Q., Li, X., Zheng, Y. & Ji, B. Cellular mechanisms of wound closure under cyclic stretching. *Biophysj* **122**, 2404–2420 (2023).
14. Zhang, J., Owen, C. R., Sanders, M. A., Turner, J. R. & Basson, M. D. The Motogenic Effects of Cyclic Mechanical Strain on Intestinal Epithelial Monolayer Wound Closure Are Matrix Dependent. *Gastroenterology* **131**, 1179–1189 (2006).
15. Lien, J. C. & Wang, Y. li. Cyclic stretching-induced epithelial cell reorientation is driven by microtubule-modulated transverse extension during the relaxation phase. *Sci. Reports 2021 111* **11**, 1–12 (2021).
16. Lien, J.-C. & Wang, Y. Cyclic Stretching Combined with Cell-Cell Adhesion Is Sufficient for Inducing Cell Intercalation. *Biophys. J. Lien J* (2023) doi:10.1016/j.bpj.2023.06.019.
17. Roshanzadeh, A. *et al.* Mechanoadaptive organization of stress fiber subtypes in epithelial cells under cyclic stretches and stretch release. *Sci. Reports 2020 101* **10**, 1–14 (2020).
18. G er emie, L. *et al.* Evolution of a confluent gut epithelium under on-chip cyclic stretching. *Phys. Rev. Res.* **4**, 023032 (2022).
19. Matsumoto, T. *et al.* Mechanical Strain Regulates Endothelial Cell Patterning In Vitro. <https://home.liebertpub.com/ten> **13**, 207–217 (2007).
20. Lee, E. *et al.* Transplantation of cyclic stretched fibroblasts accelerates the wound-healing process in streptozotocin-induced diabetic mice. *Cell Transplant.* **23**, 285–301 (2014).
21. Dukes, J. D., Whitley, P. & Chalmers, A. D. The MDCK variety pack: Choosing the right strain. *BMC Cell Biol.* **12**, 1–4 (2011).
22. Hsu, H. J., Lee, C. F., Locke, A., Vanderzyl, S. Q. & Kaunas, R. Stretch-Induced Stress Fiber Remodeling and the Activations of JNK and ERK Depend on Mechanical Strain Rate, but Not FAK. *PLoS One* **5**, e12470 (2010).
23. Lee, C. F., Haase, C., Deguchi, S. & Kaunas, R. Cyclic stretch-induced stress fiber dynamics – Dependence on strain rate, Rho-kinase and MLCK. *Biochem. Biophys. Res. Commun.* **401**, 344–349 (2010).

24. De, R., Zemel, A. & Safran, S. A. Dynamics of cell orientation. *Nat. Phys.* 2007 39 **3**, 655–659 (2007).
25. Meng, W. & Takeichi, M. *Adherens junction: molecular architecture and regulation*. Cold Spring Harbor perspectives in biology vol. 1 a002899 (Cold Spring Harbor Laboratory Press, 2009).
26. Niessen, C. M. Tight Junctions/Adherens Junctions: Basic Structure and Function. *J. Invest. Dermatol.* **127**, 2525–2532 (2007).
27. Runswick, S. K., O’Hare, M. J., Jones, L., Streuli, C. H. & Garrod, D. R. Desmosomal adhesion regulates epithelial morphogenesis and cell positioning. *Nat. Cell Biol.* 2001 39 **3**, 823–830 (2001).
28. Ariyasinghe, N. R. *et al.* Engineering micromyocardium to delineate cellular and extracellular regulation of myocardial tissue contractility. *Integr. Biol. (United Kingdom)* **9**, 730–741 (2017).
29. Hart, K. C. *et al.* E-cadherin and LGN align epithelial cell divisions with tissue tension independently of cell shape. *Proc. Natl. Acad. Sci. U. S. A.* **114**, E5845–E5853 (2017).
30. Benham-Pyle, B. W., Pruitt, B. L. & Nelson, W. J. Mechanical strain induces E-cadherin-dependent Yap1 and β -catenin activation to drive cell cycle entry. *Science (80-.)*. **348**, 1024–1027 (2015).
31. Sadeghipour, E., Garcia, M. A., Nelson, W. J. & Pruitt, B. L. Shear-induced damped oscillations in an epithelium depend on actomyosin contraction and E-cadherin cell adhesion. *Elife* **7**, 1–16 (2018).
32. Weber, G. F., Bjerke, M. A. & DeSimone, D. W. A Mechanoresponsive Cadherin-Keratin Complex Directs Polarized Protrusive Behavior and Collective Cell Migration. *Dev. Cell* **22**, 104–115 (2012).
33. Vishwakarma, M. *et al.* Mechanical interactions among followers determine the emergence of leaders in migrating epithelial cell collectives. *Nat. Commun.* 2018 91 **9**, 1–12 (2018).
34. Menke, A. & Giehl, K. *Regulation of adherens junctions by Rho GTPases and p120-catenin*. *Archives of Biochemistry and Biophysics* vol. 524 48–55 (2012).
35. Bejar-Padilla, V. *et al.* α -Catenin-dependent vinculin recruitment to adherens junctions is antagonistic to focal adhesions. *Mol. Biol. Cell* **33**, (2022).
36. Le Duc, Q. *et al.* Vinculin potentiates E-cadherin mechanosensing and is recruited to actin-anchored sites within adherens junctions in a myosin II-dependent manner. *J. Cell Biol.* **189**, 1107–1115 (2010).
37. LaCroix, A. S., Lynch, A. D., Berginski, M. E. & Hoffman, B. D. Tunable molecular tension sensors reveal extension-based control of vinculin loading. *Elife* **7**, (2018).
38. Thomas, W. A. *et al.* α -Catenin and vinculin cooperate to promote high E-cadherin-based adhesion strength. *J. Biol. Chem.* **288**, 4957–4969 (2013).
39. Birukov, K. G. *et al.* Magnitude-dependent regulation of pulmonary endothelial cell barrier function by cyclic stretch. *Am. J. Physiol. Lung Cell. Mol. Physiol.* **285**, (2003).
40. Miftakhov, R. N. & Wingate, D. L. Biomechanics of small bowel motility. *Med. Eng. Phys.* **16**, 406–415 (1994).
41. Tschumperlin, D. J. & Margulies, S. S. Alveolar epithelial surface area-volume relationship in isolated rat lungs. *J. Appl. Physiol.* **86**, 2026–2033 (1999).
42. Taylor, W. *et al.* The effects of cyclic stretch on gene transfer in alveolar epithelial cells. *Mol. Ther.* **7**, 542–549 (2003).
43. Hart, K. C. *et al.* An Easy-to-Fabricate Cell Stretcher Reveals Density-Dependent Mechanical Regulation of Collective Cell Movements in Epithelia. *Cell. Mol. Bioeng.* **14**, 569–581 (2021).
44. Yamada, S., Pokutta, S., Drees, F., Weis, W. I. & Nelson, W. J. Deconstructing the cadherin-catenin-actin complex. *Cell* **123**, 889–901 (2005).
45. Pasqualato, A. *et al.* Shape in migration. <http://dx.doi.org/10.4161/cam.26765> **7**, 450–459 (2013).

46. von der Emde, L. *et al.* Histologic Cell Shape Descriptors for the Retinal Pigment Epithelium in Age-Related Macular Degeneration: A Comparison to Unaffected Eyes. *Transl. Vis. Sci. Technol.* **11**, 19–19 (2022).
47. Kim, Y. K. *et al.* Morphometric Analysis of Retinal Pigment Epithelial Cells From C57BL/6J Mice During Aging. *Invest. Ophthalmol. Vis. Sci.* **62**, 32–32 (2021).
48. Wang, J. H. C., Goldschmidt-Clermont, P., Wille, J. & Yin, F. C. P. Specificity of endothelial cell reorientation in response to cyclic mechanical stretching. *J. Biomech.* **34**, 1563–1572 (2001).
49. Troxell, M. L. *et al.* Inhibiting cadherin function by dominant mutant E-cadherin expression increases the extent of tight junction assembly. *J. Cell Sci.* **113**, 985–996 (2000).
50. Seddiki, R. *et al.* Force-dependent binding of vinculin to α -catenin regulates cell-cell contact stability and collective cell behavior. *Mol. Biol. Cell* **29**, 380–388 (2018).
51. Koirala, R. *et al.* Inside-out regulation of E-cadherin conformation and adhesion. *Proc. Natl. Acad. Sci. U. S. A.* **118**, 2021 (2021).
52. Bazellières, E. *et al.* Control of cell–cell forces and collective cell dynamics by the intercellular adhesome. *Nat. Cell Biol.* **17**, 409–420 (2015).
53. Shoyer, T. C., Gates, E. M., Cabe, J. I., Conway, D. E. & Hoffman, B. D. Coupling During Collective Cell Migration is Controlled by a Vinculin Mechanochemical Switch. *bioRxiv* (2023) doi:10.1101/2023.01.13.523997.
54. Heydarian, A., Milani, D. & Moein Fatemi, S. M. An investigation of the viscoelastic behavior of MCF-10A and MCF-7 cells. *Biochem. Biophys. Res. Commun.* **529**, 432–436 (2020).
55. Cai, D. *et al.* Mechanical feedback through E-cadherin promotes direction sensing during collective cell migration. *Cell* **157**, 1146–1159 (2014).
56. Monemian Esfahani, A. *et al.* Characterization of the strain-rate-dependent mechanical response of single cell-cell junctions. doi:10.1073/pnas.2019347118/-/DCSupplemental.
57. Bays, J. L. & DeMali, K. A. Vinculin in cell–cell and cell–matrix adhesions. *Cell. Mol. Life Sci.* **74**, 2999–3009 (2017).
58. Stringer, C., Wang, T., Michaelos, M. & Pachitariu, M. Cellpose: a generalist algorithm for cellular segmentation. *Nat. Methods* **18**, 100–106 (2020).
59. Lang, R. A., Herman, K., Reynolds, A. B., Hildebrand, J. D. & Plageman, T. F. p120-catenin-dependent junctional recruitment of Shroom3 is required for apical constriction during lens pit morphogenesis. *Development* **141**, 3177–3187 (2014).
60. Li, B. & Wang, J. H. C. Fibroblasts and myofibroblasts in wound healing: Force generation and measurement. *J. Tissue Viability* **20**, 108–120 (2011).

2.10. Supplemental Information

2.10.A. Device construction

We implemented and constructed a uniaxial cell stretching device as previously reported⁴³. The device consisted of two PDMS components: a thin PDMS membrane and a thicker PDMS top containing the vacuum and cell channels. The mold for the top portion was 3-D printed from RGD450 resin on a Stratasys Objet30. We then mixed PDMS (*Dow*,

Sylgard 184) at a 10:1 (base: curing agent) ratio, poured it on the molds, and desiccated the PDMS for 1 hour to remove air bubbles. The PDMS was then cured on the mold at 75°C for 4 hours. To assemble the device, we cut the cured PDMS from the mold and made 3 holes using a 1 mm biopsy punch. One hole was punched in each end of the middle chamber for inserting cells and cell media. A third hole was punched into one side of the outer chamber for the vacuum. The thin PDMS membrane (~125 µm/.005", *Specialty Manufacturing Inc.*) was cut to the dimensions of the device top (1" x 3"), washed with 70% ethanol, then air dried with N₂. Using a handheld plasma wand (*Electro-Technic Products, BD-20AC*), we plasma treated the PDMS membrane for 1 minute, the PDMS top for 30 seconds, then the membrane for another 30 seconds. Immediately after plasma treatment, the top of the device was placed on the membrane to seal the channels. We applied 5 minutes of light pressure between the two PDMS bodies and reinforced the bond by placing the complete device in a 75°C oven for 5 minutes. We then incubated the device with 50 µg/mL of collagen I (*Corning, 354236*) into the middle chamber overnight at 22°C. The collagen was rinsed out with PBS before storing at 4°C until cell seeding (approximately 2-24 hours later). Prior to cell seeding, devices were UV sterilized for 10 minutes in the biosafety cabinet.

2.10.B. Cyclic stretching experiments and migration

The vacuum was supplied by a standard in-house vacuum line. Following 30 minutes of stretch, we vented the vacuum line to remove excess pressure and removed the vacuum tube prior to imaging. Approximately 8 images (488 nm and phase contrast) of the monolayer were taken before and after cyclic stretch with both 10x and 20x objectives. We utilized a custom 3-D printed holder to prevent the device from sagging during imaging, which also kept the membrane suspended during cyclic stretch. After post-stretch imaging,

we immediately set up the perfusion system for our 6-hour observation period. First, we placed the device on a 500 μm thick glass slide (*SPI Supplies, 01018T-AB*) to keep the membrane from drifting out of plane during perfusion. A syringe pump perfused cell media (as described in *cell culture and cell seeding*) through 1/32" inner diameter Tygon tubing (*McMaster-Carr, 6546T23*) into and out of the main cell channel before traveling into a waste beaker. 90-degree blunt needles (*McMaster-Carr, 75165A65*) connected the tubing to the channel holes via Luer Lock connections. The syringe pump was set to a rate of 0.3 mL/h. At the onset of perfusion, we began imaging the device. Each device was imaged at 3 regions of the channel every 5 minutes for 6 hours with a phase contrast 10x objective.

2.10.C. Particle Image Velocimetry analysis

The resulting phase contrast images from the 6-hour timelapse were aligned to remove thermal drift during imaging (*ImageJ*, linear stack alignment with SIFT). The images were then cropped to 1700 by 1150 pixels before being analyzed with PIV (MATLAB *PIVlab 2.58*, The MathWorks). PIVlab used particle image velocimetry to determine the movement of the cells within the images. The analysis in PIVlab used a FFT Window Deformation algorithm with a Gauss 2x3 point sub-pixel estimator. The interrogation pass sizes were 200, 100, and 50 for each of the three passes respectively, and each had a 50% overlap per step. In post processing vector validation, we used a standard deviation filter of 4 and a local median filter of 5. The velocity data was averaged over each frame using original MATLAB code. Migration distances were calculated using averaged velocities and the time between images.

2.10.D. Immunohistochemistry and imaging of stained devices

Devices were fixed after 4 different conditions: i) Immediately after 30 minutes of 0.1 Hz cyclic stretch, ii) immediately after 30 minutes of no cyclic stretch, iii) 30 minutes after 30 minutes of 0.1 Hz cyclic stretch, iv) or 30 minutes after 30 minutes of no cyclic stretch. 2 devices were stained for each condition (8 devices total). For the conditions involving an extra 30 minutes of relaxation, the devices were placed in the cell culture incubator before fixing and staining. All devices were washed with PBS before being fixed for 15 minutes in 4% formaldehyde (*ThermoFisher 28908*), diluted in PBS. The formaldehyde was then thoroughly washed out with PBS. For permeabilization, we used a buffer consisting of 0.1% Triton X-100 in PBS in the devices for 5 minutes at room temperature. Permeabilization was followed by a 1 hour blocking step at room temperature, using a buffer consisting of 0.3% Tween20 (1X) and 2% BSA in PBS. Primary antibodies were incubated in the devices overnight at 4°C, following by a wash with 0.1% Tween20 (1X) and 1% BSA in PBS. Secondary antibodies were then incubated with the devices for 1 hour at room temperature in the dark. Finally, the devices were washed with 0.1% Tween20 (1X) and 1% BSA in PBS before being stored in PBS for imaging.

All devices were imaged using a 20x air objective (NA=0.8) and a 63x oil immersion objective (NA=1.2) on a Zeiss AxioObserver 7 widefield microscope. 3 separate regions were imaged per device using the following excitation filters (Vinculin:405 nm, E-cadherin: 488 nm, Vinculin: 647 nm). Each image was aligned to the apical surface of the epithelium.

2.10.E. High-throughput cell segmentation and ROI filtration

After segmentation, the masks were saved as PNG files and run through the LablesToROIs plugin in ImageJ, which calculated the shape descriptors for each cell per

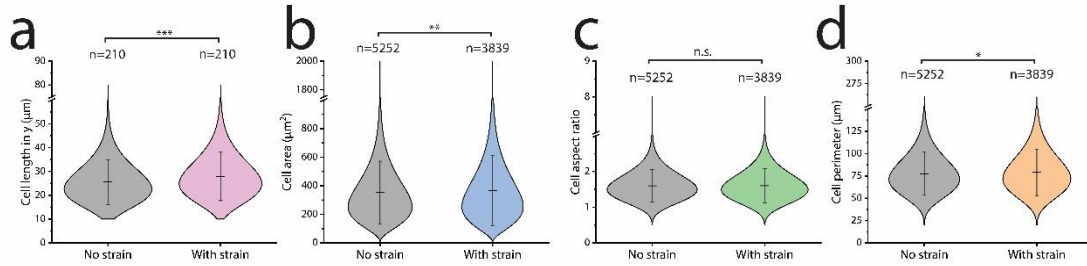
image. Cells having an area below $2 \mu\text{m}^2$ or above $2,000 \mu\text{m}^2$ were filtered out of the data sets using a custom Python script. Per shape descriptor (e.g., area, aspect ratio, solidity) all cells were then averaged per image ($\sim 2,000$ cells/image). The fitted length for cell shape measurements was determined using ImageJ's bounding rectangle feature

For Vinculin KO experiments, cell segmentation was determined using a CellMask Deep Red plasma membrane stain (*ThermoFisher, C10046*). CellMask was incubated at a 1:1000 dilution for 10 minutes before being washed out and replaced with imaging medium, after which the experiment was performed immediately.

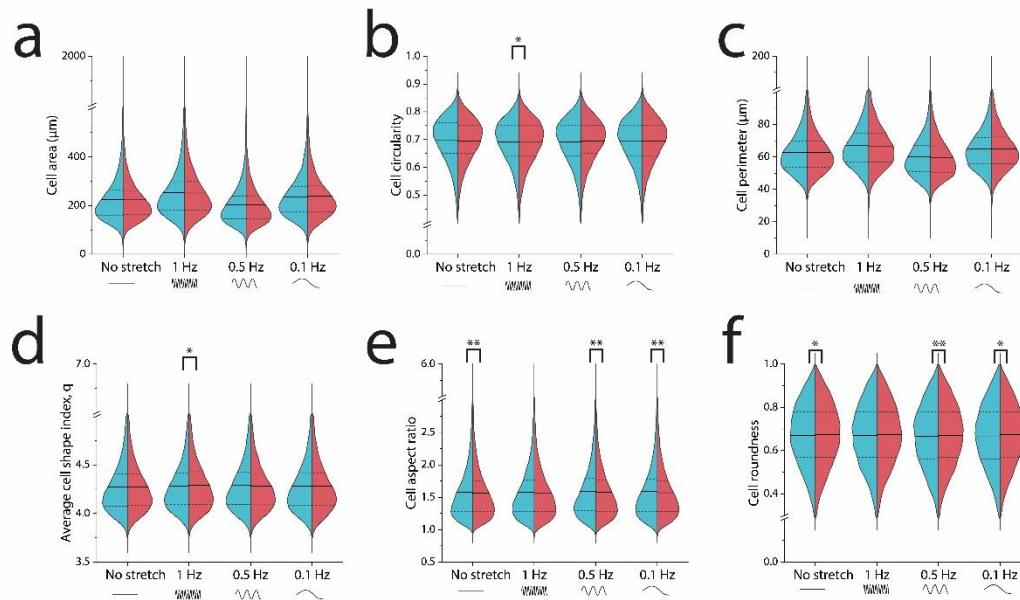
2.10.F. Analysis of vinculin localization at cell-cell contacts

First, the E-cadherin labeled images from the 63x oil immersion objective were segmented using Cellpose, as described in *high-throughput cell segmentation*. Using the LabelsToROIs plugin in ImageJ, the segmented masks were overlaid onto the corresponding vinculin labeled images. Segmented masks were then processed under 2 separate conditions: i) masks were eroded 3 pixels to remove the cell-cell contact or ii) masks were eroded 0 pixels to contain the entire cell, including the cell-cell boundary. The corresponding mean fluorescence intensities of vinculin were calculated for each cell under each condition (i.e., the mean fluorescence intensity of vinculin in the entire cell and the mean fluorescence intensity of vinculin excluding the cell-cell contact).

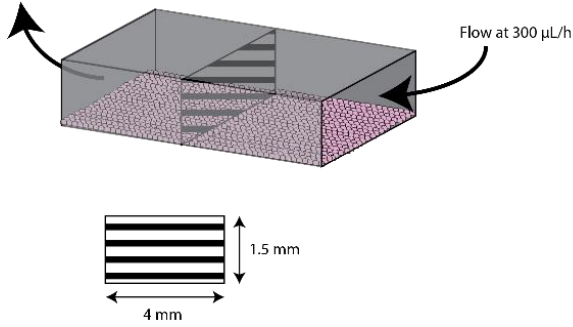
To determine the mean fluorescence intensity of vinculin at the cell-cell contacts, we calculated the approximate area fraction of the 3-pixel eroded cell to be 0.91 (Supplementary Figure 2.S6). For IHC studies of higher stretch frequencies which utilized separate controls, the area fraction was 0.94. This area fraction allowed us to calculate the mean fluorescence intensity at the cell-cell contacts.



Supplementary Figure 2.S1. Quantification of cell shape under 60 kPa static strain. (a) For 7 separate experiments, 210 cells were manually measured along the direction of stretch (ϵ_{yy}) with and without stretch, yielding a difference in approximately 10% and compared using a paired t-test. For other cell shape descriptors (b-d), cells were segmented from 20x magnification E-cadherin GFP labeled images. Stretch significantly increased cell area and perimeter, while cell aspect ratio remained unchanged. I-bars in violin plots represent mean \pm SD. Violin plots are distributed via a gamma curve. * $p < .05$; ** $p < .005$; *** $p < .0005$ using a student t test.



Supplementary Figure 2.S2. Changes in cell morphology after cyclic cell stretch. (a, c) There were no differences in average cell area nor perimeter among all cyclic stretch conditions. (b, d) However, we observed small significant changes in cell shape index, q , and cell circularity under higher frequency 1 Hz. (e, f) For aspect ratio and roundness, we observed subtle (though significant) changes in lower frequencies and the control condition. q is defined as the perimeter/ $\sqrt{\text{area}}$. $n > 10,000$ cells per half of each violin plot. Dotted lines in the violin plots represent the 25th/75th percentiles of data distribution. * $p < .05$; ** $p < .005$; *** $p < .0005$ using a student t test.



$$A = 6 \text{ mm}^2$$

$$6 \text{ mm}^2 = 6 * 10^6 \mu\text{m}^2$$

$$Q = A * v = 300 \frac{\mu\text{L}}{\text{h}}$$

$$300 \frac{\mu\text{L}}{\text{h}} = (6 * 10^6 \mu\text{m}^2) * v$$

$$v = \left(\frac{300 \mu\text{L}}{6 * 10^6 \mu\text{m}^2 \text{h}} \right) \left(\frac{1\text{L}}{10^6 \mu\text{L}} \right) \left(\frac{10^{-3} \text{m}^3}{1 \text{L}} \right) \left(\frac{10^6 \mu\text{m}}{1 \text{m}} \right) \left(\frac{1 \text{h}}{3600 \text{s}} \right)$$

$$v = 13.89 \frac{\mu\text{m}}{\text{s}} \text{Pa} = \frac{\text{kg}}{\text{m} * \text{s}^2} = P = \frac{1}{2} v^2 \rho$$

$$\rho = 1.0 \frac{\text{g}}{\text{mL}} = \frac{1.0 \text{g}}{10^{-12} \mu\text{m}^3}$$

$$P = \frac{(13.89 \mu\text{m})^2 * 1.0 \text{g}}{2 * 10^{-12} \mu\text{m}^3 * \text{s}^2}$$

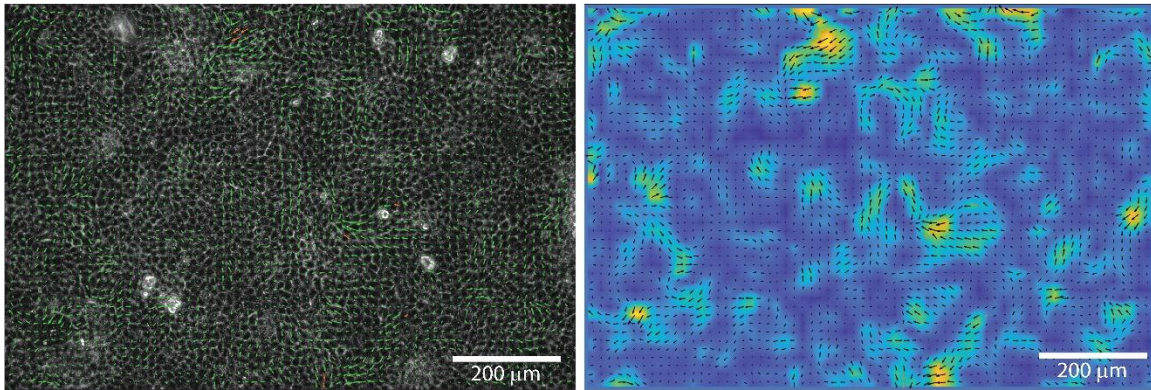
$$= 9.65 * 10^{-11} \frac{\text{g}}{\mu\text{m} * \text{s}^2}$$

$$9.65 * 10^{-11} \frac{\text{g}}{\mu\text{m} * \text{s}^2} \left(\frac{1 \text{kg}}{1000 \text{g}} \right) \left(\frac{10^6 \mu\text{m}}{1 \text{m}} \right)$$

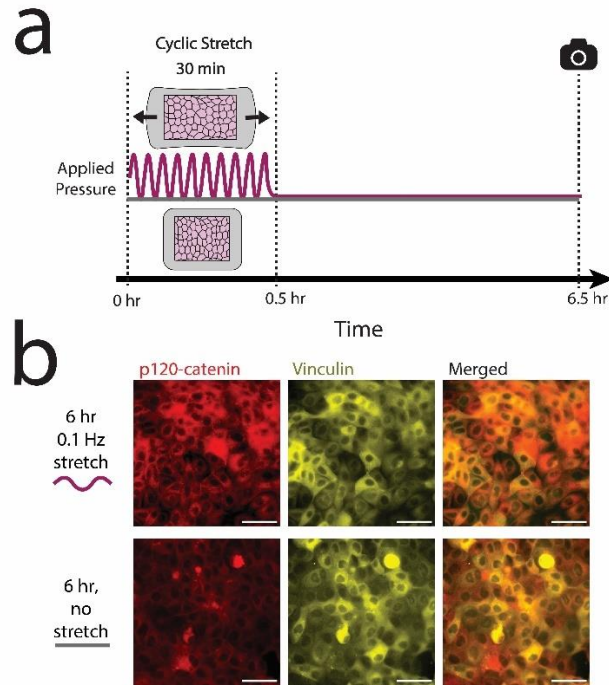
$$= 9.65 * 10^{-8} \text{Pa}$$

$$9.65 * 10^{-8} \text{Pa} \left(\frac{10 \text{dyne}}{1 \text{Pa} * \text{cm}^2} \right) = 9.65 * 10^{-7} \frac{\text{dyne}}{\text{cm}^2}$$

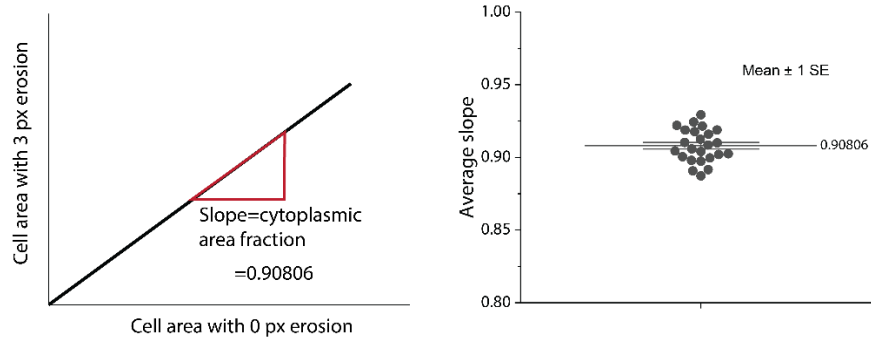
Supplementary Figure 2.S3. Calculation of shear flow on epithelial monolayer within perfusion system.



Supplementary Figure 2.S4. Confluent epithelium displays collective cell behavior. (left) Representative frame from the no stretch control with overlaid displacement vectors (green) generated by PIVLab. (Right) The same frame is shown with velocity magnitudes.



Supplementary Figure 2.S5. p120-catenin and vinculin are predominantly cytoplasmic in T151 E-cadherin mutant cells. No-stretched and stretched devices with the T151 cells were fixed and stained after the 6-hour observation period. There is no clear localization of p120-catenin nor vinculin at cell-cell contacts. Scale bars are 50 μm . IHC images shown have enhanced contrast to help visualize the proteins of interest.



$$A_{total} = \text{Total cell area}$$

$$A_{cyto} = \text{Total cytoplasmic area}$$

$$A_{AJ} = \text{Total cell contact area}$$

$$A_{total} = A_{cyto} + A_{AJ}$$

$$A_{cyto} = 0.90806(A_{total})$$

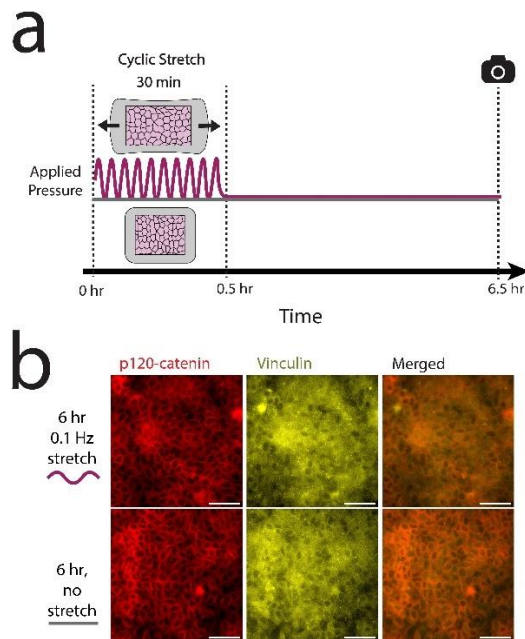
$$A_{AJ} = (1 - 0.90806)(A_{total})$$

$$I = \text{mean fluorescence intensity}$$

$$I_{total} = I_{AJ}(1 - 0.90806) + I_{cyto}(0.90806)$$

$$I_{AJ} = \frac{I_{total} - I_{cyto}(0.90806)}{(1 - 0.90806)}$$

Supplementary Figure 2.S6. Calculation of vinculin fluorescence intensity at cell-cell contacts. (left) For each data set, the cell areas of a 0 px eroded cell were plotted against the areas for the corresponding 3 ox eroded cell. (right) The average slope of these plots was 0.90806, indicating the cytoplasmic area fraction.



Supplementary Figure 2.S7. IHC staining of vinculin KO cells. No-stretch control and stretched devices with the Vinculin KO cells were fixed and stained after the 6-hour observation period. Qualitatively, p120-catenin is less localized to cell-cell contacts than for the WT MDCK cells. As expected, vinculin expression is minimal (observed signal is mostly background noise). Scale bars are 50 μm . IHC images shown are auto-contrasted to help visualize the proteins of interest.

Homemade basal medium for cell imaging experiments

The following reagents were mixed in water, pH adjusted to 7.0 using HCL, then filter sterilized with a 0.1 μm filter. Methionine, Calcium Chloride, and the MEM Vitamin Solution (100x) were added after pH adjustment.

Ingredient	Concentration (mg/L)
KCL	400
MgSO ₄ .7H ₂ O	200
NaCl	5963
D-Glucose (dextrose,monohydrate)	1000
L-arginine. HCL	126
L-cystine. 2HCL	31
L-glutamine	296
L histidine HCL. 2H ₂ O	42
L-isoleucine	52
L-leucine	52
L-lysine HCL	73
L-phenylalanine	32
L-threonine	48
L-tryptophan	10
L-tyrosine	52
L-valine	46
NaHCO ₃	1000
Na HEPES	2603
NaH ₂ PO ₄ . H ₂ O	140
Methionine	167
Calcium Chloride (CaCl ₂)	200
MEM Vitamin Solution (100x) (<i>Sigma, M6895</i>)	N/A

Chapter 3

Compression of a 2-D epithelium

3.1. Preface

The contents of this chapter previously appeared in *Biotechniques* and is reproduced here from: Dow, L.P., Khankhel, A.H., Abram, J., and Valentine, M.T., "3D-printable cell crowding device enables imaging of live cells in compression." *BioTechniques* 68.5 (2020): 275-278. Doi: 10.2144/btn-2019-0160. Adaptations have been made to section headings to be consistent with the formatting of this thesis.

In this chapter, I present a study on the design and implementation of a novel, 3-D printed device to apply compression to a 2-D epithelium for long-term live cell imaging studies. The original idea for the device originated from my BMSE colleague and mentor, Aimal Khankhel as well as Dr. Megan Valentine. The original design was created by a previous UCSB Master's student, John Abraham. While completing a rotation in Megan's lab under Aimal's mentorship, I re-designed several aspects of the device to be compatible for cell culture conditions. These contributions included developing a protocol for cell attachment on PDMS, reconstructing the device from Acrylonitrile Butadiene Styrene, and mechanically enforcing different parts of the device to mechanically withstand conditions from the cell incubator. Furthermore, I tested the strain capabilities of the device and performed the biological experiments with Aimal. Dr. Valentine and I performed additional data analysis including PIV analysis and cell compression measurements. I wrote the paper in collaboration with Dr. Valentine and John Abraham.

3.2. Abstract

We designed and fabricated, using low-cost 3D printing technologies, a device that enables direct control of cell density in epithelial monolayers. The device operates by varying the tension of a silicone substrate upon which cells are adhered. Multiple devices can be easily manufactured and placed in any standard incubator. This allows long-term culturing of cells on pre-tensioned substrates until the user decreases the tension, thereby inducing compressive forces in plane and subsequent instantaneous cell crowding. Moreover, the low-profile device is completely portable and can be directly mounted onto an inverted optical microscope. This enables visualization of the morphology and dynamics of living cells in stretched or compressed conditions using a wide range of high-resolution microscopy techniques.

Method Summary: We used 3D printing technologies to create a mechanical testing device that enables long term culture of cells on pre-tensioned substrates that can be returned to zero stress under user command. The devices are compatible with a variety of imaging platforms, enabling real-time visualization of the dynamic response of cells to in-plane compression.

3.3. Introduction

Epithelial homeostasis requires the precise regulation of cell density and has been found to be controlled by mechanical intercellular forces within the monolayer¹. In particular, when crowded above the target density, cells experience intercellular compressive forces and undergo mechanically influenced live-cell extrusion¹⁻⁵. Failure to extrude can result in tumorigenesis, while hyper-extrusion can compromise barrier function. Therefore, studies of epithelial cell mechanics and mechanobiology are critical to understanding healthy tissue maintenance, and also how dysfunction of cell migration can lead to cancer and other

diseases⁶.

Unfortunately, there are limited experimental tools to enable such studies. Several commercial cell stretching systems are available (*e.g.* from Flexcell International, Burlington NC USA; Strex, San Diego, CA USA; CellScale, Waterloo, Ontario Canada) and a number of custom-built devices using extensible silicon⁷⁻¹², piezoelectric¹³, pneumatic¹⁴⁻¹⁷ and recently dielectric actuation¹⁸ have been reported. However, microscopy studies of crowding-induced live cell extrusion are particularly demanding: cells must be cultured on stretched membranes for hours to days to reach confluency before crowding is induced, then must be imaged at high spatiotemporal resolution to observe cell morphology and dynamics. Although some current devices are amenable to imaging^{8,10,11,15,16,19}, it is not possible to maintain loading conditions continuously in culture or to move the cells in a loaded state between the incubator and microscope. This severely limits analysis of the dynamic changes that occur before, during, and after cell extrusion.

Here, we report a new approach based on the design of low-cost and completely portable cell stretching devices that allow culture of cells on pretensioned substrates and that can be easily transferred to imaging platforms without any changes in cell loading. Moreover, the ease and low cost of manufacturing (typically <\$300) allows for simultaneous use of multiple devices.

3.4. Results

3.4.A. Device requirements

To meet the needs of dynamic extrusion measurements, we asserted the following constraints: The device must be i) compatible with the existing microscope stage and

apertures (here, the Leica TCS SP8 laser scanning confocal fluorescence microscope), ii) capable of imposing uniform, repeatable compressive strains up to 30%, iii) able to be placed within a cell incubator, and easily transported to/from the microscope facility, iv) liquid-tight to ensure that culture media does not leak during transport or imaging, and v) amenable to sterilization. Lastly, the device vi) must position the cells within the desired focal depth and vii) imaging must occur directly through a glass coverslip.

3.4.B. Device fabrication and assembly

To customize the device, we employed in-house fused deposition modeling style 3D printing with a Stratasys f270 printer. F123 acrylonitrile butadiene styrene (ABS) build material was chosen due to its high resistance to thermal deformation, ease of printing, and cost-effectiveness. Quick support release (QSR) was used as the support material. Following printing of the necessary device components, the device was assembled per the instructions provided in the Supplemental Materials. All components were purchased from McMaster-Carr or 3D printed, except for the double-sided lead screw, for which a portion of the purchased threaded rod was manually reduced and re-threaded.

In operation, the user first secures both ends of a rectangular silicone substrate between the two clamps (Figure 3.1.), while threading the central portion of the substrate over the indenter. The indenter serves as a height reference for the substrate position, ensuring that the cells, which are adhered to the bottom surface of the substrate, are positioned within the objective focal depth. Several fiducial markers spaced 20 mm apart were engraved into the base of the device to allow the user to quickly apply a pre-determined strain to the substrate. To provide an aqueous environment for the epithelium, a 35 mm glass-

bottomed dish (MatTek) containing medium was magnetically held by a 3D printed holder just below the substrate.

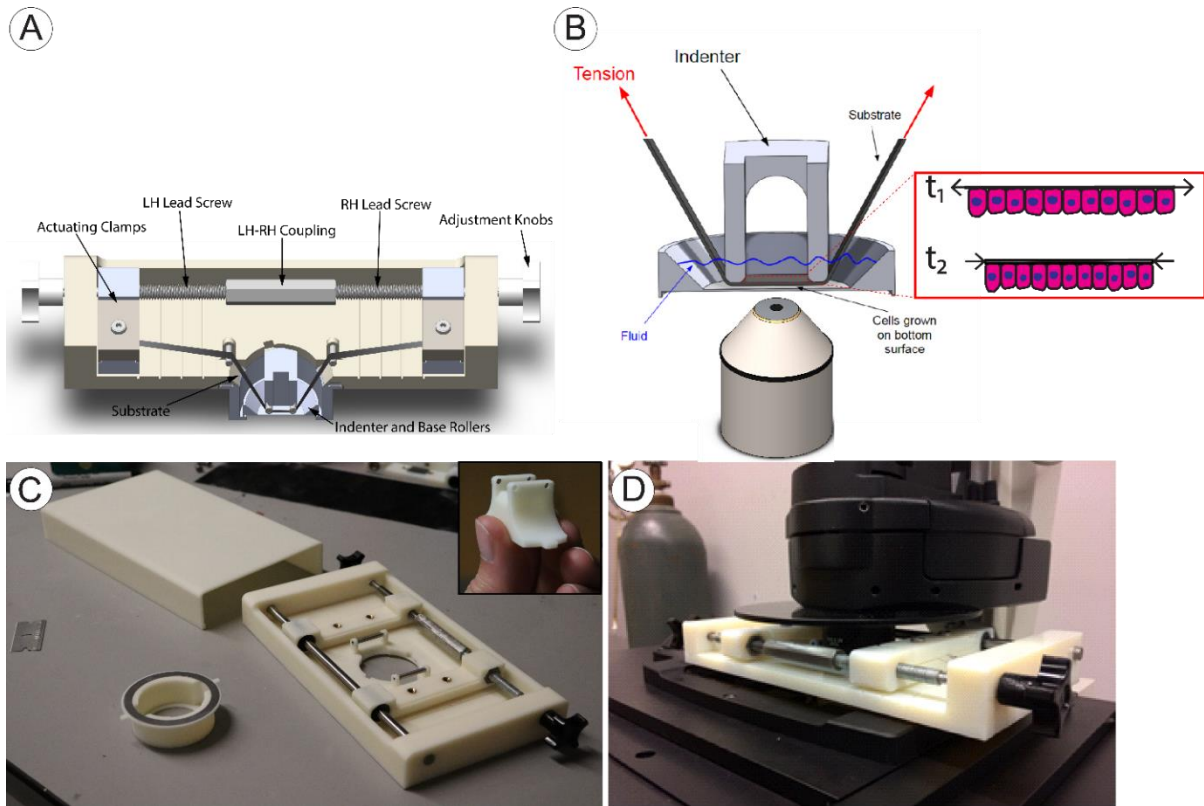


Figure 3.1. Device design and construction compatible for long-term cell culture and live-cell imaging.

(A) Schematic of device in cross-section with the substrate in tension. (B) Lead screw rotation induces substrate compression. (C) Image of assembled device with custom fit lid. (D) Device mounted on a common stage holder of an inverted fluorescence microscope in operation.

Tension within the substrate can be varied by turning a double-sided lead screw, ensuring that both clamps move outward (or inward) simultaneously and that cells located in the imaging region are not significantly laterally displaced during testing. On the opposite side of the device, a guide rail serves as a support for the actuating clamps. Linear bearings between the clamps and the guide rail provide smooth motion while two sets of stainless-steel rollers supporting the substrate reduce friction to improve uniformity of the applied strain. The lead screw rotation is fully reversible, providing compression or tension to the

substrate, as desired. To ensure self-containment and minimize contamination, a lid can be attached to the top-side of the device. Images and schematics of the completed device are provided in Figure 3.1; see Supplementary Information (*Section 3.11*) for additional schematics.

3.4.C. Quantification of membrane strain

To determine the extent and uniformity of the strain within the membrane, we used digital image correlation (DIC) to visualize the strain field (Figure 3.2.). A random uniform distribution of speckles was spray painted onto the silicone rubber, and the painted strip was then loaded into the device and imaged under various states of strain. We measured proportional strain levels respective to revolutions of the lead screw, which averaged into a linear relationship across different strain states (Figure 3.2.C). Full experimental details are provided in the Supplementary Materials.

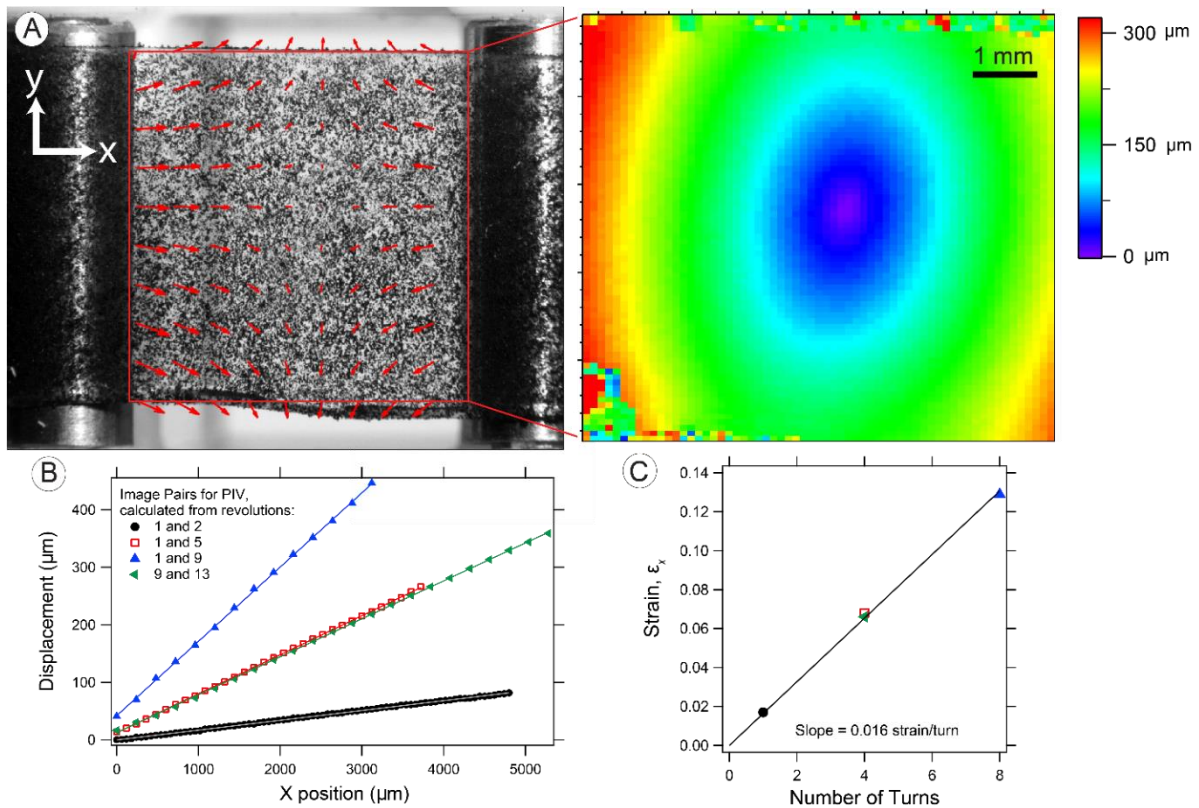


Figure 3.2. Digital image correlation demonstrates and quantifies linear strain of substrate.

(A) Image of speckled silicone rubber substrate was mapped for both pixel displacement direction (left) and magnitude (right). (B) The average lateral displacement as a function of x -position was quantified through the pair-wise comparison of images obtained across different tension states. The numbers in the legend refer to the number of revolutions of the outer knob turning the lead screw (see Supplementary Materials for details) for the two images forming the pair; the slope of each line gives the dimensionless substrate strain, ϵ_x per turn, shown in (C).

3.4.D. Uniaxial Compression of MDCK epithelial cells

To demonstrate the utility of this device for measurements of cell dynamics under compression, we used a model epithelial system of Madin-Darby Canine Kidney (MDCK) II cells expressing eGFP E-cadherin²⁰. To promote cell attachment, the silicone rubber substrate was first functionalized with fibronectin (see *Materials and Methods* for details, section 3.5.) before being placed within the cell compression device and pretensioned as desired. Once the functionalized substrate was pre-tensioned, the device was inverted and approximately

50,000 cells were deposited onto the surface over the indenter. To ensure cell adherence, the inverted device was then covered with parafilm and placed in the incubator for 3 hours. After incubation, the device was flipped and the adhered cells were rinsed with PBS before being submerged in the media-filled MatTek dish. The custom 3D printed lid was then fitted to the device, which was transported to the incubator for culture until confluency was achieved (usually after 1-2 days).

Once cells reached confluency, the device was transferred to the microscopy facility, where the tension was released by the desired amount, and the compressed cells were imaged using an inverted Leica TCS-SP8 spectral confocal microscope with a 10X air objective (Figure 3.3.). Before compression, the cell aspect ratio (height/width) was 1.07 ± 0.06 , indicating no preferred orientation within the plane of the substrate. Upon compression (30% strain), the aspect ratio increased to 1.56 ± 0.09 , due to a reduction in cell size along the compression axis and an elongation in the orthogonal axis. We also measured a ~20% increase in cell density along the compression axis (Figure 3.A.1).

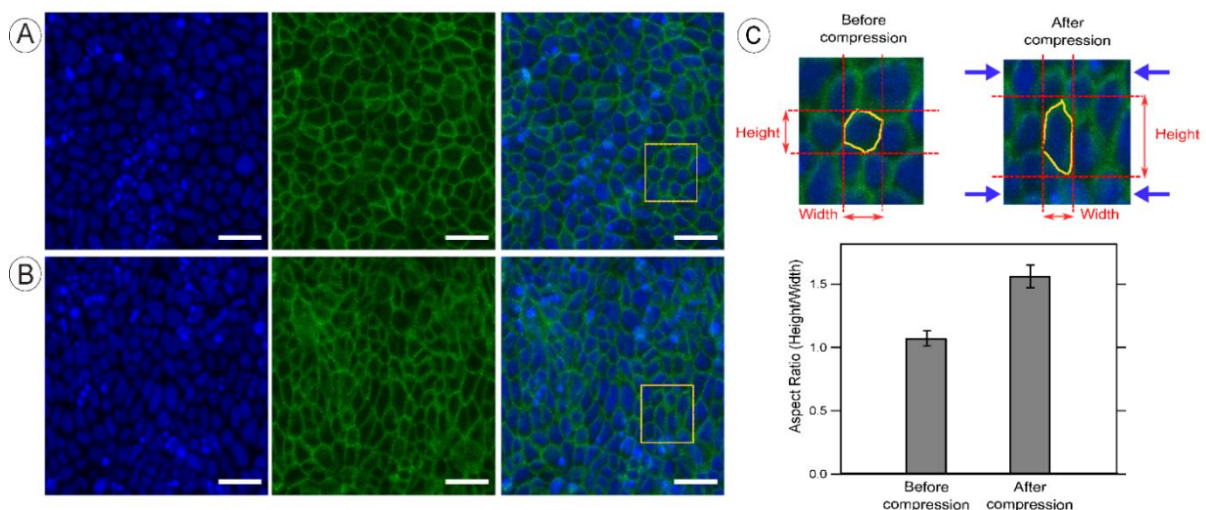


Figure 3.3. Substrate compression successfully crowds cells for live-cell extrusion studies.

(A) Uncompressed and (B) compressed epithelial cell monolayer cultured on a pretensioned (pre-strain value of 30%) silicone rubber substrate within the 3D printed compression device. (nuclei – blue, Hoechst; E-cadherin – green, eGFP; far right are merged channels. Scale bar is 30 microns. (C) Zoomed in regions of cells before and after compression. Bar graph shows mean values of aspect ratio as measured from 40 randomly selected cells from each of panels A and B. Error bars indicate standard error of the mean.

3.5. Methods and Materials

3.5.A. Strain mapping analysis

To determine substrate strain, two different software packages were used. In each case, two images obtained under different numbers of revolutions of the lead screw and thus different strain states were compared; the results obtained using the two packages are fully consistent. Images were converted to 8-bit grayscale and analyzed via cross-correlation analysis to determine the displacement field within the substrate. Here we report the displacement direction and semi-quantitative strain magnitude obtained using MATLAB PIVlab 2.02 (*MathWorks*) (Fig 3.2.A., left). Further quantification of the strain field was performed using the PIV plug-in in ImageJ. Using the cross-correlation mode, we calculated the displacement field using iterative window sizing (typically 128, 64, 32 pixels or 512, 256, 128 pixels; Figure 3.2.A., right). The substrate displacement was then measured by averaging the lateral displacement of the center portion of the silicone sheet; typically 5-10 y displacement values were averaged for each x -position. We plotted this line-averaged x -displacement versus x -position and determined the local strain from a linear fit to the resultant data (Figure 3.2.B.). This was repeated for several different numbers of revolutions. We found a linear relationship between the lateral strain and the number of revolutions of the lead screw, with 0.016 lateral strain units achieved per turn (Figure 3.2.C.). Although it is not possible to use open-source DIC analysis to determine large sample strains, as the cross-

correlation method becomes increasingly inaccurate when the displacements between the image pairs is large. We have confirmed that this linear relationship persists for at least 21 turns of the lead screw, corresponding to ~34% strain.

3.5.B. Substrate properties and functionalization

To promote cell attachment, a narrow strip of .02-inch-thick gloss silicone rubber (*Specialty Manufacturing Inc.*, Saginaw, MI) was cut into a section 8-9 mm wide and approximately 15 cm long. Per the manufacturer, the silicone sheet is formed from SILASTIC BioMedical Grade Liquid Silicone Rubber type Q7-4840, with a 5-minute press cure and no post cure processing. Per Dow Corning, the typical modulus for this material at 200% is 2.6 MPa. We measured a slightly lower value experimentally of ~1.9 MPa (for strains <5%). However, the device operates in a displacement-controlled mode, so the substrate modulus value is not particularly important to its operation, as long as the device is capable of applying enough force to achieve the desired displacement. The substrate was then sonicated in 70% ethanol for 10 minutes, rinsed with 100% ethanol, blown dry with nitrogen gas, and plasma treated at 18W for 10 minutes using a plasma cleaner with ambient room air at low pressure ~ 150 milliTorr (PDC-32G, *Harrick Plasma*, Ithaca, NY). Upon surface treatment, 100 µg/mL of human fibronectin (*Sigma Aldrich*, F2006) was added to the central region of the silicone strip and allowed to incubate overnight at room temperature.

3.5.C. Device Sterilization

The device was thoroughly wiped with 70% ethanol and placed within a biosafety cabinet for silicone strip clamping, along with cell seeding. We recommend UV exposure as an appropriate sterilization technique, but advise against autoclaving the device as the glass

transition temperature of ABS is ~ 105 °C, significantly lower than the standard autoclaving temperatures of ~ 121 °C.

3.5.D. Cell Culture

A concentrated cell suspension was prepared from a 100% confluent monolayer of eGFP E-cadherin MDCKII cells cultured in a T25 vented flask with 5% CO₂ at 37°C. The culture medium consisted of Dulbecco's Modified Eagle Medium (DMEM) (*ThermoFisher*, 12430054), 10% Fetal Bovine Serum (FBS) (*Life Technologies*, 10437028), and 1% Penicillin Streptomycin (PS) (*Life Technologies*, 15140122).

3.5.E. Imaging

Imaging was performed using an inverted Leica TCS-SP8 spectral confocal microscope with a 10X air objective (numerical aperture, NA = 0.3), at an 8,000 Hz scan speed, with a pinhole diameter of 1 AU. Imaging medium used was phenol red free DMEM (*ThermoFisher*, 21063029), supplemented with 15 mM HEPES, 10% FBS, and 1% PS. A field of view near the center of the silicone sheet was manually identified and imaged using bidirectional line-sequential scans (LineAverage=16). The first scan used 405-nm excitation with a 410-483-nm detection window to image the Hoechst-stained nuclei (10 μ M Hoechst stain; *ThermoFisher* # H3570). The second scan used a white light laser (WLL) providing 488 nm excitation with a 493-549-nm detection window to image the GFP-cadherin. For each location, a field of view with typical in-plane area of $155 \times 155 \mu\text{m}^2$ (corresponding to 800×800 pixels²) and 59.0 μ m stack height (along the optical axis z) was imaged; each scan took approximately 2 minutes to collect. This resulted in a stack of 60 2D images with an approximate difference 1 μ m between z -planes.

3.5.F. Quantification of cell crowding

To assess the changes in cell shape in response to compression, the GFP channel was isolated using Fiji/ImageJ. The heights and widths of 40 randomly selected cells were then manually measured using the line segment tool in Fiji/ImageJ, averaged, and the aspect ratio calculated. Cell density along the compressive axis was first determined by isolating the Hoechst channel, creating a maximum intensity projection of the z -stack, smoothing the image with the “smooth” tool in Fiji/ImageJ, then converting to an 8-bit binary image. Five random line segments were drawn horizontally across the image and the grayscale intensity profile was plotted using Fiji/ImageJ. Peaks, indicating the presence of a nucleus, were summed for each plot and averaged for the five line segments (Figure 3.S1).

3.6. *Conclusions*

In summary, we designed, manufactured, and tested a low-cost portable cell compression device amenable to both long-term culturing and imaging by microscopy. This innovation enables visualization of the morphology and dynamics of living cells in stretched or compressed conditions using a wide range of high-resolution microscopy techniques.

3.7. *Author contributions:*

AK and MTV conceived of project. JA and LPD designed, manufactured and tested devices. LPD and AK performed biological assays. MTV supervised the project. LPD and MV analyzed data and LPD, MTV, and JA wrote the manuscript.

3.8. Acknowledgements

We thank Sebastian Streichan for the kind gift of the E-Cadherin-GFP transfected MDCK cells and Dave Bothman for the helpful advice in design. We acknowledge the use of CNSI Innovation Workshop and Microfluidics Facility of the UCSB California NanoSystems Institute (CNSI), as well as use of the UCSB NRI-MCDB Microscopy Facility.

3.9. Financial and Competing Interests Disclosure

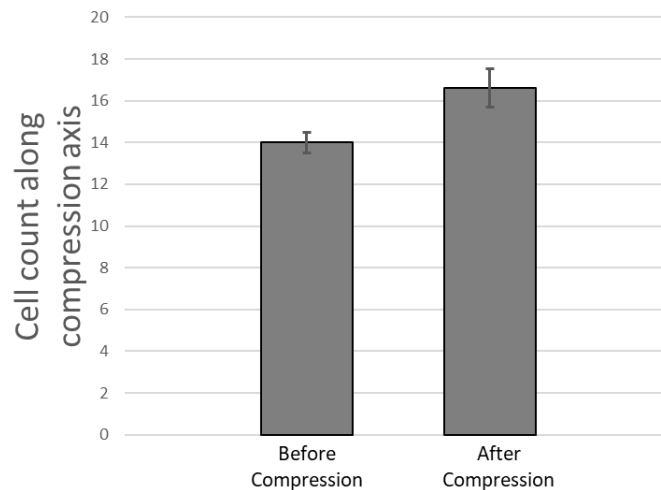
This work was supported by the US National Science Foundation (NSF) through a Graduate Research Fellowship to AHK and Award CMMI-1254893 to MTV. LPD was supported by the UCSB Biomolecular Science and Engineering Regents Fellowship. The Leica TCS SP8 Resonant Scanning Confocal Microscope was acquired by MTV under NSF Award DBI-1625770. Authors have no other financial interests or conflicts to disclose.

3.10. References

1. Gudipaty SA, Lindblom J, Loftus PD, *et al.* Mechanical stretch triggers rapid epithelial cell division through Piezo1. *Nature*. 543(7643), 118–121 (2017).
2. Eisenhoffer GT, Rosenblatt J. Bringing balance by force: Live cell extrusion controls epithelial cell numbers. *Trends Cell Biol.*23(4), 185–192 (2013).
3. Saw TB, Doostmohammadi A, Nier V, *et al.* Topological defects in epithelia govern cell death and extrusion. *Nature*. 544(7649), 212–216 (2017).
4. Kocgozlu L, Saw TB, Le AP, *et al.* Epithelial Cell Packing Induces Distinct Modes of Cell Extrusions. *Curr. Biol.* 26(21), 2942–2950 (2016).
5. Eisenhoffer GT, Loftus PD, Yoshigi M, *et al.* Crowding induces live cell extrusion to maintain homeostatic cell numbers in epithelia. *Nature*. 484(7395), 546–549 (2012).
6. Gudipaty SA, Rosenblatt J. Epithelial cell extrusion: Pathways and pathologies. *Semin. Cell Dev. Biol.*67, 132–140 (2017).
7. Ursekar CP, Teo S-K, Hirata H, Harada I, Chiam K-H, Sawada Y. Design and Construction of an Equibiaxial Cell Stretching System That Is Improved for Biochemical Analysis. *PLoS One*. 9(3), e90665 (2014).
8. Shao Y, Tan X, Novitski R, *et al.* Uniaxial cell stretching device for live-cell imaging of mechanosensitive cellular functions. *Rev. Sci. Instrum.* 84(11) (2013).
9. Tremblay D, Chagnon-Lessard S, Mirzaei M, Pelling AE, Godin M. A microscale anisotropic biaxial cell stretching device for applications in mechanobiology. *Biotechnol. Lett.* 36(3), 657–665 (2014).
10. Huang L, Mathieu PS, Helmke BP. A stretching device for high-resolution live-cell imaging. *Ann.*

- Biomed. Eng.* 38(5), 1728–1740 (2010).
11. Dan A, Huang RB, Leckband DE. Dynamic Imaging Reveals Coordinate Effects of Cyclic Stretch and Substrate Stiffness on Endothelial Integrity. *Ann. Biomed. Eng.* 44(12), 3655–3667 (2016).
 12. Sigaut L, Von Bilderling C, Bianchi M, Burdisso JE, Gastaldi L, Pietrasanta LI. Live cell imaging reveals focal adhesions mechanoresponses in mammary epithelial cells under sustained equibiaxial stress. *Sci. Rep.* 8(1) (2018).
 13. Clark WW, Smith R, Janes K, Winkler J, Mulcahy M. Development of a piezoelectrically actuated cell stretching device. In: *Smart Structures and Materials 2000: Industrial and Commercial Applications of Smart Structures Technologies*, SPIE, 294–301 (2000).
 14. Kreutzer J, Ikonen L, Hirvonen J, Pekkanen-Mattila M, Aalto-Setälä K, Kallio P. Pneumatic cell stretching system for cardiac differentiation and culture. *Med. Eng. Phys.* 36(4), 496–501 (2014).
 15. Huang Y, Nguyen NT. A polymeric cell stretching device for real-time imaging with optical microscopy. *Biomed. Microdevices.* 15(6), 1043–1054 (2013).
 16. Shimizu K, Shunori A, Morimoto K, Hashida M, Konishi S. Development of a biochip with serially connected pneumatic balloons for cell-stretching culture. *Sensors Actuators, B Chem.* 156(1), 486–493 (2011).
 17. Sato K, Nitta M, Ogawa A. A Microfluidic Cell Stretch Device to Investigate the Effects of Stretching Stress on Artery Smooth Muscle Cell Proliferation in Pulmonary Arterial Hypertension. *Inventions.* 4(1), 1 (2018).
 18. Li Z, Gao C, Fan S, *et al.* Cell Nanomechanics Based on Dielectric Elastomer Actuator Device. *Nano-Micro Lett.* 11(1) (2019).
 19. Wyatt TPJ, Fouchard J, Lisica A, *et al.* Actomyosin controls planarity and folding of epithelia in response to compression. *Nat. Mater.* (2019).
 20. Puliafito A, Hufnagel L, Neveu P, *et al.* Collective and single cell behavior in epithelial contact inhibition. *Proc. Natl. Acad. Sci. U.S.A.* 109(3), 739–744 (2012).

3.11. Supplemental Information



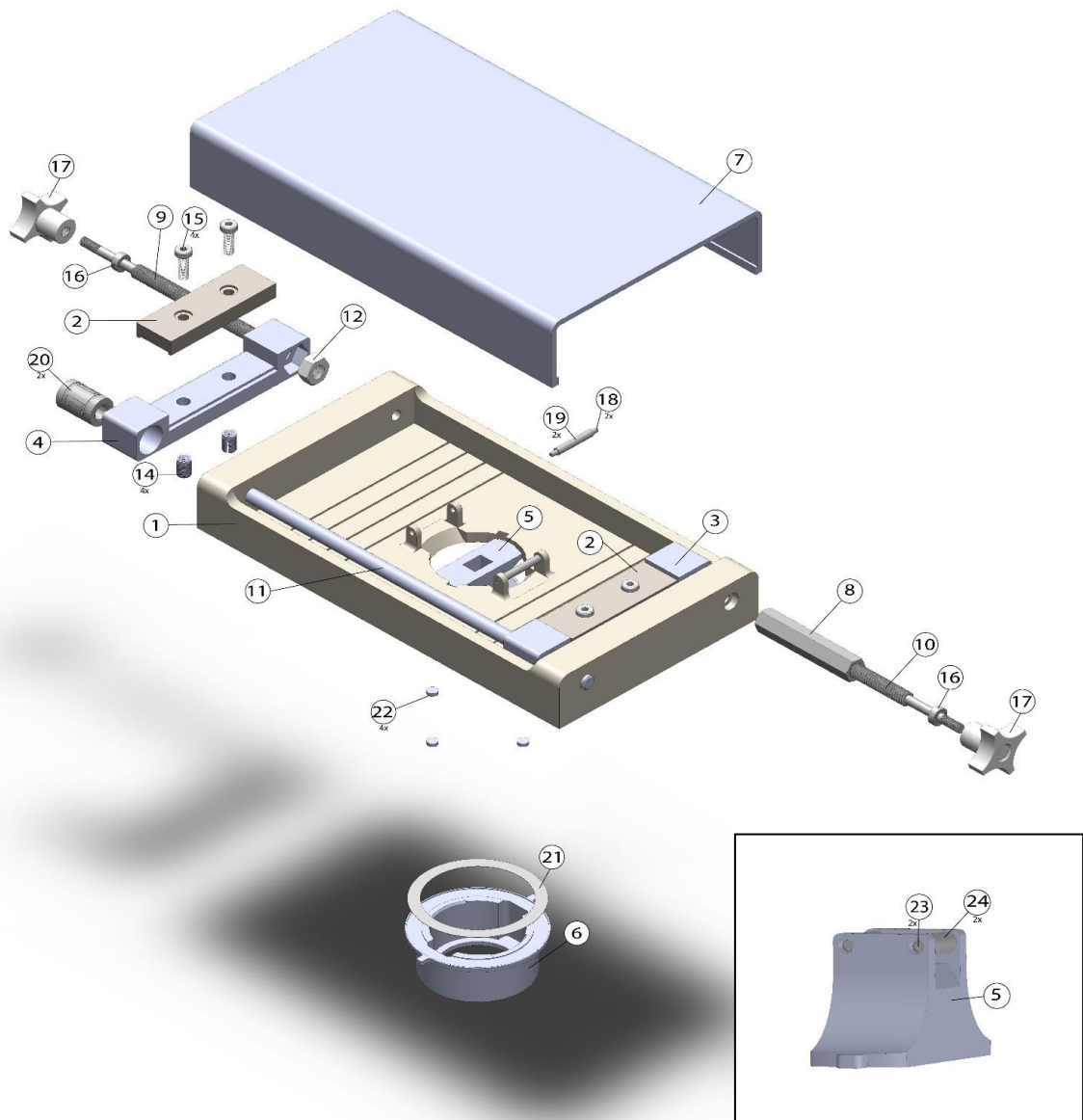
Supplementary Figure 2.S1. Cell density along the axis of compression increased approximately 20%, from 14.0 ± 0.5 to 16.6 ± 0.9 . Error bars indicate standard error of the mean. Cells were counted using the maximum intensity projections of the Hoechst channel before and after crowding.

Table 3.1. Materials List and Assembly Instructions: 3-D printed parts

Printer/material	Part Description	Annotation Number	Quantity
Stratasys f270/ABS	Base	1	1
Stratasys f270/ABS	Clamp	2	2
Stratasys f270/ABS	Clamp Holder-RH	3	1
Stratasys f270/ABS	Clamp Holder-LH	4	1
Stratasys f270/ABS	Indenter	5	1
Stratasys f270/ABS	Dish Holder	6	1
Stratasys f270/ABS	Lid	7	1

Table 3.2. McMaster-Carr Parts

Catalog Number	Part Description	Annotation Number	Quantity
97372A106	LH to RH coupling nut	8	1
90036A029	LH rod machined with 8-32 threads	9	1
98837A029	RH rod machined with 8-32 threads	10	1
6061K101	1/4" diameter, 8" long dowel	11	1
90519A029	Left hand nut	12	1
90490A029	Right hand nut	13	1
94510A040	M4 Brass threaded insert	14	4
92855A413	M4 12mm long screw	15	4
57155K371	1/4" ball bearing	16	2
5993K11	8-32 threaded knob	17	2
98380A431	Roller dowel pin	18	2
92320A475	Dowel pin unthreaded spacer	19	2
6489K61	1/4" linear ball bearing	20	2
98055A381	Shim used for magnetic attachment	21	1
5862K961	Magnet	22	4
98380A429	Indenter dowel	23	2
92321A014	Indenter roller	24	2

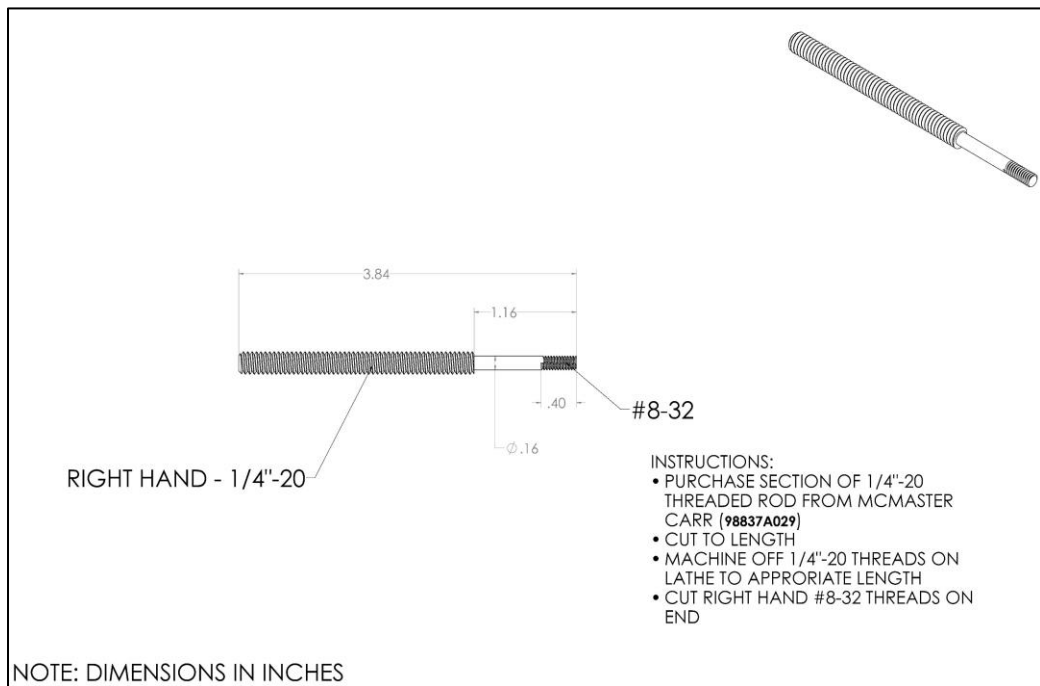
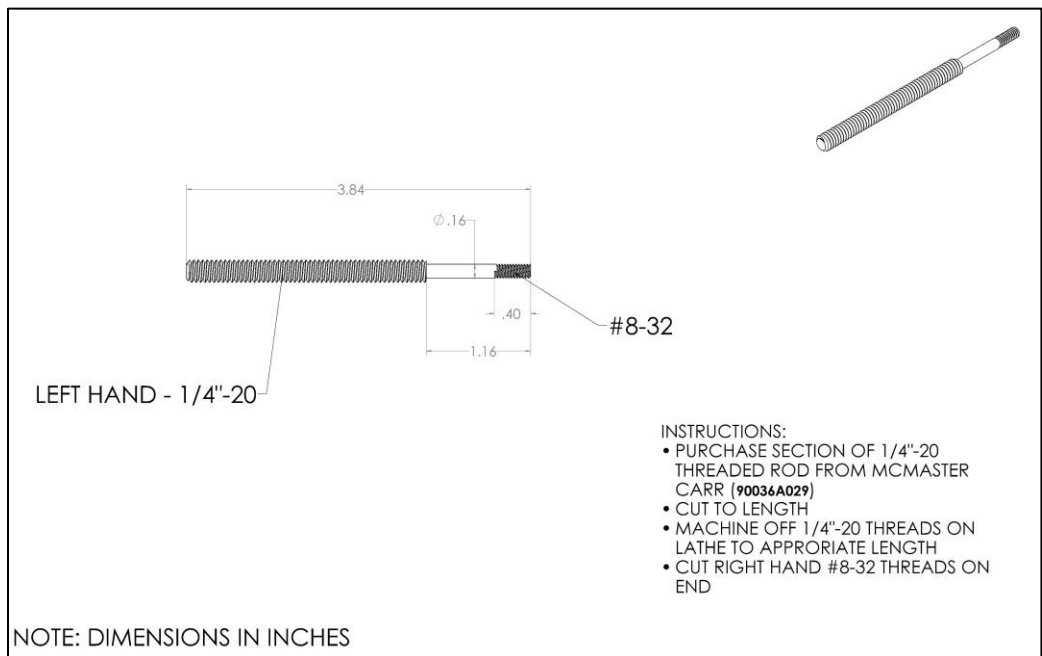


Supplementary Figure 3.S2. Exploded view of the assembled device with annotations, defined in Table 1 and Table 2 (above). Since some regions of this device experience high localized stress during tension, the 3-D printed components included structural support features such as side ribs (1) for the base plate and gussets for the indenter (5, in inset).

3.11.A. Instructions for assembly

1. Print the accompanying STL files with a 3-D printer capable of printing structural resins that can withstand high thermal stress (e.g. we used the Stratasys f270 which was capable of fused deposition modeling to print acrylonitrile butadiene styrene).
2. Purchase or obtain the necessary parts listed in the table above.

- a. The only parts that need to be modified are the threaded rods (#90036A029 and #98837A029). See instruction below



b. Assemble clamp holders

- i. For the LH clamp holder, glue the LH nut (90519A029) into the hexagonal opening and the 1/4\" linear ball bearing (6489K61) into the larger opening on the other side.

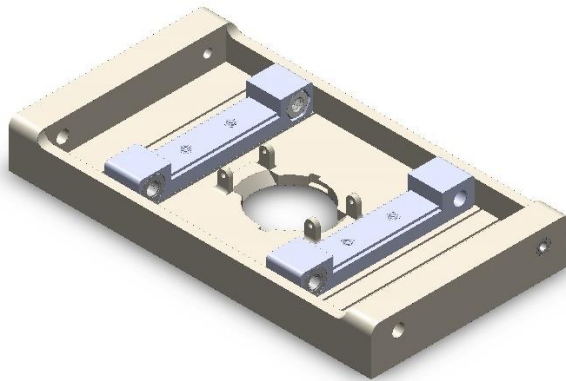
- ii. Repeat the above step for the RH clamp holder, except replace the LH nut with the RH nut (90490A029).
- iii. Insert, with glue, a brass threaded insert (94510A040) into both holes in the middle of the clamp holder.
 - 1. *Note: you may need a hammer to get it fully seated*
- iv. Allow glue to dry.

c. Assembling the lead screw through the clamp holders

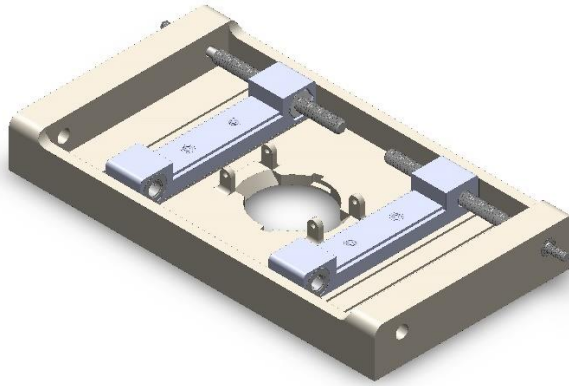
- i. On both sides of the base plate, insert the 1/4" ball bearing (57155K371) inside the 5/16" opening. Depending on the fit, you may need a rubber mallet (if too tight) or a little glue (if too loose).



- ii. Place both clamp holders inside the base plate so that the LH and RH nuts are aligned and face the center while lining up with the 5/16" outer hole.

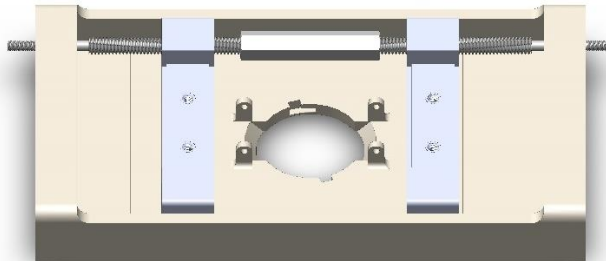


- iii. To assemble the lead screw, thread the RH and LH threaded rods from the inside into their respective nuts

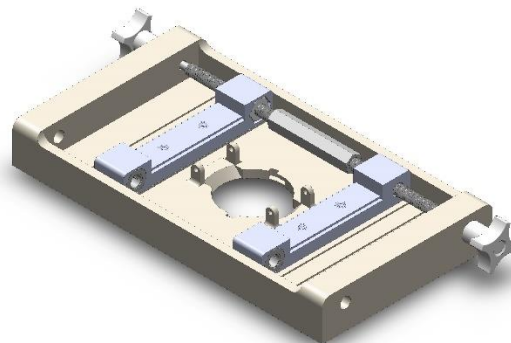


- iv. Screw both rods into the LH to RH coupling nut (97372A106) while making sure the clamp holders are centered. After this step, you can test your device by turning the lead screw and making sure that the clamp holders move between the middle and edges of the base plate equidistantly. Only then should you proceed to the next step.

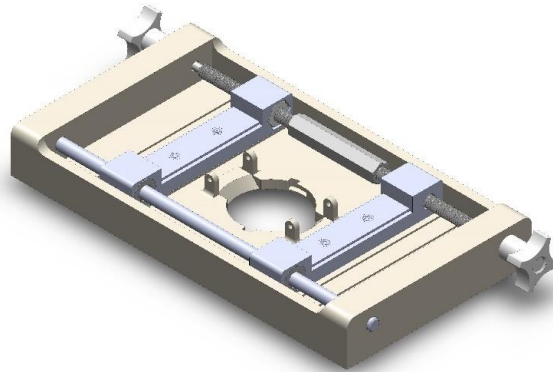
Note: This step requires extra attention: Make sure that the threaded rods are pulled as far back as possible so that you have clearance to fasten the nut. Also make sure you secure them tightly so that the assembly turns together and does not unscrew. Glue may help here.



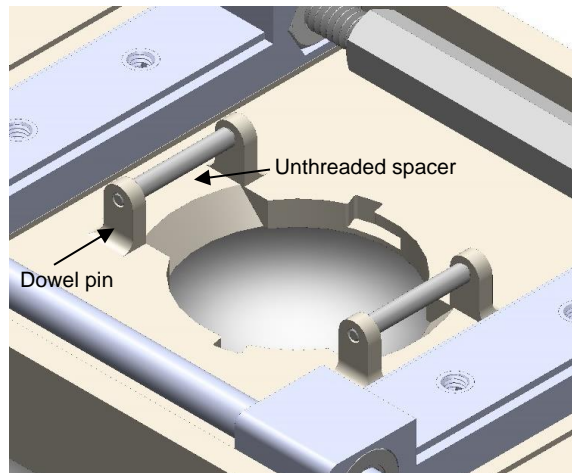
- v. Finish assembling the lead screw by attaching an 8-32 thread knob (5993K11) to the outer ends.



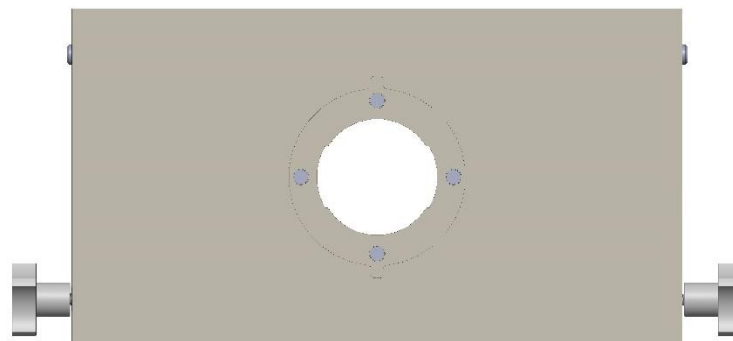
- d. Insert the ¼” diameter, 8” long dowel (6061K101) through the opposite ends of the clamp holders. Use glue on the outside to fix the rod in place.



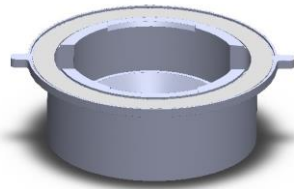
- e. Insert the stainless-steel dowel pin (98380A431) through the unthreaded spacer (92320A475) and fix, using glue, the two ends of the dowel pin between the respective holes on top of the base plate. Repeat for the other side.



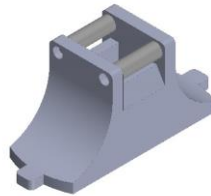
- f. Flip device over and glue in the 4 magnets (5862K961)



- g. Glue the magnetic circular shim within the corresponding indented region of the 3-D printed dish holder. Once the glue is dried, the dish holder should now magnetically attach to the base plate.

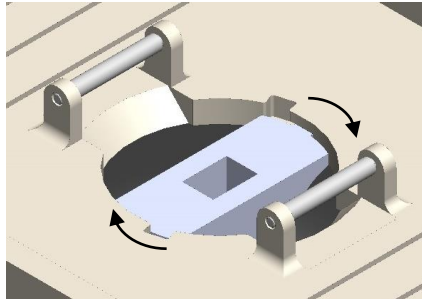


- h. In a similar fashion as step e, insert the 0.5” stainless-steel dowel pin (98380A429) through the unthreaded spacer (92321A014) and fix, using glue, the two ends of the dowel pin between the respective holes on the 3-D printed indenter. Repeat for the other side.



- i. To insert the indenter into the base plate, flip over and insert the tabs into the corresponding inserts of the base plate. Twist to lock in place.

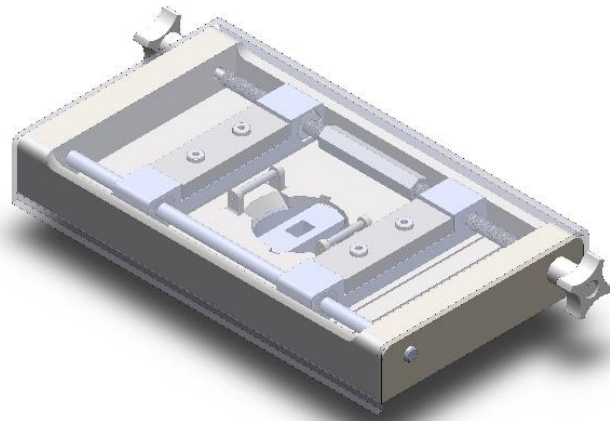
Note: In the event of a loose fit, you can cap the ends of the indenter tabs with parafilm to provide a tight fit.



- j. When threading a deformable silicone substrate within the device for experiments, screw the clamps into the clamp holders using two M4 12 mm screws (92855A413) per clamp.

Note: For better traction or if slippage occurs, adhere a thin rough material (e.g. sandpaper) to the top of the clamp holder and on the underside of the clamp.

- k. A schematic of the final assembled device is shown below. Images are provided in Figure 3.1.



Chapter 4

Boundary strain of a 2-D epithelium

4.1. Preface

In this chapter, I present a computational study based on data from previously published experiments (Sadeghipour et al., *Elife*, 2018). This project was conceived of and outlined by myself and Dr. Anna Kim, a former postdoctoral fellow of the Pruitt Lab. Before I joined the lab in 2018, two former postdocs, Dr. Ehsan Sadeghipour and Dr. Miguel Garcia had performed micromanipulation experiments using a novel MEMS device. The device applied an in-plane mechanical shear strain to an epithelium, which resulted in unique oscillatory cell migration patterns. Their original work opened new questions around the important role of cell shape in force propagation and their observed migration patterns. These questions were previously unanswered due to the difficulty in conducting high throughput segmentation of thousands of images, as well as the difficulty to accurately segment lower resolution (10x objective) images of epithelial cells. Soon after the study was published, however, the open-source segmentation tool Cellpose was published (Stringer et al., 2021, *Nature Methods*), which Dr. Kim discovered and informed me of. Cellpose integrates machine learning by training off extensive data sets, allowing it to segment cells accurately even with poor quality images. We recognized an opportunity to apply this segmentation tool to the data from these previous experiments. This opportunity would allow us to identify a relationship between local mechanical cues and shape changes within an epithelium. Our long-term goal was to build a predictive model for how these changes impacted the oscillatory migration profile observed in the original study.

I mentored an undergraduate researcher, Katya Morozov, to adapt the Cellpose segmentation tool to the thousands of images and segment millions of cells. Katya developed several Python scripts to automate the segmentation workflow. We then extracted cell shape information, filtered it to improve data accuracy, and analyzed the data to understand how a local epithelial strain could regulate cell shape in a spatiotemporally dependent manner. Simultaneously, I mentored another undergraduate researcher, Stacey Surace, who re-did the PIV analysis from the original study to make it compatible with our cell segmentation data. Sam Feinstein used the raw data generated from Katya, Stacey, and I to create Figure 4.4.

4.2. Abstract

Local mechanical signals within epithelial tissue regularly occur during morphogenesis and in dynamic adult tissues such as the gut. Recently, we have demonstrated local shear perturbation to induce specific modes of collective, global epithelial migration via actomyosin dependent intercellular signaling. However, it is unclear how morphological changes in cells contribute to these migration responses, and whether migration is induced solely via biochemical signaling cascades throughout the monolayer. Using advanced machine learning segmentation software, we will conduct a spatiotemporal analysis of how single-cell shape changes following local mechanical signals facilitate cell migration. These results will provide evidence for a physical model in which global epithelial migration patterns are determined by changes in local cellular morphologies.

4.4. Introduction

Active materials are collectives of self-driven units that locally consume free energy to execute self-sustained motion and work¹. Such active units organize in large-scale

structures to generate collective material properties. These individualistic agents that engineer changes in internal organization allow active materials to change under different environmental conditions. Active systems have enormous potential for the design of artificial matter that operates away from equilibrium and exhibits life-like properties, such as self-healing, adaptation, and growth²⁻⁴. Achieving this potential requires a quantitative understanding of how specific cues within the material microenvironment facilitate an active transition in material properties.

The spontaneous organization of active matter arises from the interplay of self vs other: i) self- each unit generates work and motion through controlled and tunable active processes and ii) other- communication with other units and with the environment drives the system to operate as a collective. The interplay of activity and interactions results in transitions between solid-like and fluid-like states within the material^{5,6} (Figure 4.1). The solid behaves like a tightly bound collective, while the fluid is dominated by individual active processes⁷. The ability for a material to spontaneously toggle between solid and fluid states serves many advantages in allowing it to adapt to its environment or serve different functions.

Biological tissues provide a remarkable realization of this behavior. Epithelial cells form continuous sheets of tissue that protect nearly all bodily organs including the skin, lungs, and gut^{8,9}. Through tight adhesive contacts, interconnected cells provide robust mechanical integrity as a barrier layer while selectively filtering solutes^{8,10,11}. However, the dynamic physiological microenvironment routinely challenges the mechanical integrity of the epithelium¹²⁻¹⁴. Therefore, epithelial tissues actively toggle material properties via internal cellular reorganization to maintain barrier function. The changes in the material state

of the tissue are controlled by the self vs other paradigm: self- individual cells are motile and contractile entities that bind to and migrate across the underlying extracellular matrix (ECM) via integrin proteins and hemidesmosomes¹⁵⁻¹⁷. These proteins anchor to the actin cytoskeleton, which generates cell tension via actomyosin contraction^{18,19}. Other- cells laterally connect to their neighbors through adherens junctions mediated by E-cadherin²⁰. Cell-cell adhesions favor collective and solid-like properties, while cell-ECM adhesions tend to favor fluid-like properties²¹.

The material state of the tissue can be quantitatively described by two main parameters: cell motility and cell morphology. Cell motility is broadly defined by direction or speed, among other descriptors²²⁻²⁴. Cell morphology is defined via cell shape (e.g., area, solidity, circularity, aspect ratio, etc.)²⁵. Parameters of cell shape have also been used as a proxy for cell fluidity, defined as the cell shape index⁴. Both cell motility and cell shape are regulated by actomyosin. For example, contracting cells utilize myosin to power contraction of the actin cortex to reduce apical cell area^{26,27}. Fluid-like tissues have high levels of cell migratory movements and cell shapes that are more irregular, often with increased apical surface area²¹. Fluid-like tissues with these morphological traits are often observed during tissue growth or tissue repair. Solid-like tissues have reduced migratory movement and more regular cell shapes/packing structure, often with reduced apical surface area²¹. Epithelia acquires solid-like elasticity as it matures in adult homeostasis²⁸.

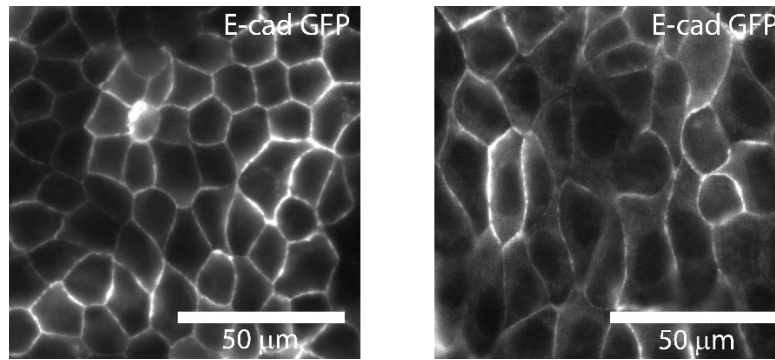


Figure 4.1. Jammed v.s. unjammed epithelium.

(left) A more solid-like, jammed epithelium is often characterized by cells with reduced cell area, increased circularity and solidity, lower motility, lower rates of cell proliferation, and an aspect ratio close to 1. (right) A more fluid-like, unjammed epithelium has higher areas, decreased circularity and solidity, higher motility, increased rates of cell proliferation, and higher aspect ratios. Both images are from a GFP E-cadherin MDCK epithelium.

Currently, there is a gap in our understanding of how active materials such as epithelia toggle their physical state to mitigate boundary perturbations. Recent studies have shown that these local mechanical cues can regulate collective cell behavior via directed cell migration²⁹. However, it is unclear how epithelia toggle cell morphology as a function of space and time to guide these migratory processes to influence the material state of the tissue. Here, we have combined recent advances in cell segmentation³⁰ with high-throughput methods to quantitatively define epithelial shape during their response to a local shear perturbation. By averaging these parameters across millions of cells from experiments, our robust analysis has revealed several insights into how epithelia regulate cell morphology and subsequently their physical state. Our results not only provide a quantitative model for how epithelia mitigate boundary perturbations, but give broader insight to how active materials combat boundary perturbations.

4.5. Results

4.5.A. Development of a high-throughput segmentation approach

To study epithelial shape change as a function of a local boundary perturbation (i.e., shear), we broke up experimental images as a function of region and time (Figure 4.2). Experiments were predominantly imaged under 4 major time periods: 60 minutes before shear application with 5-minute imaging intervals (Time Frame #1), 15 minutes before shear application with 30 second imaging intervals (Time Frame #2), 30 minutes after shear application with 30 second imaging intervals (Time Frame #3), and ~20 hours after shear application with 5-minute intervals (Time Frame #4) (Figure 4.1a). All images across all time periods were then divided into three equal regions with increasing distance from the site of boundary shear strain (Figure 4.2b). These regions were termed the Proximal region, Middle region, and the Distal region, respectively. Since the device sheared the top and bottom planks of the device in a symmetrical manner (generating technical replicates per each experiment), we divided regions in the bottom and top planks with the same spatial parameters, all approximately 80 μm wide.

Prior experiments were done under 4 conditions: shear application, no shear application, shear application with blebbistatin, and shear application with jasplakinolide. Since 3 experiments were done per condition and we divided each image into multiple regions, we generated tens of thousands of images in total for our cell study (Supplementary Figure 4.S1). Therefore, we required a high-throughput approach that could automate image segmentation. We utilized Cellpose³⁰, a recently developed cell segmentation tool capable of batch processing images for segmentation. After generating cell outlines (ROIs) for each image, we cross-checked the results by thresholding ROIs with respect to a minimum area

and identifying the number of ROIs per image (Figure 4.2c). We found that the highest quality images generated a higher ROI count and minimized variability. Other images that had subtly drifted out of focus were more difficult to segment and produced fewer ROIs, increasing statistical variability.

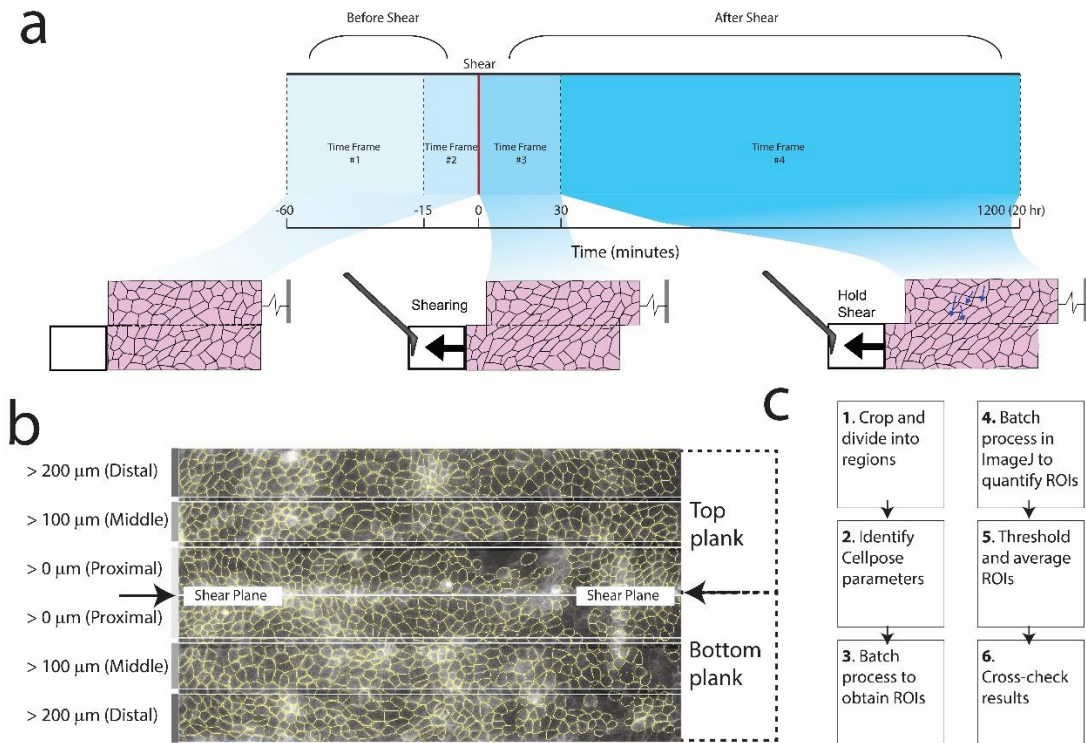


Figure 4.2. Workflow for high-throughput cell segmentation.

(a) Experimental procedure for epithelial shear experiments. Epithelial sheet was grown on two silicon planks (1000 μm x 250 μm each) and imaged for 1 hour (45 minutes at 5-minute intervals, then final 15 minutes at 30-second intervals). Epithelium was mechanically sheared mid-plane 100 μm using a tungsten probe and imaged at 30 second-intervals for 15-30 minutes before being imaged at 5-minute intervals for up to 20 hours. (b) E-cadherin fluorescent images from all experiments were batch processed for single cell segmentation and extraction of cell morphology. (c) To determine how spatiotemporal changes in morphology occurred over time, the top and bottom silicon planks were cropped into 3 regions based on their proximity to the region of mid-plane mechanical shear

4.5.B. Analysis of cell shape following shear perturbation

As previously shown²⁹, local boundary shear strain caused the migration of cells from outer regions (i.e., the Distal region) towards the shear plane (i.e., Proximal region) (Figure 4.3 b,c). This directed migratory response was shown to oscillate several times before

dampening back to an equilibrium state. However, it is unclear how changes in cell shape have contributed to these migratory responses.

After segmentation of cells from all images across the designated time intervals, we used ImageJ's open-source plugin, Labels to ROIs, to batch process extraction of shape descriptors. We first characterized the effect of boundary shear strain on cell area, aspect ratio, and the cell shape index, q ($\frac{Perimeter}{\sqrt{Area}}$).

Cell area

We found that the no shear strain control condition had a predictable non-linear decay of cell area over time equally similar across each spatial region. This expected non-linear decay can be explained by an increase in proliferation as cells reach the point of contact inhibition (Figure 4.3d). Under the application of boundary shear strain, we observed that the Proximal and Midde/Distal regions have opposite short-term effects with respect to area change. Immediately after boundary shear strain, cells in the Proximal region had a contraction of cell area, while outer regions had a dilation of cell area (Figure 4.3e). Despite the initial short-term changes in cell area with respect to each region, ultimately cells across all regions plateaued around $200 \mu\text{m}^2$ in area, independently of applied boundary shear strain. Interestingly, we also observed more uncertainty in cell area in the control no shear strain condition. This increase in uncertainty is indicated by larger confidence intervals as a function of time.

Aspect ratio

The aspect ratio (AR) linearly decreased over time for the no shear strain control condition, evidence that cells are becoming more regularly shaped as they packed more tightly on the silicon planks of the device (Figure 4.3f). We observed the same linear decrease in AR

for cells subjected to boundary shear strain across all regions (Figure 4.3g), indicating that local shear strain did not propagate significant changes across cell aspect ratio. However, we did notice that under shear strain, AR variability increased for cells. This will be discussed more in the Discussion.

Cell shape index

The cell shape index of a cell, denoted by the letter “q” and defined as $(\frac{Perimeter}{\sqrt{Area}})$, is a common metric used to quantify cell fluidity. Cells with a higher q are often more fluid-like and correlate with higher irregularity and increased migration³⁵². When the epithelium was grown on the device under the condition of no local shear strain, we observed that cells had a decreasing q value over time (Figure 4.3h). This decrease is expected as cells proliferate to the point of contact inhibition on the device. The q value did not distinctively vary from one spatial region to another, with an average value of 4.1 and decreasing towards 3.9 by the end of the imaging period.

In response to the boundary shear strain, we observed a short-term fluctuation in q (Figure 4.3i). Interestingly, despite the contraction of area in the proximal region and dilation of area in the outer regions, q was immediately reduced to approximately 4.0 for all spatial regions of the epithelium after the application of boundary shear strain. This reduction recovered in 2-3 hours in a “v” like fashion, after which it continued to reduce towards 3.9 as in the no shear strain control condition. The fluctuation in q indicates a shift from a more liquid like state to a solidification, then a ~2 hour recovery back to a more fluid-like state. Interestingly, this transition correlates with the migration reversal at the ~3 hour mark (i.e., cells compress at the Distal region of the plank resulting in solid state, then move back

towards the proximal region as tissue becomes more fluid). However, we don't see this trend for the second migratory oscillation.

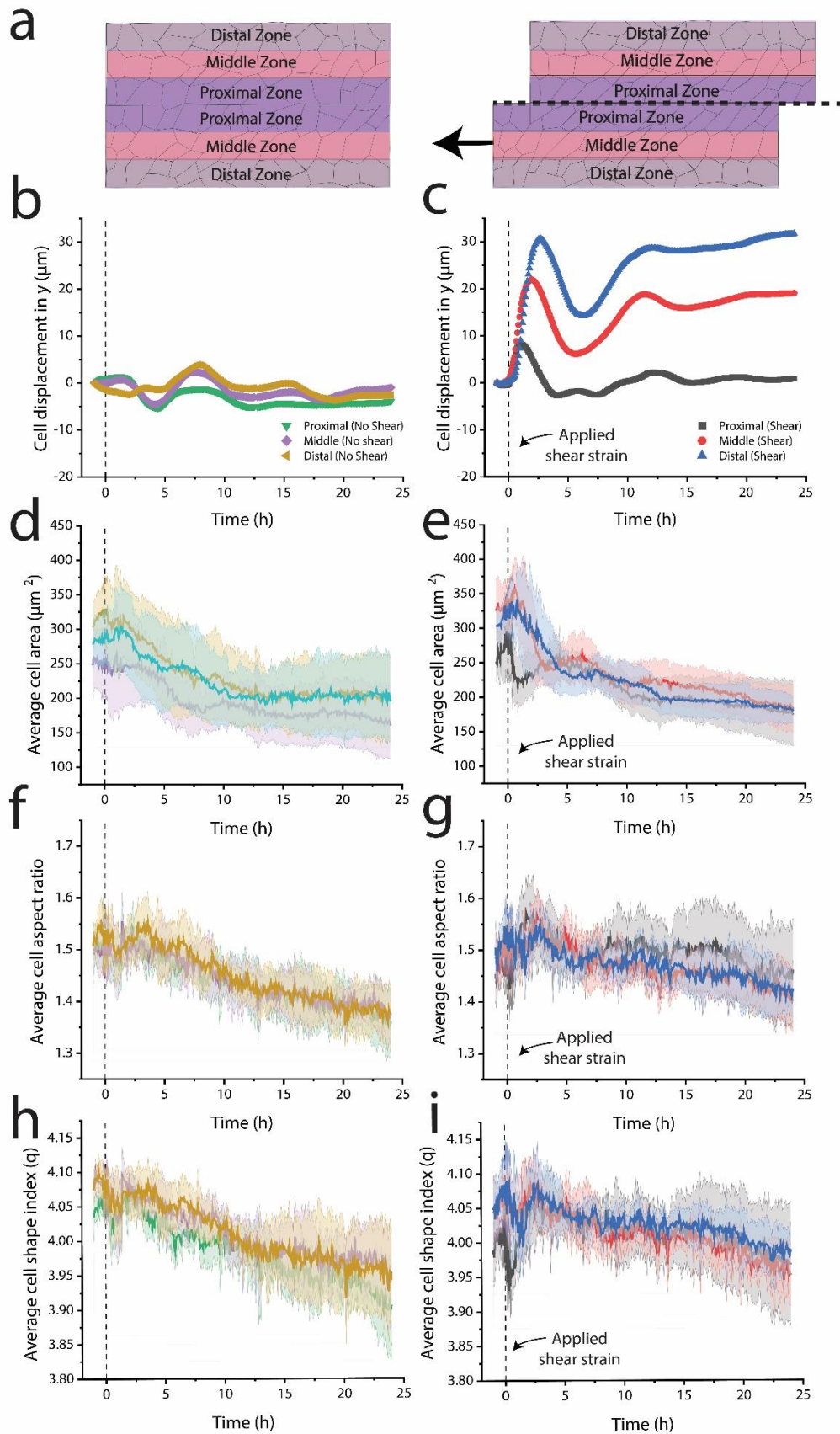


Figure 4.3. Mechanical shear propagates changes in cell shape that dissipate over time.

(a) Schematics of epithelium (left) without and (right) with a boundary shear strain, divided by regions of increasing distance from the applied shear strain (Proximal, Middle, Distal). Displacement of cells quantified by PIV (b) without and (c) with a boundary shear strain. (d) Average cell area decreases over time in a viscoelastic decay without boundary shear strain, (e) which is disrupted in the first 3 hours after boundary shear is applied. (f,g) Aspect ratio of cells linearly decreases over time (f) without and (c) with a boundary shear strain. Cell shape index, q , is defined as $(\frac{Perimeter}{\sqrt{Area}})$ and (h) decreases with time, though (i) is sharply reduced at the onset of boundary shear strain. Shaded regions represent the +/- 95% Confidence Intervals.

To determine statistical differences in shape descriptors on the epithelium as a function of boundary shear strain, we averaged the change in values across the observation period following strain application. As expected, area decreased in both conditions (Figure 4.4b), but interestingly we observed a more significant decrease in area for both the Proximal and Distal regions in response to shear strain. Despite these differences in the change in area, surprisingly we observed no significant differences in the change in cell perimeter for any region (Figure 4.4c). A loss in area without a loss in perimeter indicates that the cells may have become more irregular with lower circularity or solidity. Our results suggest this shape change is true. We also observed that despite a slight increase in circularity in the no shear strain control, shear strain influenced cells in all regions of the epithelium to maintain their starting circularity (Figure 4.4d). We observed this trend across all regions of the epithelium, though the difference in circularity change was largest in the Proximal region, where shear strain even caused a slight decrease. In other shape descriptors including aspect ratio and cell shape index, we found that shear strain caused significant changes. The aspect ratio decreased in all conditions over time, yet decreased more in the no strain control (Figure 4.4e). These results match our temporal trends previously showed, where the slope is steeper in aspect ratio over time (Figure 4.3f) for the no strain control compared to the aspect ratio in the boundary shear strain experiment (Figure 4.3g). Lastly, we measured the average change

in the cell shape index, q (Figure 4.4f). In the no shear strain control, the q value decreased as expected indicating a solidification of the tissue. However, the q value did not lower as much in the sheared epithelium. Shear did not cause a fluidification of the tissue, however, our results indicated that shear prevented the solidification of the tissue.

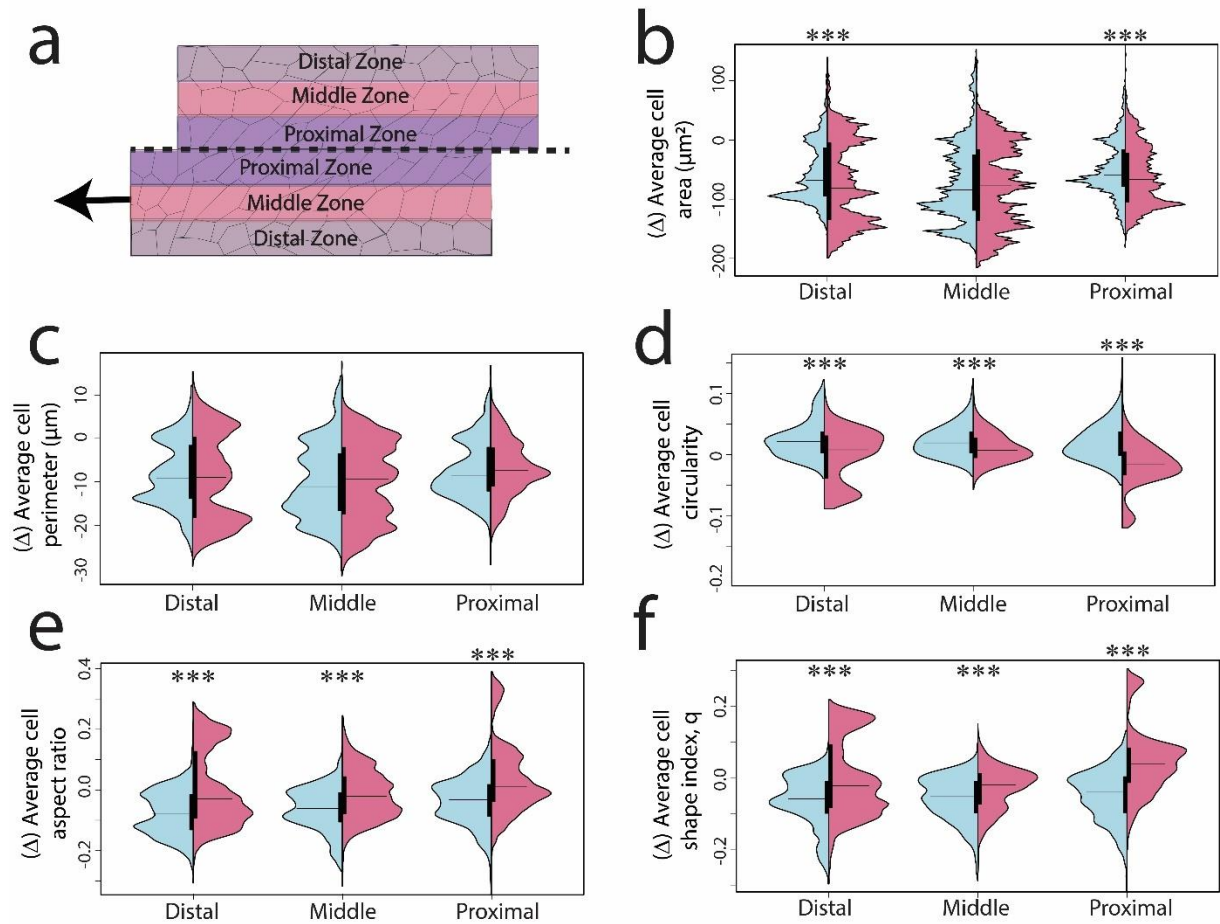


Figure 4.4. Long-term implications of boundary shear strain on epithelial cell shape.

(a) Schematic of epithelium with a boundary shear strain, divided by regions of increasing distance from the applied shear strain (Proximal, Middle, Distal). We compared the changes in several shape descriptors for each region in response to a boundary shear strain, including change in (b) area, (c) perimeter, (d) circularity, (e) aspect ratio, and (f) cell shape index, q . q is defined as $\left(\frac{Perimeter}{\sqrt{Area}}\right)$. Values were averaged at the onset of shear (0 hours to 23 hours). Solid lines in violin plots represent the mean while solid black bars represent the 25% and 75% quartiles. P values are denoted by * $p < .0001$, ** $p < .00001$, *** $p < .000001$.

4.5.C. Boundary shear strain does not regulate proliferative capacity of the epithelium

Previous studies have demonstrated that cell division rate scales with cell size³². For example, increased cell division causes a faster reduction in cell areas for subsequent daughter cell generation. Therefore, we assumed that the change in cell area over time could be used as a proxy for the rate of cell division. To determine the effect of boundary shear strain on the proliferative capacity of the epithelium, we averaged the cell areas across all regions over time. In the shear strained epithelium and no shear strain control, the cell area exhibited a one-phase viscoelastic decay over time while on the device. Interestingly, we found that the decay constant was nearly identical (no shear strain control: 7.8 hr, with boundary shear strain: 7.9 hr) for area change in both conditions (Figure 4.5). Our results suggest that the epithelium does not use proliferation as its main mechanism to regulate mechanical boundary perturbation.

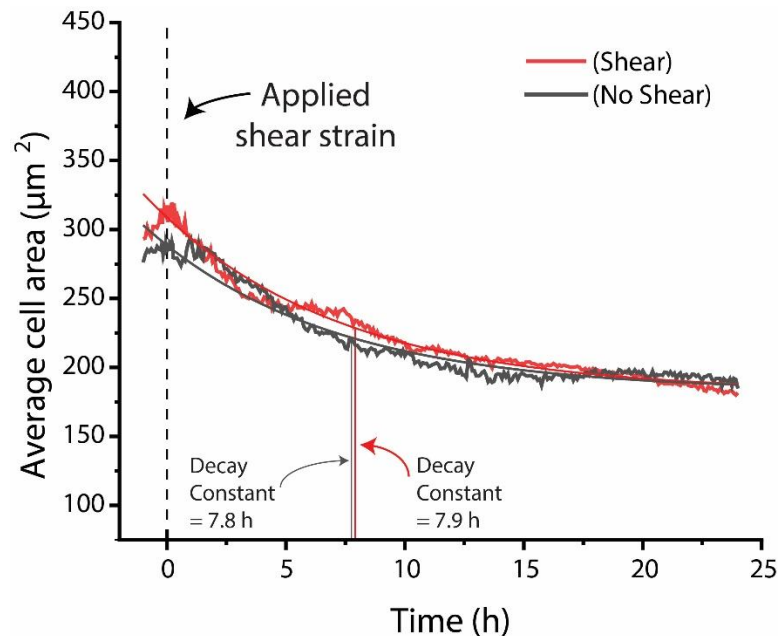


Figure 4.5. Boundary shear strain does not drive changes in proliferative capacity of epithelium.

Cell areas were averaged across all regions and plotted over time for both the no shear strain control (gray) and the shear strained epithelium (red). Data was fitted with a one-phase exponential decay model to extract time constants. Dashed line at Time=0 h indicates shear application.

4.5.D. Actomyosin regulates active cell shape response to boundary shear strain

As the previous researchers had found, blebbistatin produced no observable changes in cell migration after the application of shear. This finding has led to the conclusion that the migration response of the epithelium is regulated by actomyosin, since blebbistatin inhibits myosin II.

By isolating the Proximal region closest to the boundary shear strain (Figure 4.6a), we can distinguish how the applied strain alters cell shape from the active actomyosin generated shape changes. The shear strain has no distinguishable effect on average cell area, though seems to elongate cells as indicated by a brief increase in aspect ratio and shape index. Since these changes in aspect ratio and shape index occur without blebbistatin as well, they indicate that the short-term morphological changes in the proximal region are directly caused by shear application rather than an actively generated cell response. The strain exerted on cells within the Proximal region did not affect cells in the Middle region (Figure 4.6b). Due to actomyosin inhibition, cells had very little shape change in response to shear. The cells became more fluid-like over time, as indicated by an increase in area, aspect ratio, and cell shape index. In the Distal region, cell shape matched the same temporal trends as in the Middle region (Figure 4.6c).

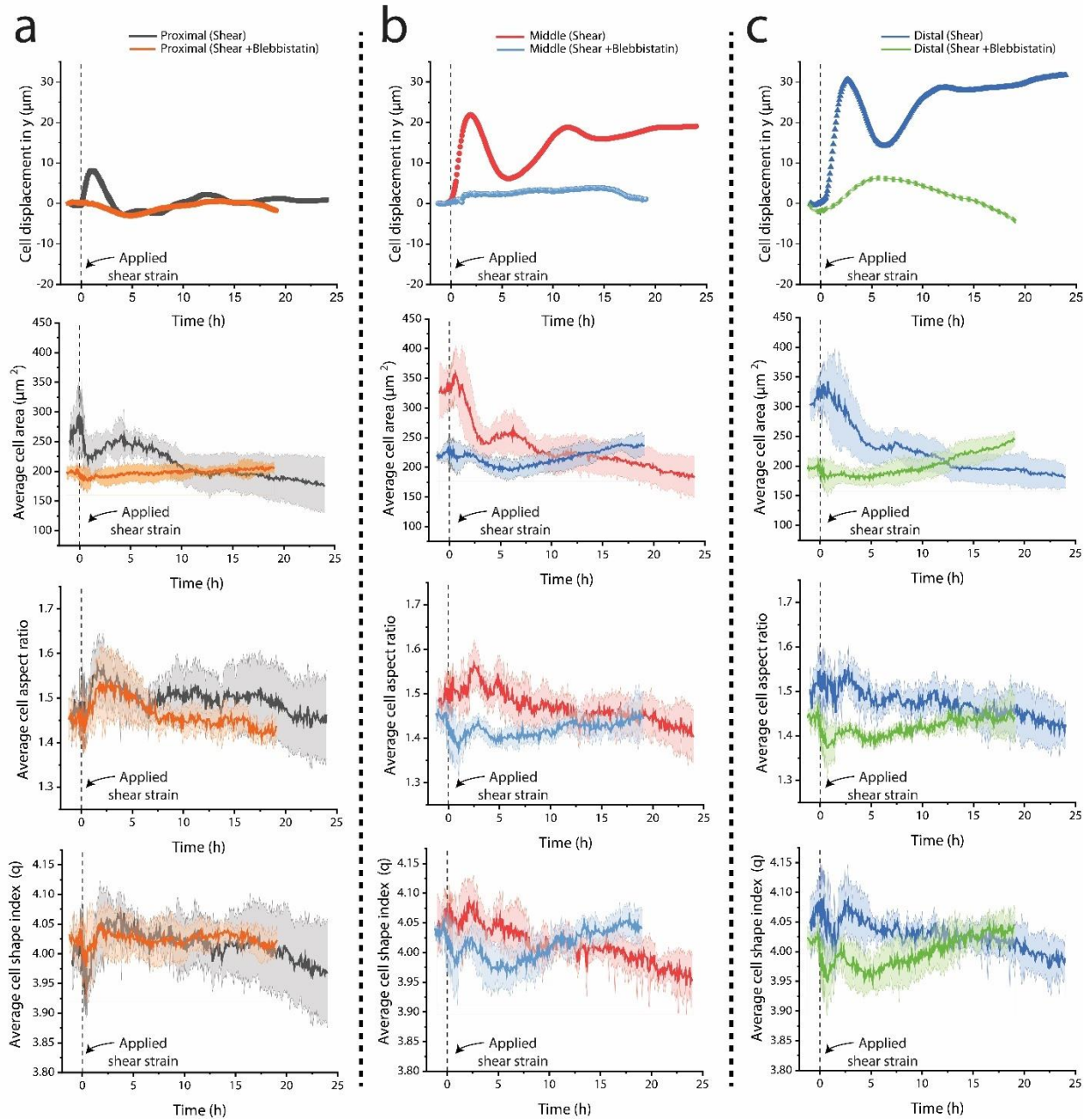


Figure 4.6. Inhibition of actomyosin isolates passive deformations of boundary shear strain on shape change.

(a) The Proximal, (b) Middle, and (c) Distal regions of the device were isolated and we measured cell shape change in response to actomyosin inhibition via blebbistatin. 50 μM blebbistatin was added 15 minutes prior to shear application (Time=0) and washed out 15 minutes after shear (T=0.25). Blebbistatin experiments were only imaged for 20 hours compared to the 24 hour no-blebbistatin experiments. Shaded regions represent the +/- 95% Confidence Intervals.

4.5.E. F-actin stabilization elasticizes collective properties of the epithelium

Since actin polymerization is critical to dysregulating and maintaining cell shape, we investigated how stabilizing actin polymerization regulated cell shape change in response to boundary shear strain.

As shown previously, jasplakinolide, which inhibits actin depolymerization, perpetuates the migratory oscillations caused by mechanical shear²⁹ (Figure 4.7 top). These migratory oscillations occur on a similar timescale, yet don't equilibrate over time due to the stabilization of F-actin. These results point towards F-actin as a sort of elastic rubber band, allowing back-and-forth cell motion without the dissipation of energy. However, it is unclear whether this lack of energy dissipation is perpetuated by cell shape or if it occurs independently. In the Proximal region immediately after shear application, there is no observable difference in cell displacement, cell area, cell aspect ratio, nor cell shape index. However, jasplakinolide has a larger impact on cell shape on a longer timescale (i.e., >3 hours). When actin is stabilized, we observed oscillatory effects of cell shape over time for all shape descriptors in parallel with migratory oscillations. These shape oscillations occur with a period of approximately 5-8 hours, which matches the periodicity of migration. While we don't observe this effect in the Middle region (Figure 4.7b), it is apparent again in the Distal region occurring on a delayed time-scale from the Proximal region (Figure 4.7c).

While we don't see a difference in the magnitude of cell shape descriptors with the stabilization of F-actin, we do observe a time delay. For example, cells Middle and Distal regions of the undrugged strained epithelia contract their area after boundary shear strain. When F-actin is stabilized via jasplakinolide, a contraction of similar magnitude occurs but delayed on a scale of 1-2 hours. We observe this same delay for cell migration.

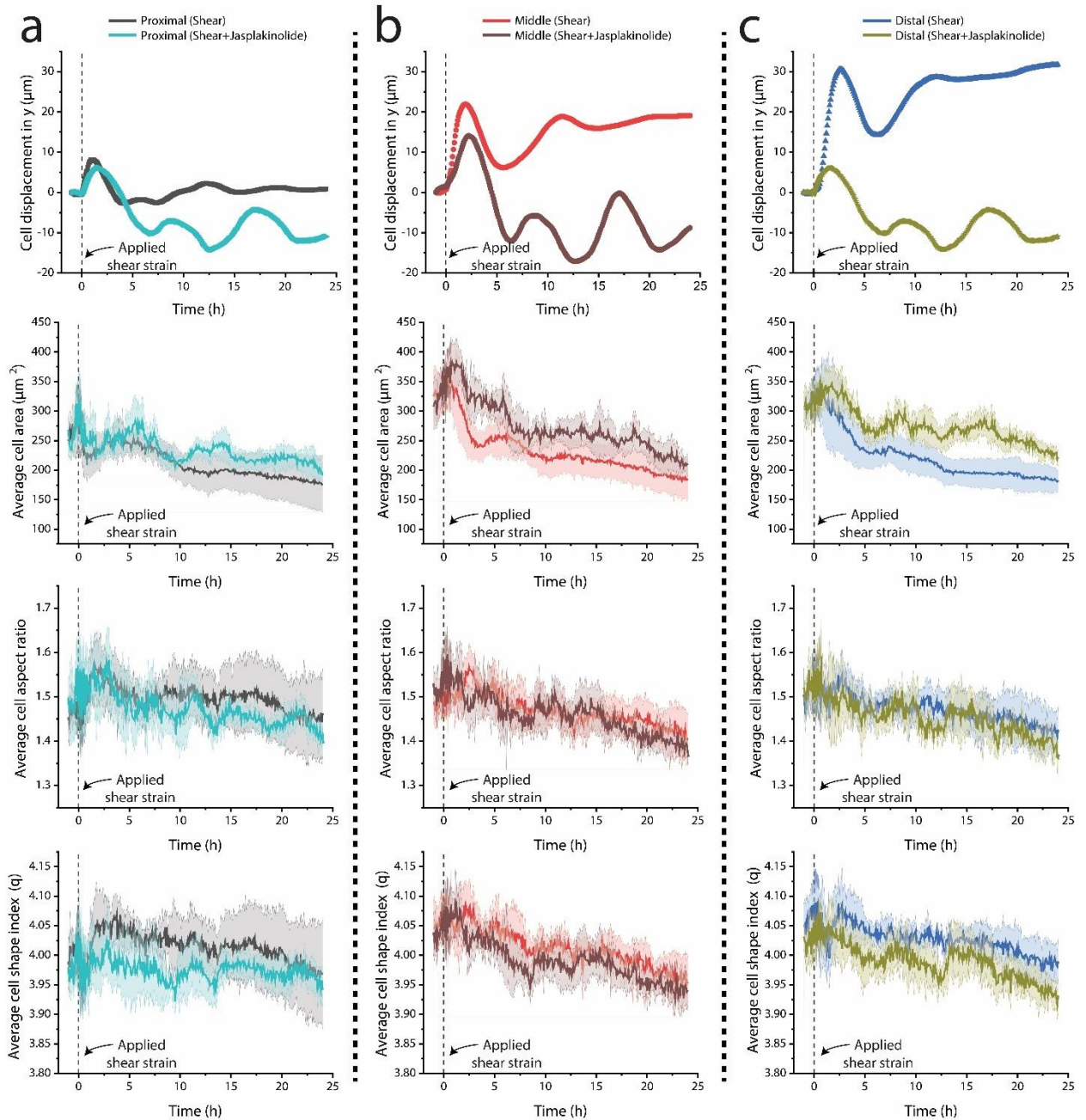


Figure 4.7. Actin polymerization drives changing morphology in response to epithelial shear.

(a) The Proximal, (b) Middle, and (c) Distal regions of the device were isolated and we measured cell shape change in response to F-actin stabilization via jasplakinolide. 200 nM Jasplakinolide was added 15 minutes prior to shear application (Time=0) and washed out 15 minutes after shear (T=0.25). Shaded regions represent the +/- 95% Confidence Intervals.

4.6. Discussion and ongoing work

In this work we have quantified changes in cell shape for the epithelium in response to boundary shear strain. Our approach integrated novel, high-throughput, and automated cell segmentation techniques to spatiotemporally map changes in collective behaviors of the epithelium. This analysis yields several main findings: i) Cells near the region of boundary shear strain experience a short-term reduction in area and decrease in shape index, which is not regulated by actomyosin, ii) boundary shear strain does not regulate the collective proliferative capacity of the epithelium over long time-scales, iii) boundary shear strain significantly impacts changes in cell circularity, aspect ratio, and cell shape index, and iv) cell shape changes outside of the Proximal region are stabilized by F-actin.

4.6.A. Effect of shear strain on the epithelium

Taken together, our results point towards a biophysical model where boundary shear strain inhibits the solidification of the epithelial tissue. To explain this conclusion, we first assume that cell solidity (and fluidity) is a function of several shape descriptors including area, aspect ratio, circularity, and shape index. In the no strain control, we observed decreased cell area, decreased aspect ratio, increased circularity, and decreased shape index. All these changes in shape descriptors are correlated with tissue solidification. In the epithelium with boundary shear strain, we observed a decrease in area, though changes in the other shape descriptors were either less significant or reversed.

Furthermore, we suggest that the reversal from solid to fluid temporally matches the regulation of cell migration in the epithelial tissue. For example, cells initially migrate towards the Proximal region in the first 2-3 hours. Around this same time, we observed a temporary solidification of the tissue in the Proximal region (as quantified by a decrease in

cell shape index and contraction of area). As the cells migrated back towards the Distal region, the tissue increased in fluidity across all regions.

4.6.B. Regulation of actomyosin dynamics via perturbation with blebbistatin and jasplakinolide

Experiments with blebbistatin demonstrated that the initial shape changes of cells were passively brought on by shear strain in the Proximal region. More interestingly, stabilization of F-actin via jasplakinolide demonstrated that shape oscillations matched the periodicity of cell migration. Taken together, these results point towards shape deformation as a regulator for migratory oscillations. In fact, the delayed shape changes we observed in jasplakinolide treated cells match the delayed (and slowed) migratory response of jasplakinolide cells²⁹

4.6.C. Current work

Currently, my lab member Sam Feinstein is continuing to explore the Cellpose generated ROIs in his lab rotation with cell shape expert, Professor Nina Miolane. Using her cell shape python package, he is helping build a predictive model between cell shape, the application of local shear, and cell migration within the epithelium. Furthermore, we will combine our efforts with Toshi Parmar and Professor Cristina Marchetti by constructing a phase-field model of the system. We intend to submit our work in the fall of 2023 for peer review.

Toshi Parmar and Cristina Marchetti are working towards a predictive model to better explain the relationship between shape change and migratory behavior. This work includes the development of a phase-field model, which will allow us to modulate the initial shape

change (e.g., contractility) in the Proximal region and investigate its impact on downstream collective migration. These experiments may also help explain the short-term solidification and long-term fluidification of the epithelium in response to boundary shear strain.

4.7. Methods

4.7.A. Image generation

The data we worked with in this study was performed by data mining previous experiments conducted in the lab and published on previously²⁹. In those experiments, the authors performed 3 separate experiments per several conditions (boundary shear strain, no boundary shear strain, boundary shear strain with blebbistatin, and boundary shear strain with jasplakinolide). Each biological experiment contained two technical replicates, providing an n of 6 for each condition (aside for blebbistatin, which only had 2 separate experiments) (Supplementary Figure 4.S1.).

Texas Red filtered images were isolated from each experiment to visualize the dsRed E-cadherin labeled MDCK cells. All images were then cropped (using a custom ImageJ macro) into 6 equal regions corresponding to the Proximal region, Middle region, and Distal region for both the top plank and bottom plank of the device. Each cropped image was approximately 1150x138 px with 10% overlap in the y direction between each image.

4.7.B. Segmentation Analysis

Segmentation was performed using the command line interface of Cellpose version 1.0³⁰. We used the “cyto” model with the additional command “exclude_on_edges”. Cellpose segmentation accurately identified the boundaries of approximately 80% of cells per image, though this accuracy was highly dependent on the image quality. Cellpose then exported png

masks of the ROIs from the segmented image, which we relabeled using a custom Python script (see Appendix “Segmentation analysis and segmentation scripts”). We then extracted ROI shape descriptors using the open-source ImageJ plugin, Labels to ROI³³. Labels to ROI generated several output files for each image, including a CSV file with all shape information and the ROIs overlaid on the original image. To organize all the files within each experiment for downstream analysis, we utilized a custom Python organizational script (see Appendix “Segmentation analysis and segmentation scripts”). Lastly, we filtered out ROIs below or above an area of 1 px or 1000 px, respectively, before averaging and further analyzing the data.

4.7.C. Particle Image Velocimetry

The same images generated for segmentation analysis were also used for PIV analysis. The resulting images of each section over the entire duration of the experiment were compiled into stacks via ImageJ. Sectioned images ranged from 1150 to 1200 pixels in length and 138 pixels in width. PIV analysis from the original experimental worked demonstrated collective movements of cells.

After clearly being compiled, the stacks for each plank segment were reverted as a sequence of images and uploaded into MATLAB PIVlab version 2.56. The images were sequenced using the time resolved style ([A+B], [B+C], [C+D], ...). Analysis of the images constituted utilizing Fast Fourier Transform (FFT) window deformation PIV algorithm with a sub-pixel displacement estimation of Gauss 2×3 point. The interrogation sizes for the window deformation included a first pass size of 64 pixels with a step of 32 pixels and a second pass size of 32 pixels with a step of 16 pixels. The data was filtered using vector validation with interpolation setting the standard deviation filter threshold to 4 and the local

median threshold to 5. The filtered velocity data along the y-axis was then exported as a MATLAB file to be used to determine displacement. The MATLAB file averaged the velocities of all the cells on one section of the planks at one point in time and used the averaged velocity to determine the displacement using 0.652 as the micrometer to pixel ratio.

4.7.D. Statistical analysis

Statistical Analysis was performed using the R statistical programming language³⁴ and the RStudio IDE³⁵. Linear regression was used to model the effect of shear on the physical parameters of displacement, area, aspect ratio, circularity, perimeter, and structural order (q). To avoid false positives the conservative Bonferroni correction was applied to adjust significance to p -value < 0.0001 . Significant p -values with $p < 0.0001$ were designated with (*), $p < 0.00001$ were designated with (**), and $p < 0.000001$ were designated with (***). Dichotomous variables (non-shear = 0, shear = 1) were used to represent shear to ensure linearity. Normality of residuals was confirmed via QQ plot. The “caret” package was used to perform ten-fold cross-validation with three replicates to confirm each regression and prevent overfitting³⁶. The “vioplot” package was used to create the split violin plots³⁷.

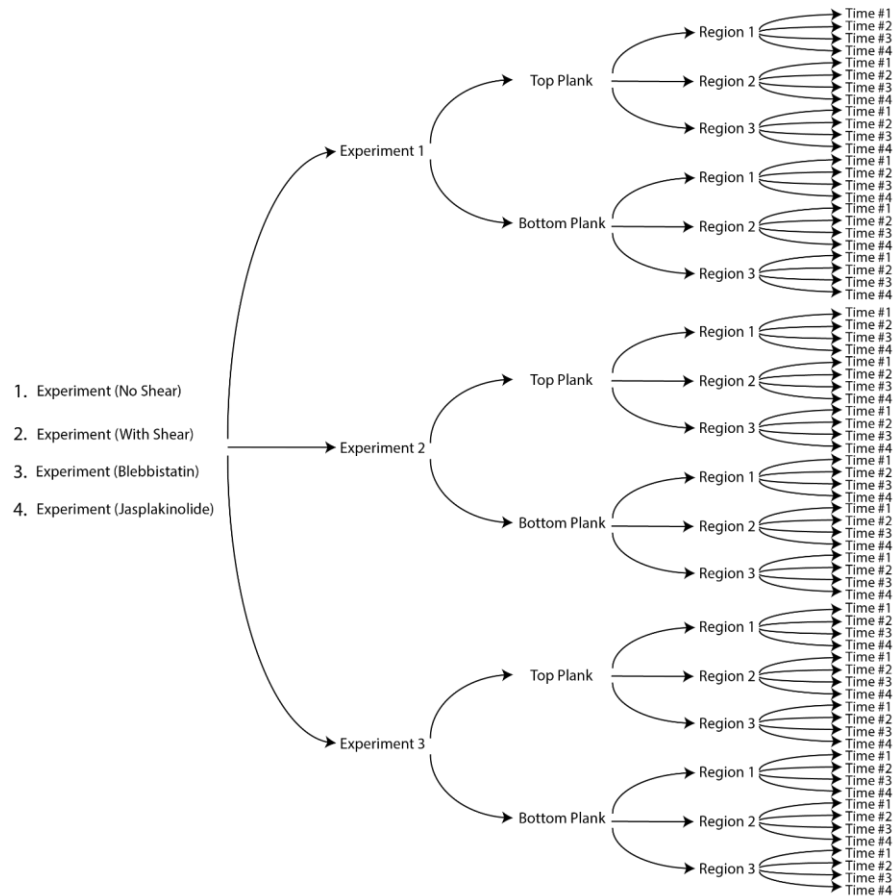
4.8. References

1. Needleman, D. & Dogic, Z. Active matter at the interface between materials science and cell biology. *Nature Reviews Materials* vol. 2 1–14 (2017).
2. Henkes, S., Kostanjevec, K., Collinson, J. M., Sknepnek, R. & Bertin, E. Dense active matter model of motion patterns in confluent cell monolayers. *Nat. Commun.* 2020 111 **11**, 1–9 (2020).
3. Bernheim-Groswasser, A. *et al.* Living Matter: Mesoscopic Active Materials. *Adv. Mater.* **30**, 1707028 (2018).
4. Marchetti, M. C. *et al.* Hydrodynamics of soft active matter. *Rev. Mod. Phys.* **85**, 1143–1189 (2013).
5. Hannezo, E. & Heisenberg, C. P. Rigidity transitions in development and disease. *Trends Cell Biol.* **32**, 433–444 (2022).
6. Bi, D., Yang, X., Marchetti, M. C. & Manning, M. L. Motility-driven glass and jamming transitions in biological tissues. *Phys. Rev. X* **6**, 021011 (2016).

7. Mongera, A. *et al.* A fluid-to-solid jamming transition underlies vertebrate body axis elongation. *Nature* vol. 561 401–405 (Nature Publishing Group, 2018).
8. Ballard, S. T., Hunter, J. H. & Taylor, A. E. Regulation of Tight-Junction Permeability During Nutrient Absorption Across the Intestinal Epithelium. <https://doi.org/10.1146/annurev.nu.15.070195.000343> **15**, 35–55 (2003).
9. Guillot, C. & Lecuit, T. Mechanics of epithelial tissue homeostasis and morphogenesis. *Science* (80-.). **340**, 1185–1189 (2013).
10. Lecuit, T. Adhesion remodeling underlying tissue morphogenesis. *Trends Cell Biol.* **15**, 34–42 (2005).
11. Runswick, S. K., O’Hare, M. J., Jones, L., Streuli, C. H. & Garrod, D. R. Desmosomal adhesion regulates epithelial morphogenesis and cell positioning. *Nat. Cell Biol.* 2001 **39** **3**, 823–830 (2001).
12. Chen, T., Saw, T. B., René-, R.-, Mè Ge, M. & Ladoux, B. Mechanical forces in cell monolayers. (2018) doi:10.1242/jcs.218156.
13. Goodwin, K. & Nelson, C. M. Mechanics of Development. *Dev. Cell* **56**, 240–250 (2021).
14. Gayer, C. P. & Basson, M. D. *The effects of mechanical forces on intestinal physiology and pathology.* *Cellular Signalling* vol. 21 1237–1244 (Pergamon, 2009).
15. Wang, S., Matsumoto, K., Lish, S. R., Cartagena-Rivera, A. X. & Yamada, K. M. Budding epithelial morphogenesis driven by cell-matrix versus cell-cell adhesion. *Cell* **184**, 3702–3716.e30 (2021).
16. Alberts, B. *et al.* Integrins. (2002).
17. Borradori, L. & Sonnenberg, A. Structure and Function of Hemidesmosomes: More Than Simple Adhesion Complexes. *J. Invest. Dermatol.* **112**, 411–418 (1999).
18. de Rooij, J., Kerstens, A., Danuser, G., Schwartz, M. A. & Waterman-Storer, C. M. Integrin-dependent actomyosin contraction regulates epithelial cell scattering. *J. Cell Biol.* **171**, 153–164 (2005).
19. Yeung, T. *et al.* Effects of substrate stiffness on cell morphology, cytoskeletal structure, and adhesion. *Cell Motil. Cytoskeleton* **60**, 24–34 (2005).
20. Hartsock, A. & Nelson, W. J. Adherens and tight junctions: structure, function and connections to the actin cytoskeleton. *Biochim. Biophys. Acta* **1778**, 660–669 (2008).
21. Farhadifar, R., Röper, J. C., Aigouy, B., Eaton, S. & Jülicher, F. The Influence of Cell Mechanics, Cell-Cell Interactions, and Proliferation on Epithelial Packing. *Curr. Biol.* **17**, 2095–2104 (2007).
22. Mueller, R., Yeomans, J. M. & Doostmohammadi, A. Emergence of Active Nematic Behavior in Monolayers of Isotropic Cells. *Phys. Rev. Lett.* **122**, 048004 (2019).
23. Banavar, S. P. *et al.* Mechanical control of tissue shape and morphogenetic flows during vertebrate body axis elongation. *Sci. Rep.* **11**, 8591 (2021).
24. Cohen, D. J., Nelson, W. J. & Maharbiz, M. M. Galvanotactic control of collective cell migration in epithelial monolayers. *Nat. Mater.* **13**, 409–417 (2014).
25. Stroka, K. M. *et al.* Loss of giant obscurins alters breast epithelial cell mechanosensing of matrix stiffness. *Oncotarget* **8**, 54004 (2017).
26. Nishimura, T., Honda, H. & Takeichi, M. Planar cell polarity links axes of spatial dynamics in neural-tube closure. *Cell* **149**, 1084–1097 (2012).
27. Martin, A. C., Kaschube, M. & Wieschaus, E. F. Pulsed contractions of an actin-myosin network drive apical constriction. *Nature* **457**, 495–499 (2009).
28. Tetley, R. J. & Mao, Y. The same but different: cell intercalation as a driver of tissue deformation and fluidity. *Philos. Trans. R. Soc. B Biol. Sci.* **373**, (2018).
29. Sadeghipour, E., Garcia, M. A., Nelson, W. J. & Pruitt, B. L. Shear-induced damped oscillations in an epithelium depend on actomyosin contraction and E-cadherin cell adhesion. *Elife* **7**, 1–16 (2018).
30. Stringer, C., Wang, T., Michaelos, M. & Pachitariu, M. Cellpose: a generalist algorithm for

- cellular segmentation. *Nat. Methods* 2020 181 **18**, 100–106 (2020).
31. Devany, J., Sussman, D. M., Yamamoto, T., Manning, M. L. & Gardel, M. L. Cell cycle-dependent active stress drives epithelia remodeling. *Proc. Natl. Acad. Sci. U. S. A.* **118**, e1917853118 (2021).
 32. Puliafito, A., Primo, L. & Celani, A. Cell-size distribution in epithelial tissue formation and homeostasis. *J. R. Soc. Interface* **14**, (2017).
 33. Waisman, A., Norris, A. M., Elías Costa, M. & Kopinke, D. Automatic and unbiased segmentation and quantification of myofibers in skeletal muscle. *Sci. Reports* 2021 111 **11**, 1–14 (2021).
 34. Ihaka, R. & Gentleman, R. R: A Language for Data Analysis and Graphics. *J. Comput. Graph. Stat.* **5**, 299 (1996).
 35. RACINE, J. S. RSTUDIO: A PLATFORM-INDEPENDENT IDE FOR R AND SWEAVE. *J. Appl. Econom.* **27**, 167–172 (2012).
 36. Kuhn, M. Building Predictive Models in R Using the caret Package. *J. Stat. Softw.* **28**, 1–26 (2008).
 37. Adler, D., Kelly, S. T., Elliot, T. & Adamson, J. vioplot: violin plot. *Github* <https://github.com/TomKellyGenetics/vioplot> (2022).

4.9. Supplementary Information



Supplementary Figure 4.S1. Tree diagram of images generated for segmentation analysis. From left to right: From four separate experimental conditions, the researchers performed 3 independent experiments from each. Each experiment contained technical replicates via the top/bottom symmetry of the device. Each replicate was then cropped into 3 separate regions (Proximal, Middle, Distal), which contained ~4 sets of time-series images from the experiment.

Chapter 5

Boundary strain of a 1-D epithelium

5.1. Preface

In this chapter I present a study that utilizes a 1-D epithelial “train” model to understand local strain on epithelial migratory behavior. The study combines both experimental work (Pruitt Lab) and theoretical work (Marchetti Lab). Only my experimental work is included in this thesis.

I conceived the original idea for this project while preparing for my candidacy exam in the summer of 2020. The main topic of my candidacy proposal was the role of local strain in regulating epithelial migration. During my literature review, I found an interesting gap in the field stuck between conflicting models of how intercellular force regulated cell migration. One series of studies indicated that intercellular force promoted migration *towards* the applied strain. These models were predominately from biological studies and aligned with leader-follower cell behavior. The other series of models indicated that intercellular force promoted migration in the direction *opposite* of the applied strain. These models were predominantly biophysical. One study in particular caught my attention (Weber et al, *Developmental Cell*, 2012). The researchers used a cadherin-coated magnetic bead to pull on a mesendoderm cell, which subsequently polarized (and migrated) in the opposite direction. However, a large limitation of the study was that their pulling experiments were confined to a single cell. During my candidacy exam, I proposed a similar experiment where instead of pulling on a single cell, the bead could pull on a train of cells within a confined 1-D track. I originally never intended to pursue this experiment, but the COVID-19 pandemic derailed my original candidacy proposal (I was supposed to train in the cleanroom for device

microfabrication). My expertise in ECM protein patterning, epithelial migration analysis, and micromanipulation allowed me to independently pursue the development of the 1-D model.

Initially I began poking cell clusters with tungsten needles and pulling on their cell-cell junctions. This technique evolved into letting cells stick to ECM coated glass micropipettes to avoid cell death. To improve cell adhesion, Dr. Pruitt recommended attaching a bead to the micropipettes. After around 6 months, I had developed an experimental setup that allowed me to create a confined 1-D epithelial train and adhere the outer end to an ECM coated bead. The bead was fixed to a micropipette on a piezo controlled micromanipulator, allowing me to exert a local mechanical strain on the system. At the time, I mentored an undergraduate researcher, Reagan Kennedy, to quantify the migration after applied strain.

After several experiments, I submitted a paper for this study to the 2021 annual microTAS meeting, which was peer reviewed and accepted for an oral presentation (presented in October 2021).

Most recently, we have collaborated with Toshi Parmar and Dr. Marchetti to understand this behavior in a predictive model. This collaboration has resulted in a fruitful study capitalizing on an innovative model in the field, which we plan to submit for peer review.

5.2. Abstract

The organization of developing embryos and tissues is dependent on the coordinated collective migration of epithelial cells. Therefore, it is imperative that we understand the environmental and cellular mechanisms that drive collective cell movements within developing tissues. Developing tissues are constantly being locally stretched, constricted, and

folded, which impose local (i.e., boundary) mechanical strains on groups of cells. However, it is not well understood how boundary perturbations within epithelia propagate forces and influence collective cell behavior. This knowledge gap exists in part due to the limitation of experimental models capable of applying boundary strains to an epithelium. Single cell epithelial studies lack the force transduction mechanisms of cell-cell contacts, while in 2-D epithelial sheets information about directional epithelial movements can be lost to both the x and y directions. Therefore, we have innovated a 1-D epithelial model with a boundary strain micromanipulation system. We then modeled our system *in silico* as a chain of cells continuum model. Our results suggest that boundary step strain directs collective cell movements towards the applied strain. We also demonstrated that the 1-D epithelium oscillates with wave-like behavior in a length-dependent manner, which allows us to understand the impact of boundary strains on the epithelium over long timescales. Lastly, we demonstrate that collective migration of a 1-D epithelium is dependent on orientation of cell-cell contacts under strain as well as throughout the epithelium

5.3. Introduction

The collective movements of epithelial cells are integral to epithelia development and repair. A key property of their collective movements is their directed motion; clusters of cells migrate with a specific purpose. During *Drosophila* oogenesis, Border Cell clusters travel from the anterior tip of the *Drosophila* egg chamber to the edge of the oocyte¹. During wound healing, epithelial cells move towards the open gap to fill and mend the wound^{2,3}.

There are several components of the epithelial microenvironment that can influence the directed motion of epithelial cells: directional fluid flow⁴, chemical gradients (chemotaxis)⁵, bio-interface cues (haptotaxis)⁶, substrate stiffness (durotaxis)⁷, and even

electrical cues (galvanotaxis)⁸. However, recent studies have indicated a role for mechanical strains between cells in regulating collective epithelia behavior⁹⁻¹²

The epithelium is a dynamic environment subjected to various mechanical deformations (e.g., folding, constricting, and bending). These mechanical deformations tug on interconnected epithelial cells, subjecting their cell-cell contacts to mechanical forces. Cell-cell junctions within these contacts such as desmosomes and adherens junctions are known to be mechanosensitive, influencing behaviors such as proliferation and extrusion^{13,14}. The mechanosensitivity of cell-cell junctions in directing cell migration is less clear.

Researchers have attempted to understand the influence of local mechanical cues on collective epithelial behavior by employing micromanipulation techniques. Some of these methods include microfabricated silicon chips that exert a local shear strain on a 2-D epithelium¹⁰, "trenches" in polyacrylamide hydrogels that can be locally strained under an epithelium¹⁵. Other approaches involve straining single cells with magnetic beads or needles^{16,17}. Despite these advances, it is difficult to capture the directionality components of 2-D systems since force vectors (as well as cell movements) can vary across both the x and y directions of a plane. On the other hand, single cell systems do not capture the complexity of cell-cell contacts.

Recently, 1-D models have gained traction as useful models to understand collective epithelial behavior¹⁸⁻²⁰. 1-D models capture the complexity of intercellular communication and force transfer between cell-cell contacts, yet reduce cell movements and force vectors to a single axis.

Our goal is to determine how intercellular force transfer via a localized strain on an epithelium alters collective cell motion. This goal requires a platform with high spatiotemporal control and must apply a local mechanical cue with a controlled rate.

In this work, we have developed a 1-D epithelial model that incorporates piezo-driven micromanipulation methods to apply physiologically relevant strains on cell-cell junctions. Using quantitative analytical tools, we measured how local strain directs the motion of the epithelium. These results reveal a unique role for intercellular strains in influencing native epithelial cell oscillations. Lastly, we teased out orientation of cell-cell contacts as regulators of force transmission and influences of collective cell behavior.

5.4. Results

5.4.A. Development of a 1-D micromanipulation model

We developed a confined 1-D epithelial model, coupled with micromanipulation techniques to apply a local strain to the multi-cellular system (Figure 5.1a). In our model system, we utilized light-induced molecular adsorption micropatterning (Primo, Alvéole) to create $20 \times 390 \mu\text{m}$ tracks of collagen I on glass (Figure 5.1b). The outer regions were made from a poly-l-lysine-grafted-polyethylene glycol (PLL-g-PEG) solution, preventing cell adhesion via steric hindrance. Madin-Darby Canine Kidney (MDCK) epithelial cells, which have well-characterized cell-cell junctions, were used as our model cell. Immediately after seeding cells on the patterns, they naturally spread out across the lines to form single file “trains” of cells (Fig 5.1c). Each line had approximately 10-20 cells. This system was short enough to investigate the effect of mechanical forces on an entire system, yet long enough to apply local strain on the outer 2-3 cells (Figure 5.1d).

To exert a local strain on end of the epithelial model, we developed a custom micromanipulation setup. We glued glass microbeads to angled pre-pulled glass pipette tips, then functionalized the probe tips with collagen I. The probes were mounted to a piezo-driven micromanipulator. Once the probe formed a stable adhesion to one end of the MDCK cell train, the micromanipulator pulled the probe 30 μm (approximately 1.5 cell lengths) laterally away from the cell line. By retaining adhesion to the bead, local cell junctions were subsequently strained at physiological rates as quantified using digital image correlation DIC) (Figure 5.1d)

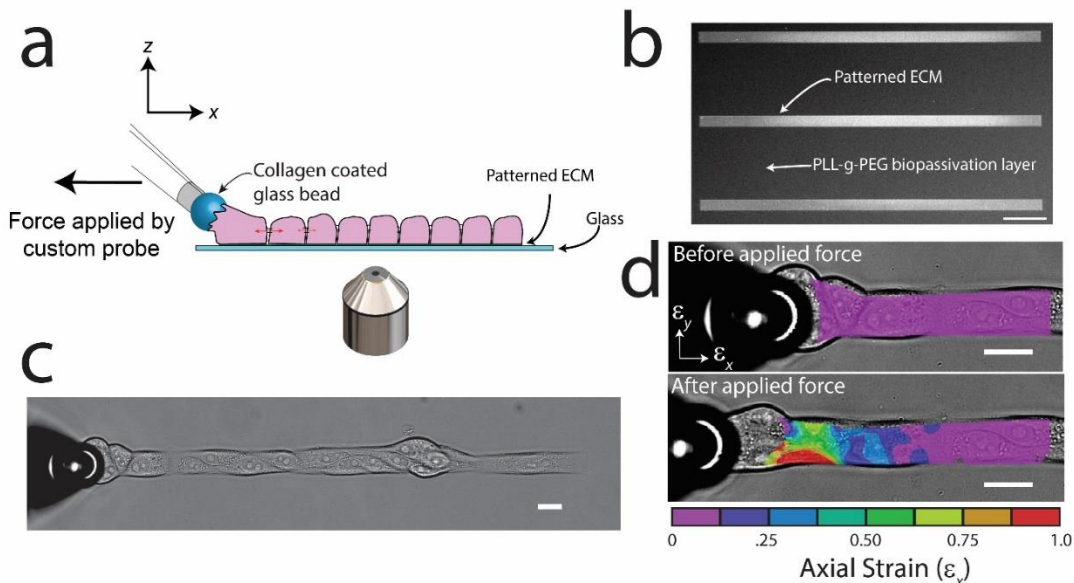


Figure 5.1. Micromanipulation of epithelial 1-D train model.

(a) Schematic of 1-D model for boundary force perturbation studies, compatible with high resolution fluorescence microscopy and traction force microscopy. (b) $390 \times 20 \mu\text{m}$ tracks for cells can be created in a high throughput manner using protein micropatterning, visualized using Oregon green gelatin. ECM lines constrain ~ 20 cells in a single file manner. (d) Following a $30 \mu\text{m}$ displacement at $1 \mu\text{m}/\text{sec}$, only the outer 2-3 cells were strained, allowing us to investigate the effects of the boundary forces on the un-strained collective. Scale bars are (b) $50 \mu\text{m}$ and (c,d) $20 \mu\text{m}$.

5.4.B. Boundary step strain promotes collective cell behavior

After the application of a local intercellular step strain to the epithelial system (time=0 hours), the strain was held and the entire train was imaged for the next 6 hours.

Some experiments were imaged for longer time periods to help inform *in silico* modeling experiments. We then employed particle image velocimetry (PIV) to quantify directional movement of the entire 390 μm long cell train to determine whether it had a migration preference following step strain. On average, we found that the entire train had an average collective cell displacement towards the applied strain (Figure 5.2a). In the 6 hours following step strain, the cluster moved a net approximately 23 μm . To determine whether this movement was an effect of the step strain or an effect of another variable in our system, we compared the cell movements before the step strain to after step strain as a function of time (Figure 5.2b). In the 4 hours prior to any strain on the system, the train had only moved approximately 3 μm . We observed the largest differences in cell movements on longer time scales (i.e., 4 hours of cell movement before strain vs after strain). These results indicate that local intercellular strain influences cell clusters to move towards the strain stimulus. However, in our hands it was not to the level of statistical significance. We saw significant variation among cell displacements (Figure 5.2b) from experiment to experiment, which can potentially be explained by fluidity of the system or inability of applied strain to overcome self-generated propulsion of the cell train.

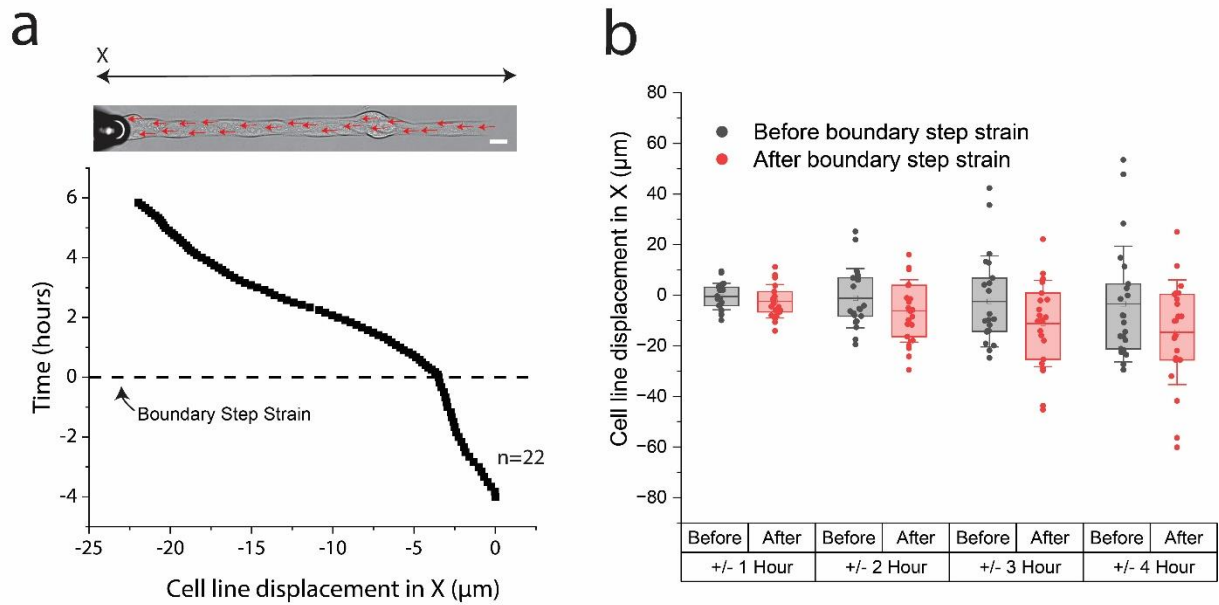


Figure 5.2. Boundary step strain on 1-D epithelium promotes collective migration.

(a) PIV results of the average collective migration of 1-D cell train along the X direction (n=22 separate experiments) before and after boundary step strain. (b) Over time, the difference in total cell line displacement separates with the largest difference occurring between 4 hour pre-strain and 4 hour post-strain. Scale bar is 20 μm .

5.4.C. Wave-like oscillations of a 1-D epithelium

To quantitatively explain the response to local step strain, we investigated the steady state conditions of an unperturbed epithelial collective moving on the ECM line of different length scales (390 μm and 200 μm). We observed collective oscillatory movements of the collective, which decreased in wavelength size with decrease line length. Periods for the 390 μm and 200 μm lines were 15.3 hours and 10.9 hours, respectively (Figure 5.3). These results and modelling are under investigation.

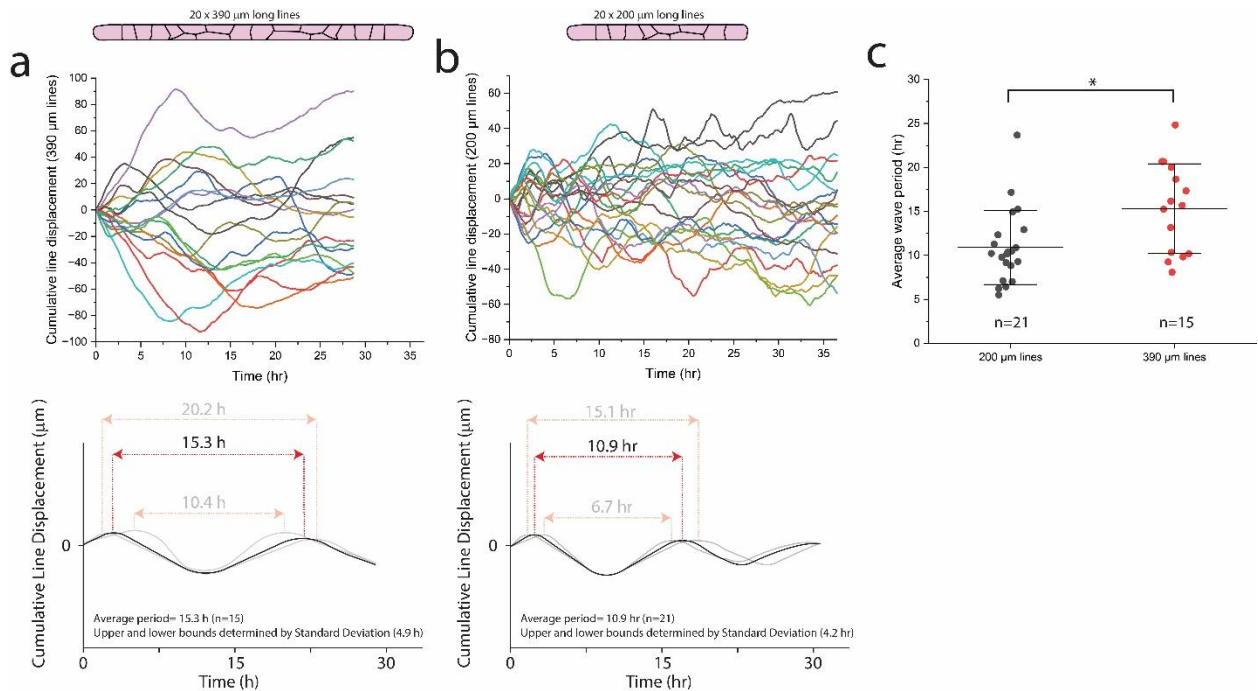


Figure 5.3. Oscillations of epithelium on lines.

Clusters of MDCK epithelial cells were seeded on (a) 20x390 μm lines or (b) 20x200 μm lines and migration quantified by PIV over 28-40 hours. (c) Periodicity of each oscillation was determined using a custom MATLAB script, which revealed a shorter wave period for the shorter, 200 μm lines. $n=21$ for the 200 μm lines on 1 biological replicate and $n=15$ for the 390 μm lines on 1 biological replicate.

5.4.D. Distinct responses of cell behavior based on cell-cell contact orientation under mechanical load

We then investigated whether orientation of cell-cell contacts under load influenced the subsequent collective behavior of the 1-D epithelium. Using a GFP label for E-cadherin, we measured the angles of strained cell-cell contacts in each experiment with respect to the normal pulling force of the bead. Contact angles (denoted by α) were either binned below 45° or above 45° , reminiscent of cell-cell contacts under shear or tension, respectively (Figure 5.4 a,b). Interestingly, we found that when the boundary strain was applied to cell-cell contacts under 45° (i.e., sheared), there was no observed change on the movement of the cell collective from 4 hours before boundary strain through the 6 hours after boundary strain

(Figure 5.4c). When the cell-cell contact under load was above 45° (i.e., tension), after approximately 30 minutes there was a large movement of the cell collective towards the boundary strain (Figure 4c). The 1-D epithelium collectively traveled $\sim 30 \mu\text{m}$ towards strained cell-cell contacts above 45° and only $\sim 3 \mu\text{m}$ towards strained cell-cell contacts below 45° (Figure 5.4d). In several experiments with a strong shear between cell-cell contacts, we also observed junction shortening and often rupture within the 6-hour observation period (Figure 5.4e).

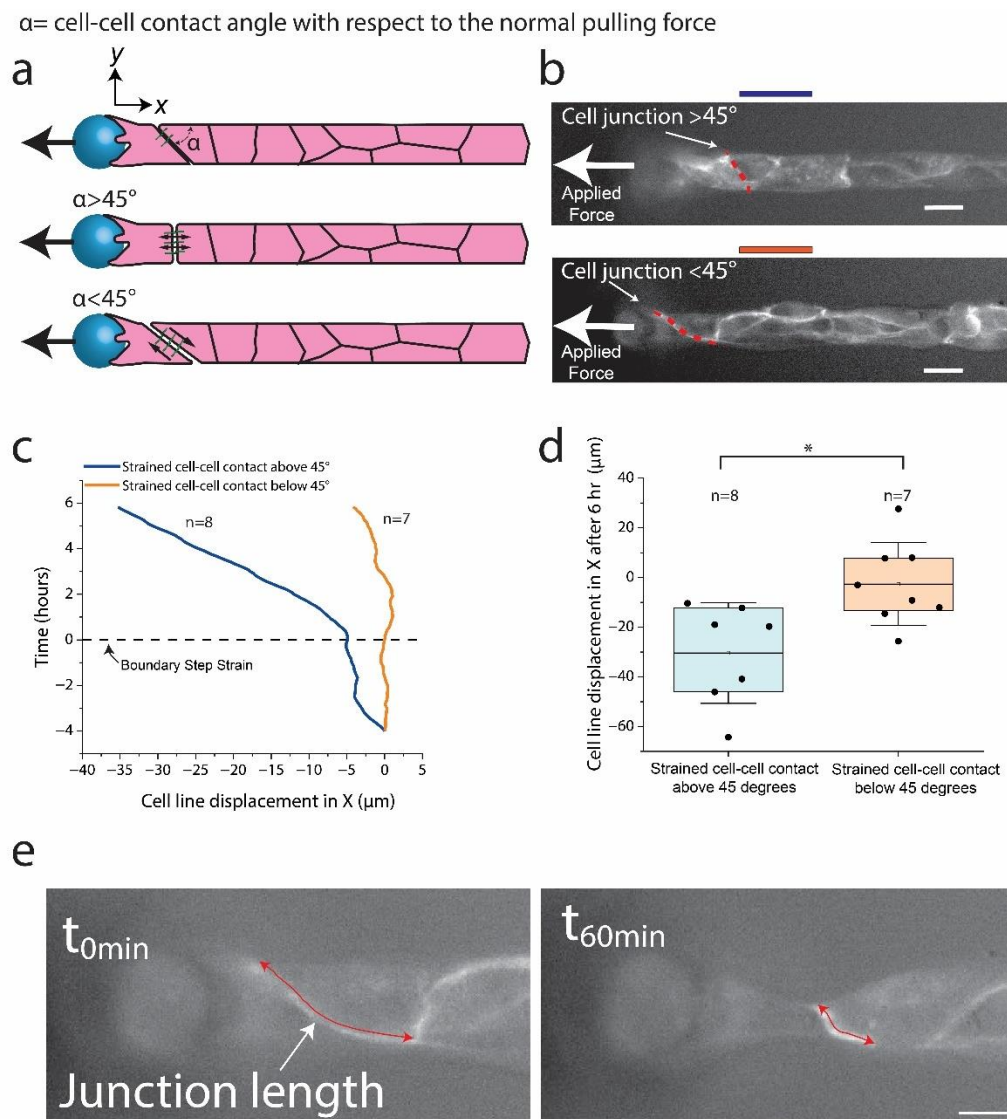


Figure 5.4. Distinct cell migration responses to either tension or shear.

(a) Experiments were binned as shear-dominated or tension-dominated using the angle, α , between the junction and line normal to the applied force. (b) E-cadherin GFP cells help visualize the junction angle under strain. (c) PIV results of the average collective migration of 1-D cell train along the X direction before and after boundary step strain on shear (n=7) and tension (n=8) dominated cell contacts. (c,d) We found that tension dominated cell-cell contacts under strain resulted in increased collective cell migration towards the boundary strain compared to shear dominated cell-cell contacts under strain. (e) In several experiments where cell-cell contacts under load experienced a low angle strain (i.e., shear), we observed a rapid junction constriction and subsequent rupture. Scale bars are (b) 20 μm and (e) 10 μm . (d) Box plots represent the 25 % and 75 % ranges, with bars representing SD. Mean is the center line.

5.4.E. Modulation of cell-cell contacts via ECM patterning alters collective migration

Now that we've introduced the behavior of confined cells, we asked if we could modulate its collective properties by changing the underlying geometry of the ECM. Previous work has demonstrated that different ECM geometries can be used to stabilize cell-cell contacts for cell pairs. For example, epithelial cell pairs patterned on "I" shape patterns maintain a stable cell-cell contact perpendicular to the vertical²¹. We expanded this design towards an epithelial cell train, which we term as "I beam tracks". The center vertical of the "I" we refer to as the "spine". We hypothesized that our modified I-beam line would stabilize the cell-cell contacts across the line, enhancing collective line behavior. We also developed other geometries of the ECM to modify cell-cell stabilization and collective behavior (Figure 4a). One design included the inverse geometry of the I-beams, which resemble railroad tracks. The goal of these patterns was to localize cell-cell contacts onto the railroad track crossties. While all the geometries varied with respect to their internal geometries, the outer geometries were conserved (20 x 390 μm). We also demonstrate that despite the modulation of ECM area, all trains formed continuous interconnected lines across each pattern.

After growing the same cells across each pattern, we imaged them over a 12-hour period and measured the average speed of each cellular collective (Figure 5.5b).

Interestingly, we found that cell lines grown on the I-beam tracks had a significantly lower collective speed (approximately 3 $\mu\text{m/hr}$ compared to cell lines grown on solid lines (approximately 5 $\mu\text{m/hr}$). The collective speed remained low even when we modified the width of the inner spine from 5 μm to 2 μm . Therefore, we attempted to inverse the pattern by creating railroad track patterns. The collective speed of cells on the railroad tracks (approximately 4.5 $\mu\text{m/hr}$, which closely matched the speed of the solid lines. We then angled the internal cross-ties of the pattern 45 degrees, yet this modification had no significant impact on the collective movement of the epithelial line.

We found that we disrupted collective cell behavior by controlling the orientation of cell-cell contacts in the I-beam. Cells preferred to align their contacts along the spine, as indicated by a higher percentage of nuclei stacked on one another (Figure 5.5c). Staining of cell-cell contacts also revealed the preferred orientation of cells. By re-orienting cells, we disrupted the collective properties of the 1-D epithelium.

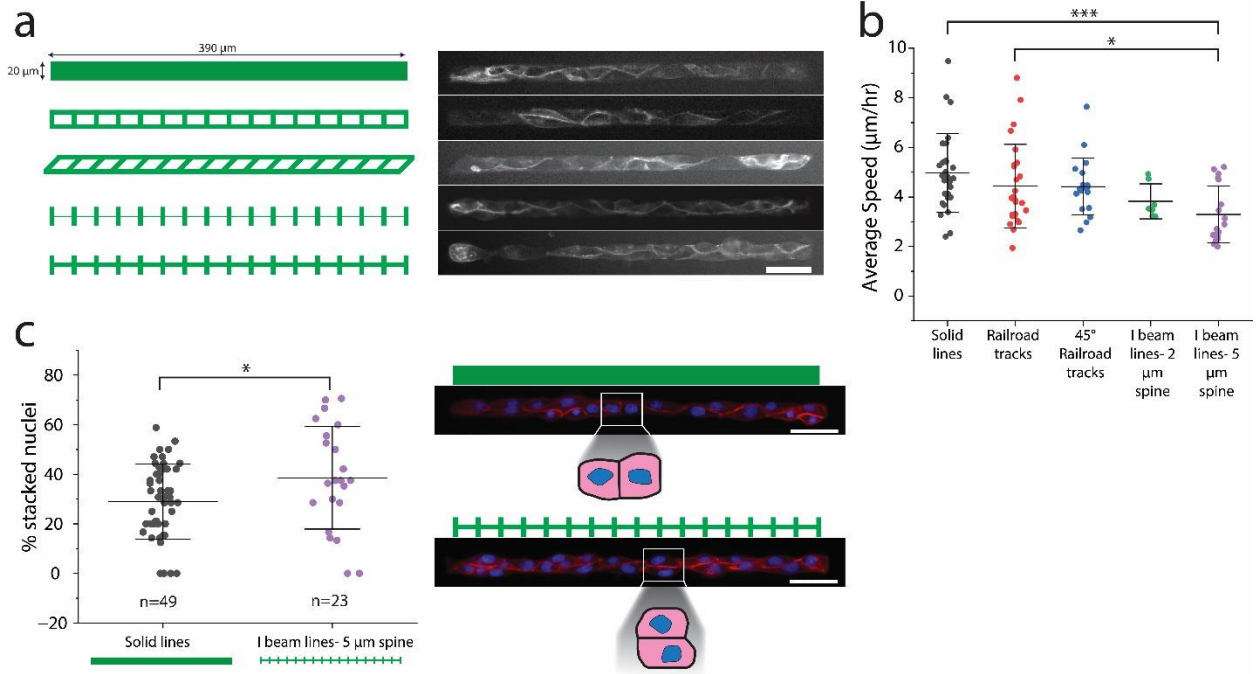


Figure 5.5. Underlying extracellular matrix organization regulates collective migration speed.

(a) (left) Schematics of different ECM patterns used to confine lines of cells, along with (right) representative images of E-cadherin GFP fluorescent images adjusted for contrast to help visualize continuous cell-cell contacts. (b) Average speed of cell collectives over 12 hours. (c) Dot plot quantifying the percentage of nuclei stacked on one another within cell lines. Scale bar is 50 μm . Replicates for b: Solid lines: $n=28$ across 2 biological replicates. Railroad tracks: $n=26$ across 2 biological replicates. 45° railroad tracks: $n=19$ across 3 biological replicates. I beam lines with 2 μm spine: $n=7$ across 1 biological replicate. I beam lines with 5 μm spine: $n=18$ across 2 biological replicates. For c: Solid lines: $n=49$ across 5 biological replicates, I beam lines with 5 μm spine: $n=23$ across 6 biological replicates. All error bars marked by \pm SD.

5.5. Methods and Materials

5.5.A. Particle Image Velocimetry

Raw brightfield images from before and after boundary strain were cropped to the confines of the cell train, excluding movement of the bead (approximately $400 \mu\text{m} \times 25 \mu\text{m}$). Image stacks were then exported as tiff files and analyzed using PIVLab (MATLAB, The MathWorks) with a sequence style of 1-2, 2-3, 3-4, etc. For analysis, Fast Fourier Transform (FFT) window deformation was selected with a Gauss 2x3-point sub-pixel estimator. The

cropped region was further refined with an ROI to yield 4-7 rows of ROI windows (i.e., 4-7 vectors in the vertical direction). For post-processing, parameters under vector validation included 4 as the standard deviation filter and 5 as the local median filter threshold. Vectors were then thresholded to exclude x velocities greater than 20 px/frame and less than -20 px/frame. Velocities in the y direction greater than 10 px/frame and less than -10 px/frame were also excluded. After data post-processing, PIV data was exported as a MAT file and analyzed using custom MATLAB code.

PIV data was concatenated to become a readable 3-D matrix and another custom MATLAB script used to average the displacement across each column and each row as a function of time. The resulting matrix is the cumulative change in position of the entire line with respect to time. These values were averaged across all experiments to produce the average trends shown in the graphs. These results corroborate the PIV analysis previously published for these experiments, which demonstrated collective cell migration.

5.5.B. Assembly of custom probes

20 μm inner diameter prepulled glass micropipette tips (*World Precision Instruments*, TIP20TW1) were angled to approximately 120 degrees using an open flame for better fixture within the micromanipulator. A glass bottom polystyrene dish was then coated with optical glue (*Norland Products*, NOA81) and 30 μm diameter borosilicate glass beads (*Cospheric*, BSGMS-2.2 27-32 μm). Using a micromanipulator (*Sensapex*, uMp-3), the probe was delicately lowered in the optical glue and pressed gently against a glass bead. The probes were then pre-cured using a handheld UV laser (*Lightfe*, UV301 365 nm), and fully cured using a 365 nm UV lamp (*Spectroline*, EN-180).

5.5.C. Probe preparation

After the bead was glued to the glass micropipette tip, probes were plasma treated using atmospheric plasma at 18W (*Harrick*, PDC-32G), and immediately incubated for 1-3 hours at room temperature with 50 $\mu\text{g}/\text{mL}$ rat tail collagen 1 (*Corning*, 354236) dissolved in 0.1% acetic acid. The probe was then rinsed with phosphate buffered saline (PBS) and mounted to a micromanipulator (*Sensapex*, uMp-3) using a probe holder (*Digitimer*, H-12).

5.5.D. Micromanipulation and Microscopy

The sample containing cell trains was placed on the stage of a Zeiss Axio Observer 7 widefield fluorescence microscope placed on a vibration isolation table (*Newport*). To ensure cell viability, the cell media was supplemented with HEPES to buffer acidity and the microscope chamber was heated to 37°C. The probe was lowered into the media containing dish, 1-2 μm above the substrate surface. Mineral oil (*Fisher Scientific*, 8042-47-5) was added to the top of the dish to seal media and prevent evaporation. After the system had stabilized from thermal drift (1-3 hours), the probe was brought flush against the outermost cell of the cell train and left to form a strong stable attachment over 4-12 hours. The micromanipulator then applied a predetermined displacement of 30 μm at a rate of 1 $\mu\text{m}/\text{sec}$ and simultaneously imaged every 2 seconds. Immediately following mechanical step strain, the cell line was imaged every 5 minutes for 6 hours with a 20x objective using brightfield imaging.

5.5.E. Strain Analysis

Boundary strain from bead displacement was calculated using digital image correlation (*DIC*, *VIC-2D Correlated Solutions*). 2-second interval images taken during strain

(BF) were cropped and loaded into the software as jpegs (unedited) and an approximately 70 μm wide ROI was drawn from the edge of the bead to encompass the region experiencing strain over the 30 second period.

To determine the angle of the cell-cell contact during applied strain, we used the following criteria: i) the angle was measured between the normal pulling force and path of the cell-cell contact being strained, ii) to account for cell-cell contacts that were not straight lines, measurements were taken to the end point of that cell-cell contact iii) if the cell attached to the bead was pulling on two cells at different angles, the angle of the longer cell-cell contact was taken, iv) if the cell-cell contact could not be visualized, data was excluded, v) if strain occurred on a large group of cells with no clear force concentration, data was excluded.

5.5.F. Protein micropatterning

35 mm glass bottom dishes (*Cellvis*, D35-20-1.5-N) were plasma treated for 5 minutes using atmospheric plasma at 18W (*Harrick*, PDC-32G). A custom cut 250 μm thick PDMS ring (8 mm inner diameter, 12 mm outer diameter) was immediately placed in the center of the glass bottom and a solution of 100 $\mu\text{g/mL}$ of poly(L-lysine)-graft-poly(ethylene glycol) (PLL(20)-g[3.5]- PEG(2)) (*SuSoS AG*, Dübendorf, Switzerland) diluted in PBS was added to the ring and left to incubate for 1h at room temperature. The PLL-g-PEG was then rinsed 10x with PBS with excess PBS removed. 20 μL of photoinitiator (PLPP, *Alvéole*) was added to the ring and the sample was then placed on the stage of a Leica DMI8 epifluorescence microscope equipped with a Fluotar 20x/0.40 N.A. objective and the Alvéole Primo photopatterning system (*Alvéole*, Paris, France). To create collagen lines wide enough for a single cell and long enough to capture long-range

force propagation within our camera field of view, we designed patterns that were 20 μm wide by 390 μm long. Digital masks for collagen lines were made using the open-source software program Inkscape⁵⁶ with a conversion determined by Primo calibration (0.277 $\mu\text{m}/\text{px}$). The Leonardo plugin (*Alvéole Laboratory*) on $\mu\text{Manager}$ software was used to create an array of digital masks, yielding 30 collagen lines per single glass bottom dish. Digital masks were projected through the glass at a dosage of 800 mJ/mm^2 from a 375 nm, 7.10 mW laser. Following light exposure, the photoinitiator was rinsed off with PBS and approximately 100 μL of 50 $\mu\text{g}/\text{mL}$ rat tail collagen 1 (*Corning*, 354236) dissolved in 0.1 acetic acid was added to the ring. The sample was left to incubate for 1 hour at room temperature before finally being rinsed and stored at 4°C with PBS.

5.5.G. Cell culture

Madin-Darby Canine Kidney (MDCK) II type G cells expressing a GFP E-cadherin reporter were cultured in low glucose DMEM (*ThermoFisher* 11885084) supplemented with 10% FBS and 1% Penicillin Streptomycin at 37°C with 5% CO_2 . Approximately 150,000 cells were seeded within the 35-millimeter glass bottom dish containing the protein patterns 1-2 days before line pulling experiments. Prior to experiments, cells were washed thoroughly with PBS to remove any cell debris or unadhered cells. Cells were imaged in a homemade phenol red free basal medium supplemented with 50 mM HEPES, 10% FBS, and 1% Penicillin Streptomycin.

5.5.H. Calculation of stacked nuclei

Cell lines were fixed with 4% formaldehyde in PBS (*ThermoFisher*, 28908) approximately 24 hours after cell seeding and labeled with Hoechst. Lines were then imaged

and Hoechst-labeled images were segmented using Cellpose version 1.0²² with the "cyto" model and a calibration of 30 pixels. Cellpose generated an ROI corresponding to nuclei from each image. We counted an instance of ROIs on top of one another as "stacked" nuclei. When counting an instance of stacked nuclei, no one cell was counted more than once per instance (e.g., 3 ROIs on top of one another or a triangle of ROIs would be one instance). Only cell lines that were fully connected end-to-end were used for analysis. Lines with >20 and <10 ROIs were also excluded from analysis.

5.7. Discussion and future directions

In this work, we have developed a novel model system for examining the effect of local intercellular strain on an epithelium at the single-cell level. Our 1-D model builds on previous epithelial models by combining new micromanipulation tools as well as quantifying the wave-like behavior of the epithelium. The combination of both innovations has allowed us to apply local boundary strains to an epithelium and model its impact on collective epithelial behavior on long time-scales.

By applying a step strain displacement of approximately 1.5 cell lengths, we successfully strained cell-cell junctions while leaving other regions of the epithelium unperturbed. We observed cell-cell contacts under strain and found that their orientations with respect to the normal pulling force correlated with downstream collective behavior. Cell-cell contacts that experience predominantly shear forces (i.e., an angle of less than 45° between the normal pulling force and cell-cell contact) have little impact on downstream cellular movements. Furthermore, we found that sheared cell-cell contacts are more prone to junction shortening and subsequent contact dissociation. What governs the orientation that the cell-cell contact takes on under strain? It is possible that having neighboring cells support

the cell-cell contact under load provide a "tension" orientation. In several experiments, it was not one cell pulling purely on another single cell, but sometimes a neighboring contact would distribute some of the load. Single cells pulled under load may be more susceptible to becoming sheared, resulting in cell-cell rupture which we observed in several experiments. However, we did not observe a correlation between cell-cell rupture and preference in movement.

We also demonstrated that ECM geometry can be used to control cell-cell contact positioning and subsequent collective cell migration. After discovering evidence that cell-cell contact orientation had implications on force transmission within the epithelium, we utilized protein micropatterning to regulate the underlying ECM geometry. Previous studies have found that specific ECM geometries can regulate the orientation of cell-cell contacts in cell pairs. We expanded this concept by creating a similar design, an I-beam geometry with the same outer dimension as our original cell lines. Interestingly, we found that the collective epithelium moved significantly slower on the I-beam geometry compared to the solid line ECM geometry. We posit that this difference is due to preferential cell-cell orientations on the I-beam lines. Contrary to our original hypothesis, cell-cell contacts preferred to align their contacts parallel to the length of the line. We hypothesize that the resulting orientations may be creating 2 layers of cells, migrating in opposite directions on top of one another. The resulting shearing events between cell-cell contacts may be disrupting collective cell behavior.

Lastly, we demonstrated that the 1-D epithelium demonstrates collective wave behavior, dependent on length of the system. Cell lines that are longer (390 μm) demonstrate oscillating waves with longer time periods than shorter cell lines (200 μm). By combining

this intrinsic behavior with our manipulation methods of the cell collective, we were able to successfully model how local mechanical cues impact collective epithelial behavior.

5.8. Acknowledgements

This work was funded by the NSF (1834760) and by cooperative agreement W911NF-19-2-0026 from the U.S. Army Research Office for the Institute for Collaborative Biotechnologies. The authors acknowledge Pruitt lab members for useful discussions, the UCSB Nanostructures Cleanroom Facility for instrumentation and equipment, and W. James Nelson for GFP E-cadherin MDCKII cells. This work was also supported by the BioPACIFIC Materials Innovation Platform of the National Science Foundation under Award No. DMR-1933487. Lastly, LPD acknowledges useful conversations with Professor Angela Pitenis.

5.9. References

1. Cai, D. *et al.* Mechanical feedback through E-cadherin promotes direction sensing during collective cell migration. *Cell* **157**, 1146–1159 (2014).
2. Begnaud, S., Chen, T., Delacour, D., Mège, R. M. & Ladoux, B. *Mechanics of epithelial tissues during gap closure. Current Opinion in Cell Biology* vol. 42 52–62 (Elsevier Ltd, 2016).
3. Poujade, M. *et al.* Collective migration of an epithelial monolayer in response to a model wound. *Proc. Natl. Acad. Sci. U. S. A.* **104**, 15988–15993 (2007).
4. Vasilyev, A. & Drummond, I. A. Fluid flow and guidance of collective cell migration. *Cell Adh. Migr.* **4**, 353 (2010).
5. Blay, J. & Brown, K. D. Epidermal growth factor promotes the chemotactic migration of cultured rat intestinal epithelial cells. *J. Cell. Physiol.* **124**, 107–112 (1985).
6. StefanooZapperi Editors, C. *Advances in Experimental Medicine and Biology* 1146 Cell Migrations: Causes and Functions.
7. Espina, J. A., Marchant, C. L. & Barriga, E. H. Durotaxis: the mechanical control of directed cell migration. *FEBS J.* **289**, 2736–2754 (2022).
8. Cohen, D. J., Nelson, W. J. & Maharbiz, M. M. Galvanotactic control of collective cell migration in epithelial monolayers. *Nat. Mater.* **13**, 409–417 (2014).
9. Dow, L. P., Parmar, T., Marchetti, M. C. & Pruitt, B. L. Engineering tools for quantifying and manipulating forces in epithelia. *Biophys. Rev.* **4**, (2023).
10. Sadeghipour, E., Garcia, M. A., Nelson, W. J. & Pruitt, B. L. Shear-induced damped oscillations in an epithelium depend on actomyosin contraction and E-cadherin cell adhesion. *Elife* **7**, 1–16 (2018).
11. Farjood, F. & Vargis, E. Novel devices for studying acute and chronic mechanical stress in retinal

- pigment epithelial cells. *Lab Chip* **18**, 3413–3424 (2018).
12. Martínez-Ara, G. *et al.* Optogenetic control of apical constriction induces synthetic morphogenesis in mammalian tissues. *Nat. Commun.* 2022 131 **13**, 1–13 (2022).
 13. Gudipaty, S. A. *et al.* Mechanical stretch triggers rapid epithelial cell division through Piezo1. *Nature* **543**, 118–121 (2017).
 14. Grieve, A. G. & Rabouille, C. Extracellular cleavage of E-cadherin promotes epithelial cell extrusion. *J. Cell Sci.* **127**, 3331–3346 (2014).
 15. Vishwakarma, M. *et al.* Mechanical interactions among followers determine the emergence of leaders in migrating epithelial cell collectives. *Nat. Commun.* 2018 91 **9**, 1–12 (2018).
 16. Weber, G. F., Bjerke, M. A. & DeSimone, D. W. A Mechanoresponsive Cadherin-Keratin Complex Directs Polarized Protrusive Behavior and Collective Cell Migration. *Dev. Cell* **22**, 104–115 (2012).
 17. Borghi, N. *et al.* E-cadherin is under constitutive actomyosin-generated tension that is increased at cell-cell contacts upon externally applied stretch. *Proc. Natl. Acad. Sci. U. S. A.* **109**, 12568–12573 (2012).
 18. Armon, S., Bull, M. S., Moriel, A., Aharoni, H. & Prakash, M. Modeling epithelial tissues as active-elastic sheets reproduce contraction pulses and predict rip resistance. *Commun. Phys.* 2021 41 **4**, 1–9 (2021).
 19. Jain, S. *et al.* The role of single-cell mechanical behaviour and polarity in driving collective cell migration. *Nat. Phys.* 2020 167 **16**, 802–809 (2020).
 20. Ron, J. E. *et al.* Polarization and motility of one-dimensional multi-cellular trains. doi:10.1101/2023.07.02.547405.
 21. Tseng, Q. *et al.* Spatial organization of the extracellular matrix regulates cell-cell junction positioning. *Proc. Natl. Acad. Sci. U. S. A.* **109**, 1506–1511 (2012).
 22. Stringer, C., Wang, T., Michaelos, M. & Pachitariu, M. Cellpose: a generalist algorithm for cellular segmentation. *Nat. Methods* 2020 181 **18**, 100–106 (2020).

Chapter 6

Structural characterization of epithelial doublets

6.1. Preface

The contents of this chapter previously appeared in *Nature Communications* and is reproduced here under Creative Commons Attribution 4.0 International License (CC BY 4.0). Full citation: Dow, L.P., Gaietta, G., Kaufman, Y., Swift, M.F., Lemos, M., Lane, K., Hopcroft, M., Bezault, A., Sauvanet, C., Volkmann, N. and Pruitt, B.L., 2022.

“Morphological control enables nanometer-scale dissection of cell-cell signaling complexes”. *Nature Communications*, 13(1), p.7831. (2022). Doi: 10.1038/s41467-022-35409-9. Adaptations have been made to section headings to be consistent with the formatting of this thesis.

In this chapter, I present a study that culminated from my work collaborating with the labs of Dr. Dorit Hanein and Dr. Neils Volkmann. When I first began working with Dr. Pruitt at Stanford, I was mentored by a former postdoc, Dr. Leeya Engel. Dr. Engel taught me the technique of protein patterning ECM proteins onto electron microscopy grids, which we originally published in 2019 (Engel et al., *Journal of Micromechanics and Microengineering*, 2019).

Once I began my program at UCSB, I continued this work by innovating new techniques to pattern EM grids. In our collaboration with Dr. Hanein and Dr. Volkmann, our goal was to control the shapes of epithelial cell pairs for cryogenic whole cell electron tomography. By controlling shapes of epithelial doublets, we could directly image the adherens junction under increased mechanical strain. This goal required new protein patterns,

new patterning techniques, and a deeper understanding of the microenvironment for cell pairs on EM grids. Furthermore, protein patterning via light-induced photomolecular adsorption of proteins is a relatively new technique. My experimental work within this manuscript included i) modifying our previously developed workflow to be entirely contactless and enable damage free transportation of samples to our collaborators, ii) implementing this protocol to pattern EM grids and ship them to our collaborators (Dr. Hanein and Dr. Volkmann), iii) designing samples for atomic force microscopy (AFM) of the PLL-g-PEG and ECM layers, iv) performing AFM indentation experiments and analysis to infer the mechanical properties of the carbon film, and v) writing of the manuscript and drafting of manuscript figures (for my contributed experimental work). From the Pruitt Lab, Dr. Yair Kaufman performed the surface characterization using AFM, Kerry Lane assisted me in performing AFM indentation experiments, and Matthew Hopcroft assisted in analysis of the AFM indentation measurements. Dr. Guido Gaietta, Mark F. Swift, Dr. Moara Lemos, Arnel Bezault, and Dr. Cécile Sauvanet from the laboratories of Dr. Hanein and of Dr. Volkmann performed the cryoCLEM, cryo-ET, and tomography analysis. The original study was conceived by Dr. Pruitt, Dr. Hanein, and Dr. Volkmann.

6.2. Abstract

Protein micropatterning enables robust control of cell positioning on electron-microscopy substrates for cryogenic electron tomography (cryo-ET). However, the combination of regulated cell boundaries and the underlying electron-microscopy substrate (EM-grids) provides a poorly understood microenvironment for cell biology. Because substrate stiffness and morphology affect cellular behavior, we devised protocols to characterize the nanometer-scale details of the protein micropatterns on EM-grids by

combining cryo-ET, atomic force microscopy, and scanning electron microscopy. Measuring force displacement characteristics of holey carbon EM-grids, we found that their effective spring constant is similar to physiological values expected from skin tissues. Despite their apparent smoothness at light-microscopy resolution, spatial boundaries of the protein micropatterns are irregular at nanometer scale. Our protein micropatterning workflow provides the means to steer both positioning and morphology of cell doublets to determine nanometer details of punctate adherens junctions. Our workflow serves as the foundation for studying the fundamental structural changes governing cell-cell signaling.

6.3. Introduction

Functional cell-cell contacts are critical to both developing tissues as well as maintaining robust barrier function in healthy adult tissue. This connectivity is mediated by distinct epithelial cell-cell assemblies including tight junctions, gap junctions, and mechanical linkers (i.e., desmosomes and adherens junctions)^{1,2}. The dynamic nature of developing tissues and the diverse external loads on epithelial barriers (e.g., stretching in the lung or gut) alter forces at cell-cell contacts that these junctions must respond and adapt to. Numerous studies have demonstrated how mechanical force transfer at these junctions regulate downstream epithelial function²⁻¹². For example, tension on the E-cadherin protein of the adherens junction has been shown to influence mitotic polarity and facilitate migration¹³⁻¹⁵. To learn how epithelial junctions function and adapt to their environments, there is a need to visualize these complex structures in native cell-cell configurations at defined functional states. This challenging task requires nanometer resolution imaging of these dynamic structures hidden deep in cell-cell contacts at different positions along a cell-cell interface.

In the last few years, cryo-ET has become the state-of-the-art technique for visualizing protein complexes in the context of the native whole cell at high resolution. Unlike traditional transmission electron microscopy (TEM) staining techniques, cryo-ET enables imaging of cellular structures in a native cellular environment, maintaining their three-dimensional nanoarchitecture while fully hydrated^{16,17}. In cryo-ET the sample is vitrified without staining, a tilt series of images from a multitude of angles is taken, and a three-dimensional (3D) reconstruction of the sample is calculated from the tilt series at nanometer resolution. Combining light microscopy with high resolution electron microscopy, for example, cryogenic correlative light and electron microscopy (cryo-CLEM) can be used to localize macromolecules and regions of interest by matching and aligning the 3D tomograms with fluorescent signals of light-microscopy images^{18,19}. These revolutionary techniques have already provided insight into key cellular structures including desmosomes²⁰ and cytoskeletal regulation^{21–23}.

Despite the power of cryo-ET imaging, there are several limitations to this technique. The electron beam can only permeate thicknesses up to 300 nm, meaning thicker cellular structures cannot be imaged without additional sample processing. This is particularly problematic considering mammalian cells are often several microns in thickness. Even in thinner regions of epithelial cell-cell contacts, junctions are buried at unknown thicknesses. Cryogenic focused ion beam (cryo-FIB) milling can be used to remove regions of excess thickness and isolate thinner regions of a thick cellular structure (lamellae), enabling imaging of the cellular interior^{24–29}, however precise spatial localization along the z axis of the region between the two modalities is not yet available. The other main limitation of Cryo-ET is that during tilt, many regions of the electron microscopy (EM) amenable substrate (the EM-grid)

are obstructed from the field of view and thus cannot be imaged. Therefore, viable images can only be obtained from specific regions of EM-grids, resulting in low throughput of sample processing.

Protein micropatterning has been introduced as a method to spatially position cells on EM-grids and improve sample throughput for cryo-ET^{23,30,31}. Cells can be positioned precisely in regions where there is no visual obstruction (i.e., center of grid and of mesh squares). Micropatterning combined with bio-passivation techniques can also reduce the adherence of cells or debris in regions of the grid that may obstruct viewing. These advantages allow a significant increase in the throughput of whole-cell cryo-ET. Furthermore, protein micropatterning provides unique opportunities for probing structure/function relationships by altering cellular shape and tension. Light microscopy, including fluorescence microscopy, has been instrumental in these findings. For example, controlling for cell geometry can influence stem cell fate and enhance maturity of cardiomyocytes^{32,33}. Light microscopy can additionally be used to assess attachment, growth, and behavior of cells experiencing different mechanical inputs. Controlling for cell geometry via protein patterns offers the potential for whole-cell structure and function assays of cell-cell contacts not previously attainable^{4,34}.

While we and others have published a few studies on the ability to pattern EM-grid substrates for electron tomography^{30,31,35} as well as attempting to increase the likelihood to obtain cell-cell contacts between protrusions³⁶, the detailed characterization of these geometrically regulated substrates for functional assays remains unaddressed. Here, we have i) adapted and optimized existing photomolecular adsorption techniques³⁷ to micropattern EM grids in a completely contactless manner, ii) provided molecular details and mechanical

properties of the corresponding cellular microenvironment using a variety of high resolution imaging techniques, iii) utilized these protein patterns to regulate the positioning and size of mature epithelial cell-cell contacts for high-throughput CLEM and cryo-ET imaging, and iv) implemented cryo-FIB to isolate and segment geometrically regulated epithelial cell-cell contacts. We successfully achieved our goal of visualizing the nanometer details of adherens junctional puncta within mature cell-cell contact sites through harnessing contactless micropatterning, light microscopy, cryo-FIB, and cryo-ET. Our additional extensive characterizations of the mechanical properties of the hydrated carbon film and nanometer-scale details of the micropatterns beneath the cells offer new insight into functional regulation of micropatterned cells for cryo-ET studies. The results from this study offer enormous potential for elucidating the complex structure and function relationships of cell-cell junctions in the dynamic cellular environment

6.4. Results

6.4.A. Contactless grid handling and micropatterning

Micropatterning of proteins on holey carbon electron microscopy grids is particularly difficult due to the fragility of the thin carbon film (~12 nm) that is deposited on a metal mesh. Our previous work overcame this challenge by utilizing contactless photomolecular adsorption to pattern ECM proteins³⁰. In that work however, a carefully positioned thin silicone mask was used to adhere the grid to a substrate, which can make the carbon film vulnerable to rips or tears. To improve on previous work, we have now developed a contactless method for grid handling as well as micropatterning (Figure 6.1). For patterning of ECM protein arrays on a conventional EM grid film (Figure 6.1a), we leveraged custom

cut PDMS shapes. A small circular PDMS platform adhered the gold metal mesh during plasma treatment, while a thicker outer PDMS ring created a hydrophobic barrier for a fully contained well of poly-L-lysine-grafted-polyethylene glycol (PLL-g-PEG) solution (Figure 6.1b). This well served three purposes: i) containment for subsequent rinse steps and protein incubation, ii) minimal working volume and reagents, and iii) sealing the buffer inside the well using a glass coverslip, allowing for robust shipping and handling procedures if necessary (Supplementary Figure 6.S1). We adapted previous techniques³⁰ by exposing the UV digital mask directly through the thin PDMS base and exposing our custom pattern geometries on the holey carbon film (Figure 6.1c). These geometries were patterned in a high-throughput manner as 10 x 10 arrays of micropatterns (Figure 6.1d) and optimized to avoid stitching errors (Supplementary Figure 6.S2).

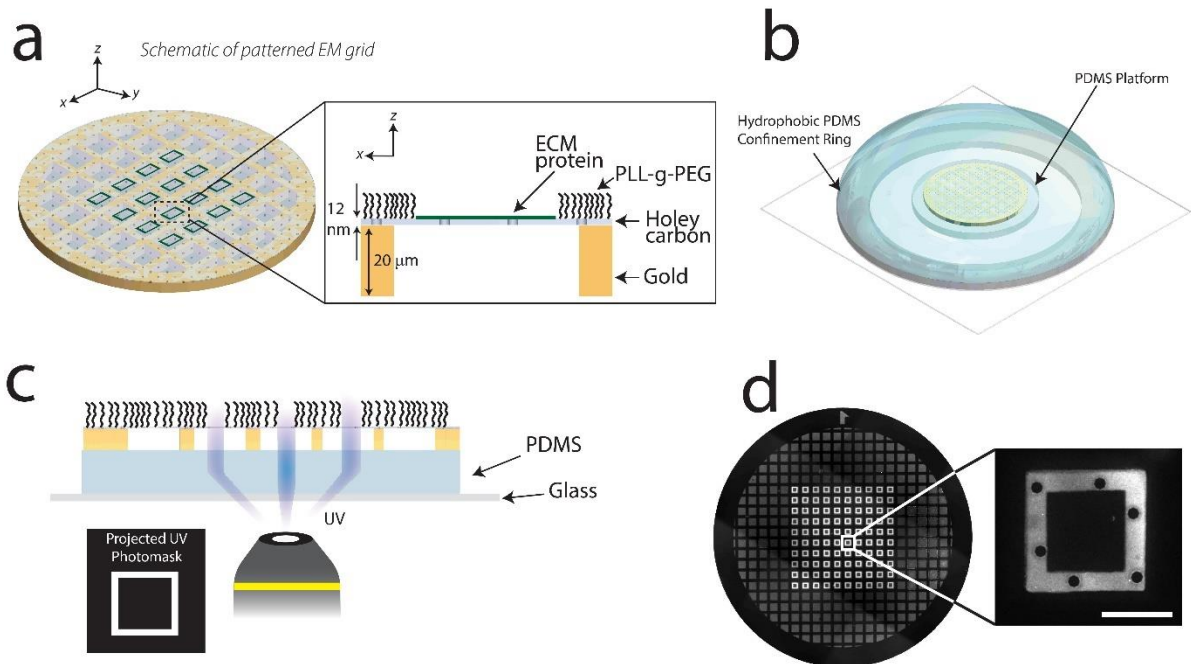


Figure 6.1. Micropatterning of holey carbon EM grids using photomolecular adsorption.

(a) Schematic of patterned holey carbon film of gold mesh grid, with custom ECM patterns surrounded by a bio-passivation layer. (b) Grids are placed on a thin PDMS platform to eliminate physical contact with the carbon film, which is encompassed by a thicker PDMS ring to confine

liquid on the grid. (c) Digital masks with custom patterns are projected through the carbon film to degrade the bio-passivation layer. (d) Adsorption of Oregon green gelatin to degraded regions of 50 x 50 μm squares within a 10x10 array. Scale bar is 30 μm .

6.4.B. Characterization of protein micropatterns

To determine whether our PLL-g-PEG bio-passivated layer was within the thickness range for electron-beam permeability, we utilized contact mode atomic force microscopy (AFM) on backfilled protein patterns on glass using similar photomolecular adsorption techniques (Figure 6.2a). We exposed a two-layer digital mask of 5 μm solid square patterns on the glass slide, with an incubation of Oregon green gelatin between UV exposures (Figure 6.2b). Therefore, the 2nd exposure ablated identical 5 μm squares in the bio-passivated region with no subsequent protein backfill. These patterns were discernable using fluorescence imaging (Figure 6.2c), which guided the placement of the AFM probe for surface scanning measurements. Our results indicated that the PLL-g-PEG bio-passivation layer was approximately 2 nm thick, while the gelatin ECM layer had a thickness of approximately 0.5 nm (Figure 6.2d, e). These thickness measurements were approximately two orders of magnitude less than the maximum thickness constraint for our sample (<300 nm), indicating that neither the thickness of the ECM protein nor the bio-passivation layer would burden the sample thickness during electron beam transmission. Interestingly, the protein patterns differ enough in thickness and density from the surrounding PLL-g-PEG that they can be visualized by electron beam transmission (Supplementary Figure 6.S3). We further verified that these thickness measurements translated onto the ECM patterns of the holey carbon grid by performing cryo-SEM (Figure 6.2f). In addition to pattern topography, we further characterized the lateral resolution of the patterns on the carbon film, which has not been

assessed before, using cryo-CLEM (Figure 6.2f). Reconstructed tomograms of the protein patterns demonstrated a clear boundary between the protein layer and the bio-passivation layer that is rather irregular at the nanometer scale despite the smooth appearance at light-microscopy resolution (Figure 6.2g).

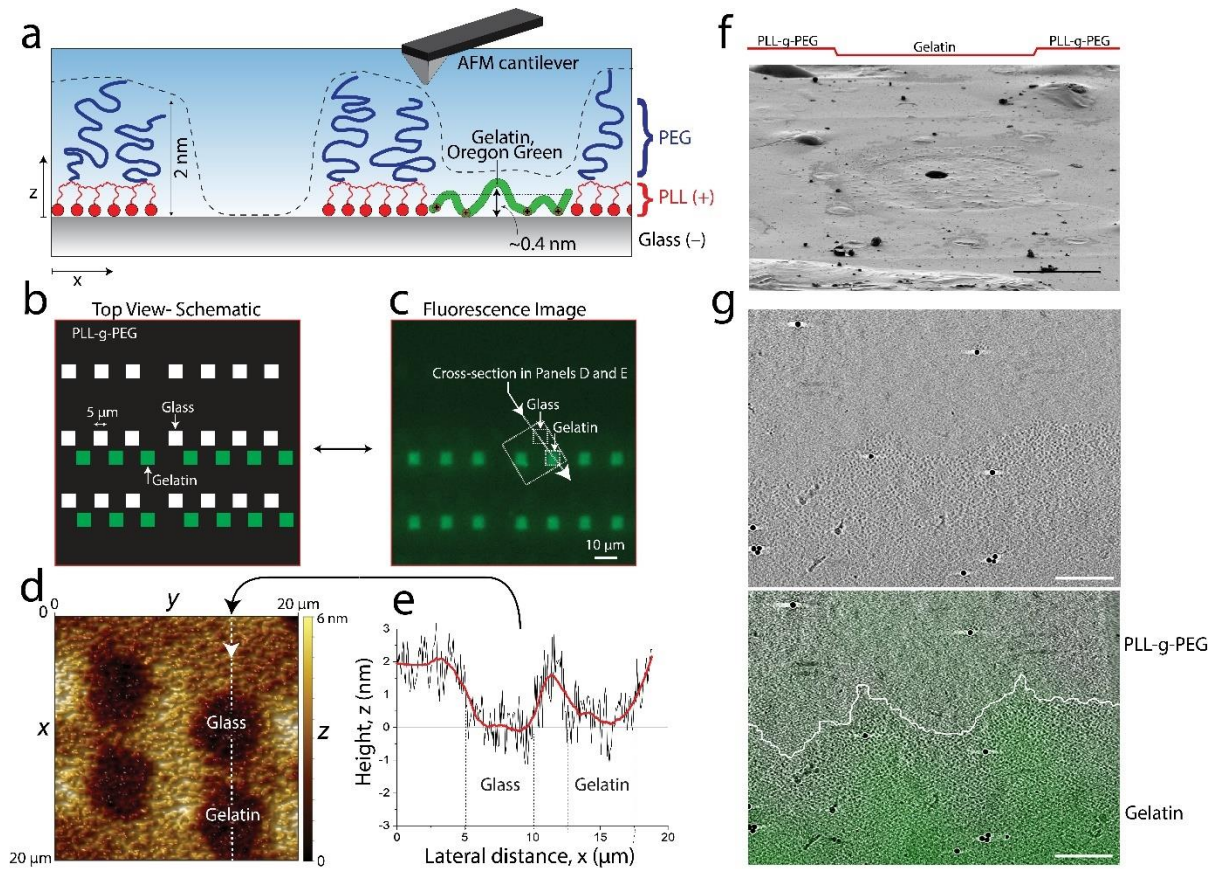


Figure 6.2. Nanoscale characterization of the micropatterning of holey carbon EM grids using photomolecular adsorption.

(a) Schematic of an AFM cantilever scanning the surface of adsorbed gelatin surrounded by PLL-g-PEG. (b) A 2-step digital mask photopatterning method was used to create 5 μm squares with and without protein, (c) which could be identified using fluorescence microscopy. (d) The probe was scanned across 3 distinct regions on the sample, which could (e) be quantified with 0.5 nm resolution. (f) Custom ECM (Oregon green gelatin) 45 μm x 45 μm square pattern surrounded by PLL-g-PEG on the holey carbon film of a gold mesh grid imaged by the scanning electron microscope beam (at 2kV) of the dual beam cryo-FIB instrument (cryo-SEM imaging mode). The pattern is clearly visible as a depression, consistent with the atomic force microscopy results shown in (d). (G) 2 nm thick slice of a tomogram of a patterned region. The fluorescence image of the ECM coating applied to the pattern was precisely overlaid on the cryo-ET image and the border between pattern and bio-passivated area was manually traced (white line). Scale bars 20 μm (F), 200 nm (g).

6.4.C. Mechanical characterization of carbon film

The mechanical properties of cell substrates have been shown to influence cellular properties, including the structure and molecular tension at cell-cell contacts^{38,39}. However, the rigidity of the hydrated carbon film on the electron microscopy grids used for cell culture is unknown. Therefore, we mechanically characterized the EM-grid squares to learn their rigidity in comparison to commonly used mechanobiology substrates (e.g., hydrogels, PDMS). We used an AFM in contact mode (see details under Carbon Film Force Deflection in Methods) to apply a force to the center of the carbon film over a grid square, i.e., to push the cantilever tip against the film (Figure 6.3a). We performed this measurement for loading rates of 100 nm/s and 1000 nm/s to verify elastic behavior of the film. By modeling both the cantilever and carbon film as elastic springs in series under load, we calculated the spring constant of the deformed carbon film (Figure 6.3b and Supplementary Figure 6.S4). The effective spring constant, k_f , for a grid square was found to be 0.85 ± 0.23 (N/m), independent of loading rate (Figure 6.3c). We used this experimentally determined spring constant, k_f , to approximate what equivalent material properties of a hydrogel would yield the same effective spring constant. For a gel having homogenous elastic modulus E_{gel} and Poisson ratio ν , the relationship of rigidity to stiffness can be modeled as an elastic half-space under vertical point load application (Equation 1).

$$k = \frac{\pi\alpha E_{gel}}{(1 - \nu)(1 + \nu)} \quad (1)$$

Assuming a gel Poisson's ratio of 0.48^{40,41} and a radius of adhesion (α) of $1 \mu\text{m}$ ⁴², we estimate the spring constant of a grid square is equivalent to that of a gel having an elastic modulus E_{gel} of 207 ± 56 kPa. This value is comparable to polyacrylamide gels used for cell

culture⁴¹. We attribute variability of this value to ambient noise in the measurements

(Supplementary Figure 6.S5), as well as heterogeneity between squares of the EM-grid.

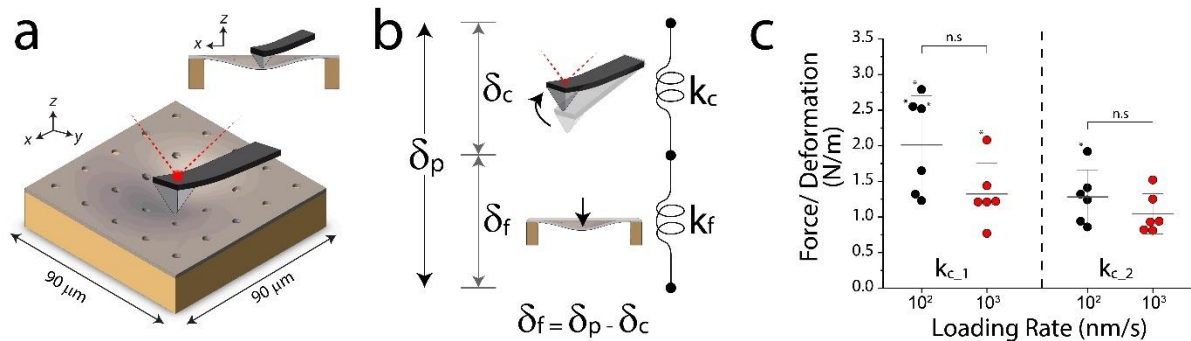


Figure 6.3. Mechanical characterization of carbon film cell substrate.

(a) Schematic of carbon square of EM grid being loaded in the center by the AFM probe. (b) Example of a single distance/force curve from loading one of the mesh squares at a loading rate of 100 nm/sec (red-approach). (c) The slopes of force/deformation curves (determined by a total least squares regression), each from a separate mesh square, were used to calculate the spring constant associated with the carbon film across 100 nm/sec ($n=6$) and 1000 nm/sec ($n=6$). Our results show no significant change between these loading rates. Error bars represent SD.

6.4.D. Confinement of epithelial cell pairs

To verify confinement of cells on the patterns, we seeded *Potorous tridactylus* kidney-1 (PTK-1) epithelial cells on carbon coated electron microscopy grids patterned with 66.5 x 66.6 μm gelatin squares (Figure 6.4). PTK-1 cells are thinner and flatter than other epithelial cells yet maintain the distinctive features of the adherens junction. Therefore, these cells were ideal for electron tomography of their cell-cell contacts. To be able to validate the maturity of the epithelial cell-cell contacts, we generated a stable cell line in PTK-1 cells expressing an EGFP tagged form of mouse alpha E catenin (Supplementary Figure 6.S6). The cells were unable to bind to the outer PLL-g-PEG layer and thus spread across the available patterned protein, filling >50% of the available patterns (Figure 6.4a-d). The square patterns facilitated a predictable cell geometry and consistent spatial control of cell-cell contacts (Figure 6.4e-g). Furthermore, our workflow allows to spatially regulate different cell

types with different ECM substrates (Supplementary Figure 6.S7 and 6.S8). However, to achieve consistent spatial regulation of cell pairs we identified several factors that must be carefully regulated; for example, cell seeding methods must be optimized and the integrity of the bio-passivation layer must be validated (Supplementary Figure 6.S9). With all parameters optimized, we currently achieve success rates between 27% and 70% (i.e., 30-73% of the patterns are empty, damaged, or overcrowded). About a third ($33.4 \pm 7.3\%$) of the patterns with adhered cells had cell-cell contacts clearly identifiable by the EGFP-alpha E catenin signal. With the patterned area of the grid restricted to the central 10 x 10 squares, this percentage results in 9-23 candidates per grid for further analysis.

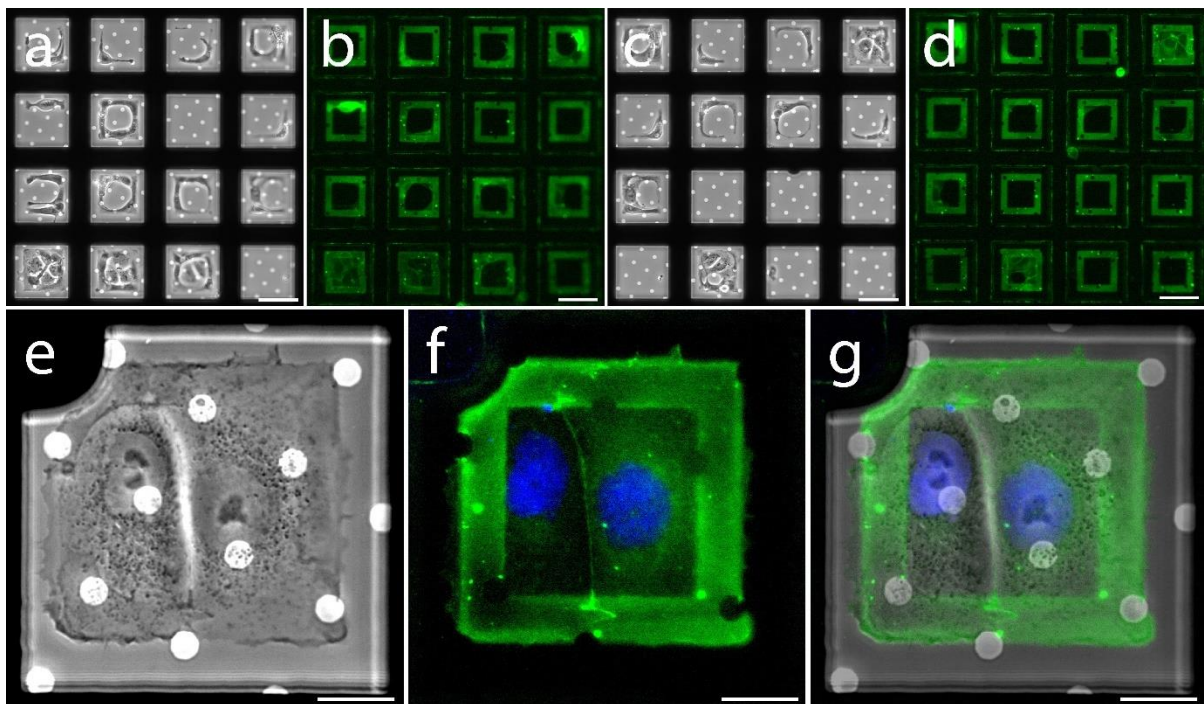


Figure 6.4. Confinement of epithelial cell pairs on patterned holey carbon electron microscopy grids.

Micropatterns are patterned on the carbon film of EM grids and surrounded by a bio-passivated layer to prevent cell adhesion outside of the patterned area, coated with Oregon Green gelatin and then populated with PTK-1 cells expressing EGFP-alpha E catenin. (a, c) Phase contrast and (b, d) corresponding fluorescence images of patterned areas are shown in the top panels. (e-g) A cell doublet fully confined within the patterned area (a- phase contrast, f- fluorescence: DAPI in blue; Oregon Green gelatin and EGFP-alpha E catenin in green, and g- overlay of phase contrast and fluorescence images). Scale bars, 60 μm (a-d) and 20 μm (e-g). All ECM patterns are 66.5 x 66.5 μm .

6.4.E. Correlative light and cryo-EM/ET visualization of cell-cell contacts

We next performed cryo-ET of spatially regulated cell-cell contacts in confined cell pairs. Since cell-cell contacts are difficult to identify using traditional light microscopy, we used the EGFP – alpha E catenin cell line we had generated in PTK-1 cells to better locate contact sites (Figure 6.5a, b). We additionally utilized cryo-CLEM to map how spatial regulation of cell-cell contacts locally altered the total thickness of the sample in the contact region (Figure 6.5c). For example, cells that adhere to larger patterns can have thinner (in z) cell-cell contacts³⁰. Therefore, we wanted to verify that stretched cells on micropatterns created regions thin enough for imaging. Our initial cryo-ET experiments indicated that while the body of the cell was often too thick for initial cryo-ET, many regions of cell-cell contact sites were thin enough for imaging. In multiple locations along the cell-cell contact, we generated tomographic reconstructions from tilt series with an angular range of $\pm 66^\circ$ (Figure 6.5d, e). When the sample is tilted, the grid bars can obscure the field of view if cells of interest grow near the edge of the grid square, even if they are fully visible in the untitled image. Furthermore, the physical edge of the grid, the clip ring that encases it, and the holder/stage itself obscure entire regions radially outward from the physical center of the grid even at lower tilts (Supplementary Figure 6.S10a). Thus, to increase the efficiency and coverage of tomography data collection, we positioned our micropatterns to confine the cells to regions that allow full tilt range of $\pm 66^\circ$ (Supplementary Figure 6.S10b). By utilizing the full tilt range, our methods allow recovery of the maximum amount of three-dimensional information.

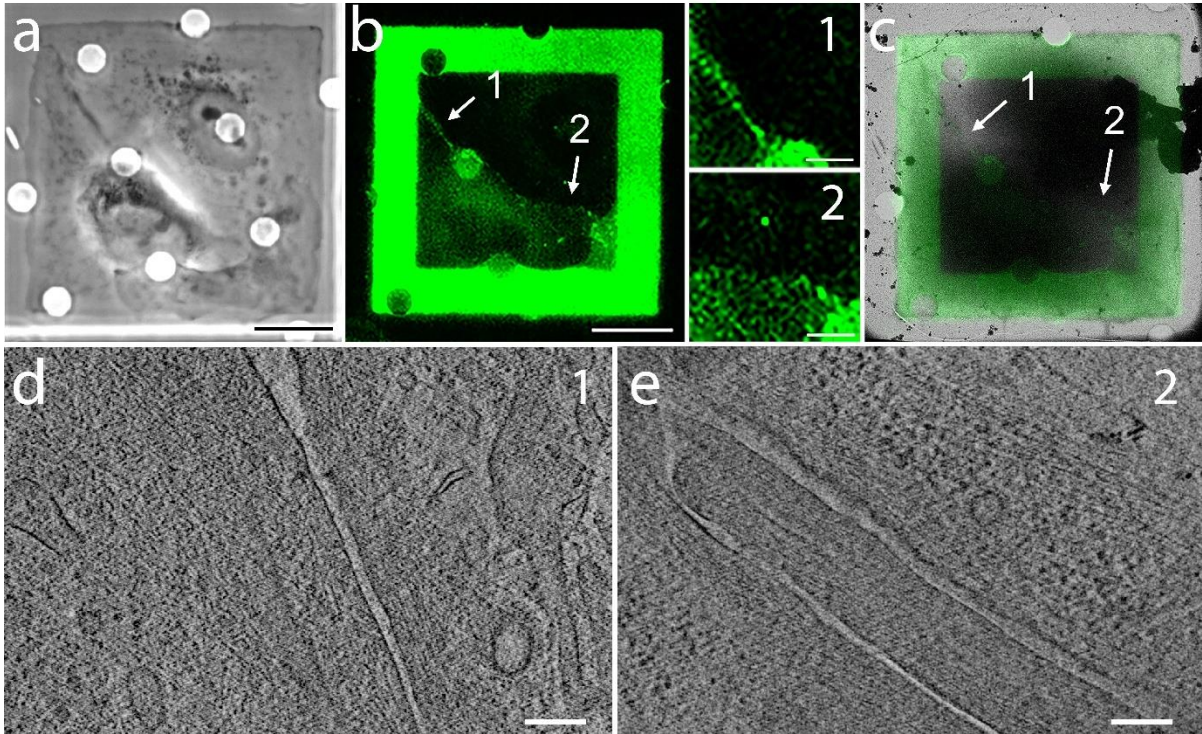


Figure 6.5. Correlative light and cryo-EM/ET visualization of cell-cell contacts in PTK-1 cells adhering to micropatterns.

PTK-1 cells stably expressing EGFP-alpha E catenin are plated on micropatterned grids treated with Oregon Green gelatin. Upon adhesion, many cells will form doublets confined into the pattern, as shown in this example. (a) Phase contrast, (b) fluorescence image of the cell pair of interest, displaying both the EGFP signal from the tagged alpha E catenin and the Oregon Green signal marking the pattern. Note that the pattern signal intensity is inherently much higher than that of the tagged protein, somewhat overwhelming the EGFP signal, which is quite robust in the absence of the pattern (see Supplemental Figures S6 and S8). The numbers “1” and “2” point to two regions rich in cell-cell contacts and thin enough for direct EM imaging. The insets to the right show the two regions at higher magnification and increased contrast. (c) Overlay of the aligned fluorescence and cryo-EM views used for identifying the same two regions selected in (b) for investigation by cryo-ET. (d, e) 2-nm thick slices from tomographic reconstructions obtained from regions 1 and 2. Scale bars, 20 μm (a-c), and 200 nm (d, e). All ECM patterns are 66.5 x 66.5 μm .

We were able to verify the integrity of our cells within confining micropatterns by imaging the plasma membrane and major cellular organelles including, mitochondria, vesicles, and actin fibers spanning different regions of the cell (Supplementary Figure 6.S11). These results demonstrate the capability of cryo-ET to faithfully image spatially regulated cell-cell contacts of healthy intact epithelial cells.

6.4.F. Cryo-FIB milling of cell-cell contacts

While we were able to successfully image cell-cell contacts, features of the adherens junction within the cellular interior remained inconclusive. Therefore, we utilized cryo-FIB milling to isolate regions of the cell-cell contact along the basal-apical axis (Supplementary Figure 6.S12). Prior reports posit the adherens junction in the upper portion of the cell-cell contact along the apical-basal axis, approximately 500 nm below the apical side of the cell⁴³. Therefore, we milled a 200 nm thin slice to isolate a lamella from this region of the cell (Figure 6.6a-b). The 3D reconstruction of the imaged area shows intricate cellular details, including the abutting plasma membranes of the two cells (Figure 6.6c). Some regions of the plasma membranes are in close contact (red box in Figure 6.6c) revealing an isolated punctum reminiscent of punctate adherens junctions observed in conventional thin-section electron micrographs^{44,45}. Near this punctum, a high density of actin filaments forming tight bundles and dense networks is visible. Segmentation analysis (Figure 6.6c, d) reveals a dense network of irregularly placed rods of 4.5-nm diameter bridging the plasma membranes with an inter-membrane distance of 15.4 ± 3.0 nm at the punctum (Figure 6.6e, red). These values are consistent with those obtained from quick-freeze deep-edge microscopy of *in situ* adherens junctions^{45,46}. A fraction of the rods cluster into larger assemblies with an increased width of up to 20.4 nm. The ratio between clustered and individual rods is 1.3, close to the 1.2 ratio between clustered and individual E-cadherin dimers observed in super-resolution light microscopy of adherens junctions⁴⁷.

The height of the lamella in respect to the cell surface should ideally be guided by the fluorescence signal of some adherens junction marker like the EGFP-tagged alpha catenin used in this study. However, technologies that allows accurate enough Z-localization of the

fluorescence signal is not currently available. An emerging technology that combines cryogenic fluorescence imaging directly with the cryo-FIB milling step⁴⁸ allows checking the fluorescence signal during milling, offering some potential guidance for lamella production. However, the required hardware is not yet widely available. Nevertheless, the geometric constraints used here generate a surprisingly high yield of junctions and thus offers a viable alternative. We found at least one junction similar to the one depicted in Figure 6 in 89% of the successful lamellae. In total, we produced 15 lamellae, 9 of which yielded interpretable tomograms. For all but one of these lamellae, at least one of the tomograms generated from the respective lamella contained one or more junctions. Our current protocol yields 9-23 candidates per grid (see above). From our current experience with operating the Aquilos 2 system, 15 -20 lamellae can be generated from a single grid sample using semi-automated milling during a standard session constituting two consecutive days. This range is a good match with the expected number of junction candidates per grid.

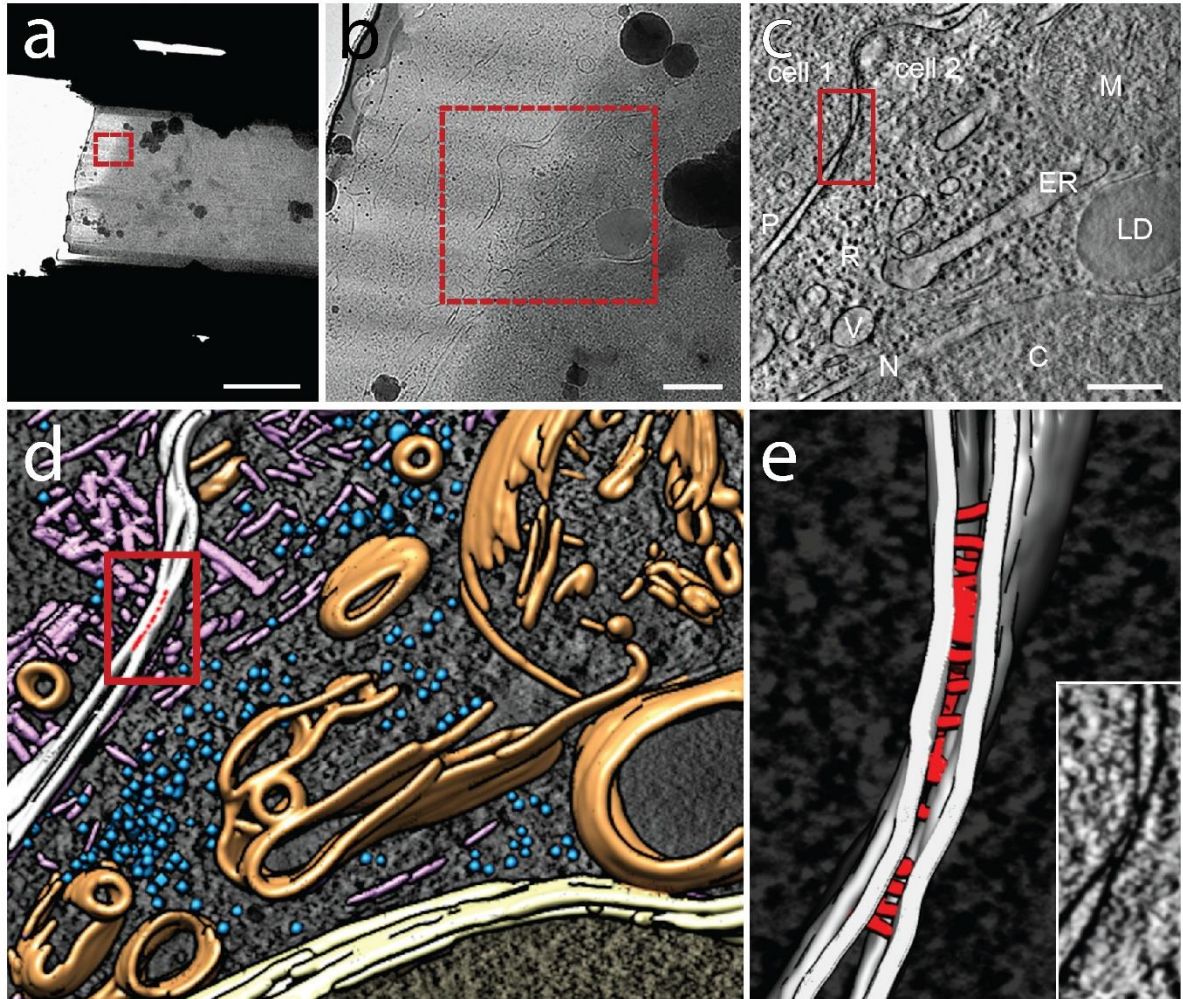


Figure 6.6. In situ cellular tomography of shape-guided thinned region of micropatterned adhering PTK-1 cell-cell contacts.

(a) Top view of a cryo-FIB-milled lamella across a vitrified PTK-1 cell-cell contact site imaged using a cryo-transmission electron microscope. The milling patterns above and below the sample were adjusted to leave a central ~200 nm thin slice (lamella) supported by the surrounding unmilled, vitrified material. The cuts below and above the lamella are for releasing stress introduced by the milling. Cell-cell contact regions are identified visually using the shape of the two interacting cells in cryo-SEM images (Fig S2-A and B illustrate shape-guided targeting of a region of interest). (b) Higher magnification of targeted region marked by the red box in (A) representing the area of tomogram acquisition. (c) 2-nm thick virtual slice through a tomogram of the lamella region marked by the red box in B, showing a clearly discernible cell-cell contact (marked by red box, P: plasma adjacent plasma membranes) between two adjacent cells. Other cellular features visible include dense packing of macromolecular complexes in the cytoplasm; R: ribosomes; ER: endoplasmic reticulum; M: mitochondrion; V: vesicle; LD: lipid droplet; N: the nuclear envelope separating the nucleoplasm from the cytoplasm and C: Chromatin within the nucleus. (d) 3D surface representations of segmented features. Plasma membranes in white, nuclear envelope in yellow, other membrane structures in orange, ribosomes in blue and actin filament assemblies in pink. The cell-cell contact is marked by a red box. A slice of the tomogram is shown in the background for reference. (e) 3D surface representation of adherens junctional punctum within cell-cell contact. Membrane is in white,

connecting rods are in red. The inset shows an enlarged view of the boxed area in (c). Scale bars in a = 5 μm ; b = 500 nm, c = 250 nm.

6.5. Methods and Materials

6.5.A. Grid preparation and handling

200-mesh R5/20 holey-carbon coated gold grids (Quantifoil Micro Tools GmbH) were first inspected for potential carbon tears and only grids with minimal damage were used. Grids were then placed carbon side up on 250 μm -thick 5 mm-diameter PDMS platforms (Specialty Manufacturing, Inc., Saginaw, MI, USA) cut from a Silhouette CAMEO 3 electronic desktop cutter (Silhouette America, Inc., UT, USA). Adhered on a #1.5 glass coverslip, the samples were plasma cleaned for 5 minutes at 18W (Harrick, PDC-32G). Immediately after plasma treatment, a 600 μm -thick PDMS ring (8mm inner diameter, 12mm outer diameter) was sealed around the grid (Supplementary Figure 6.S1). A solution of 100 $\mu\text{g}/\text{mL}$ of poly(l-lysine)-graft-poly(ethylene glycol) (PLL(20)-g[3.5]- PEG(2)) (SuSoS AG, Dübendorf, Switzerland) diluted in phosphate buffered saline (PBS) was immediately placed within the well and incubated for 1h at room temperature. The well was then rinsed thoroughly (10x) with PBS prior to micropatterning. Following micropatterning, a 12 mm glass coverslip was adhered to the outer PDMS ring to seal in buffer for transport and additional handling.

6.5.B. Photopatterning and protein functionalization of EM grids

Following PLL-g-PEG incubation, excess PBS was removed from the well containing the grid, with enough remaining to keep the sample hydrated. 15 μL of UV sensitive photo initiator (PLPP, *Alvéole*, Paris, France) was added to the well and the sample was placed on the stage of a Leica DMI8 epifluorescence microscope equipped with a Fluotar 20x/0.40

N.A. objective and the Alvéole Primo photopatterning system (*Alvéole*, Paris, France). Digital masks for ECM patterns were made using the open-source software program Inkscape⁵⁴, which were loaded onto the Leonardo plugin (*Alvéole Laboratory*) on μ Manager software⁵⁵. The pixel/ μm ratio generated by Primo calibration was used to define the geometries of ECM patterns. For each grid, a single mask consisting of a 10 x 10 array of hollow square micropatterns (50 x 50 μm or 66.5 x 66.5 μm , 8 μm thickness) were angled to the center the grid squares, then projected through the carbon film at a dosage of 2500 mJ/mm^2 from a 375 nm, 7.10 mW laser. 35 x 35 μm hollow square micropatterns were used for MDCK cells (Supplementary Figure 6.8). Since the digital masks were slightly larger than the DMD, imperfect DMD stitching between masks during patterning created subtle misalignments in several patterns (Supplementary Figure 6.S2). Alternative approaches can be used to mitigate such stitching errors. Therefore, subsequent protocols used smaller 2x3 array masks. Following micropatterning, the photo initiator was rinsed off with PBS and a 100 $\mu\text{g}/\text{mL}$ solution of Oregon Green gelatin (*ThermoFisher*, G13186) was incubated on the grid for 1 hour at room temperature in the dark. The grids were then rinsed thoroughly with PBS and stored hydrated at 4°C prior to cell seeding.

For functionalization with rhodamine fibronectin, EM grids were prepared using an overnight incubation 0.01% poly-l-lysine (*Sigma*) in a humid chamber at room temperature, washed 3x with HEPES 0.1M pH 8.4, and incubated for 1 h with freshly prepared 100 mg/mL polyethylene glycol-succinimidyl valeric acid (PEG-SVA) resuspended in HEPES 0.1 M pH 8.4. Photocission of the PEG-SVA chain was performed using a laser dosage of 1200 mJ/mm^2 and a 4.5 mW laser power. Grids were then washed in 500 μL of water and 2

times in PBS. Micropatterned grids were functionalized by incubation for 1h with 20 μL of 50 $\mu\text{g}/\text{mL}$ of Fibronectin-Rhodamine (*Cytoskeleton*) and washed 3x in PBS.

6.5.C. Atomic force microscopy

Pattern Characterization: The thickness of the PLL-g-PEG and the gelatin layers was measured using the BioScope Resolve AFM (*Bruker*) coupled with the Axio-Observer inverted fluorescence microscope (*Zeiss*). The AFM topography was measured in PBS solution at room temperature ($\sim 22^\circ\text{C}$) using PeakForce mode. The AFM probe was a MLCT silicon nitride cantilever (*Bruker*) with a spring constant of $\sim 0.1 \text{ N/m}$, as reported by the manufacturer. The image was processed using Nanoscope Analysis 2.0 software (*Bruker*). For fluorescence imaging, the Oregon Green filter-set (excitation 488 nm, emission 525 nm) was used.

Carbon Film Force Deflection: AFM loading measurements were performed with a WITec AFM (Alpha300) and a 200-mesh R 5/20 holey-carbon coated gold grid (*Quantifoil Micro Tools GmbH*). The grid was submerged in PBS and adhered to a strip of PDMS to prevent slippage. We used a cantilever probe with a tip-radius curvature of $1 \mu\text{m}$ and nominal spring constant, k_c , of 0.251 N/m (SAA-SPH-1UM, *Bruker*). Optical lever sensitivity of the cantilever probe was measured by performing force scans against a glass surface prior to carbon film measurements and was found to be 25.97 nm/V . For each measurement, the tip of the AFM cantilever was centered above the grid square before approaching the surface. The following feedback threshold parameters were used to locate the surface: 1.0 V set point (25.97 nm cantilever deflection), 1% p-gain, and 0.2% i-gain. To avoid potential hysteresis effects, each square was loaded only once. Each loading measurement was performed using WITec's Distance Curve mode with approach and retract distance settings of 100 nm (total

vertical travel of 200 nm) at speeds of 100 and 1000 nm/sec. The deformation of the carbon film was determined by taking the difference between the piezo position and the cantilever deflection (Supplementary Figure 6.S4)⁵⁶⁻⁵⁸. The spring constant from each measurement was calculated by using total least squares regression between the force applied by the cantilever and the deflection of the carbon film. We observed periodic noise in the measurement introduced by ambient noise and vibration. Based on a Fast Fourier Transform analysis of the force curves (Supplementary Figure 6.S5), the main sources for periodic background noise were ~60 Hz and ~300 Hz, which match the 1st and 5th harmonics of the electrical systems in the lab. Statistical significance between data sets was determined using a two-tailed student t-test assuming equal variance.

6.5.D. Generation of new cell line stably expressing EGFP-alpha E catenin

PTK-1 cells in log phase were electroporated with pEGFP-C1-ACAT (mouse alpha catenin subcloned into pEGFP-C1, ClonTech; EGFP is fused to the carboxyl terminus of the target protein; construct was a generous gift from Nelson's group). After selection with G418 (400 µg/mL), resistant cells went through three rounds of enrichment by sorting. Once a bulk population and single cell clones were isolated and grown, they went through testing by western blot (WB) and immunofluorescence (IF). WB was performed using cell equivalent lysates (the same number of cells was used for each lysate) from parental, bulk, single cell clones and a control stable line generated with the same construct in MDCK cells. IF was conducted according to standard protocols. Both WB and IF were done using a rabbit polyclonal antibody against alpha catenin (kindly provided by Nelson's group).

6.5.E. Preparation of micropatterned grids, cell plating and titration for cryo-ET

Micropatterned grids were rinsed once in sterile 1x PBS and screened for integrity and quality of patterns on an inverted light microscope (Eclipse TE 2000-U, *Nikon*) equipped with manual controlled shutter, filter wheels, and a 14bit cooled CCD camera (Orca II) controlled by MetaMorph software (*Universal Imaging*), using a Plan Fluor ELWD 40/0.60 Ph2 or a Plan Fluor 10/0.30 Ph1 objective lens (*Nikon*). Alternatively, micropatterned grids were imaged using a Spinning Disk (CSUX M1-L, *Solamere*) attached to a standard fluorescence widefield inverted microscope (Axio Observer 7, *Zeiss*). Grids were removed from PBS, equilibrated in complete medium for approximately ten minutes and seeded with cells in log phase. As our goal was to obtain doublets in each pattern, for as many patterns as possible, the cell density was titrated by applying 10,000-100,00 cells/mL in increments of 10,000 cells. The titrations indicated that a cell concentration around 50,000 cells/mL was ideal in obtaining a good percentage of doublets in each pattern over the course of a 12-hour incubation. Once cells had been seeded, those that had not adhered within the first two hours were removed by gentle rinsing with complete medium and then continued the course of the incubation. Upon completion of the 12-hour course, cells were fixed in a buffer composition determined in the RCIA protocol⁵⁹ where the medium was removed and replaced with a fixative solution (4% PFA diluted in minimal formulation of PHEM (0.1M Pipes, 1mM EGTA and 1mM MgSo₄). The initial 5 min were at room temperature, while the remaining 25 min were carried out over ice. After 30 min of incubation, the fixative solution was removed, and grids were gently rinsed three times in cold complete PHEM buffer (60mM Pipes, 25mM HEPES, 2mM MgSo₄, 10mM EGTA, pH 6.9)^{59,60}. The light microscopy information, collected on the inverted microscope set up described above was used to

improve the precision of selecting regions of interest for cryo-tomography data collection. For observation, each grid was flipped (cells face down) and placed in a MatTek dish in presence of PHEM. Areas of interest were identified, their positions recorded and phase contrast, fluorescence images were collected. Upon completion of this survey, grids were plunge frozen.

6.5.F. Vitrification and cryo-EM screening

Prior to vitrification, 1-2 μL of fiducial markers were added to the samples (Gold Colloid 15 nm, BBI Solutions). Vitrification was performed using a home-designed cryo-plunger; fixed and surveyed samples were manually plunge-frozen in liquid-nitrogen-cooled liquefied ethane and stored in liquid nitrogen until investigation. Freezing quality, along with assessment of sample preservation and amenability for cryo-ET investigation was conducted by an initial screening on a T12 Spirit (*ThermoFisher*) cryogenic transmission electron microscope (cryo-TEM) operated at 120 keV with an Eagle CMOS detector (*ThermoFisher*) or a Glacios (*ThermoFisher*) cryo-TEM operated at 200 keV with a Falcon 3EC direct electron detector. Using SerialEM⁶¹ we generated a montage for each cryo-grid and identified target cells for either direct imaging or cryo-FIB milling by following the finder markings on the grids. The fluorescence images of patterns and cells on patterns collected after fixation and before vitrification, were precisely aligned with images of the same targets obtained by cryo-EM, using a fiducial-less approach¹⁹.

6.5.G. Cryo-FIB Lamella preparation

Grids were clipped using special Autogrids containing a milling slot (*ThermoFisher*). The milling slot allowed the access of the gallium beam at shallow angles appropriate for the

cryo-lamellae preparation. Autogrids were transferred to the Aquilos 2 (*ThermoFisher*) dual beam cryo-FIB instrument. Cryogenic lamellae sites were chosen based on the cell-cell contact area observed by the scanning electron microscope (SEM) beam of the Aquilos 2 and correlated with the imaging obtained from the DM6 cryo-Light microscope (Leica Microsystems). Fluorescence images were aligned with the SEM tile set file using MAPS 3.14 software (*ThermoFisher*). A total of 14 cryo-lamellae were prepared using the semi-automated software AutoTEM 2.2.0 (*ThermoFisher*) for rough milling and the manual interface (XT User v20.1.0 *ThermoFisher Scientific*) for lamellae thinning and polishing with a final thickness below 300 nm. Autogrids were coated with a protective organometallic platinum layer by the gas injection system (GIS) of the Aquilos 2 for 12 s. Rectangular masks of 10 μm to 20 μm height were used for thinning and polishing steps of lamellae preparation at different currents using the gallium focused ion beam of the Aquilos 2. The rough milling step was performed at 0.5 nA ion beam current to generate a 2.5 μm thick lamella. The subsequent milling was performed at 0.3 nA ion beam current, thinning the lamellae to a thickness of 1.5 μm . The next step was performed at 0.1 nA current down to a lamella thickness of 1 μm and finally a current of 50 pA thinned the lamellae down to 500 nm. The fine polishing was performed at 30 pA ion beam current, resulting in a final thickness of 200-300 nm. Cells, patterns, and cryo-lamellae were imaged by SEM at 2 kV to 5 kV.

6.5.H. Correlative Light and Cryo-EM, cellular cryo-Tomography

Electron cryo-tomography data were collected using SerialEM⁶¹ or the Tomo package (*ThermoFisher*) on Titan Krios (*ThermoFisher*) or Glacios cryo-microscopes. The Titan Krios used for direct imaging was equipped with a Falcon 3EC direct electron detector

(*ThermoFisher*), the Titan Krios used for imaging lamellae was equipped with a K3 direct electron detector with a BioQuantum energy filter (Gatan Inc.) with energy slit set to 20 eV and using 70 μm condenser aperture and 100 μm objective aperture. Both Titans were operated at 300 keV. The Glacios microscope (*ThermoFisher*) used for some of the lamellae was operated at 200 keV and was equipped with a Falcon 3EC direct electron detector (*ThermoFisher*) and using 50 μm condenser aperture and 100 μm objective aperture. The autogrids were rotated 90° between Aquilos-2 and Glacios use to accommodate the tilt-axis orientation in the Glacios. All three instruments were equipped with extra-bright Field Electron Guns (XFEG) and were operated in parallel beam condition. For each grid, an overview image (atlas) of the entire grid was acquired to locate lamellae or pre-screened cells for direct imaging. Markings on the Finder grids, which are visible in light microscopy and cryo-EM/ET imaging modalities were used for guidance. Low-resolution images of the grid squares (pixel size 14-28 nm) containing the identified cells or lamellae enabled alignment of light microscopy and cryo-tomography images of the same cell. Following correlative identification of regions of interest were applicable, dose-symmetric tilt series ($\pm 60^\circ$, every 3°) were collected in batch mode under minimal dose conditions of about 90-120 $\text{e}^-/\text{\AA}^2$ and defocus between 8 and 14 μm with magnification resulting in a calibrated pixel size of 0.48 nm.

6.5.I. Tomographic reconstruction, volume processing and segmentation

Tomographic reconstructions were calculated automatically during data collection as implemented in the pyCoAn package (github.com/pyCoAn/distro), an extended python version of the CoAn package was employed. Briefly, immediately after acquisition, tilt series were automatically aligned and then reconstructed using the Simultaneous Iterative

reconstruction technique. Alignment and reconstruction statistics were used to determine quality scores that are provided in real time during data collection. For direct imaging (no milling), 31 tomograms from 7 cell pairs were acquired and analyzed. 15 lamellae from 14 cell pairs were prepared, and 26 tomograms were acquired and analyzed from these lamellae. 15 of these tomograms originating from 9 lamellae showed interpretable features. All interpretable reconstructions were enhanced using a Wiener-like filter accounting for the contrast transfer function at the respective defocus and an estimate of the spectral signal-to-noise ratio⁶². Segmentation of the features in the reconstructions was achieved using manual tracing of membranes with Amira⁶³ combined with fully automated and semiautomatic^{64,65} segmentation approaches as implemented in pyCoAn. Images of tomogram slices were generated with IMOD⁶⁶, images of segmentation models were generated with UCSF Chimera⁶⁷.

6.5.J. Optimization of imageable regions on 200-mesh Quantifoil copper/gold grid squares using micropatterning.

Determining the micropattern region to accommodate restrictions of the full grid: To find the regions obstructed by the rim of the grid itself when tilted, we oriented the grids such that the grid bars formed a 45° angle with the tilt axis, the orientation where the maximum amount of grid squares will be potentially obscured by tilting. We used Quantifoil R5/20 Holey Carbon 200 mesh gold grids. Eucentric height was determined and refined at the grid center, then the grid was rotated so that the grid bars and tilt axis formed a 45° angle, and tilted to +66°, the stage was moved along the X-axis and the Y-axis until the beam was obstructed. At these limits the grid was returned to 0° tilt and the location on the grid was recorded. This process was repeated after tilting to -66° to account for potential asymmetries in the setup. We found

that the mesh squares outside of the central 10 x 10 region of squares were potentially obstructed when tilting (Supplementary Figure 6.S10). Thus, we only patterned the central 10 x 10 squares of the grid.

Setting up the micropattern position within an individual grid square: For an individual square to be tested, the grid was rotated so that the grid bars and the tilt axis formed a 45° angle. Eucentric height was determined and refined at the center of the square. For each corner along the X and Y-axes, the stage was tilted to +66°, and then the stage was moved until the reticle marking the center of the detector within the viewing software was positioned in the corner of the grid square to be tested. The stage was then tilted to -66° and if the reticle was obscured, the stage was moved until it was visible again. The stage was then returned to 0° tilt, and an image was collected. In each of the 0° images the distance from the reticle to the two adjacent grid bars was measured. The greatest distance, 18 μm, defines the limit of the pattern size on a 200-mesh grid that allows unobstructed tilt series collection up to ±66°. For added tolerance, we use 20 μm as safety distance from the grid bars.

6.6. Data Availability

Tomography data are deposited at the EMDB (accession code EMD-15394) and the EMPIAR data base (accession code EMPIAR-11114). All other data supporting the findings of this study are available within the paper and its supplementary information files.

6.7. Acknowledgements

This work was supported National Institutes of Health grants R01 GM119948 (NV, DH, BP), NSF CMMI-183476 (BP) and seeding funding from UCSB CNSI. KL was supported by NSF GRFP and UCSB fellowship funding. LPD acknowledges useful

conversations with Dr. Leeya Engel (*Stanford University*). GG and DH thank the Nelson lab for their generous gift of the pEGFP-C1-ACAT plasmid and Dr. Kathleen A Siemers for helping with the plasmid, characterization work, and for providing the rabbit anti-alpha catenin antibody used in the immunofluorescence experiments. The authors acknowledge the use of the Nanostructures Cleanroom Facility and Microfluidics Lab within the California NanoSystems Institute, supported by the University of California, Santa Barbara and the University of California, Office of the President. The authors acknowledge the use of the Titan Krios, Tecnai Spirit T12 and auxiliary equipment at the cryo-EM unit of the Sanford Burnham Prebys Medical Discovery Institute, which was created in part with the support of US National Institutes of Health Grant S10-OD012372 (DH) and Pew Charitable Trust 864K625 innovation award funds (DH). The authors acknowledge access to the Titan Krios, Glacios, and Aquilos-2 instruments at the NanoImaging Core of the Institut Pasteur. The NanoImaging Core at Institut Pasteur was created with the help of a grant from the French Government's Investissements d'Avenir program (EQUIPEX CACSICE - Centre d'analyse de systèmes complexes dans les environnements complexes, ANR-11-EQPX-0008). The authors declare no competing financial interests.

6.8. Conclusions and Discussion

Cryo-ET has created an imaging revolution in structural biology over the last decade^{17,24}, but has been relatively low-throughput and is expensive and labor intensive. In recent years, there has been increased accessibility and interest in using protein micropatterns to regulate cell positioning on EM grids for cryo-ET^{30,31,35,49}. While this shift has the potential to enable higher sample throughput, the combination of regulated cell boundaries and an underlying carbon film substrate provides a poorly understood microenvironment for

cell biology. Here, we provide a nanometer scale characterization of photomolecularly adsorbed protein patterns, and of the carbon substrate. We interrogated the nanoarchitecture of the protein and bio-passivation layers using multiple imaging modalities including AFM, cryo-tomography and scanning electron microscopy correlated with light microscopy. This EM grid patterning workflow builds on and integrates previous techniques to i) tailor protein pattern sizes and seeding parameters to facilitate cell doublet formation and optimize the field of view for EM tilt tomography and ii) enable robust sample transportation for multi-site studies using remote equipment. These advances enable cryo-ET of the cell-cell interface as well as other cellular regions within epithelial doublets or single cells (before and after cryo-FIB). We identified well preserved, main cellular features (i.e., intact plasma membrane, mitochondria, ER, micro and intermediate filament, ribosomes) and captured cellular processes including endocytic events. Not only do these tomograms demonstrate the imaging resolution of our technique, but validate the functionality, vitality, and integrity of epithelial cells imaged in our samples.

Because substrate stiffness affects cellular behavior and junction activity, we investigated the mechanical behavior of the carbon films commonly used in cryo-ET studies. By comparing the effective spring constant extracted from AFM force curve measurements of hydrated carbon films on EM grids to an equivalent stiffness of a hydrogel used for cell culture, we estimate that the resistance of a cell pulling axially on the hydrated carbon film of a 200 mesh EM grid is comparable to pulling axially on a polyacrylamide hydrogel having an elastic modulus of 152-264 kPa. While this modulus would be slightly higher when in-plane traction forces are considered, this comparison places cryo-EM grids used in this study in the range of physiological epithelial tissue such as skin^{50,51} or arterial walls⁵². Thus, stiffness in

this range is frequently employed in mechanobiology studies using hydrogels^{41,53}. Our measurements provide essential parameters to predict how cells could potentially deform the carbon film in the context of our studies, as well as any future studies using the carbon film as a cell culture substrate.

Observed by standard light microscopy (resolving power > 200 nm), protein micropatterning appears to produce straight edges and reproducible patterns. However, we found that at the nanometer scale the edge of the pattern undulates due to the nature of the photopatterning method. Therefore, cells on photopatterned EM grids interact with an edge akin to the shape of a coastline viewed from an airplane, which has implications for incorporating assumptions of smooth boundaries into physical models of force distributions and may influence the localization of integrin binding sites (e.g., clustering of adhesions in nanoscale size pockets of the ECM patterns). Furthermore, the topographical differences between the ECM micropatterns and the encompassing PLL-g-PEG bio-passivation layer indicate that unlabeled ECM proteins can be visualized on the carbon film during electron tomography, facilitating flexible options for ECM proteins used for micropatterns. Our integration of multiple imaging modalities for ECM characterization (e.g., AFM, cryo-tomography, and correlative light and EM microscopies) will support molecular quantitative biophysical predictions.

Our workflow allows us to perform cryo-ET on minimally thick protein patterned samples independently of cryo-FIB. Here, the thickness of the carbon film ranges from 10-12 nm and gelatin patterns add a few nanometers in height, well within the thickness constraints of cryo-tomography (< 300 nm). These results serve as a reference for estimating thicknesses of other ECM proteins (e.g., laminin, fibronectin, or collagen) in other cryo-tomography

studies. For cellular samples or regions of interest too thick for electron permeation, our workflow incorporates cryo-FIB.

Cryo-FIB is necessary to isolate specific regions of the cell-cell contact to uncover the molecular structure of single cell-cell junctions. Cell-cell contacts can be up to several microns thick in the z direction (perpendicular to the grid surface), with a variety of junctions linking the two cells. Furthermore, different junctions can exist within the same z-plane. The punctate protein structure we revealed within the complex epithelial cell-cell contact exemplifies the pristine preservation of nanostructures within our workflow. The morphology at the imaged cell-cell contact is not consistent with the close apposition of membranes in a tight junction nor the cytoskeletal interactions or regular morphology of a desmosome. In fact, the morphology is reminiscent of punctate adherens junctions observed in conventional thin-section electron micrographs^{44,45} a dense network of irregular, rod-like connections between the plasma membranes similar to those observed with quick-freeze deep-edge microscopy of adherens junctions^{45,46}. Together, these facts lead us to believe that the imaged region is likely part of a punctate adherens junction. Future work will focus on exploring labelling methods for specific junctions under cryo-ET, allowing us to validate specific cell-cell junctions and elucidate their changes in molecular structure.

Our ability to segment single junctional structures within cell-cell contact sites serves as a significant innovation in determining the relationship between cell-cell communication and cell behavior. Future studies could therefore focus on how changes on the cellular microenvironment (e.g., ECM composition or cell shape) influence cell-cell coordination (e.g., protein localization, actin bundling, junction formation). Beyond epithelial studies, other mechanobiological systems can implement our workflow to determine the fundamental

structural changes governing cell-cell signaling. Our workflow not only can isolate these cell-cell contacts for study in the observable regions of an EM grid, but our implementation of cryo-FIB can isolate any region along the contact zone for detailed cryo-ET. Ultimately, this research paves the way for an enhanced understanding of i) how the cellular microenvironment regulates molecular changes at cell-cell contacts, and ii) how changes in epithelial contacts regulate aspects of cellular function.

6.9. References

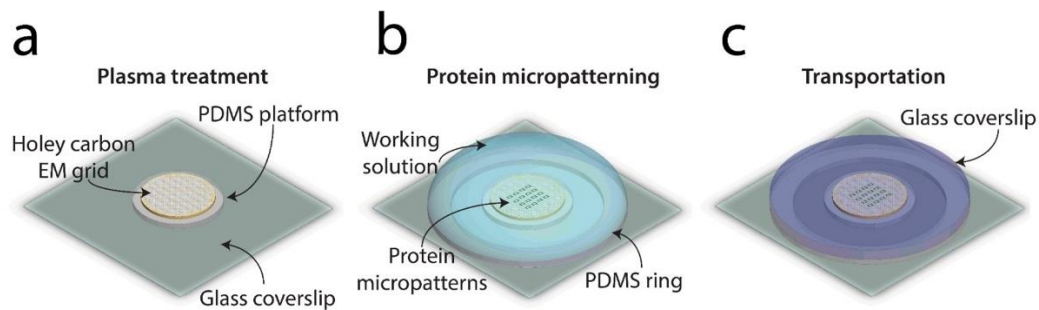
1. Barone, V. & Heisenberg, C. P. Cell adhesion in embryo morphogenesis. *Curr. Opin. Cell. Biol.* **24**, 148–153 (2012).
2. Hartsock, A. & Nelson, W. J. Adherens and tight junctions: structure, function and connections to the actin cytoskeleton. *Biochim. Biophys. Acta* **1778**, 660–669 (2008).
3. Senger, F. *et al.* Spatial integration of mechanical forces by α -actinin establishes actin network symmetry. *J. Cell. Sci.* **132**, (2019).
4. Sim, J. Y. *et al.* Spatial distribution of cell–cell and cell–ECM adhesions regulates force balance while maintaining E-cadherin molecular tension in cell pairs. *Mol. Biol. Cell.* **26**, 2456–2465 (2015).
5. Staddon, M. F., Cavanaugh, K. E., Munro, E. M., Gardel, M. L. & Banerjee, S. Mechanosensitive Junction Remodeling Promotes Robust Epithelial Morphogenesis. *Biophys. J.* **117**, 1739–1750 (2019).
6. le Duc, Q. *et al.* Vinculin potentiates E-cadherin mechanosensing and is recruited to actin-anchored sites within adherens junctions in a myosin II-dependent manner. *Journal of Cell Biology* **189**, 1107–1115 (2010).
7. Benham-Pyle, B. W., Pruitt, B. L. & Nelson, W. J. Mechanical strain induces E-cadherin-dependent Yap1 and β -catenin activation to drive cell cycle entry. *Science (1979)* **348**, 1024–1027 (2015).
8. Lecuit, T. Adhesion remodeling underlying tissue morphogenesis. *Trends Cell Biol.* **15**, 34–42 (2005).
9. Liu, Z. *et al.* Mechanical tugging force regulates the size of cell-cell junctions. *Proc. Natl. Acad. Sci. U.S.A.* **107**, 9944–9949 (2010).
10. Nishimura, T. & Takeichi, M. Remodeling of the adherens junctions during morphogenesis. *Curr. Top. Dev. Biol.* **89**, 33–54 (2009).
11. Huveneers, S. & de Rooij, J. Mechanosensitive systems at the cadherin-f-actin interface. *J. Cell Sci.* **126**, 403–413 (2013).
12. Indra, I., Troyanovsky, R. B., Shapiro, L., Honig, B. & Troyanovsky, S. M. Sensing actin dynamics through adherens junctions. *Cell Rep.* **30**, 2820–2833.e3 (2020).
13. Hart, K. C. *et al.* E-cadherin and LGN align epithelial cell divisions with tissue tension independently of cell shape. *Proc. Natl. Acad. Sci. U.S.A.* **114**, E5845–E5853 (2017).
14. Cai, D. *et al.* Mechanical feedback through E-cadherin promotes direction sensing during collective cell migration. *Cell* **157**, 1146–1159 (2014).

15. Sadeghipour, E., Garcia, M. A., Nelson, W. J. & Pruitt, B. L. Shear-induced damped oscillations in an epithelium depend on actomyosin contraction and E-cadherin cell adhesion. *Elife* **7**, 1–16 (2018).
16. Asano, S., Engel, B. D. & Baumeister, W. In Situ Cryo-Electron Tomography: A post-reductionist approach to structural biology. *J. Mol. Biol.* **428**, 332–343 (2016).
17. Turk, M. & Baumeister, W. The promise and the challenges of cryo-electron tomography. *FEBS Lett.* **594**, 3243–3261 (2020).
18. Schorb, M. *et al.* New hardware and workflows for semi-automated correlative cryo-fluorescence and cryo-electron microscopy/tomography. *J. Struct. Biol.* **197**, 83–93 (2017).
19. Anderson, K. L., Page, C., Swift, M. F., Hanein, D. & Volkman, N. Marker-free method for accurate alignment between correlated light, cryo-light, and electron cryo-microscopy data using sample support features. *J. Struct. Biol.* **201**, 46–51 (2018).
20. Sikora, M. *et al.* Desmosome architecture derived from molecular dynamics simulations and cryo-electron tomography. *Proc. Natl. Acad. Sci. U.S.A.* **117**, 27132–27140 (2020).
21. Marston, D. J. *et al.* High Rac1 activity is functionally translated into cytosolic structures with unique nanoscale cytoskeletal architecture. *Proc. Natl. Acad. Sci. U.S.A.* **116**, 1267–1272 (2019).
22. Chakraborty, S., Jasnin, M. & Baumeister, W. Three-dimensional organization of the cytoskeleton: A cryo-electron tomography perspective. *Protein Science* **29**, 1302–1320 (2020).
23. Tee, Y. H. *et al.* Cellular chirality arising from the self-organization of the actin cytoskeleton. *Nat. Cell Biol.* **17**, 445–457 (2015).
24. Rigort, A. *et al.* Micromachining tools and correlative approaches for cellular cryo-electron tomography. *J. Struct. Biol.* **172**, 169–179 (2010).
25. Lam, V. & Villa, E. Practical approaches for cryo-FIB milling and applications for cellular cryo-electron tomography. *Methods in Molecular Biology* **2215**, 49–82 (2021).
26. Arnold, J. *et al.* Site-specific cryo-focused ion beam sample preparation guided by 3D correlative microscopy. *Biophys. J.* **110**, 860–869 (2016).
27. Schaffer, M. *et al.* Optimized cryo-focused ion beam sample preparation aimed at in situ structural studies of membrane proteins. *J. Struct. Biol.* **197**, 73–82 (2017).
28. Rigort, A. *et al.* Focused ion beam micromachining of eukaryotic cells for cryoelectron tomography. *Proc. Natl. Acad. Sci. U.S.A.* **109**, 4449–4454 (2012).
29. Wang, K., Strunk, K., Zhao, G., Gray, J. L. & Zhang, P. 3D structure determination of native mammalian cells using cryo-FIB and cryo-electron tomography. *J. Struct. Biol.* **180**, 318–326 (2012).
30. Engel, L. *et al.* Extracellular matrix micropatterning technology for whole cell cryogenic electron microscopy studies. *Journal of Micromechanics and Microengineering* **29**, 115018 (2019).
31. Toro-Nahuelpan, M. *et al.* Tailoring cryo-electron microscopy grids by photo-micropatterning for in-cell structural studies. *Nature Methods* **17**, 50–54 (2019).
32. Lee, J., Abdeen, A. A., Zhang, D. & Kilian, K. A. Directing stem cell fate on hydrogel substrates by controlling cell geometry, matrix mechanics and adhesion ligand composition. *Biomaterials* **34**, 8140–8148 (2013).
33. Ribeiro, A. J. S. *et al.* Contractility of Single cardiomyocytes differentiated from pluripotent stem cells depends on physiological shape and substrate stiffness. *Proc. Natl. Acad. Sci. U.S.A.* **112**, 12705–12710 (2015).
34. Tseng, Q. *et al.* Spatial organization of the extracellular matrix regulates cell-cell junction positioning. *Proc. Natl. Acad. Sci. U.S.A.* **109**, 1506–1511 (2012).
35. Sibert, B. S., Kim, J. Y., Yang, J. E. & Wright, E. R. Micropatterning transmission electron microscopy grids to direct cell positioning within whole-cell cryo-electron tomography workflows. *J. Vis. Exp.* **2021**, (2021).
36. Engel, L. *et al.* Lattice micropatterning for cryo-electron tomography studies of cell-cell contacts. *J. Struct. Biol.* **213**, 107791 (2021).

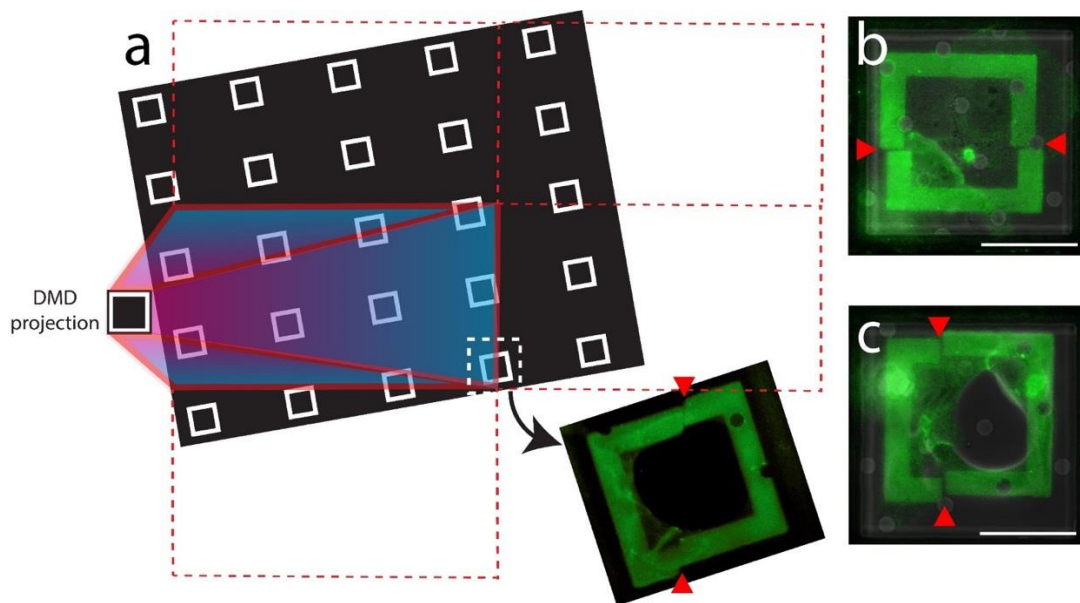
37. Strale, P.-O. *et al.* Multiprotein printing by light-induced molecular adsorption. *Advanced Materials* **28**, 2024–2029 (2016).
38. Yeung, T. *et al.* Effects of substrate stiffness on cell morphology, cytoskeletal structure, and adhesion. *Cell Motil. Cytoskeleton* **60**, 24–34 (2005).
39. Polio, S. R. *et al.* Extracellular matrix stiffness regulates human airway smooth muscle contraction by altering the cell-cell coupling. *Scientific Reports* *2019* **9**:1 **9**, 1–12 (2019).
40. Boudou, T., Ohayon, J., Picart, C. & Tracqui, P. An extended relationship for the characterization of Young's modulus and Poisson's ratio of tunable polyacrylamide gels. *Biorheology* **43**, 721–728 (2006).
41. Denisin, A. K. & Pruitt, B. L. Tuning the range of polyacrylamide gel stiffness for mechanobiology applications. *ACS Appl. Mater. Interfaces* **8**, 21893–21902 (2016).
42. Schoen, I., Pruitt, B. L. & Vogel, V. The yin-yang of rigidity sensing: How forces and mechanical properties regulate the cellular response to materials. *Annu. Rev. Mater. Res.* **43**, 589–618 (2013).
43. Harris, T. J. C. & Tepass, U. Adherens junctions: from molecules to morphogenesis. *Nature Reviews Molecular Cell Biology* *2010* **11**:7 **11**, 502–514 (2010).
44. Barth, M. *et al.* Cordial connections: Molecular ensembles and structures of adhering junctions connecting interstitial cells of cardiac valves in situ and in cell culture. *Cell Tissue Res.* **337**, 63–77 (2009).
45. Miyaguchi, K. Ultrastructure of the zonula adherens revealed by rapid-freeze deep-etching. *J. Struct. Biol.* **132**, 169–178 (2000).
46. Hirokawa, N. & Heuser, J. E. Quick-freeze, deep-etch visualization of the cytoskeleton beneath surface differentiations of intestinal epithelial cells. *Journal of Cell Biology* **91**, 399–409 (1981).
47. Erami, Z., Timpson, P., Yao, W., Zaidel-Bar, R. & Anderson, K. I. There are four dynamically and functionally distinct populations of E-cadherin in cell junctions. *Biol. Open* **4**, 1481–1489 (2015).
48. Gorelick, S. *et al.* PIE-scope, integrated cryo-correlative light and FIB/SEM microscopy. *Elife* **8**, (2019).
49. Tee, Y. H. *et al.* Cellular chirality arising from the self-organization of the actin cytoskeleton. *Nature Cell Biology* *2014* **17**:4 **17**, 445–457 (2015).
50. Iivarinen, J. T., Korhonen, R. K., Julkunen, P. & Jurvelin, J. S. Experimental and computational analysis of soft tissue stiffness in forearm using a manual indentation device. *Med. Eng. Phys.* **33**, 1245–1253 (2011).
51. Liang, X. & Boppart, S. A. Biomechanical properties of in vivo human skin from dynamic optical coherence elastography. *IEEE Trans. Biomed. Eng.* **57**, 953–959 (2010).
52. Wagenseil, J. E. & Mecham, R. P. Vascular extracellular matrix and arterial mechanics. *Physiol. Rev.* **89**, 957–989 (2009).
53. Engler, A. J., Sen, S., Sweeney, H. L. & Discher, D. E. Matrix elasticity directs stem cell lineage specification. *Cell* **126**, 677–689 (2006).
54. Tavmjong Bah. *Inkscape - Guide to a Vector Drawing Program.* (2007).
55. Edelstein, A. D. *et al.* Advanced methods of microscope control using µManager software. *J. Biol. Methods* **1**, e10 (2014).
56. Butt, H. J., Cappella, B. & Kappl, M. Force measurements with the atomic force microscope: Technique, interpretation and applications. *Surf. Sci. Rep.* **59**, 1–152 (2005).
57. Frank, I. W., Tanenbaum, D. M., Zande, A. M. van der & McEuen, P. L. Mechanical properties of suspended graphene sheets. *Journal of Vacuum Science & Technology B: Microelectronics and Nanometer Structures Processing, Measurement, and Phenomena* **25**, 2558 (2007).
58. Castellanos-Gomez, A., Singh, V., van der Zant, H. S. J. & Steele, G. A. Mechanics of freely-suspended ultrathin layered materials. *Ann. Phys.* **527**, 27–44 (2015).
59. Gaietta, G., Swift, M. F., Volkmann, N. & Hanein, D. Rapid tool for cell nanoarchitecture integrity assessment. *J. Struct. Biol.* **213**, (2021).

60. Anderson, K. L. *et al.* Nano-scale actin-network characterization of fibroblast cells lacking functional Arp2/3 complex. *J. Struct. Biol.* **197**, 312–321 (2017).
61. Mastronarde, D. N. Automated electron microscope tomography using robust prediction of specimen movements. *J. Struct. Biol.* **152**, 36–51 (2005).
62. Tegunov, D. & Cramer, P. Real-time cryo-electron microscopy data preprocessing with Warp. *Nature Methods* 2019 16:11 **16**, 1146–1152 (2019).
63. Stalling, D., Westerhoff, M. & Hege, H.-C. Amira - a Highly Interactive System for Visual Data Analysis. *The visualization handbook* **38**, 749–767 (2005).
64. Volkman, N. A novel three-dimensional variant of the watershed transform for segmentation of electron density maps. *J. Struct. Biol.* **138**, 123–129 (2002).
65. Xu, X. P., Page, C. & Volkman, N. Efficient extraction of macromolecular complexes from electron tomograms based on reduced representation templates. *Comput. Anal. Images Patterns* **9256**, 423–431 (2015).
66. Kremer, J. R., Mastronarde, D. N. & McIntosh, J. R. Computer visualization of three-dimensional image data using IMOD. *J. Struct. Biol.* **116**, 71–76 (1996).
67. Goddard, T. D., Huang, C. C. & Ferrin, T. E. Software extensions to UCSF Chimera for interactive visualization of large molecular assemblies. *Structure* **13**, 473–482 (2005).

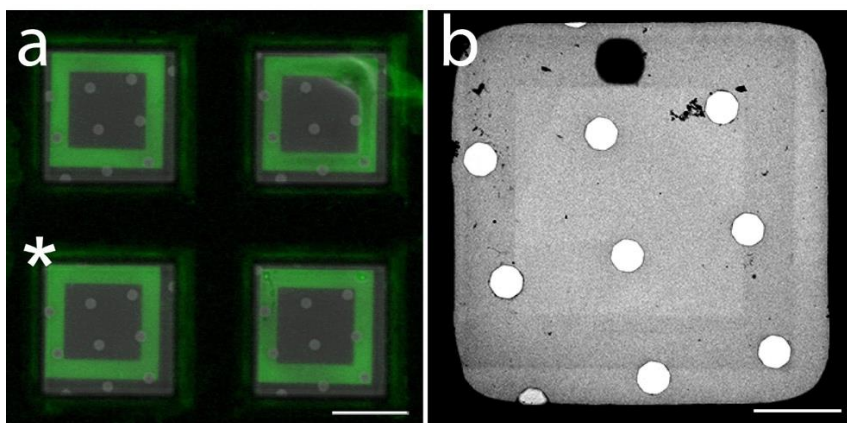
6.10. Supplemental Information



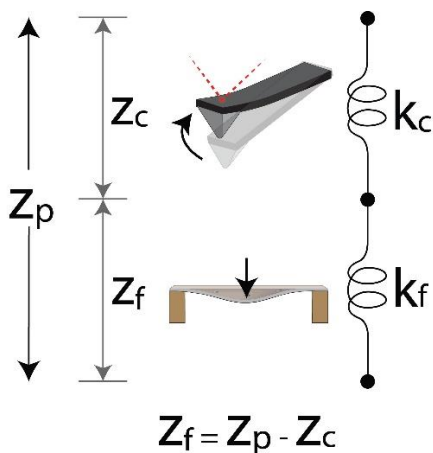
Supplementary Figure 6.S1. Protocol for grid handling and transportation. (a) A thin PDMS platform (250 μm) adheres the metal mesh of the grid, allowing the holey carbon mesh of the top side to be exposed to plasma. (b) A thicker (600 μm), 12 mm diameter PDMS ring is added around the grid following plasma treatment to create a cohesive well for protein patterning, buffer exchange, and (c) a protective and robust seal using a 12 mm glass coverslip.



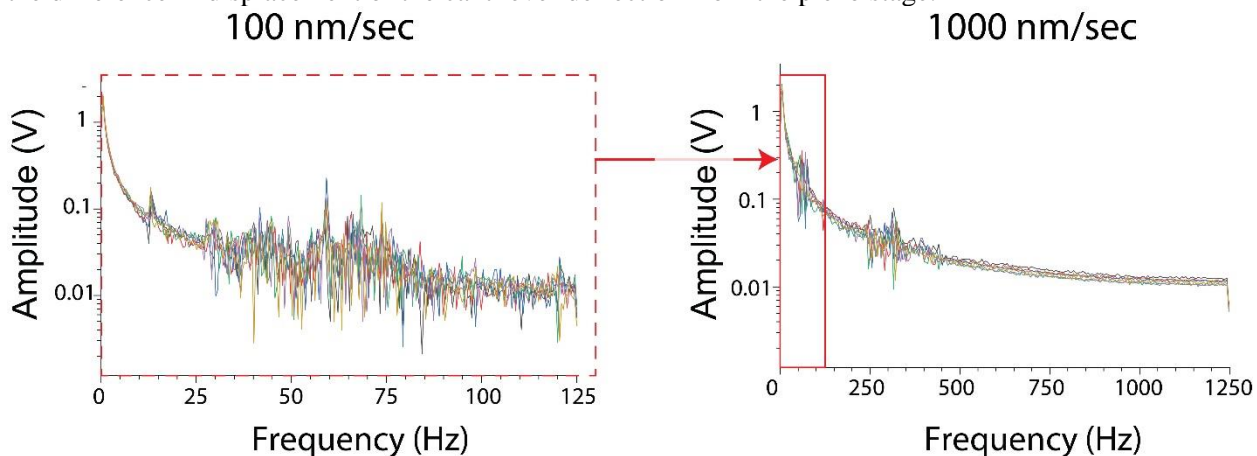
Supplementary Figure 6.S2. Stitching of DMD projections cause pattern misalignment. (a) Calibrated DMD size was 1824 px by 1140 px (approximately 506 μm by 316 μm). Using a 10 x 10 digital mask of individual patterns covering a larger area, the stitching of several DMDs resulted in several misalignments in our initial single patterns. DMD projection zones are indicated by dashed red boxes. (b, c) Misalignment errors can be mitigated using digital masks for single patterns (see Alveole Experiment Wizard) or confining arrays of patterns to single DMDs (e.g., a 4 x 4 array). Scale bars are 30 μm .



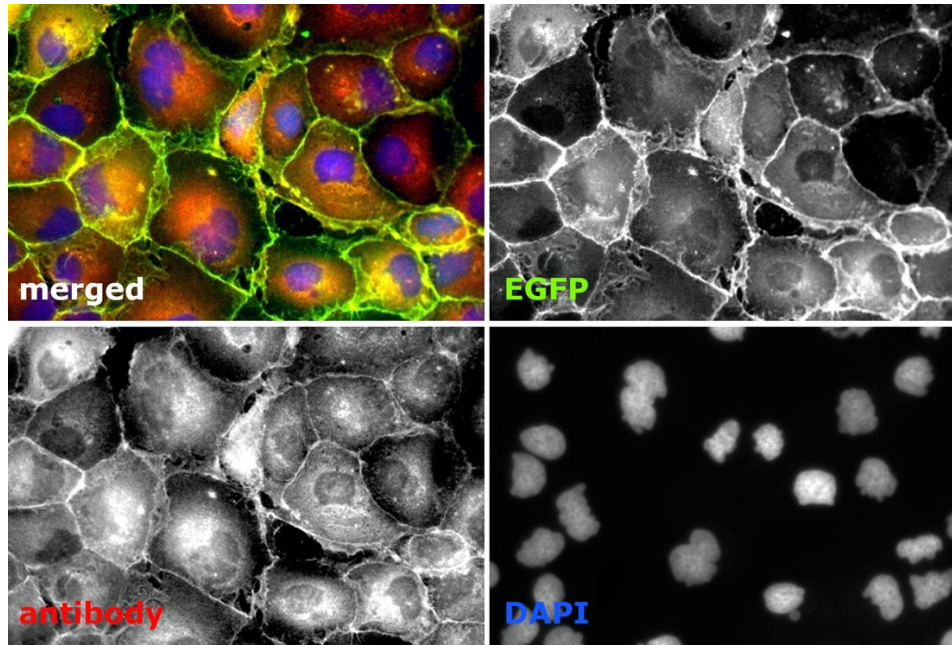
Supplementary Figure 6.S3. Pattern visualization. (a) Fluorescence and (B) cryo-EM images of micropatterned regions. The pattern marked with a white asterisk in a is shown in b after vitrification of the sample. The pattern is visible in the projection image shown in b due to the density differences between pattern and bio-passivated area. Scale bars, 40 μm (a), 20 μm (b). ECM patterns are 66.5 x 66.5 μm .



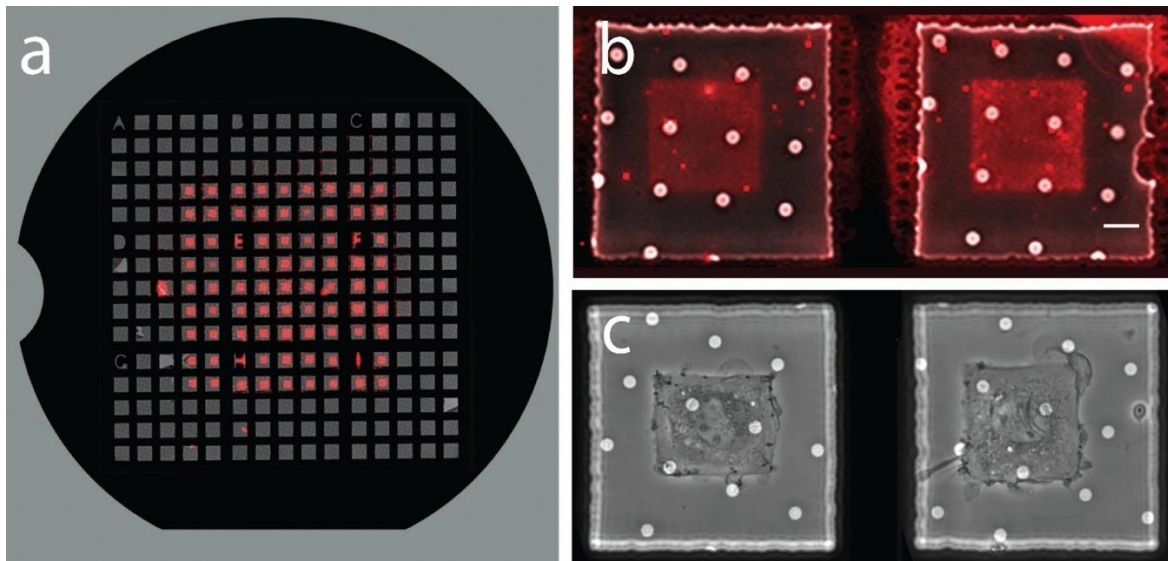
Supplementary Figure 6.S4. Dual spring model of carbon film under load. As the piezo stage moves (z_p) toward the carbon film, both the cantilever and carbon film are deflected elastically (z_c and z_f with spring constants k_c and k_f , respectively). We calculate the z_f using this dual spring model as the difference in displacement of the cantilever deflection from the piezo stage.



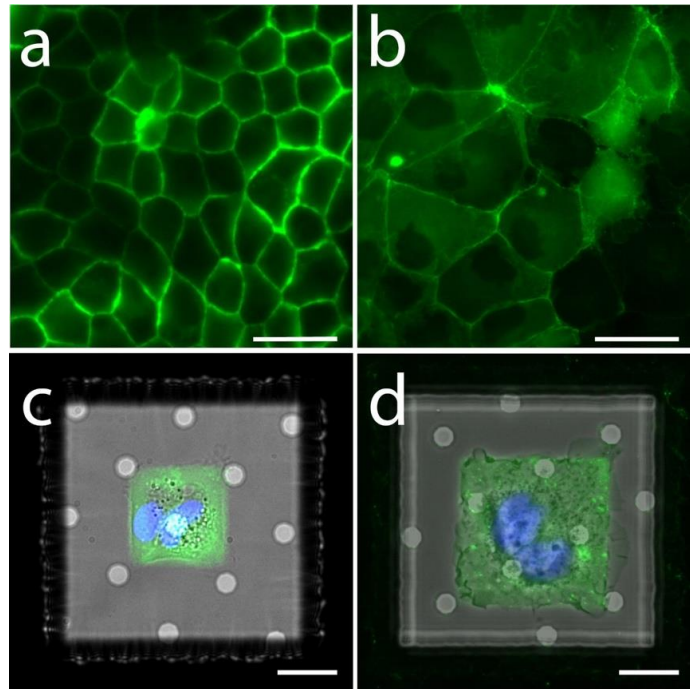
Supplementary Figure 6.S5. Fast Fourier Transform (FFT) of AFM Measurements. AFM measurements were performed at loading rates of 100 and 1000 nm/s ($n=6$ for both, each n represented as a different color). The AFM data sample rate and measurement bandwidth were proportional to loading rate (e.g. there is no frequency data above 125 Hz accessible for the 100 nm/s loading rate). The red rectangle in the 1000 nm/s graph denotes the equivalent range accessible for the 100 nm/s loading rate (dashed red rectangle). Most distinct noise sources occurred at two locations on the frequency spectra: ~ 60 Hz and ~ 300 Hz. These same sources were present for both loading rates, suggesting that the noise was not a function of the measurement procedure.



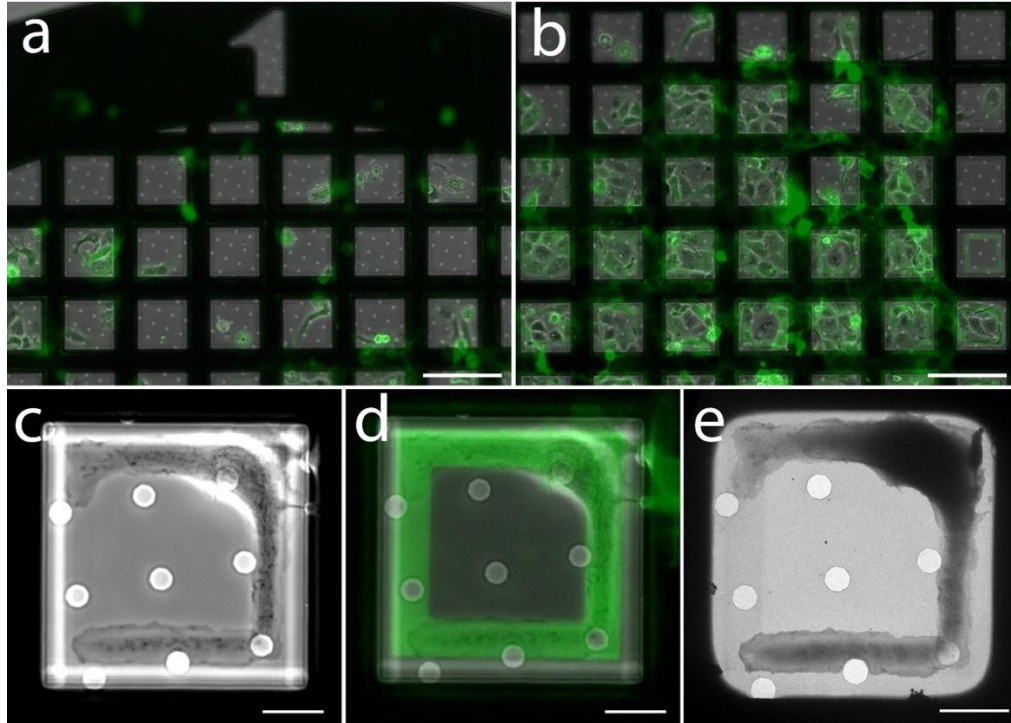
Supplementary Figure 6.S6. Characterization by immunofluorescence of the stable cell line used in this study comparing expression and localization of the EGFP-tagged alpha-E catenin (EGFP) with the native form of alpha E catenin expressed by PTK1 cells (antibody). Cells were allowed to adhere and form cell-cell contacts for 12 hours before fixation. The expression of the tagged protein is homogeneous, its signal for cell-cell contacts is strong and well defined, and its localization overlaps well with the native protein.



Supplementary Figure 6.S7. Workflow is agnostic to both ECM and cell type. (a) Phase contrast light microscopy image of entire grid area overlaid with the fluorescence image of photopatterned Rhodamine-labeled Fibronectin. The 45 μm square patterns are surrounded by bio-passivation made on the holey carbon film of the grid. The use of different ECM protein and fluorescence label, and different patterning mode from Figures 4 and S3, exemplifying the versatility of the patterning approach and ease of incorporating into the workflow. (b) Rhodamine fluorescence images overlaid with their corresponding phase contrast light microscopy images showing the fibronectin patterns within the grid squares. (c) Phase contrast light microscopy images of patterned areas with MEF cells adopting the shape of the pattern and being confined within the patterned areas. Scale bars = 15 μm .

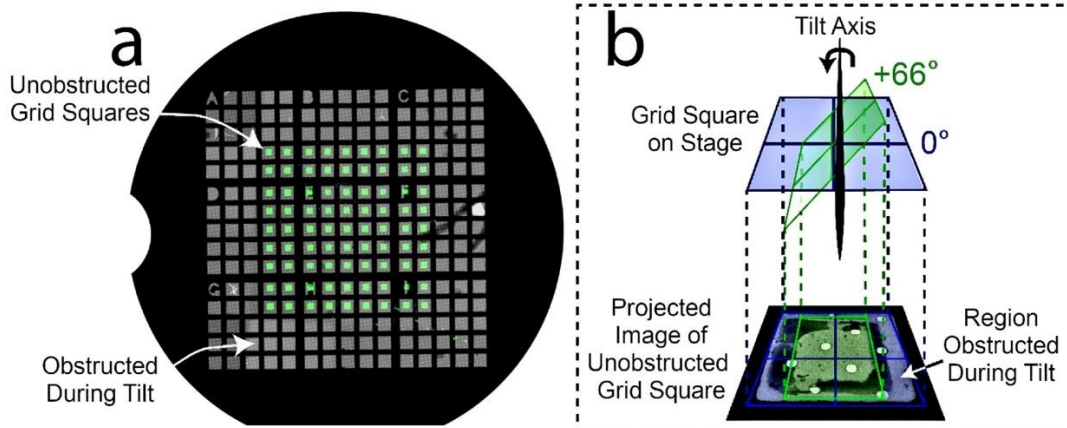


Supplementary Figure 6.S8. Micropattern sizing can be tuned to isolate cell pairs of different cell types. (a) Confluent MDCK cells (E cadherin, GFP) are on average smaller in area than (b) confluent ptk-1 cells (alpha E catenin EGFP). (c) 35 x 35 μm ECM squares successfully adhere MDCK cell pairs, while (d) larger 50 x 50 μm ECM squares successfully adhere PTK-1 cell pairs. Scale bars are 25 μm (a-b) and 20 μm (c-d). Note that the pattern's Oregon green signal intensity is much higher than that of the tagged proteins. Consequently, the protein fluorescence signals appear diminished in c and d as compared to a and b owing to adjustment of the fluorescence levels when capturing the image.

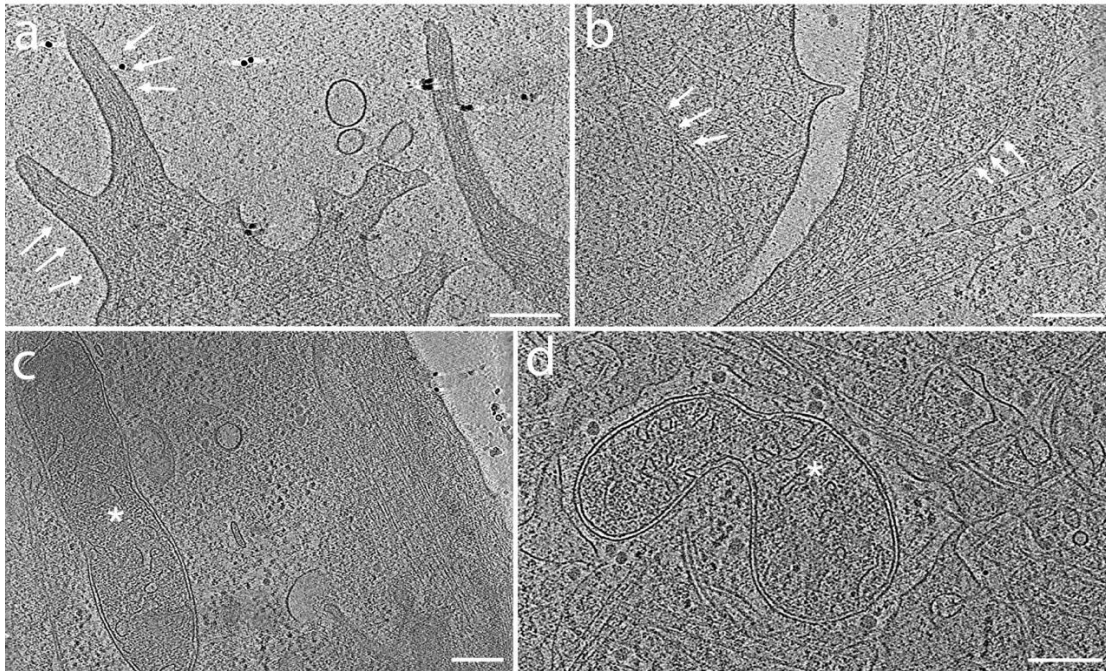


Supplementary Figure 6.S9. Optimization of pattern sizing and cell seeding parameters.

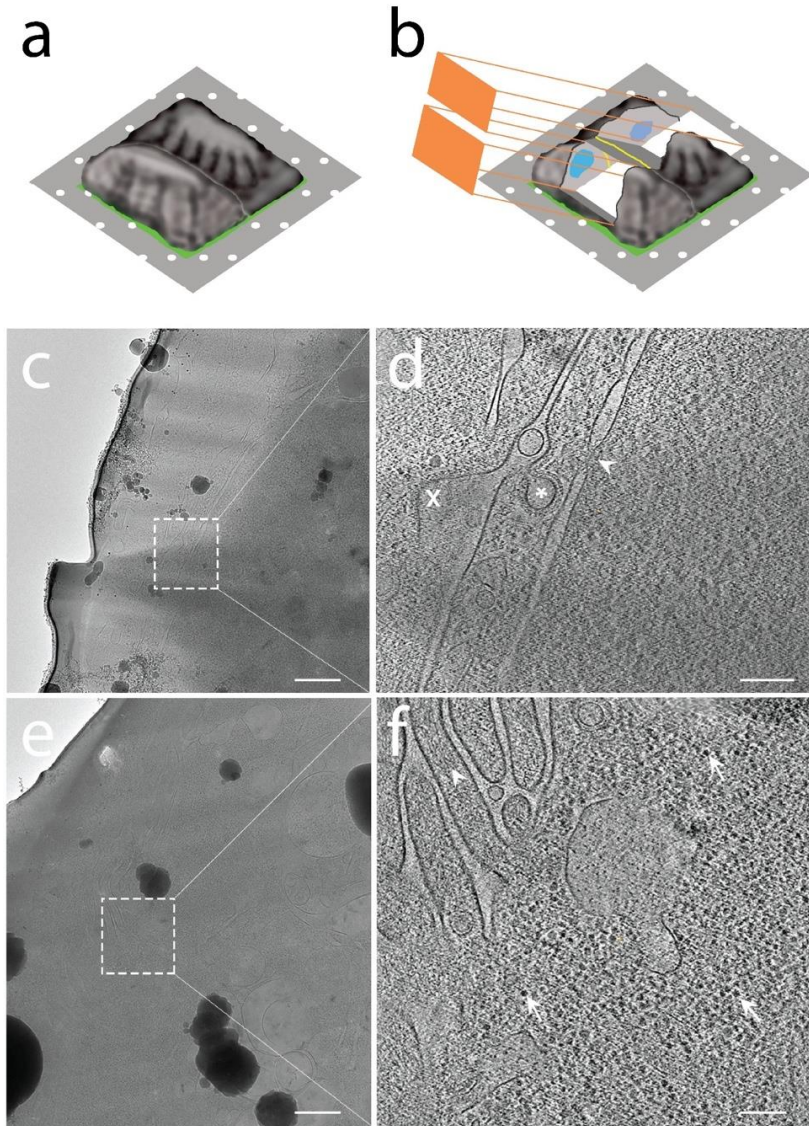
Examples of (a) incomplete bio-passivation, (b) excessive cell density at plating and (c-e) undesired cell positioning on the pattern. (A) Incomplete bio-passivation leads to cell adhesion outside of patterns, while high cell density along with unresolved cell clustering result in non-specific adhesion of large number of cells both on patterns and outside of patterns, as show in B. Large clusters of cells are also capable of adhering to neighboring patterns, forming a bridge in between them (white arrow in b). (c-e) An individual cell is shown to spread exclusively on the patterned area, while avoiding the bio-passivated regions. (c) Phase contrast, (d) overlay of fluorescence (Oregon Green gelatin and EGFP- alpha E catenin) and phase contrast images and (e) corresponding cryo-EM image. Scale bars, 100 μm (a, b) and 20 μm (c-e).



Supplementary Figure 6.S10. Determination of optimal regions on 200-mesh EM grid for tomography data collection. (a) The central 10 x 10 region of grid squares is unobstructed for $\pm 66^\circ$ tilt range and is patterned (here with Oregon-green labeled gelatin). The region outwards from this central region is potentially obstructed physically by the rim of the grid, the microscope sample holder, or the clip ring and is not patterned. (b) During tilting, an approximately 20-micron wide area on either side of the imageable region of Individual grid squares becomes obstructed by the non-transparent grid bars (red).



Supplementary Figure 6.S11. Vitrification prevents structural collapse and keeps the sample's ultrastructure close to its native state. Following fixation, treatment and plunge freezing with the suggested protocol, vitrified samples are investigated by cryo-ET. Single slices from tomograms targeting (a) plasma membrane regions (white arrows), (b) actin filaments (white arrows) and (c, d) mitochondria (white asterisk) display excellent preservation of the cellular nanoarchitecture. Scale bars, 200 nm



Supplementary Figure 6.S12. In situ cryo-lamellae of cells confined to micropatterns deposited on EM grids. (a) Illustration showing the targeting of a region of interest with tentative cell-cell contacts using the topology of cell doublets confined by a micropattern as it is visible in the cryogenic scanning electron microscope (cryo-SEM) beam of the cryo-FIB dual-beam instrument. (b) Material is removed above and below the target region by milling using the ion beam of the cryo-FIB instrument to generate a lamella thin enough for cryo-ET imaging. The orange rectangles indicate the milling pattern above and below the target cell-cell contact region as identified by cryo-SEM imaging modality. The boundary between the two cells, where the tentative cell-cell contacts are located, is shown as a yellow line. The nuclei are marked in blue. (c) Transmission cryo-EM image of a region adjacent to the area marked in Figure 6a. (d) 2-nm thick virtual slice through a tomogram of the lamella region marked by the white box in c. Two endocytotic events are visible, one in each of the cells. To the right, there is a clathrin-coated pit (marked by an asterisk), to the left, a budding endocytic vesicle (marked by x). Interestingly, the nucleus of the right cell is near the plasma membrane with a nuclear pore clearly visible (marked by an arrowhead). (e) Transmission cryo-EM image of a region from a different lamella prepared from a different PTK1 cell doublet. (f) 2-nm thick virtual slice through a tomogram of the lamella region marked by the white box in E. On the top left,

several cellular protrusions, some with clearly visible actin bundles (marked with arrowhead), are present. There is a high density of identifiable ribosomes in this tomogram (some are marked by arrows). Scale bar (c and e) = 500 nm, and (d and f) = 200 nm

Chapter 7

Mimicking cell-cell interactions in a single cell model

7.1. Preface

The contents of this chapter are reproduced (with permission) from a manuscript submitted for peer review and included within the dissertation of Kerry V. Lane. I have reproduced here only the sections which provide context for this experimental work (Abstract and Introduction), as well as the experimental work which I performed (Results). All other results and discussion on cardiomyocyte analysis have been omitted.

This chapter focuses on a study I co-led with my lab mate Kerry Lane. The study utilizes a dual protein model to investigate the effects of the adherens junction on cardiomyocyte maturity. During my PhD I have gained significant expertise in protein patterning and photomolecular adsorption of proteins. Meanwhile, a large goal of Kerry's PhD research has been to increase cardiomyocyte maturity of a single cell *in vitro* model. I led the development and implementation of the dual-protein patterning method used within this work by building on previous techniques with photomolecular adsorption of proteins. My experimental protocol is reproduced in *Methods: Protein patterning of glass coverslips*. Kerry applied these dual-protein patterns to her polyacrylamide substrates (see section *Preparation of polyacrylamide hydrogels*, reproduced here for context). These substrates with dual protein patterns were then used for single cell cardiomyocytes to mimic cell-cell junctions and detect phenotypic differences. I also aided in experiment planning, design, as well as conceptualization within this study.

This exciting study innovates the field in 2 major ways: i) we developed and applied a dual protein patterning method with high resolution spatial control to mimic cell-cell junctions, and ii) we integrated this cell-cell junction mimic to alter cardiomyocyte regulation.

7.2. Abstract

Human induced pluripotent stem cell-derived cardiomyocytes (hiPSC-CMs) are a promising human model for studies of heart structure and function. However, their immaturity (e.g., lower sarcomere alignment and contractility) relative to adult human CMs limits their physiological relevance. While controlling cellular shape with protein micropatterning has enhanced maturity of single-cell hiPSC-CMs, they lack a key driver in CM maturity: cell-cell contacts. N-cadherin is a key protein in cell-cell contacts, playing an important role in adherens junctions, desmosomes, and gap junctions. Here, we used a novel dual-protein patterning process to geometrically control single single-cell cardiomyocytes while imitating cell-cell interactions with N-cadherin. We first photopatterned two proteins on a glass coverslip using a two-step process with photomolecular adsorption of proteins. A laminin rectangle served to mimic the cell-ECM interaction, which was flanked by N-cadherin caps to mimic cell-cell contacts. After both photopatterning steps were complete, we transferred the pattern from the coverslip to a physiologically relevant ~10 kPa polyacrylamide hydrogel. We seeded α -actinin-tagged hiPSC-CMs on the dual-protein-patterned hydrogel and verified interaction between the hiPSC-CMs and the N-cadherin caps via immunofluorescent staining. We found hiPSC-CMs on dual-protein patterns have a higher cell area and contractility in the direction of sarcomere organization than those on single-protein patterns, but no difference in sarcomere organization or force production. This indicates that N-cadherin modestly improves the single-cell patterned hiPSC-CM model but

is not sufficient to replicate the role of cell-cell contacts in CM development for in vitro hiPSC-CM systems.

7.3. Introduction

Human induced pluripotent stem cell derived cardiomyocytes (hiPSC-CMs) are a promising model to bridge the gap between human heart function and the studies of the human heart in animal models¹⁻⁴. Developments in cardiomyocyte (CM) differentiation protocols have expanded the use of hiPSC-CMs⁵, however, there remain limitations to the use of hiPSC-CMs as models for mature human CMs. There are critical differences in structure and function between hiPSC-CMs and mature human CMs, including CM morphology, sarcomere organization, and contractile force^{1,6}. Mature human CMs have an elongated shape with an average length-to-width ratio of approximately 7:1 and highly aligned sarcomeres. hiPSC-CMs are smaller and irregularly shaped with unaligned sarcomeres, similar to fetal human CMs^{1,7}. Structure dictates function, and more organized and elongated CMs produce higher contractile forces than unorganized, irregularly-shaped CMs^{1,7}.

One approach to improving hiPSC-CM structural and functional maturity is by regulating the morphology of single hiPSC-CMs⁸⁻¹². Morphological control is often accomplished by culturing cells on rectangular extracellular matrix (ECM) protein patterns in aspect ratios similar to those of mature human CMs^{1,7,13,14}. Patterned hiPSC-CMs present more highly aligned myofibrils than unpatterned hiPSC-CMs, which produce greater contractile forces and other markers of improved maturity (e.g., calcium transient anisotropy⁷). While patterned hiPSC-CMs are a significant advancement in enhancing

maturity of single hiPSC-CMs, a current limitation of this single cell model is that it lacks cell-cell junctions.

In the heart, CMs attach to the ECM along the length of the cell via focal adhesions and to neighboring CMs at the ends of the cell at intercalated discs¹⁵. Intercalated discs are made up of three junction types - adherens junctions, desmosomes, and gap junctions¹⁵. Adherens junctions and desmosomes link CMs mechanically, while gap junctions mediate small molecule and ion transport between CMs¹⁶. N-cadherin plays a key role in adherens junctions and desmosomes and while it is less abundant in gap junctions, it has been shown to play an important role in their functioning¹⁶⁻¹⁸.

Few studies have investigated the role of N-cadherin in hiPSC-CMs, but multiple studies have looked at N-cadherin in murine and other animal models, with results indicating the importance of N-cadherin in myofibril formation and stability and the role of N-cadherin in myocyte development and disease¹⁹⁻²⁴. Studies of neonatal ventricular rat myocytes have shown that N-cadherin plays a role in sarcomere organization and that force transduction and subcellular organization via N-cadherin are unique from those mediated by focal adhesions^{22,23}. These results indicate that N-cadherin is relevant to myocyte structure, function, and development, making N-cadherin a good candidate for improving the hiPSC-CM model. Here, we propose replicating both cell-ECM and cell-cell interactions to enhance the maturity of the single cell hiPSC-CM model.

In this study, we improved the single-cell hiPSC-CM model by mimicking cell-cell and cell-ECM interactions via spatially accurate dual protein patterns of Laminin and N-cadherin. We sought to develop a method for consistent and precise dual-protein patterning and to apply dual protein patterning to our single-cell hiPSC-CM model.

7.4. ¹Results and discussion

To create a reductionist model of CM-CM contacts found in native heart tissue, we created two single cell patterns: i) single protein patterns consisting of laminin rectangles, and ii) dual protein patterns, consisting of laminin rectangles flanked by N-cadherin caps. To achieve this goal, we utilized photomolecular adsorption of proteins. We first plasma treated glass coverslips and incubated them with a bio passivation layer, poly(l-lysine)-graft-poly(ethylene glycol) (PLL-g-PEG). Using a two-step UV exposure process, we patterned both protein A and laminin ECM in specific orientations of the glass coverslip (Figure 7.1a). Our method of creating an alternating array of single and dual protein patterns enabled both control (no N-cadherin mimic) and experimental (with N-cadherin mimic) cells on the same sample. We then transferred these patterned coverslips to a ~10kPa polyacrylamide (PA) hydrogel, which was incubated with N-cadherin for binding with protein A (Figure 7.1b). This process yielded up to 360 separate patterns for single cells on each PA hydrogel (Figure 7.1c). We used a 10 kPa PA hydrogel because of its physiologically relevant stiffness and its amenability to TFM. We verified the patterning and the pattern transfer to PA hydrogel using a laminin antibody and a pan-cadherin antibody (Figure 7.1d). To determine if these dual protein patterns sufficiently replicate adherens junction CM-CM interactions and enhance hiPSC-CM maturity, we assessed hiPSC-CM morphology, force production, and sarcomere organization and contractility on single and dual protein patterns.

¹ Section 7.4 is adapted from the original study to provide additional context on the protocol used for dual protein patterning

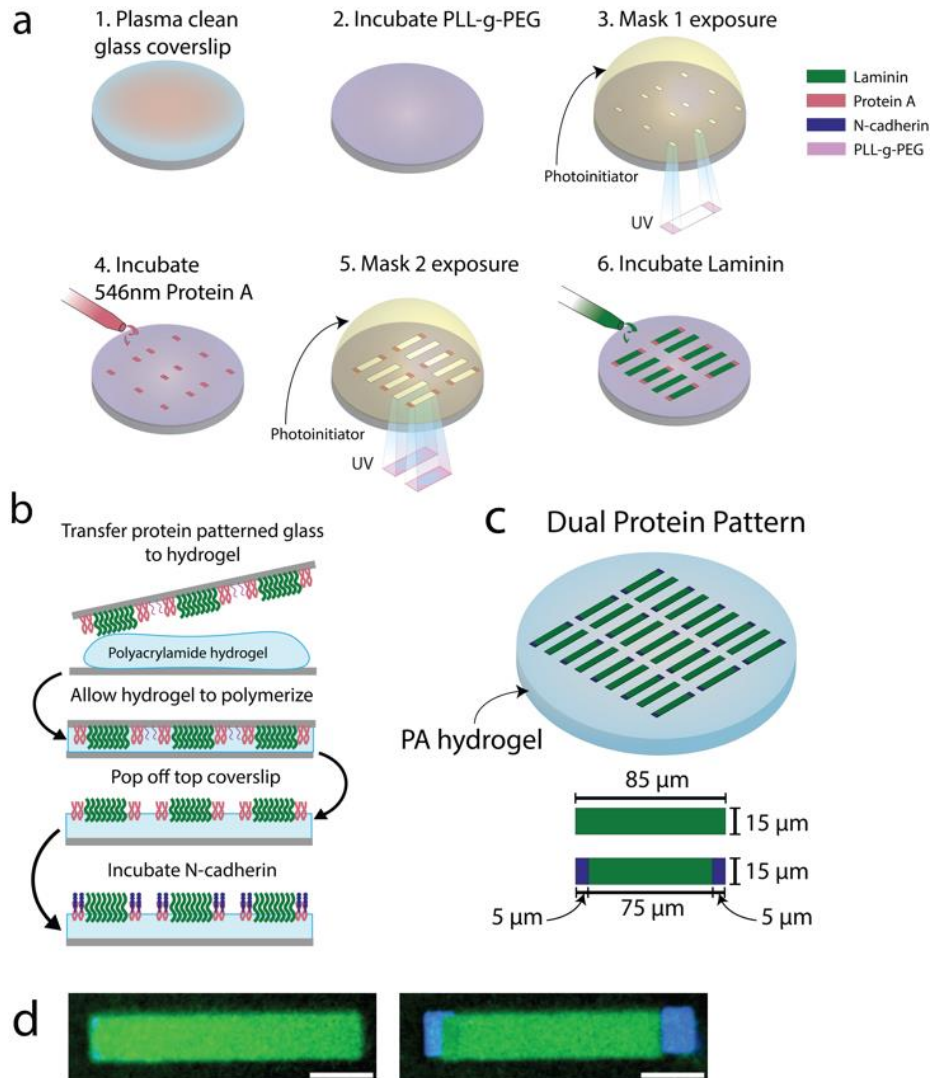


Figure 7.1. Dual-protein patterning of PA hydrogels.

(a) Process flow of dual protein patterning on a glass coverslip using photomolecular adsorption. (b) Process flow of transfer of dual protein pattern from glass coverslip to PA hydrogel and incubation of N-cadherin. (c) Schematic of final result – alternating single- and dual-protein patterns on PA hydrogel. (d) Representative image of single- and dual-protein patterns on PA hydrogels. Green is laminin and blue is N-cadherin. Scale bar is 20 μm .

7.5. Methods and Materials

7.5.A. Protein patterning glass coverslips

18mm diameter #1 glass coverslips were plasma treated for 5 minutes at 18W (*Harrick*, PDC-32G). Immediately after plasma treatment, an 8mm inner diameter PDMS ring (*B&J Rubber Products*) cut from a Silhouette CAMEO 3 electronic desktop cutter (*Silhouette America*) was sealed to the center of the glass coverslip. A solution of 100 μ g/mL of poly(l-lysine)-graft-poly(ethylene glycol) (PLL(20)-g[3.5]- PEG(2); *SuSoS AG*) diluted in phosphate buffered saline (PBS; *Gibco, ThermoFisher*, 10010049) was immediately pipetted within the ring and incubated for 1 hour at room temperature. The PLL-g-PEG was then rinsed thoroughly (10x) with PBS prior to micropatterning.

Following PLL-g-PEG incubation and rinsing, 20 μ L of UV sensitive photo initiator (PLPP; *Alvéole*) was pipetted into the ring on the glass coverslip, which was placed on the stage of a Leica DMI8 epifluorescence microscope equipped with a Fluotar 20x/0.40 NA objective and the Alvéole Primo photopatterning system (*Alvéole*). Digital masks for the protein A “cap” patterns as well as the main laminin patterns were made using the open-source software program Inkscape (<https://inkscape.org>). The pixel-to-micron ratio generated by Primo calibration was used to define the geometries of all patterns. Laminin patterns for single cells were 14 μ m wide by 85 μ m tall. For single cell dual protein patterns, Protein A cap patterns were 14 μ m wide by 10 μ m tall with laminin bodies 14 μ m wide by approximately 68.9 μ m tall. The protein A patterns were designed to have a ~10% overlap with the laminin body to account for any spacing artifacts, giving the total height of the dual protein patterns 85 μ m.

The digital mask containing protein A “caps” was loaded onto the Leonardo plugin (*Alvéole Laboratory*) on Micro-Manager software, made into a 6 x 6 array with 150 μ m spacing, then illuminated onto the glass coverslip at a dosage of 1,000mJ/mm² from a 375 nm, 7.10mW laser. Following micropatterning, the photo initiator was rinsed off with PBS and a 100 μ L of a 100 μ g/mL solution of 546 nm fluorescently tagged Protein A (*ThermoFisher*, P11049) was incubated on the glass coverslip overnight at 4°C. The protein A was then rinsed thoroughly from the glass coverslip using PBS, then another 20 μ L of PLPP photoinitiator was added before being illuminated with a second digital mask on the Primo at a dosage of 1,000mJ/mm² from a 375 nm, 7.10mW laser. This second mask contained alternating laminin bodies for both dual protein patterns and single protein patterns. The shortened laminin bodies within the digital mask were aligned to the protein A “caps” using a Texas Red fluorescent excitation filter before UV illumination. Following this second UV illumination step, the photo initiator was rinsed off with PBS and incubated with a 500 μ g/mL solution of laminin (*Corning*, 354232) for 2 hours at room temperature. Finally, the patterns were rinsed with PBS and the PDMS containment ring was removed prior to gel transfer.

7.5.B. ²Preparation of polyacrylamide hydrogels

After patterning both laminin and protein A on a glass coverslip, the proteins were transferred to a ~10kPa polyacrylamide (PA) hydrogel with a covalent linker to firmly attach the protein. The covalent linker-functionalized PA hydrogels were prepared following a

² Experimental techniques in section 7.5.B. were performed by Kerry V. Lane, but reproduced here to provide context for preparation of dual protein patterned hydrogels.

previously published protocol with some adjustments¹¹. Briefly, we began by oxidizing N-Hydroxyethyl acrylamide (HEA; *Sigma*, 697931) by adding 0.01g of sodium metaperiodate (*Sigma*, 71859) to 2.338mL of HEA, then incubating in the dark on a shaker for 4 hours. To adhere the PA hydrogels to the glass bottom dishes used in this work, we treated the glass with bind-silane. We prepared a solution with 950 μ L of 100% ethanol, 50 μ L of acetic acid, and 3 μ L of 3-(Trimethoxysilyl) propyl methacrylate (Bind-silane; *Sigma*, M6514). Then, we treated the glass with oxygen plasma for 30 seconds at 18W (*Harrick*, PDC-32G). Directly after plasma treating the glass, we added \sim 50 μ L of the bind-silane solution to the glass surface. The solution was incubated on the glass for 1 minute, after which the excess bind-silane solution was removed. The remaining solution was left to react for 10 minutes, after which the glass was rinsed twice with 1mL of 100% ethanol and dried with nitrogen gas.

To prepare the PA hydrogel solution, we combined 732 μ L of 40% Acrylamide solution (*Bio-Rad*, 1610140) and 260 μ L of 2% Bis-acrylamide solution (*Bio-Rad*, 1610142) with 4.008mL MilliQ water. For experiments used in traction force microscopy (TFM) analysis, we added 326 μ L of 1.0 μ m-diameter blue fluorescent microbeads (*ThermoFisher*, F8814) and decreased the MilliQ volume to 3.682mL to maintain the total volume of 5mL. Finally, we added 200 μ L of oxidized HEA, bringing the total volume to 5.2mL. Separately, we prepared a 10% weight by volume (w/v) solution of ammonium persulfate (APS; *Sigma*, A9164) in MilliQ water.

To begin polymerization, we added 2.6 μ L of N,N,N',N'- tetramethylethylenediamine (TEMED; *Sigma*, 411019) and 260 μ L of the 10% w/v APS solution to the PA solution. The solution was mixed gently with a P1000 pipette and then 35 μ L of the solution was pipetted onto the bind-silane-treated glass surface. One protein patterned coverslip was then placed on

top of the solution, sandwiching the PA solution between the bind-silane-treated glass and the protein patterned glass. After casting, the hydrogel polymerized in the dark for 30 minutes before being hydrated with PBS and left to fully polymerize at 4°C for 6-8 hours. After full polymerization, the protein patterned top coverslip was removed and discarded.

Following the removal of the top coverslip, PBS was aspirated from the dish and each PA hydrogel was incubated with ~50µL of 100µg/mL N-cadherin (*R&D Systems*, 1388-NC-050) for 3 hours at 4°C. After 3 hours, the PA hydrogel was washed three times with 1mL PBS and then stored overnight at 4°C in PBS with 10% Antibiotic-Antimycotic 100X (Anti-Anti; *Gibco, ThermoFisher*, 15-240-062) and 1% bovine serum albumin (BSA; *ThermoFisher*, PI37525). The following day, the hydrogel was washed three times with 1mL PBS and then stored in PBS + 10% Anti-Anti until cell seeding.

References

- 1 Yang, X., Pabon, L. & Murry, C. E. Engineering adolescence: Maturation of human pluripotent stem cell-derived cardiomyocytes. *Circulation Research* **114**, 511-523 (2014).
- 2 Chen, V. C. *et al.* Development of a scalable suspension culture for cardiac differentiation from human pluripotent stem cells. *Stem Cell Res* **15**, 365-375 (2015).
- 3 Sayed, N., Liu, C. & Wu, J. C. Translation of Human-Induced Pluripotent Stem Cells: From Clinical Trial in a Dish to Precision Medicine. *J Am Coll Cardiol* **67**, 2161-2176 (2016).
- 4 Schroer, A., Pardon, G., Castillo, E., Blair, C. & Pruitt, B. Engineering hiPSC cardiomyocyte in vitro model systems for functional and structural assessment. *Progress in Biophysics and Molecular Biology* **144**, 3-15 (2019).
- 5 Zhang, J. *et al.* Functional cardiomyocytes derived from human induced pluripotent stem cells. *Circulation Research* **104** (2009).
- 6 Sheehy, S. P. *et al.* Quality metrics for stem cell-derived cardiac myocytes. *Stem Cell Reports* **2**, 282-294 (2014).
- 7 Ribeiro, A. J. *et al.* Contractility of single cardiomyocytes differentiated from pluripotent stem cells depends on physiological shape and substrate stiffness. *Proc Natl Acad Sci U S A* **112**, 12705-12710 (2015).
- 8 Kane, R. S., Takayama, S., Ostuni, E., Ingber, D. E. & Whitesides, G. M. Patterning proteins and cells using soft lithography. *Biomaterials* **20**, 2363-2376 (1999).
- 9 Tang, X., Yakut Ali, M. & Saif, M. T. A. A novel technique for micro-patterning proteins and cells on polyacrylamide gels. *Soft Matter* **8**, 7197-7206 (2012).

- 10 Moeller, J. *et al.* Controlling cell shape on hydrogels using liftoff protein patterning. *PLoS ONE* **13**, 1-17 (2018).
- 11 Sarker, B., Walter, C. & Pathak, A. Direct Micropatterning of Extracellular Matrix Proteins on Functionalized Polyacrylamide Hydrogels Shows Geometric Regulation of Cell-Cell Junctions. *ACS Biomaterials Science and Engineering* **4**, 2340-2349 (2018).
- 12 Nelson, C. M., Raghavan, S., Tan, J. L. & Chen, C. S. Degradation of micropatterned surfaces by cell-dependent and -independent processes. *Langmuir* **19**, 1493-1499 (2003).
- 13 Bray, M.-A., Sheehy, S. P. & Parker, K. K. Sarcomere alignment is regulated by myocyte shape. *Cell Motility and the Cytoskeleton* **65**, 641-651 (2008).
- 14 Wang, G. *et al.* Modeling the mitochondrial cardiomyopathy of Barth syndrome with induced pluripotent stem cell and heart-on-chip technologies. *Nature Medicine* **20**, 616-623 (2014).
- 15 Simmons, C. S., Petzold, B. C. & Pruitt, B. L. Microsystems for biomimetic stimulation of cardiac cells. *Lab on a Chip* **12**, 3235-3248 (2012).
- 16 Li, J., Patel, V. V. & Radice, G. L. Dysregulation of cell adhesion proteins and cardiac arrhythmogenesis. *Clin Med Res* **4**, 42-52 (2006).
- 17 Li, Y. *et al.* The N-cadherin interactome in primary cardiomyocytes as defined using quantitative proximity proteomics. *Journal of cell science* **132** (2019).
- 18 Schinner, C., Erber, B. M., Yeruva, S. & Waschke, J. Regulation of cardiac myocyte cohesion and gap junctions via desmosomal adhesion. *Acta Physiologica* **226**, e13242 (2019).
- 19 Goncharova, E. J., Kam, Z. & Geiger, B. The involvement of adherens junction components in myofibrillogenesis in cultured cardiac myocytes. *Development* **114**, 173-183 (1992).
- 20 Simpson, D. G., Decker, M. L., Clark, W. A. & Decker, R. S. Contractile activity and cell-cell contact regulate myofibrillar organization in cultured cardiac myocytes. *Journal of Cell Biology* **123**, 323-336 (1993).
- 21 Wu, J. C., Sung, H. C., Chung, T. H. & DePhilip, R. M. Role of N-cadherin- and integrin-based costameres in the development of rat cardiomyocytes. *J Cell Biochem* **84**, 717-724 (2002).
- 22 Chopra, A., Tabdanov, E., Patel, H., Janmey, P. A. & Kresh, J. Y. Cardiac myocyte remodeling mediated by N-cadherin-dependent mechanosensing. *American Journal of Physiology - Heart and Circulatory Physiology* **300**, 1252-1266 (2011).
- 23 Chopra, A., Patel, A., Shieh, A. C., Janmey, P. A. & Kresh, J. Y. α -Catenin Localization and Sarcomere Self-Organization on N-Cadherin Adhesive Patterns Are Myocyte Contractility Driven. *PLoS ONE* **7** (2012).
- 24 McCain, M. L., Lee, H., Aratyn-Schaus, Y., Kléber, A. G. & Parker, K. K. Cooperative coupling of cell-matrix and cell-cell adhesions in cardiac muscle. *Proceedings of the National Academy of Sciences of the United States of America* **109**, 9881-9886 (2012).

Chapter 8

Conclusions and future directions

The aim of this thesis was to develop and apply novel engineering approaches to study epithelial mechanobiology. Specifically, I have focused on how forces through intercellular contacts influence collective cell behavior. These projects have covered a range of spatial scales, from 2-D sheets to 1-D lines to cell doublets to a cell-cell mimic in single cell system.

8.1. Application of reductionist epithelial models

Each epithelial model has advantages and disadvantages when trying to answer biological questions. One of the most common epithelial models in literature are 2-D epithelial sheets. These models are easy to develop, amenable to culture on different materials (e.g., metals, plastics, glass), and can be observed easily with light microscopy. We leveraged the 2-D epithelial model in 3 of the studies presented here: Cyclic stretch of the epithelium, compression of the epithelium, and boundary strain of the epithelium. For each of these studies, we required an epithelial model that could grow to confluency on unique materials (PDMS or silicon in these studies), were amenable to widefield microscopy, and had cell-cell contacts in all directions across a lateral plane.

1-D epithelial models, while spatially more reductionist compared to the 2-D sheet, are more complex to develop. As discussed in the introduction, they require microfabricated channels or protein patterned ECM tracks. We utilized the 1-D epithelial model in the study of local boundary strain and collective oscillations. We generated this 1-D model using photomolecular adsorption of proteins, creating an ECM track roughly the width of a single

cell. The 1-D model enabled us to isolate the directionality component of cell-cell contact forces in addition to cell movements. In 2-D epithelial sheets, cells move in both the x and y directions and information about migration directionality can be lost among scattered movements. The 1-D model encourages cell-cell signaling along a single axis, allowing us to better understand the impact of cell-cell signaling. Therefore, when the scientific question is about directionality of cell movements, a 1-D model is more appropriate compared with a 2-D model. Furthermore, it is analytically simpler and can be modeled more easily *in silico*.

Cell pair or cell doublet epithelial models also have their place, which we leveraged to isolate and structurally understand the adherens junction. Cryo-ET enables the highest quality resolution of cellular structures, but requires cells to be cultured on thin carbon films of 3 mm wide metal grids. Furthermore, only specific regions of these grids can be imaged by electron beams given the blind spots of tilt series acquisitions. Morphological control of cell doublets enables us to control the positioning of cell-cell contacts (i.e., cell-cell junctions) in optimal regions of imaging. While more complex epithelial models (e.g., 2-D or lines) can be grown and imaged on EM grids as well, we lose control and positioning of single cell-cell contacts.

I am thankful that during my PhD I had the opportunity to explore these different models. I emphasize future researchers to first identify a clear goal or question, then identify the optimal model or system to address that goal. Sometimes, the most prevalent tool is not always the best tool. Sometimes, you must make your own tool.

8.2. New methods contributed and expansion of existing methods

Across the different studies I have presented in this thesis, there is a combination of new and existing experimental and analytical tools. The goal of this section is to highlight

those that are novel, those that I built upon, and the novel biological results that I obtained from the integration of both.

8.2.A. Experimental tools

A key part of this thesis was to exert mechanical strains on the epithelium.

Experimentally, I used several different tools to exert these strains in different forms across different studies. I utilized a pneumatically regulated elastomeric cell stretcher, a 3-D printed cell compression device, micromanipulator actuated custom glass probes, and ECM protein patterning to regulate cell morphology.

Pneumatically regulated elastomeric cell stretcher: This cell stretching device had previously been developed in the Pruitt Lab and used in several studies before the one presented here.

While I made no changes to the device design itself, I made substantial changes to the typical experimental setup to address our biological questions. To image the device over long periods of time, we had to address the issue of evaporation, which is a common issue among cell stretchers in the mechanobiology field. After testing several humidifying options to reduce evaporation, we ultimately found it was not sustainable for long time scales.

Therefore, we (Stacey and I) integrated the device with a microfluidic based perfusion system. This innovation enables future users to easily conduct long-term experiments during or after mechanical strain.

3-D printed cell compression device: I re-designed and re-built several aspects of the original design, which was made by a previous lab member. Furthermore, I analyzed the strain range for the device and developed a protocol to make the device amenable to cell culture (and ultimately, experiments). My innovations to the platform enabled us to perform epithelium compression studies under a known strain in conjunction with live cell imaging.

Micromanipulator actuated custom glass probes: This experimental setup combines 1-D micropatterned lines and external force application probes. I designed and implemented both experimental aspects into this project. First, I developed the 1-D lines by building off my experiences in creating protein patterns for cell doublets. Secondly, I designed the probes and micromanipulation system after inspiration from two papers (Borghi et al., *PNAS*, 2012 and Sadeghipour et al., *Elife*, 2018)^{1,2}. My goal was to pull directly on cells in a precise fashion. The glass probes could be functionalized with protein for cell attachment, and the piezo micromanipulator could be integrated within my microscopy setup to have high spatiotemporal control over the glass probe. My experimental innovations resulted in a clearer way to address the impact of local strains on collective epithelial behavior. I hope others can adopt and improve this experimental system for other applications.

Protein micropatterning: Micropatterning of ECM proteins has been around for decades. However, I made several innovations for biological applications by innovating the technique of photomolecular adsorption of proteins. I originally learned how to micropattern proteins using this technique from Dr. Leeya Engel (now an Assistant Professor, Technion University). We developed a method to pattern proteins on EM grids³. After working with Dr. Engel, I continued to innovate our method with new substrate preparation techniques. My innovations reduced damage to the EM grids, simplified user handling, and rendered them amenable to damage-free transportation (cryo-EM projects often involve inter-university collaborations). These developments enabled us to i) consistently orient epithelial doublets on EM grids for Cryo-ET studies and ii) allowed collaborators to image the structural composition of the epithelial adherens junction.

I bridged my skills in micropatterning of proteins to mimicking cell-cell interactions with single cell iPSC cardiomyocytes. Dual patterning of proteins using photomolecular adsorption of proteins has been presented as a proof of concept by others, but we integrated this technique into a functional study with a specific biological question (i.e., impact of cell-cell contacts on cardiomyocyte maturity).

8.2.B. Analytical tools

Quantitative image analysis has been necessary from the experimental systems described above. Using these methods, we were able to improve analytical throughput, eliminate bias, and improve statistical power among the results of our studies.

Cell segmentation: The epithelium is a sheet (sometimes multiple) of interconnected cells that exert energy, often in the form of actomyosin regulation. Epithelial cells regulate their actomyosin complex to modulate their morphology, which governs their function and collective behavior of the epithelium. Image segmentation allows us to extract these morphologies as a function of time in response to experimental inputs. I employed the open-source Python-based algorithm, Cellpose, for all cell segmentation used in this thesis⁴. Unlike other segmentation tools, Cellpose is built on a trained data set and employs machine learning to predict the outline more accurately for cell shapes. Cellpose helped increase our statistical power by segmenting more cells from microscopy images.

A novel analytical development within this thesis based on cell segmentation is our method to quantify vinculin expression at cell-cell contacts. Traditionally, researchers manually measure the fluorescence intensity of proteins at cell-cell contacts. Unfortunately, manual measurements can be subject to user-bias and low throughput. I developed a segmentation-based approach to extract information on protein recruitment at cell-cell

contacts, as detailed in Chapter 2: Cyclic stretch of a 2-D epithelium. This approach removes bias, increases statistical power, and can quantify nearly every cell from an image.

High-throughput ROI analysis: In combination with Cellpose for cell segmentation, we utilized a set of custom Python scripts to run segmentation in a high-throughput manner (i.e., for thousands of images). To integrate high-throughput segmentation with high-throughput ROI analysis, we leveraged the open-source ImageJ plugin, Labels to ROIs. Ultimately, we (Katya and I) created a process flow that extracts hundreds to thousands of images of epithelial sheets, segments the cells in each image, extracts the morphological parameters for each cell in each image, filters these parameters depending on user preferences, then averages and combines the filtered data for a simplified analysis. We employed this process flow for two studies in this thesis: Chapter 2: Cyclic stretch of a 2-D epithelium and Chapter 4: Boundary strain of a 2-D epithelium.

Strain mapping and particle image velocimetry: Tracking cell migration is a widely used technique to track cell migration. It is particularly useful for microscopy images generated from brightfield imaging. Therefore, we employed the same technique to track cell movements given our similar experimental outputs. Similarly, digital image correlation (DIC) is based on tracking pixel displacements across images for the purpose of measuring mechanical strains. Therefore, we employed DIC to measure the strain exerted on our 1-D system as well as the PDMS strain exerted in our 3-D printed compression device. Both PIV and DIC enabled us to track cell movements in response to applied mechanical cues, as well as quantify the extent of those applied mechanical cues.

Epithelium oscillation quantification: A portion of our 1-D epithelial study included quantification of the oscillation period for different length ECM lines. To quantify the back-

and-forth movements of the epithelial collective, I developed a MATLAB script that can take any number of experiments as an input, then plot the displacement of each cell line as a waveform. The script then calculates and averages the distances between waves (i.e., periods), which is a key metric that describes the oscillatory nature of the cell collective. Please see Appendix for the script, “Determining wave period from 1-D oscillations”.

8.3 Expanding on biology

The overarching question I set out to answer in this work involved how mechanical strains influence signaling through cell-cell contacts within the epithelium. There are many ways to approach this large and complex question. After all, mechanical strains within epithelia vary in rate, amplitude, localization, and direction among other factors. Furthermore, they regulate several tiers of biology from protein and subcellular structures to large-scale cell and tissue behavior. Within this thesis I’ve developed several unique approaches to answer different forms of this question, teasing out the contributions of specific mechanical inputs and measuring the corresponding biological outputs. This work involved building and implementing tools within several different epithelial models. The advantages and disadvantages of each model have been discussed above. Below, I will integrate my contributions in tool and model development with the biological results obtained from these studies (8.3.A.). Finally, I will connect the contributions from these biological results to relevant *in vivo* systems (8.3.B.).

8.3.A. How does mechanical stretch regulate epithelial behavior?

Overall, the epithelium is a dynamic tissue independent of external force perturbations. It can toggle between fluid and solid states^{5,6}, adjust cellular morphologies⁷,

adjust migration direction and speed⁸⁻¹⁰, and regulate levels of turnover (i.e., proliferation and death)¹¹⁻¹⁴. In this thesis, my diverse set of experimental platforms allowed us to directly probe the biological outcomes from a protein level to a tissue level.

Global stretch of an epithelium

One part of my studies included mechanical strain of the global 2-D epithelium (via compression and cyclic stretch). The results from these studies corroborate the viscoelastic nature of the epithelium^{15,16}. On short time scales, epithelial cells deform nearly proportionally to the strain input of the system. We observed these changes when we compressed a confluent epithelium on a pre-strained stretching platform. On longer time scales, however, we observed active responses by the epithelium. For example, in response to low strain rates (i.e., low stretch frequency), we observed a reorientation of cell shape that was not observed at faster, higher frequency stretches. Furthermore, these cell reorientations occurred in correlation with an arrest of cell movements and an increase in vinculin recruitment to cell-cell contacts. Prior to this work, few studies utilized time-lapse microscopy to investigate the long-term response of the collective epithelium after global cyclic stretch. Furthermore, studies directly comparing different strain rates have been limited to investigation of stress fibers at the cell-ECM interface, often of single cells^{17,18}. My work supplements these studies by bridging them to epithelial sheets and helping elucidate the implications of strain rate for collective cell behavior. While our focus was primarily on changes in collective cell behavior via shape change and cell migration speed, there are extensive new avenues to explore, as discussed below in section 8.4: Future directions and shortcomings.

Local stretch of an epithelium

Local (i.e., boundary) mechanical strains are omnipresent in developing and adult epithelial tissue^{11,19-21}, yet incredibly difficult to re-capitulate *in vitro*. As discussed in Chapter 1, *in vitro* models that exert local strains are necessary to understand the causal effect of a local mechanical cue on the epithelium, rather than its correlative function in the *in vivo* environment. However, only recently has the effect of local boundary mechanics been studied in the context of epithelial collective behavior. This limitation is partly due to the lack of experimental *in vitro* tools. In the two studies presented here that investigated local step strain (Chapters 4 and 5), both demonstrated a downstream response on the direction of collective cell migration. In the 1-D study, cells migrated towards the local step strain on a time scale of hours. In the 2-D study, cell collectives also migrated towards the step strain, though on a faster time scale (~1 hour). This difference may be the result of a larger step strain amplitude applied to the system. In our work, the 2-D study also provides insight into *how* local strain propagates through a tissue to promote cell migration. Previous research in the Pruitt lab revealed that local strain promotes collective migration via E-cadherin signaling¹. Our extensive characterizations of spatiotemporal changes in cell shape following boundary strain indicate that a sudden solidification of the tissue near the boundary strain (as measured by cell shape index) precedes migratory movements. While we did not quantify cell shape in our 1-D study, we were able to attribute the impact of local step strain on collective behavior to the orientation of cell-cell contacts under mechanical strain. One limitation of our 1-D study was that we only observed the migration response to step strain after 6 hours. Longer experiments would enable a more complete understanding of the long-term implications on collective behavior and would also provide context for 1-D *in silico* models. However, both local strain studies (1-D and 2-D) indicate that more mature cell-cell

contacts may be necessary for force propagation and subsequent migration changes within the epithelium. This notion is corroborated by *in vivo* experiments, where actomyosin constriction of the mature adherens junction is necessary to drive invagination of the mesoderm²².

The local step strain studies presented here start to reveal an interesting distinction in how mechanical strain regulates collective epithelia compared to global strain studies. Many studies in literature have demonstrated how global static strain regulates extrusion (via compression)^{13,23,24} or proliferation (via stretch)^{12,25}. However, local boundary strain has primarily been shown to alter collective properties via migration. Together, our studies of boundary strains serve as a foundation for future work in which predictive modeling can help understand this behavior.

Geometrically regulated cell-cell tension

A large limitation of our studies using mechanical manipulation platforms on cell sheets or lines is that biological behavior is generally inferred from microscopy outputs. Our widefield fluorescence microscopy studies have limitations in how much we can understand regarding subcellular organization and structural changes within the cell. For example, we found an increased recruitment of vinculin at cell-cell contacts under cyclic mechanical stretch, though this conclusion is derived from fluorescence intensity measurements (as is common in the field). Furthermore, we assume that fluorophore labeled proteins on cells do not impact their native behavior or the native properties of cell-cell contacts. Therefore, our developed workflow for patterning epithelial cell pairs for cryo-EM studies is particularly critical to supplement existing widefield microscopy studies. In this thesis, I demonstrated a highly reproducible protocol that enables direct observation (cryo-EM performed by Hanein and

Volkman labs) of subcellular features including F-actin at the adherens junction. Future studies that leverage ECM pattern sizing to regulate cell-cell contact force on EM grids will greatly benefit our understanding of subcellular changes in response to intercellular forces and help fill the gap between mechanobiology and structural biology. However, one caveat for these studies is that mechanical strain applied to cell-cell contacts via ECM modulation is different than strain applied with other micromanipulation systems (e.g., cell stretching devices). On ECM patterns, cells have ample time (hours to days) to reinforce cell-cell junctions in ways that may not occur on short timescales typically used in cell stretching platforms. For example, F-actin reinforcement at cell-cell contacts develops on a timescale of 90 minutes²⁶. While cryo-EM studies will help elucidate how junctions are reinforced under mechanical load, researchers must use caution when directly comparing these structural changes to cellular changes observed on short time scales.

8.3.B. *In vivo* relevance

As discussed throughout this dissertation, mechanical strains exist in several forms throughout different types of epithelia. During development, tissues fold, bend, and constrict^{20,21,27,28}. Adult epithelia, such as the lungs or gut, are also mechanically strained²⁹⁻³¹. Furthermore, while mechanical strains of epithelia are a normal aspect of epithelial homeostasis, they can become dysregulated in many disease contexts^{29,32}. Despite differences between tissues, collective migration and cell-cell coordination via the adherens junctions are hallmark features integral to epithelial function.

This thesis is not meant to answer questions regarding a specific epithelial system nor study epithelial pathology. Rather, this thesis is meant to address i) the development of micro-engineered systems to better study hallmark features of epithelia and ii) how the

epithelium fundamentally regulates its collective behavior as a material through cell-cell signaling. However, there are several ways in which the studies presented here connect to *in vivo* systems.

Epithelia can be migratory or non-migratory, depending on their function in the body. Migratory epithelia are commonly associated with wound healing and developing tissues³³⁻³⁵. Non-migratory epithelia are commonly associated with mature epithelia⁵. Transitions between migratory and non-migratory states (e.g., unjammed and jammed) have been associated with development³⁶, or diseases such as cancer invasion^{37,38} or asthma⁵. For example, increased cell movement has been shown to increase permeability of the epithelium³⁹, which may be critical (or dysregulated in pathological conditions) to tissue function such as filtration or absorption.

Collectively, our studies indicate that mechanical forces strengthen cell-cell contacts to reduce cell migration speed in a strain rate dependent manner. This change may indicate that low strain rates play a pivotal role in maturing epithelial tissue. For example, solidification of tissue occurs during zebrafish body axis elongation³⁶. Meanwhile, higher strains in our studies indicated an increase in cell fluidity, as determined by an increase in cell shape index ($\frac{Perimeter}{\sqrt{Area}}$). *In vivo* studies of the airway epithelium have found that higher frequency (1 Hz) mechanical stretch⁴⁰, especially at large amplitudes (37%)⁴¹, increase the permeability of the epithelium. This increase in permeability can result from over distension caused by mechanical ventilators, leading to lung injury. Lung injury via over distension can also be caused by free diving, a condition known as Pulmonary barotrauma⁴². Our results from cyclic stretch of the epithelium revealed that lower frequencies (slower rates) reduced migration. These results corroborate alveolar epithelial studies, which showed reduced

healing in response to cyclic stretch⁴³. Therefore, it is possible that low frequency mechanical stretch may *decrease* the permeability of the epithelium.

Permeability is also critical to homeostatic functioning of the gut, which regulates nutrient absorption. Peristaltic contractions of the smooth muscle in the gut continuously exert mechanical strains on the intestinal epithelium and can be dysregulated in response to several factors, including starvation or IBS^{44,45}. Interestingly, *in vivo* studies demonstrated that starvation reduced cell migration in the gut⁴⁵, which is accompanied by reduced peristaltic contractions⁴⁶. Based on our studies, peristaltic contractions may directly reduce cell migration via mechanical cues.

Perhaps a limitation of our *in vitro* studies is that they were mostly conducted on the ECM protein collagen I, which is highly prevalent across many epithelia. It is worth noting that several ECM subtypes exist *in vivo* (e.g., laminin, fibronectin, etc.), which may have consequences for collective epithelial behavior in response to mechanical cues. For example, previous studies have shown that the strain response of intestinal epithelial cells is matrix dependent⁴⁷. Fibronectin can increase with inflammation and change the behavior of intestinal epithelial cells⁴⁷. Though our results indicate a slowing of speed in epithelial cells under low frequency stretch, it is possible that the body alters ECM composition to regulate this strain response. For example, increasing levels of fibronectin may increase migration of intestinal epithelial cells in response to specific environmental cues, or to decrease permeability. Alternatively, highly inflammatory states may increase tissue fluidity and adversely affect the gut epithelium. These collective changes in the epithelia may regulate physiological functions of the gut including nutrient adsorption.

Boundary strains and migration

In vivo, boundary strains have been observed in dynamic migratory epithelia though its direct influence on regulating migration direction has been unclear. Local boundary strains in our *in vitro* studies indicate that these mechanics cause cells to collectively migrate towards the boundary strain. These results corroborate studies *in vivo* in several aspects. For example, during invagination of the epithelial embryo⁴⁸, apical constriction of cells near the center is followed by a flow from cells in outer regions⁴⁹. Local mechanical contractions also occur in the developing *Drosophila* wing³⁵. Contraction at the base of the wing is followed by cell flows leading to the solidification of the wing epithelium. In both *in vivo* processes, our studies highlight the role of boundary mechanics in promoting epithelial flows across a tissue towards the strained region. Our studies of cell shape also indicate that local rigidification of tissue (as quantified by cell shape index) may have a role in driving cell flows, which are also actomyosin driven.

Cell shape

Aside from the influence of mechanics, characterization of cell shape can help us understand the physical state of epithelia. We can then bridge specific changes in cell shape in our model epithelium to changes in cell shape for *in vivo* epithelia. Solidity ($\frac{A_{cell}}{A_{convex}}$) is one important shape descriptor that can be used to describe the health of mature epithelia. For example, age related macular degeneration is associated with a decrease in cell solidity^{7,50}. In our studies, we found that cell solidity was reinforced in a less motile epithelium, which we attribute to a stabilization of cell-cell contacts. Since the retinal epithelium is relatively non-migratory, it is possible that macular degeneration is also accompanied by a breakdown of cell-cell contacts, leading to changes in permeability of the degenerated retinal epithelium or

its physical state. Perhaps reinforcing the stability of cell-cell adhesions in the retinal epithelium could slow macular degeneration.

8.4. Future directions and shortcomings

With every experiment and project, there are always new questions to answer. From the various studies presented in this thesis, there are extensive additional experiments I would love to see others perform. I will outline a few of these potential directions with respect to each epithelial model I worked with.

2-D epithelial models

For my work within the 2-D epithelial model, there is potential to investigate the effects of cyclic stretch on other forms of collective behavior. For example, contact stability is necessary for collective cell migration. As cells reorganize and slip past one another, cell-cell contacts are broken and reformed via recycling of intercellular proteins (e.g., E-cadherin)⁵¹. For example, E-cadherin is constantly recycled from the cell membrane as connections break and reform¹⁶. An important question would be how mechanical cues such as cyclic stretch or compression regulate the turnover of E-cadherin and subsequent stability at the cell-cell contact. To answer this question, fluorescence recovery after photobleaching (FRAP) could be implemented for fluorescently labeled E-cadherin after the application of a specific mechanical cue.

There is also additional room to map the relationship between the temporal aspects of mechanical inputs and subsequent response of epithelial behavior. For example, are collective responses such as migration exacerbated with longer periods of cyclic stretching? Are responses exacerbated with higher magnitudes of stretch? Does the density of the

epithelium alter the degree of force transmission and subsequent collective response? When applying a local boundary strain, are forces propagated on different timescales with different rates of boundary perturbation? Our studies of cyclic stretch indicate that the likely answer is “yes”.

There are other biological outputs worth investigating besides the adherens junction. For example, desmosomes also have a role as a mechanosensor^{52,53}, yet their role is not as well characterized as the adherens junction. Future experiments that target and visualize elements of the desmosomes would greatly aid in our understanding of other cell-cell junctions in regulating mechanical cues between epithelial cells.

1-D epithelial models

There are extensive experiments that can be implemented in our 1-D epithelial model. For example, traction force microscopy can be integrated within our experimental system. By measuring cell traction forces, we can better map out collective cell migration and more accurately understand the effect of local mechanical strain. There also exists an array of different mechanical inputs that can be applied to our system. For example, how do different step strain rates or strains of different magnitudes regulate migratory movements? Our cyclic stretch studies indicate that strain rates may influence how cell collectives move away or towards a local strain stimulus. Alternatively, specific local strain rates may not affect collective migration at all.

In addition to potential mechanical inputs used in our 1-D studies, there are several biological inputs and outputs we can modulate. For example, we demonstrated that cyclic strain results in vinculin recruitment in our 2-D model. Is vinculin recruitment from 1-D step strain also recruited at cell-cell contacts? Does this potential vinculin spatial gradient in a cell

have a role in directing polarization and migration of an epithelial cell? Since we have shown that contact stability is connected to collective behavior, there are potential experiments to enhance or degrade cell-cell stability. For example, calcium is required to rigidify E-cadherin ectodomains⁵⁴, allowing for strong adhesion at the adherens junction. Disrupting calcium concentration of cell trains may influence contact stability and subsequent collective cell behavior. Besides calcium, we could also dysregulate a protein that regulates E-cadherin turnover. For example, p120-catenin binds to E-cadherin to prevent endocytosis⁵⁵. By reducing p120-catenin expression via siRNA or shRNA, we could increase E-cadherin turnover and downregulate cell-cell contact stability.

We could also improve several aspects of the experimental system. For example, in theory, the glass probe used for cell adhesion at the end of the cell line can be functionalized with any protein. While we used collagen in our studies, future experiments could target specific cell interactions or signaling pathways

Epithelial doublets

In our studies we demonstrated morphological control of epithelial doublets and cryo-ET of the adherens junction within those regulated doublets. Our foundation has set the stage for future studies that image the adherens junction under different mechanical cues. The techniques that we have developed enable future users to pattern any geometry of ECM on EM grids for cell doublets. For example, we could use different size ECM patterns to increase force at the cell-cell contact of the doublet. While this method of cell-cell force regulation has been implemented before⁵⁶, it is unclear how the force regulates structural changes within the adherens junction. For example, does an increase in actin bundling reinforce the additional load? There is also potential to use different ECM geometries such as

I-beam to enhance the cell-cell contact stability of cell doublets. When the adherens junction stabilizes, how does it change at a structural level? Many of these changes have never been directly observed.

Lastly, we could also dysregulate other mechanosensitive proteins within the adherens junction (e.g., vinculin) and determine the structural changes on the adherens junction. It is possible that vinculin recruitment is necessary for increased F-actin bundling which is necessary for mature adherens junction adhesions.

Single cell epithelial models

The single cell model in this thesis is focused on enhancing the maturity of cardiomyocytes by mimicking cell-cell contacts. However, future studies can apply the experimental concepts to epithelial cells. The two main experimental changes include i) employing E-cadherin instead of N-cadherin and ii) adjusting the geometry of the underlying ECM pattern. This study would be the first single cell epithelial model with cell-cell contact mimics. Other cell-cell junctions could also be mimicked besides the adherens junction. For example, instead of flanking the ECM pattern with protein A/cadherin, we could use a protein central to desmosomes (e.g., desmoglein). This single cell epithelial model would allow us to answer questions around how the epithelial adherens junction regulates traction force or cytoskeletal structure.

8.5. Concluding remarks

This thesis builds extensively on the existing field of epithelial mechanobiology in several ways. First, I have highlighted the importance of studying local vs. global mechanical cues in regulating collective epithelial behavior. Previous studies have focused on

manipulating the mechanics of one cell or a sheet of cells. Furthermore, I have identified the range of epithelial model systems and how they can be equipped with different modes of micromanipulation tools to answer biological questions. Second, I have innovated new tools for several of these epithelial model systems (2-D, 1-D, cell doublets, and single cells) to study force transmission at cell-cell contacts. Third, I have implemented these experimental systems to answer biological questions, which largely focus on the role of cell-cell contact forces in regulating collective epithelial behavior. The culmination of this research will enable a new class of studies for epithelial mechanics and a stronger understanding of epithelial behavior.

8.6. References

1. Sadeghipour, E., Garcia, M. A., Nelson, W. J. & Pruitt, B. L. Shear-induced damped oscillations in an epithelium depend on actomyosin contraction and E-cadherin cell adhesion. *Elife* **7**, 1–16 (2018).
2. Borghi, N. *et al.* E-cadherin is under constitutive actomyosin-generated tension that is increased at cell-cell contacts upon externally applied stretch. *Proc. Natl. Acad. Sci. U. S. A.* **109**, 12568–12573 (2012).
3. Engel, L. *et al.* Extracellular matrix micropatterning technology for whole cell cryogenic electron microscopy studies. *J. Micromechanics Microengineering* **29**, 115018 (2019).
4. Stringer, C., Wang, T., Michaelos, M. & Pachitariu, M. Cellpose: a generalist algorithm for cellular segmentation. *Nat. Methods* **2020 181 18**, 100–106 (2020).
5. Park, J.-A. A. *et al.* Unjamming and cell shape in the asthmatic airway epithelium. *Nat. Mater.* **14**, 1040–1048 (2015).
6. Needleman, D. & Dogic, Z. Active matter at the interface between materials science and cell biology. *Nature Reviews Materials* vol. 2 1–14 (2017).
7. Kim, Y. K. *et al.* Morphometric Analysis of Retinal Pigment Epithelial Cells From C57BL/6J Mice During Aging. *Invest. Ophthalmol. Vis. Sci.* **62**, 32–32 (2021).
8. Peyret, G. *et al.* Sustained Oscillations of Epithelial Cell Sheets. *Biophys. J.* **117**, 464–478 (2019).
9. Cohen, D. J., Nelson, W. J. & Mahabiz, M. M. Galvanotactic control of collective cell migration in epithelial monolayers. *Nat. Mater.* **13**, 409–417 (2014).
10. Smith, J. T., Elkin, J. T. & Reichert, W. M. Directed cell migration on fibronectin gradients: effect of gradient slope. *Exp. Cell Res.* **312**, 2424–2432 (2006).
11. Kuranaga, E. *et al.* Apoptosis controls the speed of looping morphogenesis in *Drosophila* male terminalia. *Development* **138**, 1493–1499 (2011).
12. Gudipaty, S. A. *et al.* Mechanical stretch triggers rapid epithelial cell division through Piezo1. *Nature* **543**, 118–121 (2017).
13. Eisenhoffer, G. T. *et al.* Crowding induces live cell extrusion to maintain homeostatic cell

- numbers in epithelia. *Nature* **484**, 546–549 (2012).
14. Eisenhoffer, G. T. & Rosenblatt, J. Bringing balance by force: Live cell extrusion controls epithelial cell numbers. *Trends in Cell Biology* vol. 23 185–192 (2013).
 15. Esfahani, A. M. *et al.* Characterization of the strain-rate-dependent mechanical response of single cell–cell junctions. *Proc. Natl. Acad. Sci. U. S. A.* **118**, (2021).
 16. Iyer, K. V., Piscitello-Gómez, R., Paijmans, J., Jülicher, F. & Eaton, S. Epithelial Viscoelasticity Is Regulated by Mechanosensitive E-cadherin Turnover. *Curr. Biol.* **29**, 578–591.e5 (2019).
 17. De, R., Zemel, A. & Safran, S. A. Dynamics of cell orientation. *Nat. Phys.* 2007 39 **3**, 655–659 (2007).
 18. Lee, C. F., Haase, C., Deguchi, S. & Kaunas, R. Cyclic stretch-induced stress fiber dynamics – Dependence on strain rate, Rho-kinase and MLCK. *Biochem. Biophys. Res. Commun.* **401**, 344–349 (2010).
 19. Diaz de la Loza, M. C. & Thompson, B. J. *Forces shaping the Drosophila wing. Mechanisms of Development* vol. 144 23–32 (2017).
 20. Fierling, J. *et al.* Embryo-scale epithelial buckling forms a propagating furrow that initiates gastrulation. *Nat. Commun.* **13**, (2022).
 21. Pérez-González, C. *et al.* Mechanical compartmentalization of the intestinal organoid enables crypt folding and collective cell migration. *Nat. Cell Biol.* 2021 237 **23**, 745–757 (2021).
 22. Roh-Johnson, M. *et al.* Triggering a cell shape change by exploiting preexisting actomyosin contractions. *Science (80-.)*. **335**, 1232–1235 (2012).
 23. Dow, L. P., Khankhel, A. H., Abram, J. & Valentine, M. T. 3D-printable cell crowding device enables imaging of live cells in compression. *Biotechniques* **68**, 275–278 (2020).
 24. Franco, J. J., Atieh, Y., Bryan, C. D., Kwan, K. M. & Eisenhoffer, G. T. Cellular crowding influences extrusion and proliferation to facilitate epithelial tissue repair. *Mol. Biol. Cell* **30**, 1890–1899 (2019).
 25. Hart, K. C. *et al.* E-cadherin and LGN align epithelial cell divisions with tissue tension independently of cell shape. *Proc. Natl. Acad. Sci. U. S. A.* **114**, E5845–E5853 (2017).
 26. Michael, M. *et al.* Coronin 1B Reorganizes the Architecture of F-Actin Networks for Contractility at Steady-State and Apoptotic Adherens Junctions. *Dev. Cell* **37**, 58–71 (2016).
 27. Pérez-Verdugo, F., Reig, G., Cerda, M., Concha, M. L. & Soto, R. Geometrical characterization of active contraction pulses in epithelial cells using the two-dimensional vertex model. *J. R. Soc. Interface* **19**, (2022).
 28. Roellig, D. *et al.* Force-generating apoptotic cells orchestrate avian neural tube bending. *Dev. Cell* **57**, 707-718.e6 (2022).
 29. Gayer, C. P. & Basson, M. D. *The effects of mechanical forces on intestinal physiology and pathology. Cellular Signalling* vol. 21 1237–1244 (Pergamon, 2009).
 30. Trepatt, X. *et al.* Viscoelasticity of human alveolar epithelial cells subjected to stretch. *Am. J. Physiol. - Lung Cell. Mol. Physiol.* **287**, 1025–1034 (2004).
 31. Savla, U., Sporn, P. H. S. & Waters, C. M. Cyclic stretch of airway epithelium inhibits prostanoid synthesis. *Am. J. Physiol. - Lung Cell. Mol. Physiol.* **273**, (1997).
 32. Birukov, K. G. *et al.* Magnitude-dependent regulation of pulmonary endothelial cell barrier function by cyclic stretch. *Am. J. Physiol. Lung Cell. Mol. Physiol.* **285**, (2003).
 33. Vasilyev, A. & Drummond, I. A. Fluid flow and guidance of collective cell migration. *Cell Adh. Migr.* **4**, 353 (2010).
 34. Friedl, P. & Gilmour, D. Collective cell migration in morphogenesis, regeneration and cancer. *Nat. Rev. Mol. Cell Biol.* **10**, 445–457 (2009).
 35. Aigouy, B. *et al.* Cell flow reorients the axis of planar polarity in the wing epithelium of *Drosophila*. *Cell* **142**, 773–786 (2010).
 36. Mongera, A. *et al.* A fluid-to-solid jamming transition underlies vertebrate body axis elongation. *Nature* vol. 561 401–405 (Nature Publishing Group, 2018).

37. Blauth, E., Kubitschke, H., Gottheil, P., Grosser, S. & Käs, J. A. Jamming in Embryogenesis and Cancer Progression. *Front. Phys.* **9**, (2021).
38. Kang, W. *et al.* A novel jamming phase diagram links tumor invasion to non-equilibrium phase separation. *iScience* **24**, 103252 (2021).
39. Vagin, O., Tokhtaeva, E., Yakubov, I., Shevchenko, E. & Sachs, G. Inverse Correlation between the Extent of N-Glycan Branching and Intercellular Adhesion in Epithelia: CONTRIBUTION OF THE Na,K-ATPase β 1 SUBUNIT. *J. Biol. Chem.* **283**, 2192–2202 (2008).
40. Cohen, T. S., Cavanaugh, K. J. & Margulies, S. S. Frequency and peak stretch magnitude affect alveolar epithelial permeability. doi:10.1183/09031936.00141007.
41. Davidovich, N. *et al.* Cyclic stretch-induced oxidative stress increases pulmonary alveolar epithelial permeability. *Am. J. Respir. Cell Mol. Biol.* **49**, 156–164 (2013).
42. Schipke, J. D., Lemaitre, F., Cleveland, S. & Tetzlaff, K. Effects of Breath-Hold Deep Diving on the Pulmonary System. *Respiration* **97**, 476–483 (2019).
43. Desai, L. P., Chapman, K. E. & Waters, C. M. Mechanical stretch decreases migration of alveolar epithelial cells through mechanisms involving Rac1 and Tiam1. *Am. J. Physiol. - Lung Cell. Mol. Physiol.* **295**, 958–965 (2008).
44. Abrahamsson, H. Gastrointestinal Motility in Patients with the Irritable Bowel Syndrome. <http://dx.doi.org/10.3109/00365528709090996> **22**, 21–26 (2009).
45. Brown, H. O. *et al.* Inhibition of intestinal epithelial cell renewal and migration induced by starvation. *Am. J. Physiol.* **205**, 868–872 (1963).
46. Luckey, A., Livingston, E. & Tache, Y. Mechanisms and Treatment of Postoperative Ileus. *Arch. Surg.* **138**, 206–214 (2003).
47. Zhang, J., Owen, C. R., Sanders, M. A., Turner, J. R. & Basson, M. D. The Motogenic Effects of Cyclic Mechanical Strain on Intestinal Epithelial Monolayer Wound Closure Are Matrix Dependent. *Gastroenterology* **131**, 1179–1189 (2006).
48. Oda, H. & Tsukita, S. Real-time imaging of cell-cell adherens junctions reveals that Drosophila mesoderm invagination begins with two phases of apical constriction of cells. *J. Cell Sci.* **114**, 493–501 (2001).
49. Ng, M. R., Besser, A., Danuser, G. & Brugge, J. S. Substrate stiffness regulates cadherin-dependent collective migration through myosin-II contractility. *J. Cell Biol.* **199**, 545–563 (2012).
50. von der Emde, L. *et al.* Histologic Cell Shape Descriptors for the Retinal Pigment Epithelium in Age-Related Macular Degeneration: A Comparison to Unaffected Eyes. *Transl. Vis. Sci. Technol.* **11**, 19–19 (2022).
51. De Beco, S., Perney, J.-B., Coscoy, S. & Amblard, F. Mechanosensitive Adaptation of E-Cadherin Turnover across adherens Junctions. (2015) doi:10.1371/journal.pone.0128281.
52. Runswick, S. K., O'Hare, M. J., Jones, L., Streuli, C. H. & Garrod, D. R. Desmosomal adhesion regulates epithelial morphogenesis and cell positioning. *Nat. Cell Biol.* **3**, 823–830 (2001).
53. Tariq, H. *et al.* Cadherin flexibility provides a key difference between desmosomes and adherens junctions. *Proc. Natl. Acad. Sci.* **112**, 5395–5400 (2015).
54. Van Roy, F. & Berx, G. The cell-cell adhesion molecule E-cadherin. doi:10.1007/s00018-008-8281-1.
55. Thoreson, M. A. *et al.* Selective uncoupling of p120(ctn) from E-cadherin disrupts strong adhesion. *J. Cell Biol.* **148**, 189–201 (2000).
56. Sim, J. Y. *et al.* Spatial distribution of cell–cell and cell–ECM adhesions regulates force balance while maintaining E-cadherin molecular tension in cell pairs. *Mol. Biol. Cell* **26**, 2456–2465 (2015).

Appendix

A.1 Segmentation analysis and segmentation scripts

1. Open the Anaconda command prompt using the search menu on Windows. Right click and select “run as administrator”
2. Input the following commands, in this order:
 - a. “conda activate cellpose”
 - b. “python -m cellpose --dir **image_folder** --pretrained_model **cyto** --diameter 0 --no_npy --save_png --exclude_on_edges”
3. Other notes on the commands³:
 - a. Be aware, the above commands are a template and must be customized depending on the application
 - b. For **image_folder** replace it with the full file path leading to your folder of images (ex: C:\Users\Ldow\Desktop\Images). You can do this by right clicking on the folder name and choosing “copy address”
 - c. **Important:** There must be no spaces in any of your folder names. Separate all words with underscore characters, “_”
 - d. Choose your pretrained model (cyto or nucleus, depending on what you need to segment). I have only used “cyto”
 - e. There are lots of other commands you can include, just look at the list in the CellPose Documentation (see link in footnotes)
4. Cellpose will save masks as PNG files in the folder with the original images with the name “original_image_name_cp_masks”. To run through the Labels to ROI ImageJ plugin, all mask PNG images need to have their name changed to “original_image_name_label”. This can be done manually or automatically with the following script:

```
import os
from tkinter import Tk
from tkinter.filedialog import askdirectory
path = askdirectory(title='Select Folder') # shows dialog box and return the path
print(path)
os.chdir(path)
#os.chdir("C:/Users/Liam Dow/Desktop/Data")
#send in path to determine your working directory
#>>> os.chdir('/Users/hruys/OneDrive/Desktop/Python_Test')#
os.getcwd() #to check what that you're working with the right directory
for f in os.listdir():
```

³ This protocol was originally written by Katya Morozov and edited/adapted by Liam P. Dow. This protocol assumes you are working on a computer with Cellpose installed. As of July 17, 2023, cellpose is installed on both Hawk (i.e., Rincon) and Butterfly computers. Otherwise, the software can be installed using these instructions: <https://github.com/MouseLand/cellpose>.

```

new_name = f.replace('_cp_masks', '_label') # this is if your masks are .png,
os.rename(f, new_name) #if they're .tifs, it should be ('_cp_masks.tif',
'_label.png')

```

5. Open up ImageJ and run the Labels_To_Rois plugin (otherwise install)
6. Click browse and find the folder location with all of your images
7. Set measurements
8. Run, and save the ROIs as well as CSV tables
9. An organization script (shown below) can be used to sort the output data

```

import os
folder_names = ['Labels','Outlines','ROIs','Data','OG','.tifs']
for f in folder_names:
    os.makedirs('Parent Folder name/' + f) #make new folders

```

10. Cellpose will often segment false shapes, characterized by abnormally small areas (e.g., 1 px). Use the following script to filter ROI data from the CSV files. Adjust the thresholding parameters as necessary. In the example below, I filtered out ROIs starting with the filename “20x” having an area below 2 or above an area of 2,000

```

import pandas as pd
import glob
from glob import glob
import os
import shutil
from tkinter import Tk
from tkinter.filedialog import askdirectory
path = askdirectory(title='Select Folder') # shows dialog box and return the path
print(path)
os.chdir(path)

filenames=glob('20x*.csv')
for f in filenames:
    df=pd.read_csv(f)
    df=df.loc[(df['Area'] <2000 )]
    df=df.loc[(df['Area'] >1 )]
    path='Image'+str(f)+'.csv'
    df.to_csv('Filtered'+str(f)+'.csv', index=False)
    print(df)

```

11. After filtering the ROIs, I often averaged them per CSV file (to create an average cell per image). In the following script, I averaged nearly all shape descriptors for any filename starting with the name “Filtered”. All averages were saved into a new CSV file named “Combined”. This script can be modified as necessary for any other shape descriptors

```

import pandas as pd

```

```

import glob
from glob import glob
import os
import shutil
from tkinter import Tk
from tkinter.filedialog import askdirectory
path = askdirectory(title='Select Folder') # shows dialog box and return the path
print(path)
os.chdir(path)

filenames=glob('Filtered*.csv')
for f in filenames:
    df=pd.read_csv(f)

    df['Average Area']=df['Area'].mean()
    df['Average Circularity']=df['Circ.'].mean()
    df['Average Aspect Ratio']= df['AR'].mean()
    df['Average Round']=df['Round'].mean()
    df['Average Solidity']=df['Solidity'].mean()
    df['Average Perim.']=df['Perim.'].mean()
    df['Average Major']=df['Major'].mean()
    df['Average Minor']=df['Minor'].mean()
    df['Average Angle']=df['Angle'].mean()
    df['Average Skew']=df['Skew'].mean()
    df['Average Box Width']=df['Width'].mean()
    df['Average Box Height']=df['Height'].mean()
    df['Average Feret']=df['Feret'].mean()
    df['Average Feret X']=df['FeretX'].mean()
    df['Average Feret Y']=df['FeretY'].mean()
    df['Average Feret Angle']=df['FeretAngle'].mean()
    df['Average min Feret']=df['MinFeret'].mean()
    df['Average Median']=df['Median'].mean()

    df=(df.loc[[1]]) #isolate 1st row of data, which contains all the averages
    path='Image'+str(f)+'.csv'
    df.to_csv('AveragedROI'+str(f)) #saves each as new csv file
    #print(df)

#Read in the new CSV files and combine them into 1

dfs = (
    pd.read_csv(p, encoding='utf8') for p in glob('Averaged*.csv')
)
res = pd.concat(dfs)
print(res)

```

```
res.to_csv('Combined'+'.csv') #saves new csv file with combined averaged ROI data
across timepoints
```

A.2. Particle Image Velocimetry Scripts for 1-D line analysis

Averaging X vector displacements for 1-D line data

```
%This script was originally written by Reagan Kennedy and adapted by Liam P. Dow
%
% It is used for the graphing of the average x displacement for the
% single line cell strain experiment. The code averages displacement vectors %throughout the
% line, then plots the results. The code also has capabilities to
% plot and calculate average displacements for different sections of the
% line (e.g., front half and back half)
```

```
%xaxis = (0:((670/60)/25):(670/60)); %initializes x axis with proper scale ***75 is (number
of frames-1)***375 is (75*5)
```

```
xvalues_1 = zeros(1,249); %Second number should be one above number of frame to
account for time 0
```

```
%xvalues_2 = zeros(1,75);
```

```
xvalues_1(1) = 0;
```

```
%xvalues_2(1) = 0; %Uncomment if dividing the line into multiple columns
```

```
for i = 1:248 %this for loop averages the displacement vectors in its matrix over 248 time
frames, specifically for a line that has 5 vectors in the y direction
```

```
    xvalues_1(i+1)= xvalues_1(i) + 0.293*((mean(uData(1, :, i)) + mean(uData(2, :, i))...
    + mean(uData(3, :, i)) + mean(uData(4, :, i)) + mean(uData(5, :, i)))/5); %If you are
analyzing a line with >5 vectors (e.g., 75x6x248), add in an element to average in the 6th
vector
```

```
% Would include the code below (modified per data) if you want to split up
% the line into two halves. Xvalues_2 would average just the second half of
% the data
```

```
% xvalues_2(i+1)= xvalues_2(i) + 0.293*((mean(uData(1,50:105,i)) +
mean(uData(2,50:105,i))...
```

```
% + mean(uData(3,50:105,i)) + mean(uData(4,50:105,i)) +
mean(uData(5,50:105,i))+mean(uData(6,50:105,i))+ mean(uData(7,50:105,i))+
mean(uData(8,50:105,i))+ mean(uData(9,50:105,i)))/9);
```

```
end
```

```
%Modify the below commands for plotting the displacement data generated above
```



```

% clf %reset command
% a = 0;
% plot (xaxis, xvalues_1, 'LineWidth', 3,'color', 'black')
% hold on
% %plot (xaxis, xvalues_2, 'LineWidth', 3, 'color', 'red')
% %plot specifications
% xlabel("Time(h)", 'fontweight', 'bold', 'fontsize', 16)
% ylabel("Cell Position", 'fontweight', 'bold', 'fontsize', 16)
% xlim([0,(375/60)])
% set(gca, 'linewidth', 2)
% title('Movement in x EXP024 post pull 5 min intervals', 'fontsize',16)
% set(gca,'fontweight','bold')

```

Generating a kymograph from PIV data

```

%Created by Liam Dow 1/20/23
%The following script was written to produce a kymograph
%of the 1D cell line experiment to spatiotemporally visualize the effects of mechanical cues
on different groups of cells

```

%DIRECTIONS FOR GENERATING KYMOGRAPH DATA

```

% 1) Load in PIV MAT file generated from PIV lab
% 2) average the values across each column (this should result in a matrix thats ~1x90x150
(rows x columns x frames)
% 3) Concatenate all frames to create an array (each new row represents new time frame,
while each column corresponds to position along x axis
% 4) Plot kymograph

```

```

% %0.293 is um/px conversion
M=mean(uData)*0.293; %should generate a 1 x columns x time frames matrix

```

```

%Turn our 3-D matrix into 2-D by concatenating all the 1 x column matrices
%across time points

```

```

%Goal is array of columnsxtime (e.g. 90x150).
prompt= "How many time frames are there in this experiment?"
tf=input(prompt)
K=[];
    for i=1:tf
        Time=[M(1, :,i)];
        K= [K; Time];
    end
end

```

```

clf
h=heatmap(K)
%caxis([-5, 5]);

h.Title='Kymograph of Cell Movement along X direction';
h.XLabel= 'X Position';
h.YLabel= 'Time Frames';
%h.XData= ["Hello" "World" "Thursday"]
h.Colormap = jet
hHeatmap = struct(h).Heatmap;
hHeatmap.GridLineStyle = ':';

```

Determining wave period from 1-D oscillations

```

% Written by Liam Dow 4/26/22
% Purpose of code is to take standing wave experiments of cells moving back
% and forth on linear micropatterned line and following PIV analysis, align
% their local maxima to further asses wave characteristics (e.g. average
% period and amplitude

clc;
clear all;
%load matrix with data
%Change depending on experimental data sheet
A = xlsread('Standing waves','20x200Lines_Filtered')
figure;
hold on;
y(1)=0;
x=A(1,:);

%Use minpeak distance if you want to change how often peaks occur
%pks1=findpeaks(y1, 'MinPeakDistance',15)
%https://www.mathworks.com/help/signal/ref/findpeaks.html
T=nan(1,21)
for i=1:21
    y=A(i+1,:);
    [pks,locs]= findpeaks(y,'MinPeakProminence',4,'Annotate','extents')
    x_peaks=x(locs);
    figure (1)
    plot(x,y,x_peaks,pks,'pg')
    xlabel("Time(h)", 'fontweight', 'bold', 'fontsize', 16)
    ylabel("Cumulative Line Displacement (um)", 'fontweight', 'bold', 'fontsize', 16)
    xlim([0,41]);
    % ylim([-60,120]);

```

```

grid off
cycles=diff(x_peaks);
meancycle=mean(cycles)
T(:,i)=meancycle;
%Comment out lines below if you don't care to save a video of plot
% F(i)=getframe(gcf);
% drawnow
end

```

A.3. Fabrication and preparation of pneumatic uniaxial cell stretching devices

1. Mix PDMS at 10:1 (base:curing agent) ratio (by weight) in plastic cup
 - a. Typically, using 25 g of base and 2.5 g of curing agent covers two molds in aluminum foil boat
2. Balance the cup in Thinky Mixer and mix using standard procedure (should be default settings, 3 min in each direction)
3. Pour mixed PDMS over the molds in aluminum foil boat
 - a. Use compressed air to ensure molds are clean before pouring PDMS
 - b. Molds are printed from RGD450 using Objet 30. 3-D STL file can be found from the following paper: (Hart et al., *Cellular and Molecular Bioengineering*, 2021)
 - c. Ensure they are flat before pouring PDMS. Since RGD450 has a relatively low glass transition temperature, they can be flattened by letting sit in the oven for ~5 minutes, taken out, and left to cool flat on the bench
4. De-gas/desiccate for at least 1h (or until all bubbles are gone)
5. Put in oven for 4 hours at 75° C
6. Take out of oven and let cool for at least 5 minutes
7. Cut out device from the molds
 - a. Cut edges very closely to mold to make sure there are no ridges at the bottom of the device where the membrane is going to lay flat on
 - b. Once edges around molds are cut, carefully remove molds from the device
8. Use a 1 mm biopsy punch to poke three holes through the device:
 - a. One hole goes over one side of the vacuum chamber for the pressure controller
 - b. Two holes go at the ends of the cell chamber to be the inlet/outlet for cells and cell culture media
9. Ensure the devices are mostly clean from dust and small pieces of PDMS (tape is useful for picking up debris off device)
10. Cut out the bottom PDMS membrane from the 125 μm sheet (use mold as size guide)
11. Wash PDMS membranes in container of 70% ethanol and dry with compressed air
12. Plasma treat membrane using plasma wand (as well as the bottom of device)

- a. Plasma treat the PDMS membrane for 1 minute, switch to bottom of device for 30 seconds, then return to PDMS membrane for another 30 seconds
13. Quickly flip PDMS membrane so that the side that has been plasma treated connects to the device and tap down membrane going from one side to another
14. Place weight on top of assembled device for 5 min to secure membrane seal
15. Place in oven (75° C) for around 5 minutes to further enhance seal
 - a. Wait a few minutes for device to cool after being in oven
16. Incubate the middle cell channel with 50 µg/mL of collagen I overnight at room temperature
 - a. The collagen I should be dissolved in 0.1% acetic acid to enhance adsorption
17. Flush out the collagen I with PBS
18. Store the device in the 4C fridge with PBS in it until ready for cell seeding
19. Immediately before cell seeding, sterilize the device for 10 min under UV

A.4. Setting up microfluidic perfusion system for pneumatic cell stretcher

1. Use an empty syringe to calibrate the auto-off on the syringe pump
2. Put blunt needle on syringe and collect up to 10 mL of cell media into syringe for each experiment run that day
3. Evacuate all air from the syringe by flicking and pushing out air
4. Place the syringe (with the needle) into syringe pump. Adjust the clasp mechanisms as needed
5. Cut two tube lengths (Tygon tubing), roughly a foot and a half and fit a lure lock adapter and blunt needle on one end of each tube
6. Use the other end of one of the tubes and connect it to the syringe. Start the syringe pump so that the fluid fills the entire tube
7. Keep the tube connected to the syringe partially inside the chamber
8. Once the cyclic stretch for the device is complete and it is ready for long-term perfusion, complete the following steps to finalize the setup
 - a. Gently open the holder and lift the device out so that the device can be laid onto a flat thin piece of glass
 - b. Lay the device on the glass by holding it just barely over the glass and putting just one end down. Then work your way along the device slowly putting it on the glass. This is to limit the amount of air bubbles between the glass slide and the membrane of the device
 - c. Begin running the syringe pump at 0.3 mL/hr. Wait until a drop of cell media forms at tip of the needle before putting it in the port on one end of the device
 - d. Attach the draining tube to the other port with the blunt needle, which will go to your “waste beaker” (i.e., a petri dish)
 - i. Place the outlet drain tube in the waste beaker and tape it inside the chamber microscopy chamber. Then tape the end of the drain tube to the container so that the cell media flows from the syringe to the device and out into the container

- e. Ensure the media is not leaking out anywhere and successfully perfusing through the device
- f. Image the device with desire parameters

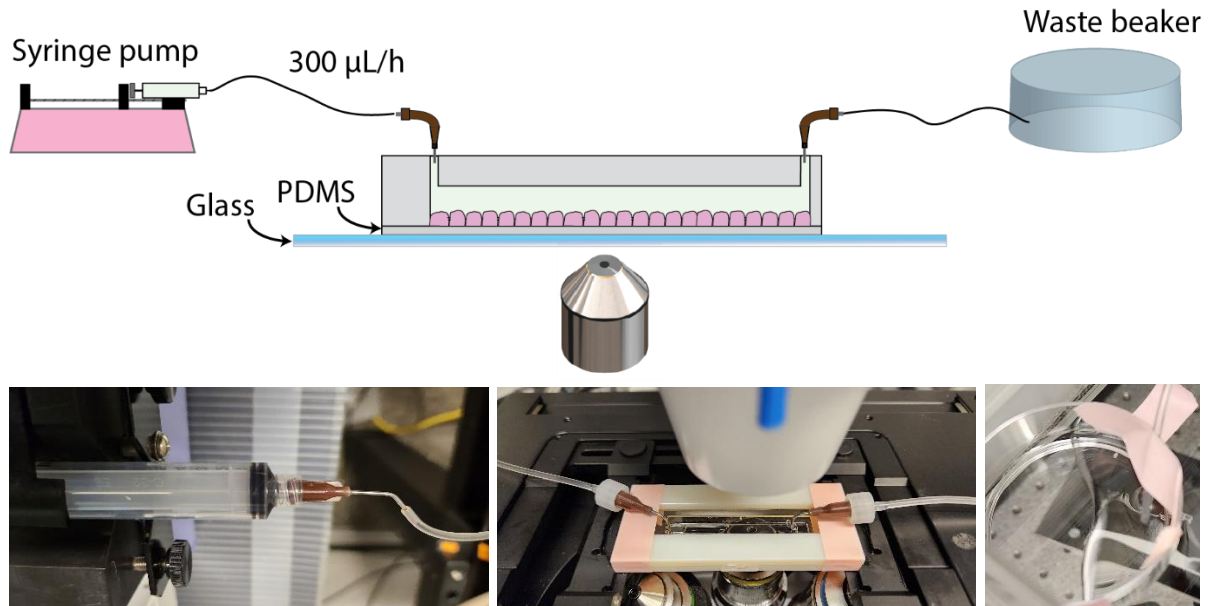


Figure A.0.1. Perfusion setup for cyclic cell stretching experiments

A.5. MDCK Cell Culture

1. Thaw cell vial from LN₂ storage and bring to culture in a T25 vented flask
2. Grow cells in dishes or flasks to ~75% confluence
3. in DMEM+10% FBS+ antibiotics (concentrations listed below).
4. Once cells reach desired confluency, split/passage the cells at a 1:10 ratio:
 - a. Aspirate off old media
 - b. Wash with 3-4 mls of sterile 1X PBS
 - c. Aspirate off PBS
 - d. Add 0.05% Trypsin-EDTA until cells visibly round up and come off dish (5-10 minutes)
 - e. Place trypsinized cells into sterile tube containing small volume (6-10 mls) of DMEM+10%FBS (this neutralizes trypsin) and centrifuge at low speed (200g or 200 rcf) for 5 minutes to pellet cells.
 - f. Aspirate off supernatant above the pellet
 - g. Resuspend cells in desired volume of culture media and plate at a 1:5 dilution (e.g., Take 200 uL of cell suspension If you resuspended in 1 mL)
5. Cells will need to be passaged every 3-4 days

6. Use the following culture media:
 - a. Low glucose DMEM (with phenol red)
 - b. 10% FBS
 - c. 1% PS

Recipe for basal medium used for microscopy experiments

The following reagents were mixed in water, pH adjusted to 7.0 using HCL, then filter sterilized with a 0.1 μm filter. This base media was then stored at 4°C for up to one year. When used for working media, Methionine, Calcium Chloride, and the MEM Vitamin Solution (100x) were added. For experiments, supplement the base medium with 50 mM HEPES, 10% FBS, and 1% PS.

Ingredient	Concentration (mg/L)
KCL	400
MgSO ₄ .7H ₂ O	200
NaCl	5963
D-Glucose (dextrose,monohydrate)	1000
L-arginine. HCL	126
L-cystine. 2HCL	31
L-glutamine	296
L histidine HCL. 2H ₂ O	42
L-isoleucine	52
L-leucine	52
L-lysine HCL	73
L-phenylalanine	32
L-threonine	48
L-tryptophan	10
L-tyrosine	52
L-valine	46
NaHCO ₃	1000
Na Hepes	2603
NaH ₂ PO ₄ . H ₂ O	140
Methionine	167
Calcium Chloride (CaCl ₂)	200
MEM Vitamin Solution (100×) (<i>Sigma, M6895</i>)	N/A

A.6. Primo micropatterning

Sample Preparation

1. Cut out PDMS “rings” from prefabricated sheets of silicone rubber (see “Protocol for cutting PDMS stencils” further down) with dimensions of 8 mm inner diameters and 12 mm outer diameters
2. Clean PDMS ring(s) by rinsing with 70% ethanol and air drying with N₂ gas
3. Plasma treat glass substrate⁴ (or glass bottom petri dish) for 5 minutes in the Harrick Plasma chamber on “high”
4. Immediately after plasma treatment, add the clean (and dry) PDMS ring to the center of the glass
5. Immediately add 100 μ L of PLL-g-PEG solution (100 μ g/mL)
6. Incubate PLL-g-PEG for 1 hour at room temperature

Patterning

1. To avoid dehydrating the sample, pull off ~85 μ L of the PLL-g-PEG, then rinse the inside of the PDMS ring (i.e., your patterning region of interest) thoroughly with PBS. This means ~10x washes
 - a. Do not touch the sample with the pipette tip!
2. Again, pull off ~85 μ L of the PBS so there is just a thin film covering the surface of the sample
3. Add 20 μ L of PLPP photoactivation agent to the sample (just enough to cover the sample surface)
4. After calibrating the PRIMO to the thickness of interest, place sample on the stage
5. Conduct your light exposure with digital masks and settings of interesting (will be different from project to project)

Protein Adsorption

1. When the light exposure for protein patterning is finished, remove ~10 μ L of the PLPP (again, we don't want to dry out the sample)
2. Rinse 5x with 150 μ L of PBS
 - a. Do not touch the sample with the pipette tip!
3. With just a thin film of PBS covering the sample, add 50-100 μ L of protein of interest (e.g. 100 μ g/mL of Oregon green gelatin)
4. Incubate for 1 hour in dark at room temperature

⁴ This protocol assumes patterning of #1.5 glass, but can be adapted easily for many other materials

5. Remove ~40 μL of the protein, leaving a thin film
6. Rinse the sample at least 10x with 150 μL of PBS. You do not want any residual protein in your solution
7. Leave the protein patterns in PBS for cell seeding, imaging, etc.

A.7. Gluing beads on micropipettes for custom probes

List of materials

- BIC Pocket Lighter
- Pulled glass micropipette tips (e.g., 20 μm diameter- WPI TIP20TW1)
- Borosilicate glass beads (e.g., 30 μm diameter, Cospheric)
- Micromanipulator
- NOA 81 optical glue (Norland)
- Pipette tip holder (e.g., MXP Series Probe Holder, Siskiyou)
- Glass bottom dish, 50 mm outer diameter (FD5040-100)
- Handheld UV flashlight
- UV lamp

Protocol

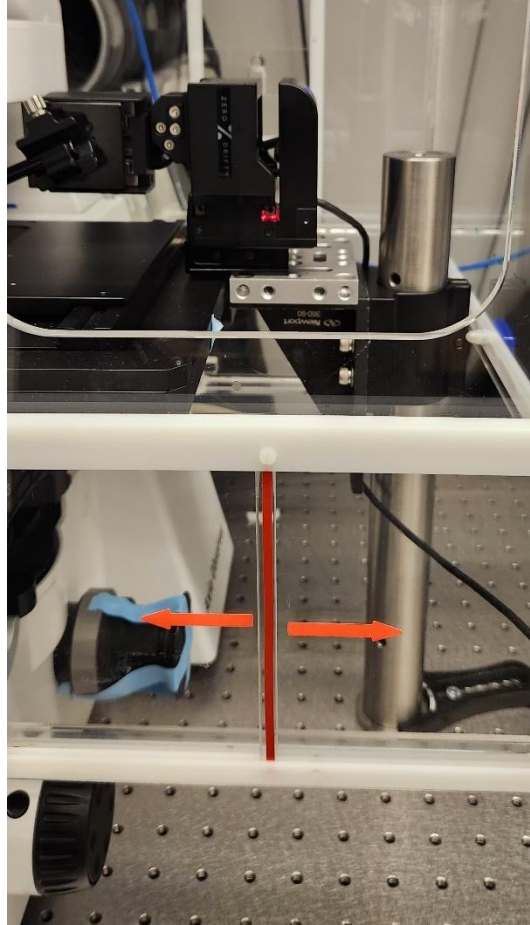
1. On the glass bottom dish, sprinkle your glass beads on one half of the dish and spread the optical glue on the other half of the dish
2. Put the dish on the stage of a microscope (I've used the Chewbacca microscope for this), which should also have a micromanipulator mounted to it. I've used the Sensapex piezo micromanipulator
3. Create a 45° bend 2/3 of the way towards the tip of the pulled glass micropipette tip using the BIC lighter. It will happen very quickly, so be cautious!
4. Insert the (no bent) pulled glass micropipette tip into the probe holder
5. Mount the probe holder onto the micromanipulator
6. Adjust the probe holder so that the pulled glass micropipette tip is pointing straight towards the bottom of the dish
7. Using the micromanipulator, move the pulled glass micropipette tip over the region with glue (using a 10x objective) and *gently* lower into the glue, no more than 5 microns. It will be clear when it contacts the glue. This part takes practice!
8. Move the glue-coated pulled glass micropipette tip to the region with beads, and align the circle of the pipette tip over any bead that is spaced out from other beads.
9. Gently lower the pipette tip down onto the bead. You will see it get pulled onto the pipette tip.

10. Raise probe as high as possible, remove it from the micromanipulator, and pre-cure the glue using the handheld UV flashlight for ~ 10 seconds.
11. Repeat steps 1-10 for as many probes as you would like to make
12. To finalize the UV cure, put all probes under a UV lamp for ~1 minute.
13. Store your probes (I've used old pipette tip boxes)

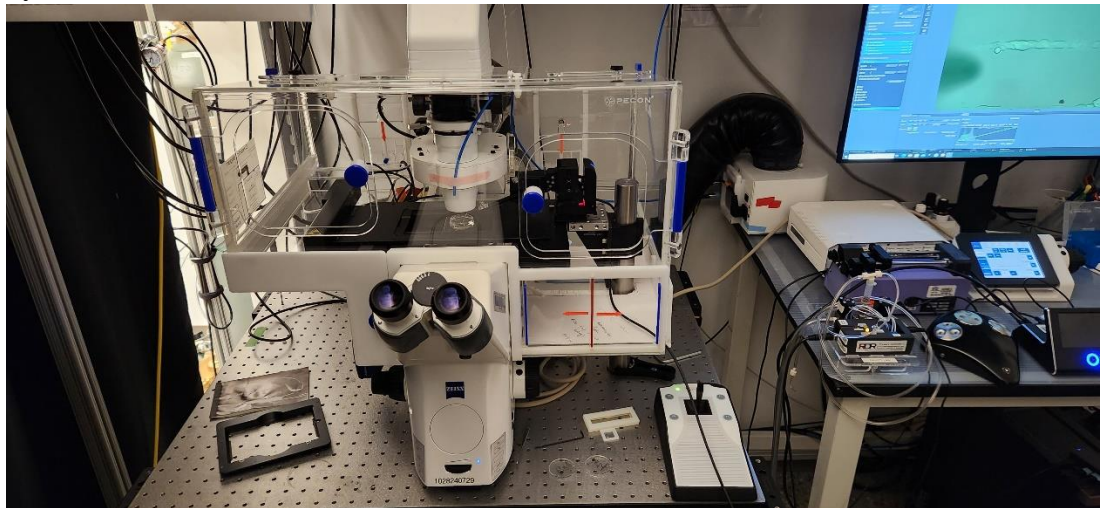
A.8. Setting up 1-D micromanipulation experiments

These experiments are not trivial to set up and have taken months of optimization and development. I've outlined a general procedure below, but the experiments will still take practice to set up. There are two unique elements to this setup: i) Custom micromanipulator mount for the microscope and ii) custom probes, as discussed in the preceding section

1. Remove the right acrylic panel of the microscope incubation chamber
2. Mount the Sensapex micromanipulator on a custom mount and bolt it to the optical table. You'll want to get the micromanipulator as close as possible to the stage without hitting it



3. Since the acrylic panel will no longer enclose the incubation chamber because of the rod supporting the micromanipulator, use a custom cutout from something like styrofoam

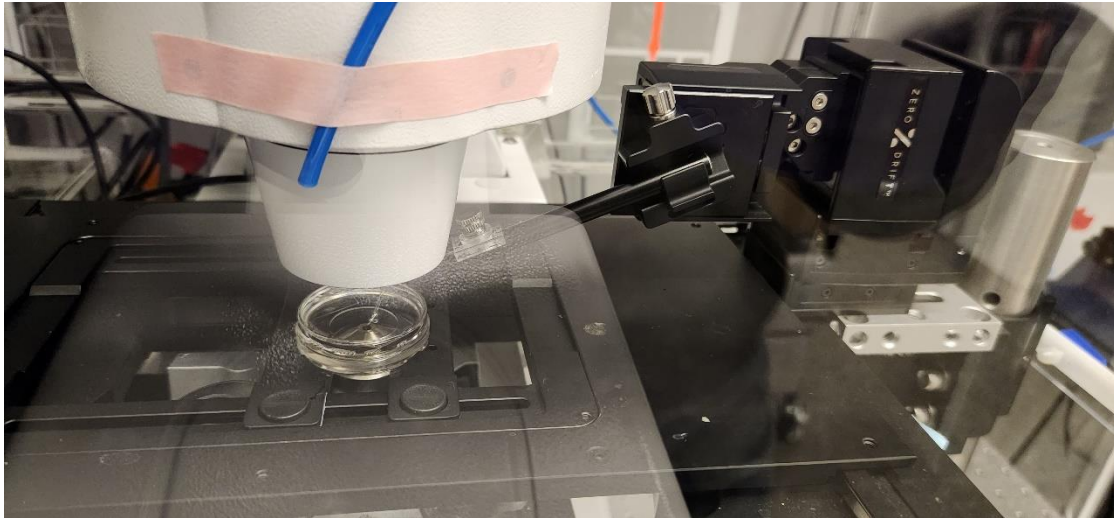


4. Let the chamber heat up for a minimum of 3 hours before experiments. There will be thermal expansion of the metal components you have now added to the chamber
5. Prepare/functionalize a bead-tipped glass micropipette (made from preceding section)

- a. On a 100 mm polystyrene dish, tape down the probe with kapton tape so that the bead is sticking up in the air
 - b. Plasma treat for 1-5 minutes in Harrick Plasma chamber on high
 - c. While the probe is being plasma treated, prepare a well of collagen I solution (50 $\mu\text{g}/\text{mL}$, 100 μL) in an 8 mm inner diameter PDMS ring. This should be in a new dish
 - d. When the probe is plasma treated, immediately rest the probe on the PDMS ring so only the tip is incubated in the collagen I solution
 - e. Incubate for 1 hour at room temperature
 - f. Rinse the probe with PBS and store at 4°C until experiment
6. Prepare 1-D epithelial lines for experiment
 - a. Assuming you've already grown the 1-D lines, wash them thoroughly with PBS. It is important to have no unadhered cells in your solution. Do not use vacuum to rinse, or this will rip off the lines. Use a p1000 for rinsing and aspirating PBS 10x.
 - b. After rinsing the lines, add 3 mL of homemade imaging media (see MDCK Cell Culture)
 7. Place your 35 mm glass-bottom dish with cell lines on the stage holder of the microscope
 8. Rotate the dish so that the lines are perfectly lined up with the camera, maximizing the amount of line that you can see per field of view
 9. Remove the lid of the dish
 10. *This step is tricky:* Place your collagen coated probe in a probe holder, then mount it to the micromanipulator
 - a. Make sure the micromanipulator is raised all the way before doing this step
 11. The goal is to mount the probe so that the tip with the bead is just a few mm above the media
 12. Lower the probe with the micromanipulator until it hits the liquid. Then stop immediately
 13. By eye, adjust the probe tip with the micromanipulator in the x and y directions so that it is directly over the objective.
 14. Using the 10x objective, find the tip of your probe
 15. Once you find the tip of your probe, gently lower and probe until you get it ~150 μm above the glass surface
 16. Add 3.5 mL of light density mineral oil to the top of the dish, sealing the media and preventing evaporation
 17. Let the sample sit for 1-2 hours to overcome thermal drift and get to equilibrium
 18. You are now ready to begin your experiment!
 - a. Move to the 20x objective
 - b. Lower the probe (slowly) until it is ~10 μm above the glass surface
 - c. Find a continuous line of cells (15-20 cells total) that cover the entire line and bring the bead near it

- d. Lower the probe so that it is $\sim 1 \mu\text{m}$ above then surface. The bead circumference should be clearly in focus and if you lower against the glass the bead will start deflecting to the side
- e. Move the bead flush against the end of the cell line. You may need to push 1-2 microns against the cell.

19. Begin imaging and rest of experiment



⁵A.9. Immunohistochemistry protocol

Necessary Solutions:

- Permeabilization buffer - PBS + 0.1% Triton X-100
 - Ex: 250mL PBS + 250 μL Triton X-100
- Blocking buffer - PBS + 0.3% Tween20 (1X) + 2% BSA
 - Ex: 250mL PBS + 37.5 μL 20X Tween20 stock solution + 50mL 10% BSA stock solution
- Antibody dilution buffer - PBS + 0.1% Tween20 (1X) + 1% BSA
 - Ex: 250mL PBS + 12.5 μL 20X Tween20 stock solution + 25mL 10% BSA stock solution
- Wash buffer - PBS + 0.1% Tween20 (1X) + 1% BSA
 - Ex: 250mL PBS + 12.5 μL 20X Tween20 stock solution + 25mL 10% BSA stock solution
- **Note:** 0.1% Tween20 means 0.1% of the 1x solution (and 0.3% means 0.3% of the 1x solution)

⁵ This protocol was originally written by Orlando Chirikian and Kerry V. Lane, and has been adapted here

- Ex: for 250mL of wash buffer, you would use 12.5μL from the 20X Tween20 stock bottle
- **Note:** 1% BSA means 1% in the final solution (not 1% of the stock solution)
 - Ex: for 250mL of wash buffer, you would use 25mL (1:10 dilution) from the 10% BSA in PBS stock bottle

Protocol:

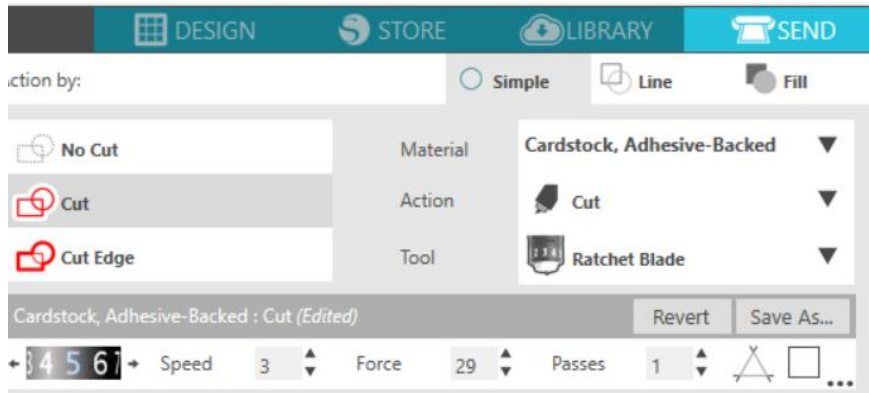
Fixing cells

1. Incubate with 4% PFA at room temperature for 30 minutes
 - a. Can instead incubate with cold methanol (-20°C) at room temperature for 10 minutes
2. Aspirate the PFA and dispose in the specific PFA waste container
3. Rinse 3 times with PBS
 - a. Add ~1.5mL PBS, let sit for 5 minutes, aspirate, add another ~1.5mL PBS [repeat 3 times]
 - b. Note: the first rinse with PBS should also be disposed of in the PFA waste container. After the first rinse, the rest can go in normal waste
4. Store in PBS until ready to proceed with staining
5. Staining with antibodies
6. Incubate with ~1mL/well permeabilization buffer at room temperature for 5 minutes
7. Aspirate permeabilization buffer, then incubate ~1mL/well blocking buffer at room temperature for 30 minutes to an hour
8. Aspirate blocking buffer, then incubate with primary antibody for 1 hour at room temperature or overnight at 4°C
 - a. Dilute your antibody in dilution buffer described above
 - b. Check/optimize antibody dilution for your specific primary antibody, we commonly dilute primary antibodies 1:200
 - c. Use as little antibody as possible! These are very expensive
9. Aspirate antibody solution, then wash 3 times with 1mL wash buffer
10. Aspirate wash buffer, then incubate with secondary antibody for 1 hour at room temperature in the dark
 - a. Again, dilute your antibody in dilution buffer described above
 - b. We use 1:500 dilution for most of our secondary antibodies
11. Aspirate antibody solution, then wash 3 times with 1mL wash buffer
12. Store in PBS, covered in foil to prevent bleaching of secondary antibody fluorophores

A.10. Protocol for custom PDMS stencils

1. Make your design in SilhouetteStudio software on the “design” tab, then click on the “send” tab when finished

2. Plug in computer/laptop to the Silhouette Cameo via USB
3. Click on the power button on the Silhouette Cameo (right side)
4. Remove the clear cover sheet of the cutting mat and adhere a sample of your PDMS sheet
 - a. For pre-made PDMS sandwiched in plastic sheets, remove the top side and stick the plastic side against the mat. This leaves the PDMS face up
5. Lift the front hood to reveal the cutting mechanism and front rollers and align/insert the mat between the white rollers (indicated by blue arrows)
6. Click “load” on the screen of the Silhouette Cameo, locking in the cutting mat
7. Depending on the thickness of your sample, you may need to adjust the cutting depth (bottom left of image below)
 - a. 1 for thin samples, 10 for very thick samples
 - b. 5 is a good default (used for 200 um thick PDMS)
8. Adjust the settings to those shown below and hit the send button at the bottom



- a.
9. When the job is finished, be sure to press “unload” before removing the cutting mat
10. When finished, re-cover the cutting mat with its cover sheet
11. Turn off the Silhouette Cameo using the same power button as before (right side)